The University of Nottingham

Institute of Engineering Surveying and Space Geodesy

Real-time Deformation Monitoring of Bridges Using GPS/Accelerometers

by

Xiaolin Meng

Thesis submitted to the University of Nottingham

for the degree of Doctor of Philosophy

May 2002

Abstract

The need for conducting real-time bridge deformation monitoring is addressed in the context of the development of bridge management system (BMS) and land transportation safety in this thesis. Current instruments used for bridge dynamic deformation monitoring are compared in terms of system productivity and reliability. An integrated sensor system of Global Positioning System (GPS) receiver and triaxial accelerometer is then proposed with the capabilities to accurately monitor long-term deformation and short-term dynamics of a bridge. Since the investigation of the bridge dynamic responses is of great importance in research and practice, the emphasis of this thesis is on the monitoring of dynamic bridge deformation.

Zero baseline (ZBL) and short baseline (SBL) tests are conducted to evaluate the performance of three types of Leica GPS receivers at 10 Hz sampling rate. Statistic characteristics of positioning solutions and the achievable accuracy of each receiver type are analysed, which are employed to design optimal filters for various GPS error suppressions. By using a moving average (MA) technique, millimetre baseline accuracy can be achieved even with a single frequency receiver. It demonstrates the possibilities to conduct millimetre bridge deformation monitoring if appropriate filtering techniques are applied to the positioning solutions and integer ambiguity has been fixed. A simple but accurate triaxial accelerometer calibration technique is proposed in the thesis with a solid mathematical derivative to evaluate the precisions of estimated parameter offsets.

A specially designed cage is used to house a GPS antenna with a triaxial accelerometer to avoid complex sensor alignment and simplify the coordinate transformations between different reference frames. The determination of instantaneous attitude of an accelerometer body frame is realised by three GPS stations on the deck of a bridge at a rate of 10 Hz and the sensed 3D accelerations are then transformed into a bridge coordinate system (BCS) simultaneously. BCS is the computation frame of a hybrid bridge deformation monitoring system (BDMS).

Important issues in sensor integration such as local gravity determination, synchronisation of time series from different sensors are addressed.

Bridge trials are briefed with the emphasis on the instrument configuration for effective error mitigation and sensor integration. A group of reference stations consisting of two reference stations closely setup near a bridge and the permanent continuous GPS stations are recommended for reducing relative tropospheric delay, multipath, and receiver noise both at reference stations and monitoring sites.

GPS satellite sky distribution and its impact on propagating ranging errors in mid latitude areas such as in the UK and high latitude areas are analysed both with analytical and simulation approaches. The error propagation formulae are derived to analyse the defects of current satellite constellation on the GPS positioning solutions in each direction of a BCS. This is further exploited to improve the component accuracy of particular interest through changing the dilution of precision (DOP) values. The degree of positioning improvement is illustrated with GPS/GLONASS positioning. A simulator according to ranging error propagation is used to simulate the achievable accuracy from the *best* and the *worst* GPS constellations. Modified precise satellite ephemeris by inserting the positions of pseudolites is employed to investigate the changes of DOP values in each direction of a BCS. The summaries of this simulation have universe significance in guiding the selection of the best locations of pseudolites.

Adaptive Finite Impulse Response (FIR) filtering or adaptive filtering (AF) for short and important application issues are addressed in the thesis. Autocorrelation lags of ZBL and SBL tests of each type of receiver are used to determine the filter lengths according to the fundamentals of low pass and high pass filter designs. A real-time AF algorithm is introduced and widely employed as an analytical tool in the error mitigation and real bridge deformation signal extraction. The application defects of MA technique in bridge deformation monitoring are compared with AF approach according to the component analysis of GPS positioning solutions. A recursive AF algorithm is proposed to gradually isolate actual bridge deflection signals from multipath and receiver noise both at reference stations and monitoring sites. Spectral analysis is applied to the input and output signals to investigate the efficiency of the

designed filter. In order to effectively isolate actual bridge deformation, misalignment and its consequence are demonstrated with day-to-day shifted time series of bridge deflection. Cross-correlation is also used to analyse the feasibility and efficiency of the proposed AF algorithm.

Acceleration aided AF approach is detailed in the thesis. A simple algorithm, based on the principles of digital signal filtering and optimal filter design, is proposed to estimate relative displacements of bridge sensed by a triaxial accelerometer in three dimensions. With the relative displacements, GPS receiver noise has been filtered out and the cleaned displacements are obtained. AS another data fusion approach, a software package based on discrete Fourier transform (DFT) to integrate GPS and accelerometer data with a position output rate up to that of a triaxial accelerometer is introduced.

Relative tropospheric delay is another major error source identified in GPS-based bridge deformation monitoring. Methods applied to distinguish the impacts of multipath and tropospheric delay are presented. The cause for relative tropospheric delay is analysed and microclimate effect is recognised as the major impact factor in this particular environment. Numerical calculations also confirm the assumption. The way to effectively remove relative tropospheric delay is recommended.

The research emphasis in this thesis is to develop a prototype of a hybrid BDMS to achieve centimetre level positioning accuracy at each epoch in three dimension of a BCS. The findings from this research are summarised and the future work is predicted.

Acknowledgements

This research was carried at the Institute of Engineering Surveying and Space Geodesy (IESSG) within the School of Civil Engineering at the University of Nottingham. The research was partially sponsored by Leica Geosystems Ltd. (UK), the University of Nottingham, and Mott MacDonald.

I would like to express my sincere thanks to Dr Gethin Roberts and Professor Alan Dodson for their supervision, encouragement, and trust.

The author would like to give special thanks to all members of the IESSG, past and present, who have helped with this thesis. Mr Mark Concannon and Ms Juliet Ezechie of Leica Geosystems Ltd. (UK) are highly appreciated for providing the opportunity and resources required for this research. Special thanks are due to Dr Andrew Evans and Mr Andrew Nesbitt who helped data collection and instrument preparation. Ms Emily Cosser, Dr David Baker, and Dr Evans again are acknowledged for having proofread some chapters of this thesis and provided invaluable suggestions. The author is very grateful to Professor Yongqi Chen in Hong Kong Polytechnic University, Professor Terry Moore, Dr Richard Bingley, Dr Martin Smith, Dr Wu Chen, Mr Norman Teferle, Dr John Owen, Dr Chris Hill, Dr Caroline Noakes, Mr Theo Veneboer, Mr Michael Pattinson, Mr Christopher Hide, and Ms Clare Spencer for their long-term support, concern, and advice. Mr Chris Brown of Brunel University is acknowledged for his advice in data processing.

The author would like to thank Severn Trent Water and Arup for permitting the trials on the Wilford suspension footbridge in Nottingham and the London Millennium Bridge.

Thanks also go to Dr Junfei Yin of Cranfield University and Mrs Ping Shen for their sincere helps in many aspects.

Finally, I would like to express my deep gratitude and appreciation to my wife, Jun Ye, my son, George Meng, my parents-in-law and my own parents, and my grandmother for their understanding, love, continuous support, encouragement and great sacrifice throughout the years of my study. Special thanks should go to my sisters for accompanying our parents since I started my university life twenty-two years ago.

Table of Contents

Chapter 3 Instrumentation and Quality Evaluation

Chapter 4 Hybrid Sensor System for BDMS

Chapter 5 Bridge Trials

List of Figures

Chapter 2 GPS-Based Bridge Deformation Monitoring

Chapter 3 Instrumentation and Quality Evaluation

Chapter 4 Hybrid Sensor System for BDMS

Chapter 5 Bridge Trials

Chapter 6 GPS Satellite Sky Distribution and Its Impact on Positioning Accuracy for Bridge Monitoring

Chapter 7 Adaptive Filtering (AF) and Its Applications in BDMS

Chapter 8 Applications of AF and Spectral Analysis to GPS/Triaxial Accelerometer-Based BDMS

Chapter 9 Relative Tropospheric Delay and Its Estimation

List of Tables

Chapter 8 Applications of AF and Spectral Analysis to GPS/Triaxial Accelerometer-Based BDMS

Chapter 9 Relative Tropospheric Delay and Its Estimation

Chapter 1

Introduction

1.1 Bridge Deformation Monitoring

Bridges are important infrastructures in the national economy. They serve as the crucial links in the transport network. Owing to many bridge failures caused by the normal or abnormal loadings bridge safety and its monitoring are the vital tasks in bridge maintenance and management. With the developments of the economy, more and more long span and flexible bridges will be built to meet the demands of daily increasing traffic. Bridge safety will become an even more serious problem faced by bridge authorities.

Data about bridge performance are used to detect potential bridge failures and help improve future bridge design codes. The ability to collect large, timely, and accurate bridge performance data, such as the change in the bridge's geometric dimensions and the dynamic responses to the varying loadings in a real-time or near real-time mode, is of great interest to bridge agencies.

A suspension bridge usually characterises two kinds of distinct deformations, i.e. the long-term movement caused by foundation settlement, bridge deck creep and stress relaxation, and the short-term dynamic motion of the bridge, such as those induced by wind, temperature, tidal current, earthquake, and traffic. Unlike the long-term bridge deformation, which is irrecoverable, the latter deformation is called a deflection since the deformable object will recover to its original status with the release of loadings, unless under an extreme loading, permanent damage or deformation is caused.

Conventional instruments and analysis techniques used in bridge deformation monitoring usually have one drawback or another and hence they cannot serve as appropriate tools in monitoring those two kinds of bridge deformations simultaneously.

As an alternative, Global Positioning System (GPS) technology has shown its many merits in deformation monitoring in its earlier development stage. The advance of GPS technology makes satellite positioning a more reliable and accurate technique. Like any other developing technology, GPS technology has its defects when it is applied for precise engineering applications. Achievable accuracy of GPS positioning solution is recognised as a major barrier, which is affected by many factors and restraints. In particular, multipath is one of the major limitations. Even though many efforts have been made in multipath mitigation, an effective solution is still elusive.

Slow sampling rate is another limitation when GPS technology is employed to monitor short-term bridge deflections of high frequency vibration.

GPS has been used to monitor long suspension bridges in the world in recent years. Examples are the GPS trials on the Humber Bridge (Roberts et al. 1999), the Akashi Kaikyo Bridge (Fujino et al. 2000), and the Tsing Ma Bridge (Wong et al. 2001). While GPS positioning demonstrates that it is a viable technique for detecting large deflections with slow vibration frequencies, its capability to monitor the vibration amplitudes of several centimetres with high vibration frequencies is uncertain since multipath and other errors can reach several centimetres. To obtain and maintain centimetre positioning accuracy within a dynamic environment of bridge vibration and continuous changes of satellite constellation is far from an easy task by GPS system alone.

The accuracy of GPS positioning solutions is affected by the satellite sky distribution. Various ranging errors can propagate into positioning solutions via dilution of precision (DOP). The error propagation has been analysed in WGS84, in terms of latitude, longitude, and height. However, the sky distribution of the GPS satellites and its impact on 3D positioning accuracies of bridge deflections in a bridge coordinate system (BCS) has not been studied yet.

Since the height differences between stations at long suspension bridge sites can reach several hundreds of metres, relative tropospheric delay can introduce positioning errors of several centimetres (Roberts, 2001b). To conduct GPS-based bridge deformation monitoring and establish a practical bridge deformation monitoring

system (BDMS), more detailed research is needed to cope with the impact of relative tropospheric delay.

Due to the inherent defects of GPS-based BDMS, inclusion of other independent sensors into this system to form a more reliable and robust system is a direct consideration. A triaxial accelerometer can be used to identify high frequency bridge vibration accurately, and more importantly, it is a self-contained system. External interferences will have less impact on its operation. A triaxial accelerometer can remedy the defects of a GPS-alone system and largely increase whole system's reliability and productivity by providing more measurements. The problems in sensor integration and data fusion need to be further addressed. Since the positioning errors of accelerometers can grow rapidly over time, approach and algorithm also need to be developed in order to overcome this problem before the displacements measured by two independent sensors can be compared.

1.2 Research Objectives

The main objectives of this research are to develop a prototype of a hybrid BDMS to achieve centimetre level positioning accuracy at each epoch with the current GPS technology aided by a triaxial accelerometer. The whole system and methodology employed in data processing and analysis can be transplanted to monitor the deformations of other flexible structures.

The achievable accuracy of GPS receivers used by BDMS needs to be quantified. Zero baseline (ZBL) tests can be used to evaluate the magnitude of the GPS receiver related random noise. Short baseline (SBL) tests are employed to address the performance of GPS receivers when exposed to various error sources. Conventional ZBL and SBL tests focus on the GPS receiver's performance at a relative slow sampling rate, for instance, a period rate of thirty seconds. The performance of the GPS receivers used for kinematic positioning at a high sampling rate needs to be studied. Zero biases and scale factors of a triaxial accelerometer are two kinds of important parameters in the determinations of the accelerations sensed in each input axis (IA). These parameters change their magnitudes from wear and tear. Finding a

way to check these changes regularly and accurately is the prerequisite for the formation of a precise hybrid sensor system.

A triaxial accelerometer has been included into a hybrid BDMS for two reasons. Firstly is to expand the measurable frequency band of GPS-alone BDMS. Secondly, if appropriate treatments have been applied to the accelerations, the accelerometer can provide accurate 3D displacements of a bridge. This second benefit is more important in a BDMS. To fully explore the advantages of a hybrid sensor system of GPS receiver and triaxial accelerometer, sensor integration, algorithm, and data fusion are one of the research focuses of this thesis.

The reliability and feasibility of instruments, dedicated software developed for this integrated system, and analysis techniques can only be verified through the real bridge deformation monitoring trials. The lessons learnt and the findings can help form a more practical and reliable system. The ability to conduct real bridge trials for evaluating overall sensor system is an important objective of this thesis.

GPS data gathered, processed, and analysed from the London Millennium Bridge and also from other bridge trials and the comparisons of GPS positioning solutions with deformations sensed by a triaxial accelerometer reveal the deficiency of the GPS satellite sky distribution, particularly in mid latitude areas, as in the UK, and high latitude areas. Further research into the various ranging error propagation through GPS satellite constellation and relevant improvement strategy is required which is one important research objective of this thesis.

High-level multipath signature both at reference stations and monitoring sites on bridge deck is evident in the positioning solutions of GPS measurements. It is very difficult to detect the information about the actual bridge deformation from such highly polluted positioning solutions. Research on an effective multipath mitigation technique in the context of bridge monitoring is one of the research emphasis in this thesis.

Real-time adaptive filtering (AF) can be employed to detect various error sources and extract real bridge deformations. Filter design, mainly filter length and convergence

parameter, signal identification including information extraction of bridge deformation, error modelling and analysis, and bridge deformation interpretation are important aspects of this research.

Relative tropospheric delay under the scenario of bridge deformation is characterised by resulting positioning error of several centimetres. The effective way to evaluate and remove the impact of relative tropospheric delay from the kinematic positioning solutions of a BDMS is essential for achieving centimetre positioning accuracy, which is another important task of this thesis.

1.3 Thesis Overview

There are ten chapters in this thesis.

The first chapter is a brief introduction of the research objectives attempted to achieve in the thesis.

Chapter 2 is the document review. The importance of bridge safety monitoring is briefed with the development of bridge management system (BMS). As a sub-system of a BMS, current BDMS research is summarised. The advantages and defects of GPS-based BDMS over other monitoring techniques are compared. The need to augment a GPS-alone BDMS with triaxial accelerometers to form a uniformed and reliable BDMS is emphasised.

Chapter 3 is an introduction to the experiments and associated approaches used to evaluate the quality of GPS receivers and a triaxial accelerometer. The results from ZBL and SBL tests with three types of Leica receivers and antennas are analysed and compared, with the focus on the evaluation of the achievable accuracy of each kind of receivers. The autocorrelation coefficients calculated from ZBL and SBL tests are further exploited to determine the AF filter lengths, which are important parameters in the optimal filter design. A simple but accurate approach for triaxial accelerometer calibration is proposed at the end of this chapter.

The issues of a hybrid BDMS are discussed in Chapter 4. Algorithms and approaches of coordinate transformations between different reference frames are proposed. Particular attention is on the determination of the accelerations in a BCS in a real-time mode, which is the basis of GPS and accelerometer data integration.

Controlled platform tests and actual bridge trials supporting this thesis are summarised in Chapter 5. The data collected from these experiments are employed as sample data sets in the following chapters for the discussion of each specific topic.

Satellite sky distribution and its impact on the positioning accuracy degradation in mid to high latitude area are analysed within a BCS in Chapter 6. The solutions to improve positioning accuracy under current GPS satellite constellation are proposed. How to improve positioning solutions by an integrated system of GPS and GLONASS is demonstrated with the data collected from Humber Bridge trials. A simulator is developed with Matlab M-programming technique to analyse the effects of the *optimal* and the *worst* GPS/pseudolite constellations and the potential accuracy improvement in each direction of a BCS. Simulations using the modified precise GPS satellite ephemeris by inserting in each epoch positions of the pseudolites are further conducted to help select the optimal locations of pseudolites under the actual scenarios in the deformation monitoring of the London Millennium Bridge. The conclusion from these simulations can be employed as the general criteria for the future work.

The fundamentals of adaptive finite impulse response (FIR) filtering are introduced in Chapter 7 with the emphases on how to apply it for the data processing and analysis in the context of bridge deformation monitoring. Issues in the optimal filter design are addressed, which include filter length determination and convergence parameter calculation. A real-time Matlab AF software package is developed based on an optimal filter design. Included in this chapter is a discrete Fourier transform (DFT) and inverse DFT (IDFT) based algorithm used for integrating data from a GPS receiver and a triaxial accelerometer. Detailed software development and the results from a controlled platform test which is described in Chapter 5 are introduced.

The practical applications of the developed AF approach in the GPS noise suppression and the extraction of the real bridge deformation are introduced in Chapter 8 with sample data sets from the bridge trials introduced in Chapter 5. A recursive AF approach is proposed and its efficiency is verified in the data processing and deformation analysis. Spectral analysis technique is employed to identify the frequency band of bridge deflections. A simple algorithm is proposed to cope with the drift problem in the acceleration integral for the relative displacement estimation. An acceleration aided AF approach is invented to isolate real bridge deformation and again the efficiency of the proposed approach has been validated by spectral analysis of the input and output signals.

Relative tropospheric delay is recognised as the major error source in GPS-based BDMS. Height differences are recognised as one of the main factors responsible for the delay. For the Nottingham Wilford suspension footbridge, the height differences between two reference stations of 3.6km plane distance are within several tens of meters but the kinematic positioning solutions of the reference stations characterises an apparent *moving* pattern at a magnitude of several centimetres. Multipath impact has been excluded out from the potential impact factors by analysing the cross-correlation coefficients and the magnitudes of day-to-day positioning solutions at the reference stations. Local microclimate is identified as a major impact factor causing such a relative tropospheric delay. Numerical examples using the actual meteorological parameters collected at both reference stations also suggest the similar amplitudes of relative tropospheric delay. Usage of an AF approach, for a real-time relative tropospheric delay estimation, is illustrated and its potential meteorological applications are predicted.

Included in the final chapter are the conclusions, recommendations, and suggestions for future work.

Chapter 2

GPS-Based Bridge Deformation Monitoring

2.1 Introduction

Bridges are designed to withstand various forces, such as wind, traffic, temperature, tidal current, and extreme loadings, for example earthquake, flood, and typhoon. These forces are the main factors considered in bridge design and govern in part the bridge's performance and life expectancy. Unlike long-term settlement of bridge foundations, which can be easily monitored with conventional surveying instruments, the dynamic deformation behaviour or deflection of bridge has been of concern to civil engineers for many years. Typical examples of dynamic performance in long flexible structures are lateral vibration caused by wind, vertical movement induced by traffic and change of ambient temperature or operating forces in machinery, and accelerating movement immediately proceeding the failure of geotechnical structures such as anchorages.

In recent years a large number of bridges have incurred damage attributed to impact and fatigue. Obviously, the ageing and increase of vehicular weights and traffic volumes in the last two to three decades have been the contributing factors.

For instance, about half of the 600,000 highway bridges in the United States were built before 1940 (NCHRP 1987). Most of these bridges were designed for less than current traffic volumes, smaller vehicles, lower speeds, and lighter loads than are presently found on the highway networks. Additionally, even for some newly constructed bridges, deterioration caused by service conditions and deferred maintenance is a growing problem. Almost half of these bridges have been classified as structurally deficient or functionally obsolete by the Federal Highway Administration (FHWA) of the USA. The cost of remedied work and replacement was estimated at more than $50 billion (in 1987). However, only about $2 to $3 billion annually has been available which is insufficient to address all deficiencies.

The limited funds therefore must be carefully allocated to bridges which are of the greatest significance to transport network as a whole.

Transport authorities in other countries are in a similar situation. For instance, the UK's Kingston Bridge in Scotland had a major repair and retrofitting program to fix critical defects (Duff and Hyzak 1997). The London Millennium Bridge was closed on 12 June 2000 due to unexpected lateral movements (Dallard et al. 2001).

Since 1988, capital expenditure on the UK trunk road bridge maintenance has exceeded £800 million (Das 1997). The main driver for more than 80% of this expenditure has been the need for safety improvement.

On the other hand, advances in bridge design techniques and innovative construction materials as well as rapidly increasing traffic volumes, have resulted in more *efficient* bridges. Detailed bridge monitoring is required to investigate the performance of these new types of bridges. Table 2.1 lists the ten longest suspension bridges in the world, as measured by their main spans in metres (http://www.hut.fi/). The final column lists the year of opening to the public.

No.	Bridge Name	Span(m)	Location	Country	Year
1	Akashi Kaikyo	1991	Kobe-Naruto	Japan	1998
2	Great Belt East	1624	Kosor	Demark	1998
3	Runyang	1490	Zhenjiang-Yangzhou	China	2005
4	Humber	1410	Kingston-up-Hull	UK	1981
5	Jiangyin	1385	Jiangyin	China	1999
6	Tsing Ma	1377	Hong Kong	China	1997
7	Verrazano-Narrows	1298	New York City	USA	1964
8	Golden Gate	1280	San Francisco	USA	1937
9	Hoga Kusten	1210	Kramfors	Sweden	1997
10	Mackinac	1158	Mackinaw City	USA	1957

Table 2.1. Ten longest suspension bridges

Currently, the world's longest suspension bridge is in-service in Japan, and there are plans for even longer main span bridges, both in Japan and elsewhere. Japanese officials indicated that they tried to extend the main span length to 2,400 meters, clearly a daunting challenge for suspension bridge design, construction, and

management in the new millennium (Cooper 1998). Undoubtedly, this trend will challenge the bridge monitoring community to provide new systems and approaches to assure the safe operation of bridges.

Generally speaking, the external environment encountered by a suspension bridge is hostile, which makes bridge safety a very complicated issue. Environmental factors include:

- High speed scour of tidal current and wind
- Risk of ship's collision with the bridge's main piers
- High level of bridge corrosion due to the damp and saliferous air (oceanic environment)
- Proximity to an earthquake epicentre (for instance, there is a potential of a 8.5 Richter scale earthquake 150km away from the Akashi Kaikyo Bridge (Kashima et al. 2001))
- High density traffic loading
- Material deterioration and development of structural faults over time

Other factors affecting bridge safety would include inadequate original specifications of materials and methods, as well as design requirements.

Because of dense traffic volume and the huge investment in bridge design, construction, maintenance, and their critical roles in a transport system, any structural failure or damage would cause huge loss of life and property, and possibly affect the national economy. For instance, there are about 6 million vehicles each year passing across the Humber Bridge (http://www.humberbridge.co.uk/) and the total investment in the Akashi Kaikyo Bridge is over $3.6 billion with ten-year intensive construction (Cooper 1998).

2.2 Current Bridge Management System (BMS) Research

Long span suspension bridges are normally the vital links in the nation-wide transport system. These structures are very flexible and vulnerable to various types of loads, especially dynamic loads such as earthquakes and wind. Continuous monitoring of the structure is indispensable to ensuring traffic safety and structural soundness. Monitoring can also help reveal the real performance under severe loading, which can provide extremely useful information for understanding structure performance (Fujino et al. 2000). Data collected from monitoring procedures will form the most important part in a BMS. In a BMS, a BDMS acts as a sub-system for supplying timely bridge performance to a BMS.

Faced by factors such as increasing concerns about transport safety due to a series of bridge collapses and failures in recent years, and the fact that there are more than 10,000 new bridge defects reported each year, FHWA of the USA issued the Intermodal Surface Transportation Efficiency Act (ISTEA) in 1991. This aimed to improve land transportation safety and efficiency, and mandated the implementation of a quantitative computerised BMS by 1996 (http://www.tfhrc.gov/, http://www.bts.gov/).

A number of BMSs are now being developed and applied in various countries. The most advanced of these is the PONTIS system developed in the USA in 1991 (Thompson 1993). PONTIS is a network-level BMS, comprising three main modules: recommendations; optimisation and improvement to optimise budgets; and programmes for maintenance and improvement of a state's full inventory of up to 42,000 structures. This research was motivated by ISTEA, a series of highly publicised bridge failures, and emerging professional consensus within the USA on what essential ingredients a BMS should contain. PONTIS is in fact a planning tool; a decision support system which helps bridge managers to make use of the vast database of bridge inspections and the information provided by other agencies to make more informed policy and programming decisions.

In 1988, the UK Department of Transport (DOT) started a major programme of bridge inspection on the trunk road network, in accordance with the Department's Bridge

Assessment Code (Das 1997). The DOT first published an assessment code for older bridges in 1967. This formed the basis of an assessment called *Operation Bridge Guard* which considered highway bridges with a capability less than that required by the then national bridge design standard. When carrying out an assessment programme involving a large number of structures, it is necessary to provide assessing engineers with reliable tools and information on both historical and current situations to enable consistent engineering assessment. The latest technical information, which will give a more realistic picture of actual structural strength, should be made widely available. This emphasises the importance of adopting standard quantitative and accurate bridge inspection methods to feed a BMS database with timely, accurate, and reliable bridge condition information which is then given to the field engineers (Harding et al. 1996). It is well known that the analysis results that the system could provide are only as good as the original information. No matter how sophisticated and elaborate the analysis is and no matter how elegant the algorithms employed are, in the final analysis, the recommended decisions cannot be any better than the data upon which they are based.

In the past, most BMS researches have focused on the implementation of the system as well as the improvement of the mathematical models. Very little work has been published on improving the quality of the information that is required for these models or how to narrow the gap between the data required for the models and current inspection processes. In the USA in the 1990s, improvements in data acquisition technology for BMS became the research focus in the National Corporative Highway Research Program (NCHRP 1990).

Today these data are based almost entirely on the visual inspection of a bridge's condition. A bridge is given a rating according to indications of deterioration and distress. Whilst the rating of bridge element is defined in quantitative and engineering terms, this inspection system can only record condition on a overall rating, and does not provide detailed description of the condition that gave rise to the rating. There is no mechanism currently in place to record any other inspection information other than the condition rating in a current BMS. For example, the deterioration that does not manifest some visible symptom is not detected or quantified. This is especially true for certain types of hidden deterioration, such as corrosion of reinforcement in

concrete or cumulative fatigue loading in steel bridges. If the information about a bridge is inaccurate, the resulting analyses will not be optimal and totally wrong conclusions could be even reached from such an analysis.

Nondestructive Evaluation (NDE) testing including GPS technology, is the branch of engineering which is concerned the detection and evaluation of flaws in structural materials. Since bridge flaws can affect the serviceability of the materials or structures, NDE is an important approach in guaranteeing safe operation of structures as well as realising structure quality control and assessing bridge life span. The flaws may be cracks or corrosions in welds and castings, or variations in structural properties that can lead to loss of strength or failure in-service which cannot be detected by visual inspection.

For a BMS, NDE testing is used for in-service inspection and structural condition monitoring. It is also used for the measurement of components and spacing and for the measurement of physical properties such as hardness and internal stress. The essential feature of NDE is that the test process itself produces no deleterious effects on the material or structure under test (http://www.bindt.org/NDT.html).

By using NDE technique and also visual inspection, data about bridge performance are collected from a number of sources/nodes and transferred to a BMS database. A sophisticated analysis of the data is then performed. This generates a prioritised programme for bridge replacement and maintenance strategies for various funding and resource scenarios. It can predict the bridge deterioration over time and provide powerful decision-support tools to help formulate the best program for bridge management. The implementation of such a system will have tremendous benefit for bridge authorities. These procedures form the conceptual basis of a ‘Smart Bridge’ (Oshima et al. 2000). It is worth pointing out that as on e of NDE techniques GPS can be employed to detect geometric deformations of the monitored bridge. However, GPS cannot be used to detect the potential material corrosions and fatigues directly. The viability of GPS applications in these areas is the current research of a joint project between Cranfield University and the IESSG (Meo et al. 2002).

2.3 Bridge Dynamics and Evaluation

Wind tunnel tests are employed to study the dynamic responses of a bridge designed for wind loading. Loading tests that are required by a BMS, as an *afterwards* approach, are conducted to obtain the actual bridge dynamics supplemented by other in-service bridge monitoring techniques.

In a controlled loading test, a bridge is subjected to vehicular loading to generate dynamic forces with corresponding deflections and stresses in the bridge's components. In practice, the dynamic response of a bridge to a transiting vehicle is a complex process.

Research has revealed that bridge dynamic response is affected mainly by the dynamic response characteristics of the bridge (including the mass distribution, natural frequencies of bridge vibration, and vibration damping system); the dynamic characteristics of the vehicle (including speed, natural frequencies of vehicle vibration, suspension system, weight and number of axles); and the bridge's surface conditions (including roadway roughness, joint discontinuity, and approach slab condition). These various parameters interact with one another, further complicating the determination of a bridge dynamic response (NCHRP 1998).

Failure to properly account for dynamic loading can lead to excessive bridge stress that may be caused in sections or change of the structure of the bridge. Dynamic loading must also be considered when estimating the stress cycles that contribute to fatigue in bridge components. In the current Standard Specifications for Highway Bridges of American Association of State Highway and Transportation Officials (AASHTO), dynamic loading is expressed as an impact factor that is a function solely of the span of the bridge. The AASHTO impact factor is derived empirically and based originally on experiments with dynamic forces generated by steam locomotives on the railway bridges in the early part of twentieth century.

The current AASHTO equation for impact factor calculation has remained essentially unchanged since the 1920s. It is a simple equation that attempts to account for the complex dynamic response of a bridge due to a crossing vehicle. However, modern

bridge design uses lighter materials and longer spans, and some questions have been raised regarding the appropriateness of the AASHTO impact provisions (NCHRP 1998).

In response to this, highway agencies have conducted controlled loading tests to determine a bridge's dynamic characteristics, including natural frequencies, damping, and dynamic increment. In bridge dynamic increment tests, a bridge is tested dynamically using a single, fully loaded, dual-axle lorry. Deflection is measured whenever possible at the critical point of the bridge, which is normally at the midpoint of the maximum span. In many instances deflection is measured at additional points on the superstructure to obtain global deflections of the bridge.

Fig. 2.1 depicts the midspan deflections of a bridge in response to a crossing vehicle.

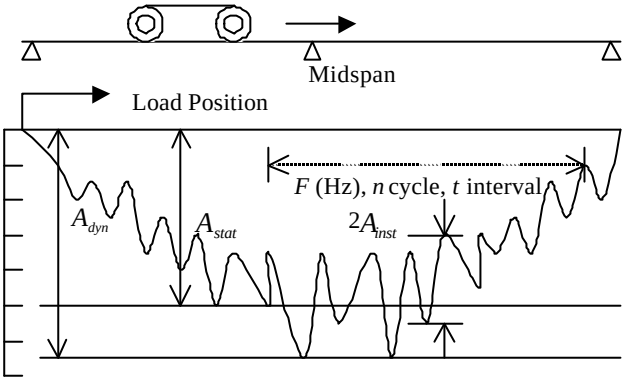

Fig. 2.1. Midspan deflection caused by a moving vehicle
(Modified according to Fig. 2 in Cantieni (1983))

If an accurate time measurement t has been recorded along with the signal, then the natural frequency F in Hz, can be established by counting the number of periods n in a given portion of the decay process (Cantieni 1983).

$$F = n / t \tag{2.1}$$

Damping d can be determined from the same time interval. This requires measurements of the first and last signal amplitudes having the same phase

$$\boldsymbol{d} = \frac{1}{n}\ln(A_0 / A_n)\,. \tag{2.2}$$

Where A_0 and A_n are the first and last amplitudes of the same phase.

The dynamic increment of a bridge reads

$$\Phi = \frac{A_{dyn} - A_{stat}}{A_{stat}} \cdot 100\,. \tag{2.3}$$

Where A_{dyn} is the peak value of the bridge dynamic response during a passage of the test vehicle and A_{stat} is the deflection observed under static loading with the same vehicle. A_{dyn} may be read straight from the measurements but the determination of A_{stat} may be problematic.

In most cases, the dynamic response of a bridge results from vibration generated by a vehicle oscillating on its suspension system. A more complete description of the dynamic response of a bridge should include the mass distribution within the system, natural frequencies and modes of vibration of both the bridge and vehicle, initial condition of both bridge and vehicle, damping characteristics of both bridge and vehicle, and road surface profile. All these dynamic factors are finally incorporated in bridge design through impact factor. The impact factors cannot be determined by the current instrumentation of loading tests to accurately depict the deflection at sufficient density on the bridge.

A significant amount of research has been conducted into bridge dynamics in the last few decades, with both analytical and experimental studies. Dynamic response is influenced by many parameters as discussed in the previous paragraphs, and as a consequence, many of the studies have resulted in different conclusions even with same set of dynamic data. Such confused results in loading tests require more accurate deflection data to confirm their soundness.

Wind loading is another important dynamic force affecting the flexible bridges, causing lateral deflection and a relatively small longitudinal displacement. Unlike controlled vehicular loading tests, it is very difficult to study the characteristics of wind loadings from a pure tunnel test. Appropriate consideration of wind loading in the determination of dynamic response of a bridge will result in more realistic conclusions.

Ambient temperature change will cause bridge deck shrinkage and elongation and as a consequence, it will introduce vertical bridge displacement and relative longitudinal movement. The exact relationship between dynamic response and temperature could not be determined by pure experiment due to the complexity of the bridge's structure.

Fig. 2.2 shows the dynamic loading test results of various railway bridges (Fryba 1996). The vertical axis refers to natural frequencies detected and the horizontal axis to main span length. It can be seen that the highest fundamental frequency of a railway bridge could reach 50Hz. As a general rule, the vibration frequency of a bridge is inversely proportional to bridge span.

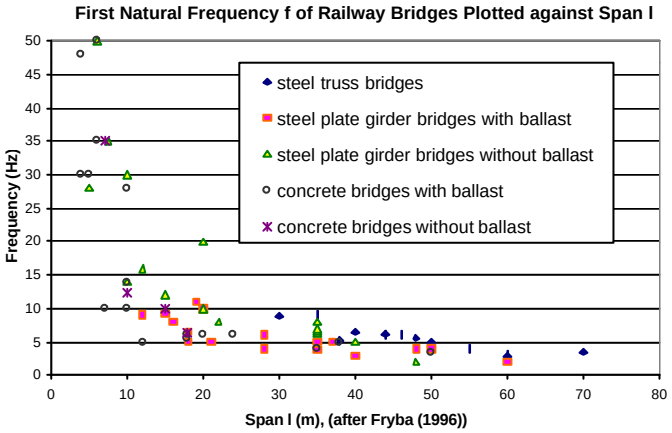

Fig. 2.2. Railway bridge natural frequency versus main span length

Between 1958 and 1981 the Swiss Federal Laboratories for Materials Testing and Research (EMPA) performed a series of dynamic loading tests on a large number of beam and slab-type highway bridges (Cantieni 1983).

The distribution of the natural frequencies of these bridges is shown in Fig. 2.3. Eq. 2.4 is the regression function and its standard deviation (SD) is derived from the natural frequency measurements f and span L. In those tests, the maximum bridge span is about 118.8m and the minimum span is about 11.0m. The highest frequency measured could reach 10 Hz. According to Eq. 2.4, similar conclusion as railway bridges about the relation between vibration frequency and bridge span could be reached for highway bridges. However, as it is discussed in this section, bridge dynamic response is affected by many factors and hence the vibration frequency of a bridge can be a function of bridge and vehicle dynamic characteristics and bridge surface condition.

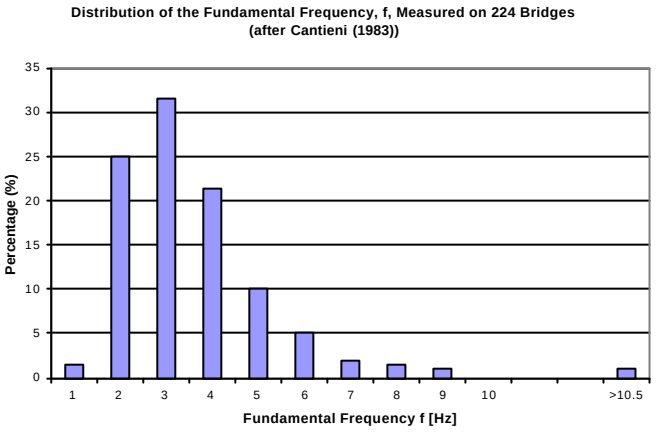

Fig. 2.3. Natural frequency distribution of highway bridges

$$f = \frac{100}{L[m]} + 0.6$$
$$\sigma_f = \pm 0.81 Hz \qquad (2.4)$$

These results that were determined by short span tests with large SD of regression function have limited practical use in the estimation of the frequency response of long flexible bridges according to their main span lengths. Few studies have been undertaken to make comprehensive analyses of dynamic response of longest suspension bridges. Further work needs to be carried out in this area. Recent research has shown that first natural frequencies in vertical and lateral directions of the Humber Bridge are about 0.116 Hz and 0.052 Hz respectively, as determined using a GPS-alone system, and further confirmed by finite element method (FEM) (Roberts et

al. 1999). The first natural frequencies in the vertical and lateral directions of the Tsing Ma Bridge in Hong Kong with similar main span as the Humber Bridge, are 0.117 Hz and 0.068 Hz respectively, determined by modelling techniques (Xu et al. 2000).

To improve the accuracy of a loading test and establish a reliable relationship between dynamic response and loading, it is necessary to improve monitoring techniques to acquire large spatially and temporally accurate displacement data, whether in a controlled environment or in-service scenario.

2.4 GPS-Based Deformation Monitoring System

Recent advances in GPS technology and data processing software have made GPS a much more convenient, accurate and cost-effective tool for deformation monitoring of natural and man-made structures.

To date, GPS is widely used to monitor volcano eruptions (Rizos et al. 2000a, 2000b), crustal movements (Hudnut et al. 2001), vertical land movements (Teferle et al. 2001), landslides (Brunner et al. 2000), earth structures (Forward et al. 2001), dams (Hudnut and Behr 1998), buildings (Lovse, et al. 1995; Guo and Ge 1997), and bridges (Fujino et al. 2000; Roberts 1997; Roberts et al. 1999; Wong et al. 2001).

In general, these applications can be roughly categorised according to their GPS station spacing as large, medium and local scales.

The GPS Earth Observation Network (GEONET) of the Geographical Survey Institute (GSI) in Japan and the Southern California Integrated GPS Network (SCIGN) are two examples of the typical large scale, permanent continuous GPS (CGPS) networks.

GEONET consists of 1,000 stations covering the whole Japan with an average GPS station intervals of the order of 25km, to monitor crustal deformation (Imakiire and Nakahori 2001). Crustal deformation data are considered important for the evaluation process of seismic and volcanic activity. Geodynamic information can also be

extracted from the analysis of GEONET data. The data collected from all stations at a sampling rate of 30 seconds are downloaded and analysed every day to determine the three-dimensional position of each station. The results can achieve accuracies better than 2mm horizontally and 6mm in height using dual frequency receivers (Rizos et al. 2000a).

SCIGN in the USA will consist of an array of 250 GPS stations when it is completed (Hudnut et al. 2001). Stations are distributed throughout Southern California with larger density in the greater Los Angeles metropolitan region (http://www.scign.org/ari/). SCIGN is used to monitor potential earthquakes throughout Southern California and to investigate geodynamic phenomena caused by earthquakes. The data collected from SCIGN will also benefit the surveying, engineering and Geographical Information System (GIS) communities by providing a spatial reference frame for their work (Hudnut et al. 2001). To increase the resolving power of this new instrumentation, continuous efforts are underway to reduce observation noise and model noises, which cannot be reduced or eliminated, for examples GPS receiver noise and the errors caused by multipath and propagation media.

Nowadays, many other countries have established or plan to construct their own CGPS station network for crustal or seismic deformation monitoring purposes (Teferle et al. 2001) (http://www.linz.govt.nz/). These networks could be included into the catalogues of continental- or nation-wide examples of GPS deformation applications according to their sparse station locations.

On a medium scale, Bingley et al (2001) at the IESSG of the University of Nottingham presented an example of a GPS-based vertical land movement monitoring system for selected sites of the UK National Tide Gauge Network.

GPS based volcano eruption monitoring networks are other examples of these catalogues, such as those on the Augustine volcano in Alaska, the Kilauea volcano in Hawaii, the Popacatepetl volcano in Mexico, and the Rabaul volcano in Papua New Guinea (Lowry and MacLeod 1997)(http://www.unavco.org/; http://www.usgs.gov/). The inter-station distance is usually set to an order of several kilometres to monitor subtle changes in the earth's surface. The receivers used usually are cheap GPS OEM

boards. Telemetry is also employed to transmit the collected data to a control centre for processing and analysis. The activity in this field reflects a growing interest in continuous GPS monitoring systems for volcano.

The third level of GPS based monitoring applications takes place on a variety of natural or man-made structural deformation and deflection monitoring in the local scale. Since modern GPS receiver technology enables L-band phase measurements to be made with a resolution of better than 1mm even 0.1mm level (Cross 2000), GPS is increasingly used to monitor engineering structures such as dams, slopes, bridges, offshore platforms, etc (Rizos et al. 1997).

2.5 GPS-Based Bridge Deformation Monitoring System (BDMS)

A suspension bridge exhibits two distinct types of deformations. The first deformation of bridge is the long-term movement caused by the foundation settlement, bridge deck creep and stress relaxation. This is a permanent, unrecoverable one-way deformation. The second is the short-term motion of the bridge, or bridge deflection, such as those activated by wind, tidal current, earthquake, or traffic. Bridge deflection is a recoverable deformation in most cases. Bridge will recover from deformation with the release of external forces.

When GPS is applied to monitor bridges, it is required that two different kinds of deformation could be distinguished simultaneously. In many cases, the analyses of short-term irregular loading are much more important in terms of risk of major damage, and are more difficult to monitor compared with long-term semistatic movements. Deformation such as foundation settlement, concrete creep, loss of prestress and thermal expansion/contraction generally occurs over relatively long periods. Thus, averaging times of GPS data of a few hours or more can be used, producing positions of a few millimetres accuracy. To measure deformations occurring over a time interval of a few seconds or less, less or even no averaging times would be allowed to improve accuracy better than a few millimetres level. This restricts the utility of GPS, in monitoring short-term movements of more flexible

structures. Also, to measure short-term effects, sampling rates must be significantly increased, which will incur heavier processing and data communication overloads.

In order to improve design codes, transport agencies and researchers have strong interests in measuring true short-term dynamic behaviour of structures, Of particular interest is the dynamic response of flexible structures such as cable-stayed and suspension bridges. Very few sensor systems are capable of measuring the displacement behaviour of large bridge structures, especially at the macro-scale where overall bridge movements are measured relative to the fixed ground stations.

GPS has been used in a number of bridge monitoring studies. For example, GPS receivers were employed to monitor the displacement of France's Normandy Suspension Bridge with proof loading tests (Fairweather 1996); the Danish Road Directorate has employed GPS to determine the as-built geometry and assess temporal deformations of Denmark's Storebaelt Bridge and others (Norgard 1996); and the Applied Research Laboratory of the University of Texas at Austin (ARL) in the USA has conducted a series of research on GPS-based structural deformation monitoring since the beginning of 1990s and already published many valuable articles on relevant topics (Duff 1997; Duff and Hyzak 1997; Duff 1998; Hyzak 1997; Hyzak and Leach 1995; Leach 1992; Tolman and Craig 1997).

The research of ARL is focused on the practicality and potential cost savings of GPS-based structural deflection monitoring systems with millimetre level accuracy. Low cost OEM boards employing both code and carrier phase data on the L1 frequency were tested in actual bridge monitoring. A detailed picture of how the overall shape of a bridge changed under various loadings, through varying environmental conditions, and over time, was determined through the analysis of post-processed data. The ARL system achieved this by strategically positioning a network of sensor nodes on the deck of a bridge. The BDMS proposed consisted of a RF spread spectrum data communications system, a central data processing, and an analysis station (Fig. 2.4). Each sensor node consisted of a single frequency GPS receiver, microcontroller, data radio, and power-conditioning unit to form the basic configuration. In this system, the GPS board employed at each sensor node must have high data sampling rate, little

power consumption, a low price, and the ability to mitigate the typically largest error sources.

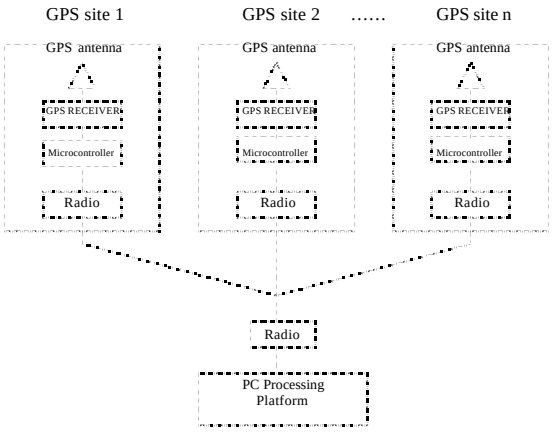

Fig. 2.4. System architecture of GPS-based BDMS (cited from Hyzak (1997))

Research at ARL emphasises are also on the analysis of the capabilities and limitations of real-time deformation monitoring with GPS, operational issues, system design and performance, affordability, and technology development, together with the analysis and mitigation of dominant error sources. The main error mitigation technique introduced by ARL was time averaging, but in the most cases, this technique was proved not to be sufficient to improve the accuracy of the positioning solutions and to feasibly monitor the dynamic characteristics of bridges.

Leach et al. (1992) presented the results of a three-day experiment in which GPS technology was used to measure the motion of a cable-stayed suspension bridge over the Mississippi River near New Orleans. The goals of this experiment were to verify the feasibility of using GPS to achieve centimetre level accuracy in bridge deflection monitoring, and to evaluate the practicability and limitations of the whole system. Twelve Trimble 4000 SST GPS receivers were used in the test. Two receivers were located on the shore at the known reference sites about 10m apart approximately 1.6km away from the bridge. This approach made it possible to distinguish real bridge motion from GPS induced biases or errors in the data processing. The remaining ten GPS receivers were situated at the critical bridge sites where minimum and maximum bridge displacements were expected. A 10-second data rate was chosen because the expected bridge motion during a 10-second period was considered to be negligible,

and this allowed all the data to be stored on receivers. The result showed a maximum relative vertical displacement of about 7cm caused by a change in ambient temperature during the experiment. The results revealed strong relationship between vertical position of the bridge roadbed and change in ambient temperature. Multipath also made significant error contribution to the positioning solution and caused problems in the displacement analysis. It was clear that the cables and metal surroundings, the bridge sites, coupled by the traffic, had induced severe multipath environment and additional multipath analysis and mitigation techniques apparently were needed. Even 10-second data rate was used, up to 20 cm abnormal vertical displacements have appeared over a 10-minute interval for three times in the positioning solutions. The cause for this abnormal displacement was unknown.

From October 14 to 18, 1996, the staff of ARL conducted another field GPS-based monitoring test on a long span bridge, the Fred Hartman Bridge over the Houston Ship Channel near Baytown, Texas that was anticipated to have measurable traffic- and wind-induced movements (Hyzak 1997).

The goals of this test were to:

- Assess the quality of GPS measurements in the presence of the high supporting towers and cables
- Compare GPS-measured displacements with those of servo accelerometers
- Assess the reliability and performance of system components
- Compare measured response to causal forces

Unlike their previous trial in which receivers with a low sampling rate were used to investigate long period bridge movements, the focus of this trial was to measure the dynamic response of the cable-stayed bridge to the wind and traffic loadings with 10 Hz GPS receivers.

Preliminary results from ARL indicated that GPS is a viable tool for detecting transient deformations of flexible bridge structures as well as long period movements. It was recognised that the big challenge with GPS-based BDMS was to eliminate or reduce the impact of multipath.

The main limitations of large-scale GPS applications to structural deformation monitoring are the relatively high cost of dual frequency GPS receivers, effects of a number of potential errors, large volumes of GPS data at a high sampling rate, and high precision requirements. Rizos et al. (1997) presented a data processing strategy and system architecture of a proposed structural deformation monitoring system. This system consists of two distinct networks: a local dense array of relatively cheap single-frequency GPS receivers to monitor the deformation in-situ and sample the spatial distribution of structural deformations which surrounded by a small number of sparsely distributed, high precision dual-frequency GPS receivers. The external *fiducial* network is used to mitigate residual biases due to ionospheric and tropospheric refraction, and satellite ephemeris errors, by generating and applying corrections to the station coordinates of the internal network. The external network is located outside the active area of deformation, but on the same local tectonic plate. It was suggested that with an observation span of the order of one hour or so this configuration could achieve millimetre horizontal and centimetre vertical accuracies.

The development in GPS technology in terms of accuracy, sampling rate, and ruggedness is the main drive for the application of GPS-based BDMS to monitor the world's longest suspension bridges in recent years.

The Akashi Kaikyo Bridge in Japan was constructed using a newly developed wind and seismic resistant design. It is necessary to confirm design assumptions and constants during strong winds and severe earthquakes (Fujino et al. 2000). Navigation is extremely difficult and there have been many shipping accidents in the 110m wide Akashi Strait due to the environmental conditions as noted in Section 2.1. To keep the world's longest suspension in a safe operating condition and also to study the dynamic response of various loads, Leica provided precise dual frequency GPS receivers in 1999 to monitor bridge deformation in a real-time mode (http://www.leica-gps.com/gps/). The monitoring system comprised three Leica MC1000 GPS receivers, connected through a network of optical fibre cables. Two units were mounted atop the towers at either end, and the third at the bridge midpoint. The system could detect the movements of the bridge structure with millimetre-level accuracy, enabling engineers to determine exactly how far the bridge was moving, including critical movements outside the structure's design specifications.

The first results from the monitoring of the Akashi Kaikyo Bridge, using a modified GPS receiver configuration were presented by Fujino et al. (2000). GPS receivers were setup at three sites, constituting a reference station at the anchorage on Kobe side of the bridge and two monitoring stations on the top of a tower and at midspan to monitor three-dimensional displacement. Wind load and temperature data were also collected. Six-month displacement time series were analysed with the recorded measurements of wind and temperature. The instantaneous gradients of displacement and temperature were calculated. The regression functions established could be used to identify future abnormal deflections after attacks of strong wind loads and earthquakes. The GPS data were averaged every 10 minutes and recorded.

Whilst this averaging procedure can remove multipath signatures with a period of several minutes and identify the semistatic movements of the bridge caused by wind and temperature loads, it cannot be employed to detect the bridge's dynamic responses activated by the same loads. For such a long suspension bridge, a three GPS receiver configuration was insufficient to monitor the global displacements of the bridge. The reference station setup was also unsuitable for monitoring the bridge movements since it was situated on the same structure. Cancellation effect between reference and monitoring stations is the reason why the measured displacements were smaller than the predicted values from an FEM. It seems no strategies were undertaken to cope with the GPS error sources on the Akashi Kaikyo Bridge, which unavoidably affect the correctness of further analysis and interpretation of actual bridge dynamics.

Since the research to date on the Akashi Kaikyo Bridge was mainly concerned with the long-term semistatic responses of the bridge to the changes of temperature. Data sampling rate and instrumentation are insufficient to detect bridge dynamic abnormalities that are caused by the wind, temperature, and other dynamic loadings.

The Tsing Ma Bridge in Hong Kong is the fifth longest suspension bridge in the world (Table 2.1) and it is the longest single span suspension bridge that carries both road and rail traffic.

In January 2001, 29 Leica CRS1500 dual frequency GPS receivers were added to the existing monitoring system consisting of 774 sensors of seven types, to monitor the bridge heath conditions. GPS was introduced due to its improved measurement efficiency and accuracy (Wong et al. 2001). Two receivers were setup as reference stations, 12 were used as the monitoring stations on the bridge deck, four pairs monitored the bridge deck itself, one pair setup on the towers and one pair monitored the cable at midspan. Other receivers were installed onto two cable-stayed bridges near the Tsing Ma Bridge to form a large monitoring system in the region. Data were collected at a sampling rate of 10 Hz continuously, and optical fibres were used to transmit the collected data from each station to a processing centre to prevent the interferences from external electromagnetic waves and lightening.

The focus of this research was mainly on the hardware arrangement and implementation. The only data analysis and validation carried out was the direct comparisons of the results from GPS and level sensing stations, which sample the vertical displacements at a rate of 2.56 Hz. The data quality issues and further interpretations of the bridge dynamics have not been mentioned in their research yet. These aspects are also essential parts in a practical BDMS as the hardware implementation. Only with appropriately processed reliable results, a full picture about the bridge performance conditions could be drawn and the information extracted from can be used to help bridge management and supply a safe transport environment.

Researchers at the IESSG in the University of Nottingham have conducted a series of trials using state-of-the-art dual frequency GPS receivers, to monitor the movements of suspension bridges and other structures (Ashkenazi et al. 1997; Roberts 1997; Roberts et al. 1999; Young 1998).

In particular the IESSG was joined by researchers from the Brunel University and the Humber Bridge Board, to conduct a controlled GPS deflection monitoring trial on the Humber Bridge (Roberts et al. 1999). The test was carried out in the late evening /early morning of 15/16 February 1998. The viability of GPS technology to monitor the displacements of the Humber Bridge subjected to known loading conditions was verified. This test showed not only the possible use of GPS to monitor large structural

deflections, but also to accurately measure vibration frequency. Displacements and first natural frequency of the bridge calculated from GPS measurements were compared with those predicted by FEM. Extremely close agreements were obtained. Moving average (MA) technique was employed in the analysis of longer period bridge movements and short-term bridge dynamics by calculating the difference between filtered and original signals. The limitations in positioning accuracy and sampling rate (5 Hz) of the GPS receivers were also identified by the authors.

Whilst MA was employed to analyse long-term movement, according to Fig. 3 of Roberts et al. (1999), the amplitudes of longitudinal and lateral movements extracted from kinematic positioning solutions were at the same level. This is contrary to normal bridge dynamics. Thus, while GPS demonstrated the potential to monitor large vertical deflection, in the order of 60cm, the reliability of the results in longitudinal and lateral directions was uncertain owing to satellite geometry. This will be addressed in Chapter 6. Deflections could be easily identified from the vertical time series, but multipath with a period of several minutes could distort the smoothed coordinates by an MA filter. When a 100s averaging length MA filter was applied to the original coordinates, the multipath could not be removed due to the low pass nature of the MA filter, and one day's data is insufficient to detect day-to-day multipath signature for mitigation purpose.

It is obvious that further research is required on how to separate real bridge movement from multipath. A sensor system that could be employed to detect deflection of a magnitude from centimetre to metre needs to be developed.

The initial research focus at the IESSG was on the viability of GPS technology to monitor both long-term bridge settlements and dynamic response to external loads. Through the endeavour of many years, a systematic approach for sensor integration, algorithm and software development, data collection, quality control, data processing, detailed data analysis and interpretation, and visualisation interpretation have been developed (Roberts et al. 2000a; Roberts et al. 2000b; Dodson et al. 2001; Roberts et al. 2001a; Roberts et al. 2001b; Meng et al. 2002; Roberts et al. 2002a; Roberts et al. 2002b).

2.6 Hybrid BDMS of GPS Receivers and Triaxial Accelerometers

Due to the severe environments encountered in the bridge deflection monitoring, the instruments used must be lightweight, portable, reliable, and easy to install. The results must be easy to interpret. These are of great importance under extreme loading scenarios such as strong wind, volcanic eruption, and earthquake shock. At the same time, for correctly interpreting the dynamics of monitored bridges, the measurements should meet accuracy specification requirements. This means the deflections of the bridge should be measurable with available surveying instruments. For instance, in order to measure centimetre level deflections the internal accuracy of a GPS receiver should be better than a few millimetres level, and multipath and other error sources should be appropriately mitigated or modelled.

Conventional surveying methods such as levelling have been used in the past to monitor static displacements of engineered structures with millimetre level or higher accuracy, and will certainly continue to be used in the future.

Modern levelling sensing stations could provide one-dimensional 2-millimetre accuracy at a sampling rate of 2.56 Hz (Wong et al. 2001). Surveying robots, EDM, theodolites, surveying total stations, photogrammetry, and other surveying instruments could be employed to monitor structural deformation. However, the inherent disadvantages of these terrestrial surveying systems have greatly limited their applications. The main disadvantages of these surveying approaches are as follows:

- Long-term intervals between measurements (days or even months)
- Averaging of data over a relatively long time span (often some hours are smoothed which leads to smoothing effects that could hide real movements of the stations)
- Relatively low data sampling rate and a poor level of automation
- Batch mode analysis (data is collected, transmitted to a computer and evaluated a few hours later).

Due to the above limitations of terrestrial surveying methods, they cannot be employed to monitor structures with dynamic structural deflection and semistatic movements at the same time.

Accelerometers have been used extensively for bridge dynamic monitoring. These sensors are used to sense accelerations, and triaxial accelerometers could measure three orthogonal accelerations simultaneously. Compared with other surveying systems, triaxial accelerometers have some special advantages when they are used for bridge monitoring. The sampling rate can be 1000 Hz depending upon application requirements, which is a very important characteristic when monitoring a bridge with high dynamic. Triaxial accelerometers are superior to other sensors since they are not dependent on propagation of electromagnetic waves, and therefore avoid the problems of refraction, line of sight connections to the terrestrial or space objects, and do not have visibility problems caused by weather. An accelerometer could form a completely self-contained system, utilising only measurements of accelerations to infer the positions of the system, through integration based on the laws of motion.

However, the positional drift of an accelerometer grows extremely rapid with time and can reach hundreds of metres after intervals of several hours (Chen 1992). The main error sources come from the instrumental biases and scale factor offsets and the unknown gravity of the earth. These issues are addressed in Section 3.4 and Section 4.2. In normal applications, continuous updating is used to avoid error accumulation. These are operations, which allow the errors either to be directly measured or to be modelled. The most common update is the Zero Velocity Update (ZUPT). Another method is the Coordinates Update (CUPT). It is the need to update that has severely restricted the widespread applications of accelerometer technology as a standalone positioning method in surveying. In bridge deflection monitoring, it is impossible to conduct ZUPT. Only CUPT aided with GPS fixes could be a realistic option to overcome drift problem of accelerometer.

Like accelerometers, tiltmeters, strain gauges, and other sensors are used to measure deflections and displacements in bridge inspection. These instruments are high cost, complex to install and maintain, and need frequent re-calibration. They are also very vulnerable to the environments. The collected raw data need to be interpreted to

obtain direct geometric results, which in many ways is a very complicated procedure. For instance, the vibration periods are very low on long span suspension bridges, and there exist both semistatic and dynamic displacements. It is very difficult for accelerometers to accurately detect these very slow movements of 0.1~0.3 Hz vibration frequencies.

Measurability of the instruments used for bridge monitoring is another issue. The lateral movements are usually activated by the wind loads and the vertical displacements are mainly caused by the change of ambient temperature and traffic loads. These loads will introduce relative small movements in the longitudinal direction. The mean lateral movements of the Akashi Kaikyo Bridge monitored by GPS could reach 5.13m with vibration amplitude of 0.78m but the longitudinal movements are only several centimetres.

Interferometric synthetic aperture radar (InSAR) could provide dense spatial coverage of the deformation body in a cost-effective manner. It can be used to detect deformation with sub-millimetre accuracy. However, its temporal coverage is limited by the repeat periods of the satellites, which are 35 days for ERS-1 and 44 days for JERS-1 (Ge et al. 2000b). It is apparent that InSAR techniques could not be used to monitor bridge deformations with high resolutions both temporally and spatially.

Ground-based laser scanning techniques can be used to collect a large amount of precise 3D points of the monitored objects over a range of 5~350m (Gordon et al. 2001). This emerging technique could also be employed to detect surface deformations. However, the technique is limited by range of operation, a low sampling rate, a requirement of semistatic status of the monitored targets, and the long time spent in image processing. All these limitations exclude these technique from the instrumentation list for long span suspension bridges.

Whilst terrestrial surveying methods require *line of sight* between stations, GPS can conduct unattended, continuous field operations with high sampling rates, and an integrated communications network technique. Reduction of GPS data gathered at a high sampling rate is more complex than it is for conventional surveying methods. Robust automation of highly precise GPS data collection, quality control, data

processing, and analysis, are all now reasonable routine. GPS does not have range limitation and it is explicitly connected to an absolute reference frame.

Hyzak (1997) summarised some advantages of GPS for structural deflection monitoring,

- All weather observations
- Various levels of accuracy to meet different application requirements, for instance GPS could provide 1 cm (instantaneous) to 1 mm (with averaging) positioning accuracy
- 3D positions in an uniformly defined world reference (WGS84)
- Continuous monitoring with data rates up to 20 Hz
- Automated operation with less human intervention, and near real-time capability
- Kinematic methods for efficient data collection
- No long-term sensor drifts (in fact, the accuracy of a GPS observable can be increased over time).

GPS observations can also serve as the spatial reference frame for other types of measurements such as those from accelerometers and strain gauges. GPS can be integrated with other sensors to form a totally automated and continuously operating system.

As an increasingly developing technology, GPS has its own limitations aforementioned when it is used to monitor long flexible structures. In general, GPS accuracy depends on a geometric distribution of the satellites. It could be very difficult to obtain ideal DOP values for precise real-time GPS positioning all the time, depending on the location, because of the deficiency of the design of satellite sky distribution. GPS has limited measurement redundancy in real-time kinematic positioning mode. With pure GPS techniques, the level of redundancy is insufficient to monitor the quality of the observations.

Loss of lock to satellite signals due to the signal blockages by surroundings and the changes of satellite geometry, and also bridge deformations, is another major problem

for kinematic GPS bridge monitoring. It will introduce new ambiguities to be solved. For instance the mean lateral movements at midspan of the Akashi Kaikyo Bridge could be larger than 5m with over 2m vibration in the typhoon seasons (Kashima et al. 2001), exhibiting itself a typical deformation behavior of such type of bridges. Signal recapturing usually takes time, depending on the receiver quality and observation conditions, and will cause discontinuous observations.

Relatively low data rate (maximum 20 Hz currently) could not meet the requirement to monitor higher structural dynamics. For example, this sampling rate is insufficient to monitor the vibration frequency higher than 10 Hz (Nyquist frequency > 10Hz).

Multipath signature is still the bottleneck for the highly precise bridge monitoring, even though many efforts have been put into this field at the very beginning of GPS positioning, practical and efficient approaches to mitigate the impacts of multipath are needed to be further investigated.

Tropospheric delay could cause problems as well when GPS is used for flexible structure monitoring in a real-time kinematic mode. The difference in tropospheric delay patterns on two ends of a baseline could introduce several centimetre position errors due to the unequally distributed water vapor between rover and reference stations, and temperature or humidity. This will produce a varying time series of relative tropospheric delay into the kinematic positioning solutions, which will distort the reasonable interpretation of bridge deflection. To cope with this, meteorological parameters can be employed.

Since averaging techniques cannot be used, it will be very difficult to maintain the positioning accuracy on each epoch basis in the kinematic mode. It has been found that there are significant interferences that come from ambient environmental factors. Examples are dense cables and passing vehicles obstructing the GPS signals, which will cause cycle slips and multipath. Roberts et al (1999) reported outliers of several decimeters in the Humber Bridge positioning solutions, which might have been introduced by the cycle slips. A lot of other studies have also revealed that the special observation environments and particular characteristics of multipath signatures make the mitigation techniques a restriction for GPS engineering applications.

GPS receivers integrated with triaxial accelerometers could provide an improved overall system in terms of productivity and reliability. The sensor integration and data fusion techniques need to be further studied. Interpretation and comparison of GPS positioning solutions with the results predicted by models or measured by other techniques are important in GPS/accelerometer based BDMS. The methodologies, algorithms, and visualisations of the results need to be developed. All these issues form the main contents of this thesis. The findings and conclusions from these studies are based on the author's initiatives.

Suspension bridges are capable of movements from a few decimetres to metres at the middle spans, under wind and traffic loadings or dead loadings from earthquake shocks. With the above endeavours, the use of kinematic *on the fly* (OTF) GPS positioning technique aided by triaxial accelerometers at strategic points upon the bridge decks should enable accurate and detailed monitoring of the bridge's dynamic responses. Such real-time system could be used to monitor the performance of the bridge at different loadings and warn of potentially dangerous bridges. Moreover, future bridge designs and traffic management schemes could also benefit from such a deformation monitoring system through more detailed understanding of the relationship between loading and response.

2.7 Summary

The need in real-time bridge deformation monitoring is addressed according to the development of BMS for land transport safety. Loading tests are employed to study bridge dynamic response and information extracted from these tests is used to evaluate the performance of a bridge. Under defect analysis of current dynamic loading tests, requirement on improving data collection about bridge deformation by using sophisticated satellite positioning techniques is emphasised. Applications of GPS structural deformation monitoring on three different levels are presented and the activities of GPS-based BDMS for monitoring the world's longest suspension bridges are overviewed. The advantages and disadvantages of GPS-based BDMS over other systems are compared. To improve productivity and reliability of whole monitoring system, a hybrid sensor system consisting of GPS receivers and triaxial accelerometers is proposed to monitor the bridge deformations, which characterise

long-term irrecoverable displacement and short-term deflection. Based on the functionality analysis to the proposed system, the research emphasis is outlined in this chapter.

Chapter 3

Instrumentation and Quality Evaluation

3.1 Introduction

Zero baseline (ZBL) tests are used to examine the performance of GPS receivers. Since the two receivers are connected to the same antenna with a low-noise amplifier (LNA), all common errors due to multipath, LNA noise, satellite orbit perturbation, impacts from propagation media, etc. are eliminated in the GPS data processing.

In short baseline (SBL) tests, the receivers are operated following the procedures used in typical high accuracy GPS survey applications. These tests address the performance of full sensor system, which consists of antennas, cables, and receivers. Each tested receiver pair is operated on a known baseline. The residuals caused by various error sources can be obtained through the comparison with the known baseline, or the known coordinates by fixing one receiver as a reference station and designating another one as a rover.

Unlike the traditional ZBL and SBL tests with focus on the average quality evaluation of raw measurements at a slower sampling rate, for instance, 30 seconds, the emphases of the kinematic ZBL and SBL tests are on the performance of the GPS system on an each epoch basis at an obtainable high data sampling rate.

Leica GPS receivers were used as the main instruments in this research. To meet the requirement of millimetre positioning accuracy in bridge deflection monitoring, there is need to quantify the performance of the instruments used. To date, the following types of Leica GPS receivers have been applied in the different trials, which are 10 Hz CRS1000 dual frequency receivers, 10 Hz SR510 single frequency receivers, and 10 Hz SR530 dual frequency receivers. Three CRS1000 receivers on loan from Leica Geosystems Ltd. (UK) were initially used as the main instruments for this project. With the purchase of four SR530 receivers by the IESSG, this new type of Leica dual

frequency receivers gradually replaced CRS1000 receivers as the main instruments based on the improved receiver performance. Ten SR510 single frequency receivers were then bought with the EPSRC funds at the end of 2001. Some ZBL and SBL tests have already been performed with this type of receivers using the facilities at the IESSG. More trials will be planned to evaluate their performance for actual bridge deflection monitoring.

The antenna types used in this project were Leica AT302 and AT502 lightweight dual frequency antennas, AT503 and AT504 chokering antennas, and AT501 lightweight single frequency antennas. Refer to Leica's specifications for the receiver and antenna details (http://www.leica-geosystems.com).

In Section 3.2 and 3.3, ZBL and SBL tests conducted with different types of receivers and antennas are presented. Methods used to qualify the performance of each type of receiver are introduced. A proposed simple, cost-effective, but accurate accelerometer calibration approach is described in Section 3.4. Some conclusions are made at the end of this chapter.

Unless otherwise stated, the epoch interval for GPS data collection was 10 Hz with 15° elevation cutoff angle. The data rate for accelerometer was set to 200 Hz in the trials.

3.2 ZBL Tests Using Leica GPS Receivers

Sample data sets of ZBL tests are used as the representative for each type of receiver in this section. GPS raw measurements from CRS1000 and SR530 dual frequency receivers are processed in a kinematic OTF mode with Leica SKI-Pro GPS post-processing software (Leica 1999a, 2001). In the data processing, one receiver is designated as reference station and another one as a rover. *Stop and Go* mode with known coordinate initialisation is used in the data collection with SR510 single frequency receivers. These data sets are also processed with SKI-Pro. Statistic characteristics of 3D coordinate residuals are analysed. Autocorrelation coefficients of the coordinate residuals are calculated to evaluate the data quality of each epoch

positioning solution. The time lag of ZBL positioning solution combined with that of SBL is further exploited for the determination of optimal filter length in AF multipath mitigation. The details are introduced in Section 7.3.

3.2.1 ZBL Tests Using Leica CRS1000 Dual Frequency Receivers

Leica CRS1000 GPS receiver is a rugged, dual frequency receiver that provides rapid updates as often as ten times per second. Its main features include (Leica 1998):

- 12 dual frequency tracking channels
- Real Time Kinematic (RTK) centimetre accuracy
- Automatic OTF ambiguity resolution

Between November 1999 and August 2000, a series of ZBL tests were conducted together with SBL trials using the facilities at the IESSG Building. Leica CRS1000 dual frequency GPS receivers and Leica AT504 dual frequency chokering antennas, a signal splitter were employed in the data collections. The GPS raw measurements are post-processed with Leica SKI-Pro software (Leica 1999a), Ashtech Office Suite for Survey (AOSS Ashtech 1998) and an IESSG's GPS Analysis Software (GAS) package (IESSG 1998). At the time the tests were conducted, Leica CRS1000 receivers were one of the few commercial dual frequency receivers available on the market that provided 3D centimetre positioning accuracy at a data sampling rate of 10 Hz (Leica 1998).

Three Leica CRS1000 GPS receivers were employed in the initial ZBL tests. In the tests, a Leica AT504 chokering antenna was installed above a point with known coordinates on the turret of the IESSG building. With a dedicated Leica low noise cable about 10m in length, the AT504 antenna was connected to two receivers by a specially designed signal splitter (Fig. 3.1, Fig. 3.2) in the GPS laboratory. Two desktop PCs running with Leica MC-CDU software were used to log the GPS raw measurements in a Leica high-speed lb2 (Leica binary data format version 2) data format (Fig. 3.2). Leica translator l2r2 was then used to convert the raw data files in a

lb2 format into a RINEX data format (version 2). The data files in RINEX format were then post-processed using AOSS, SKI-Pro, and GAS.

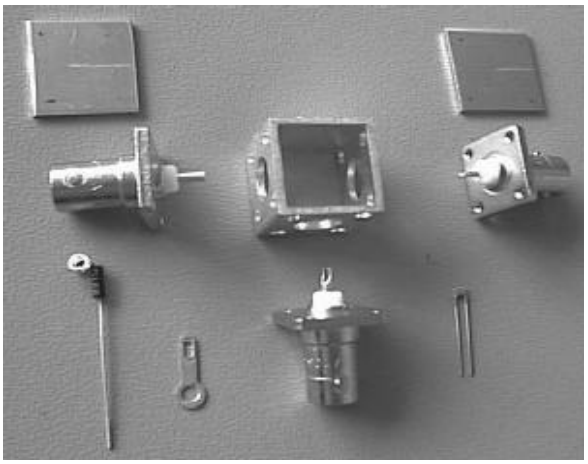

Fig. 3.1. The components of a ZBL splitter
(Specs: http://www.unavco.org , supplied by Dr. C Hill at the IESSG)

Fig. 3.2. ZBL test hardware configuration

Three possible combinations could be chosen from three CRS1000 GPS receivers for the ZBL tests, i.e. sensor 1 with sensor 2, sensor 1 with sensor 3, and sensor 2 with sensor 3. Investigations on the receivers' performance at varying sampling rates (for instance, 0.1, 0.2, 0.5, 1.0, 2.0, 3.0, 4.0, 5.0, 10.0, 30.0 seconds) were conducted. Appendix A1 lists the partial ZBL tests made with CRS1000 GPS receivers in 1999. Other ZBL trials were carried out together with SBL tests in 2000 and 2002.

To save the space but without losing the completeness of the tests, only the results from some of the tests that are most relevant to this research are presented. The results

from the highlighted data sets in the Appendix A1 are used as examples to evaluate the CRS1000 receiver performance. Since the research interest of this project is the quality evaluation of the positioning solutions at the highest available sampling rate from Leica GPS receivers, results demonstrated are mainly from post-processed 10 Hz kinematic data in OTF mode. Also a two-day data set of 10-second sampling rate is used to illustrate the performance of long-term data logging with CRS1000 receivers. The resistance levels of the two cables attaching receivers to the splitter are identical to avoid the impact of any unbalanced cable noises on the raw data sets.

Fig. 3.3, 3.4, and 3.5 are 15-minute 3D coordinate residual time series. The raw data sets were recorded by CRS1000 receiver at a 10 Hz sampling rate on 11 November 1999. The raw measurements were decoded by translator l2r2 first and then processed with Leica SKI-Pro in an OTF kinematic mode by designating one receiver as reference station in a static mode and another one as rover in a moving mode. The residuals are obtained through the comparison of the positioning solutions with the known coordinates in WGS84. With such a hardware configuration and receiver firmware, the receiver internal accuracies are 1.17cm, 0.44cm, and 1.31cm for X, Y, and Z coordinates (99.7% probability, which is three times of RMS), respectively. Fig. 3.6 is the baseline residual time series. Since the distance residual is the root of the squared sum of the 3D coordinate residuals at each epoch and hence does not obey a normal distribution, three times standard deviation (SD) can not be used to quantify the baseline residual range. Chi-square density function can be used to estimate the residual range of ZBL baseline (Mikhail, 1976).

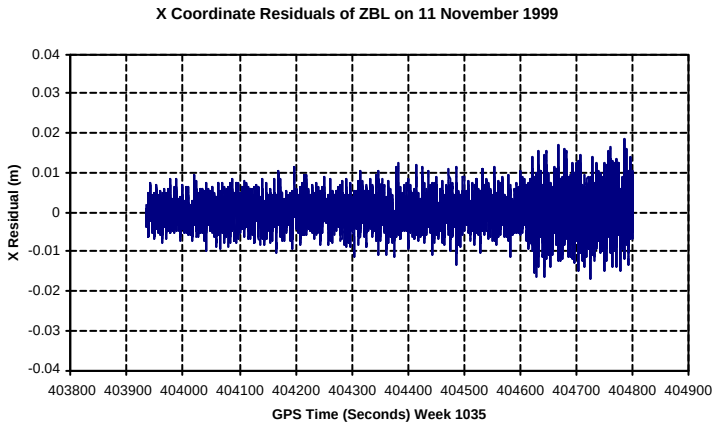

Fig. 3.3. X coordinate residual (CRS1000)

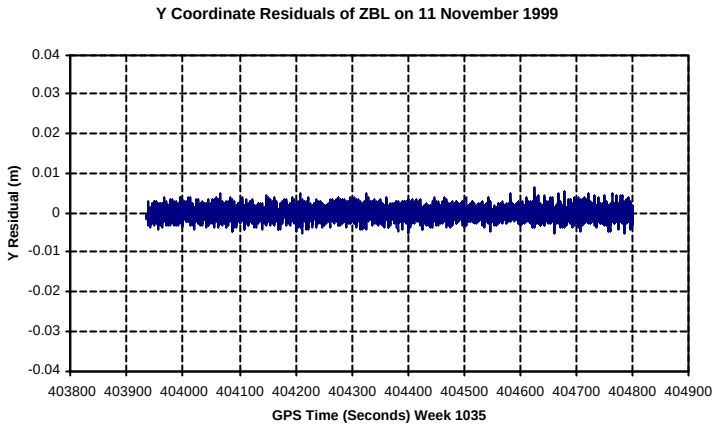

Fig. 3.4. Y coordinate residual (CRS1000)

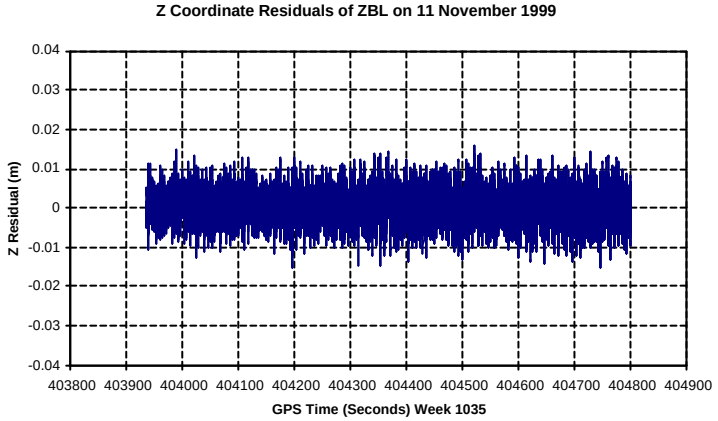

Fig. 3.5. Z coordinate residual (CRS1000)

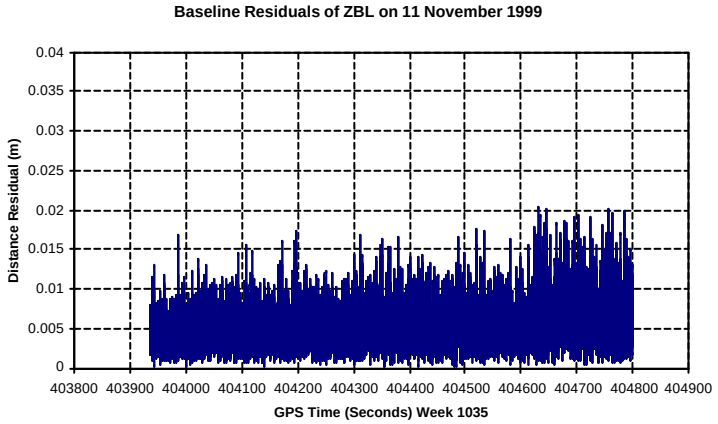

Fig. 3.6. Baseline residual (CRS1000)

Autocorrelation analysis is applied to X, Y, and Z coordinates to study the random characteristics of the residual time series themselves using a Matlab script (Mathworks 2000). Only the autocorrelation coefficients of the X coordinate residuals

are presented here. Similar results have been found from Y and Z coordinate residuals. The results reveal the autocorrelation time lags of the three coordinate time series are one second (Fig. 3.7). In this case, the accuracy evaluation formulae applied to the Leica GPS raw measurements can appropriately describe the quality of the data sets without overestimating the data quality if this 1-second data correlation has been treated.

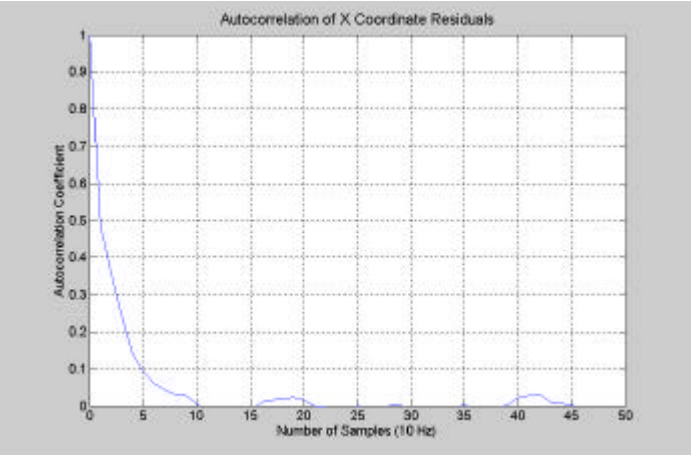

Fig. 3.7. Autocorrelation of X coordinate residual (CRS1000)

Fig. 3.8, 3.9, and 3.10 are the comparisons of normal distributions with the histograms of the coordinate residuals to verify their normality from a statistic point of view. The theoretical normal distribution curves are drawn with the means and SD calculated from the residual time series. The vertical axes of these graphs refer to the number of samples located in specific intervals. The abscissas represent the possible error ranges. It can be concluded from the graphs that residuals caused by the receiver noise obey a normal distribution and hence they can be treated as random sequences. Least-squares adjustment can be applied to the raw measurements to obtain correct positioning solutions without bringing model errors into the final coordinates. Detailed statistic tests of the normality of random sequences could be found from Meng et al. (1996).

Since in many cases GPS receivers will be used to record long-term bridge deflection data, it is necessary to investigate the performance of the total system in such a circumstance. It is very difficult to log long-term data at 10 Hz data rate due to limitations in data storage. Data volume experiments showed that with 10 Hz

sampling rate CRS1000 receivers could create a 10Mb lb2 format data file within one hour, depending on the number of satellites tracked. This binary data file is equivalent to a RINEX data file of more than 20Mb in size.

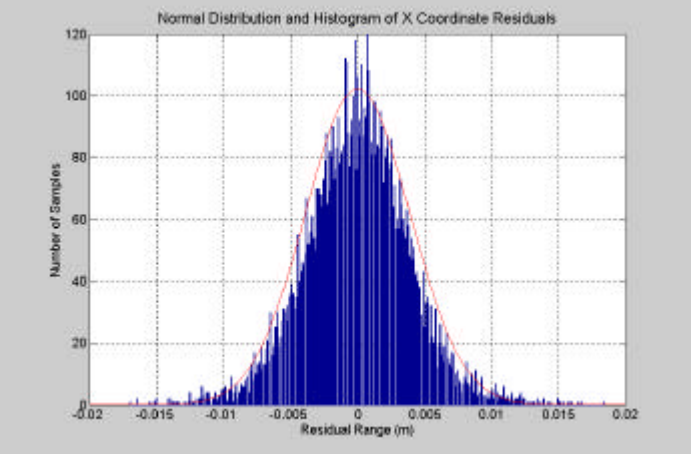

Fig. 3.8. Statistic test of X coordinate (CRS1000)

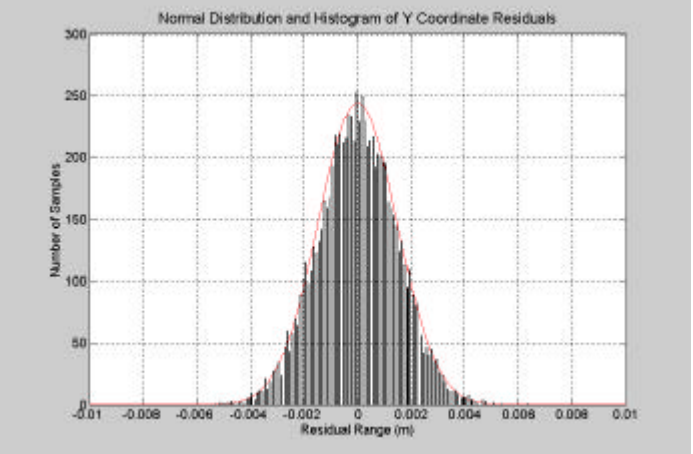

Fig. 3.9. Statistic test of Y coordinate (CRS1000)

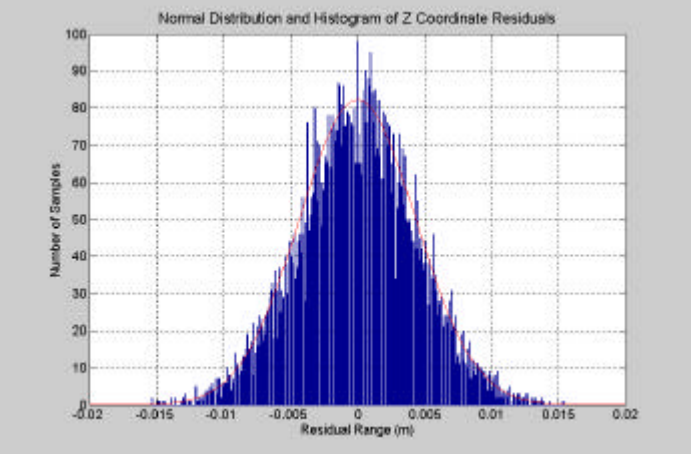

Fig. 3.10. Statistic test of Z coordinate (CRS1000)

Fig. 3.11 to Fig. 3.14 are the residual time series of X, Y and Z coordinates with a 10-second sampling rate. Fig. 3.15 is the enlarged part of Fig. 3.11. Data were collected for about 24 hours from 15 to 16 November 1999. The red arrows in the graphs show the data gaps that were caused by very poor satellite geometry starting at around 21:37 on 15 November 1999 when only 4 or 5 satellites were tracked by the receivers. These outliers have been removed from the residual time series. The biggest outlier is about 6 metres. Appendix A2 is the partial report from data processing using SKI-Pro, which shows very big DOP values due to the geometry deficiency of the tracked satellites. Data processing also reveals that there were 121 cycle slips during the data collection.

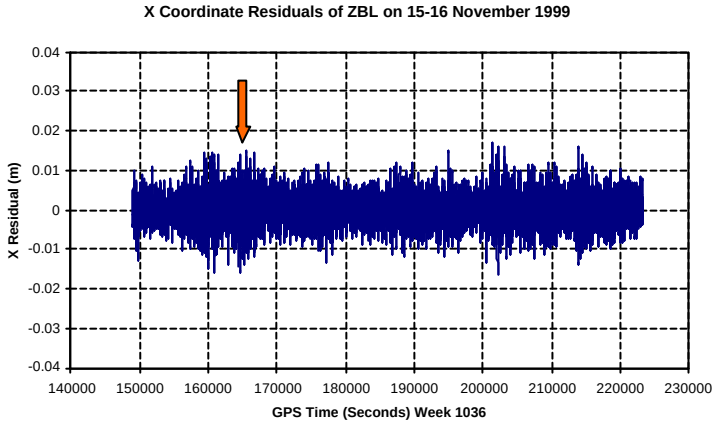

Fig. 3.11. X coordinate residual (CRS1000)

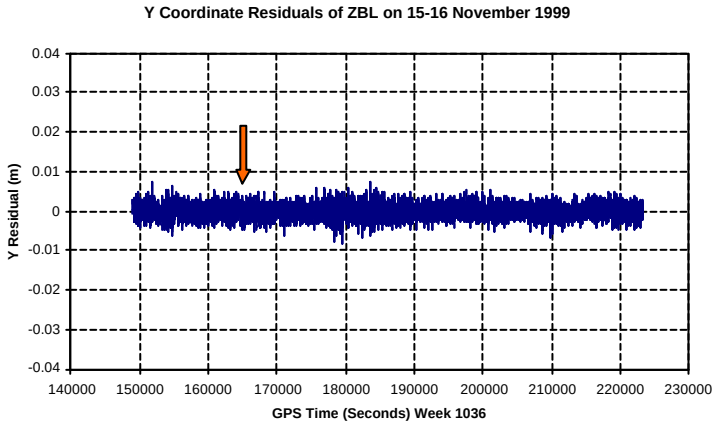

Fig. 3.12. Y coordinate residual (CRS1000)

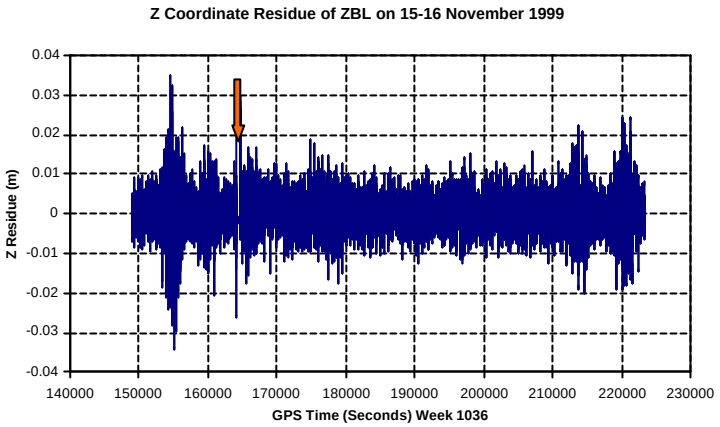

Fig. 3.13. Z coordinate residual (CRS1000)

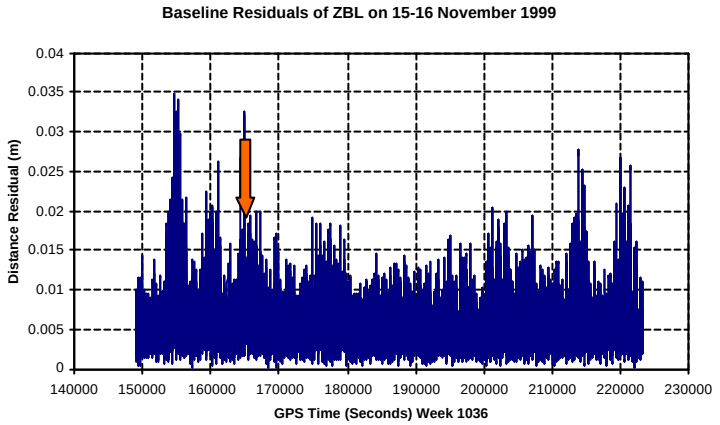

Fig. 3.14. Baseline residual (CRS1000)

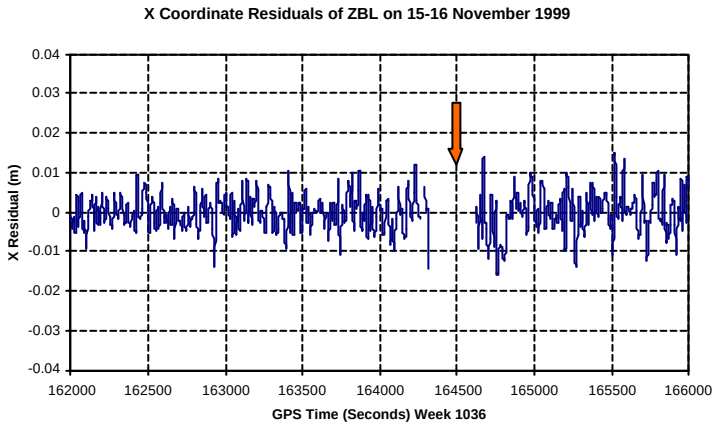

Fig. 3.15. Enlarged part of Fig. 3.11 (CRS1000)

The dated CRS1000 receiver firmware resulted in relatively poor GPS solutions for this 24-hour data set as expected (Leica 1999b). The overall coordinate errors with 99.7 percent probability of X, Y and Z are 1.19cm, 0.53cm and 1.54cm respectively,

after removing the outliers. The unsolved bugs in the firmware introduced by the GPS End-of-Week (EOW) rollover induced other problems in the correct decoding of the raw data. It inserted negative measurement numbers into the header section of the RINEX data file when long-term data logging (>1 hour) with a 10 Hz sampling rate was conducted. Leica solved the problems by providing a newly developed data logging and decoding software package (Leica 2000).

A T-Test is used to verify whether the calculated zero baselines have zero means (null hypothesis). The hypotheses are as follows

$$H_0 : m = m_0, \quad H_1 : m \neq m_0 . \tag{3.1}$$

The statistic value is

$$u = (\bar{x} - m_0) \times \sqrt{n} / s \ . \tag{3.2}$$

Where

$$\bar{x} = \sum_1^n x_i / n \tag{3.3}$$

is the sample mean; m_0 is the expectation; n is the observation number; and s is the SD. Under the null hypothesis, $u \sim N(0,1)$.

When s is unknown, substitute s with its estimate S

$$S^2 = \sum_1^n (x_i - \bar{x})^2 /(n-1) \tag{3.4}$$

and use the statistic value u to test null hypothesis H_0.

Table 3.1 lists some T-Test results for the ZBL residuals. It shows the null assumption exists with critical value α=0.05.

Test No.	Sensor Combination/ Sampling No	Means (mm)			Calculated Statistic Value			Critical Value with α=0.05
		X	Y	Z	X	Y	Z	
1	1 & 2/ 654	1.7	1.0	3.7	64.28	65.61	67.87	1.96
2	1 & 2/ 786	1.9	0.4	1.7	64.48	56.14	66.84	1.96
3	1 & 2/ 679	0.9	3.0	15.5	34.86	34.50	34.86	1.96
4	1 & 2/ 591	1.6	0.9	3.7	51.89	46.29	55.69	1.96
5	1 & 2/ 396	1.6	0.9	3.7	44.57	40.41	47.14	1.96
6	2 & 3/ 623	1.3	0.8	2.8	39.18	43.46	52.09	1.96
7	1 & 3/ 785	1.2	0.8	2.9	51.18	45.82	58.58	1.96
8	1 & 2/ 446	1.4	0.8	3.0	43.66	41.31	48.29	1.96
9	2 & 3/ 622	1.2	1.0	2.8	61.00	64.20	66.67	1.96
10	1 & 3/ 406	1.6	0.9	3.6	39.00	35.84	41.86	1.96

Table 3.1. T-Test of ZBL (CRS1000)

ZBL accuracy of the positioning solutions with different sampling rates was further investigated. The raw measurements were collected in a combined ZBL and SBL test carried out on 1 February 2000 using three CRS1000 receivers with the upgraded firmware. RINEX format data sets were then processed by AOSS software with different frequency options. The positioning solutions with L1 and L2 carrier phases and pseudoranges are summarised in Appendix A3. Fig. 3.16 to Fig. 3.21 are 3D coordinate residuals calculated with L1 and L2 phase measurements.

With 10 Hz sampling rate and L1 carrier phase used in processing the baseline, 0.62cm, 0.33cm and 0.75cm 3D positioning accuracies can be achieved (99.7% probability). The quality of these results is much higher than the previous results using an old firmware. The positioning accuracies of L2 carrier phase are 1.37cm, 0.64cm and 1.3cm for X, Y and Z coordinates (99.7%), respectively.

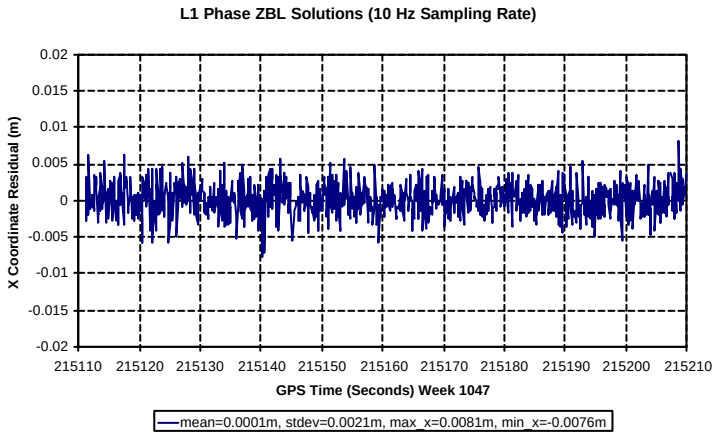

Fig. 3.16. L1 phase solution of X residual (CRS1000)

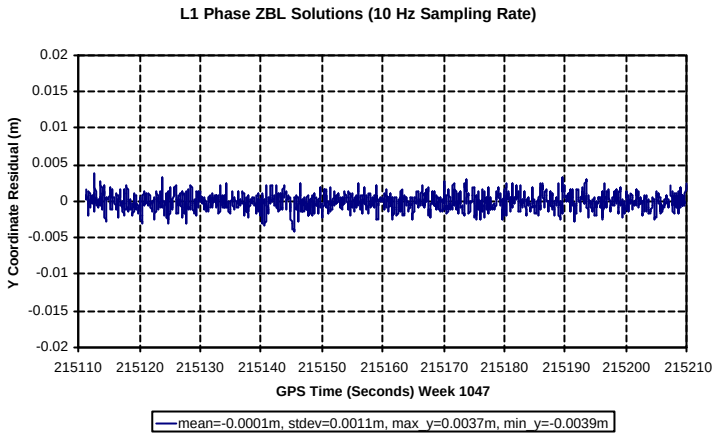

Fig. 3.17. L1 phase solution of Y residual (CRS1000)

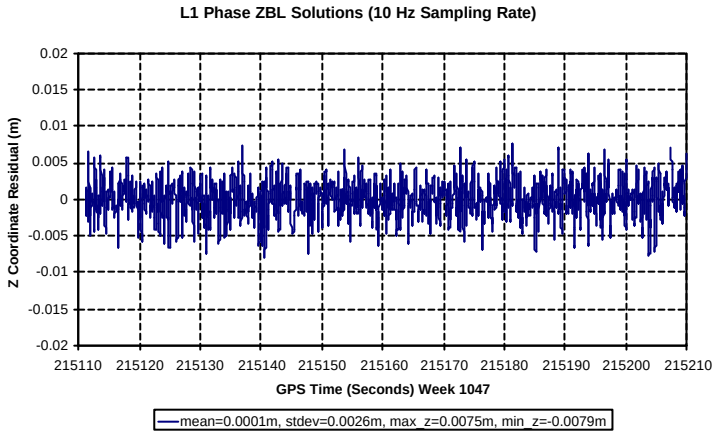

Fig. 3.18. L1 phase solution of Z residual (CRS1000)

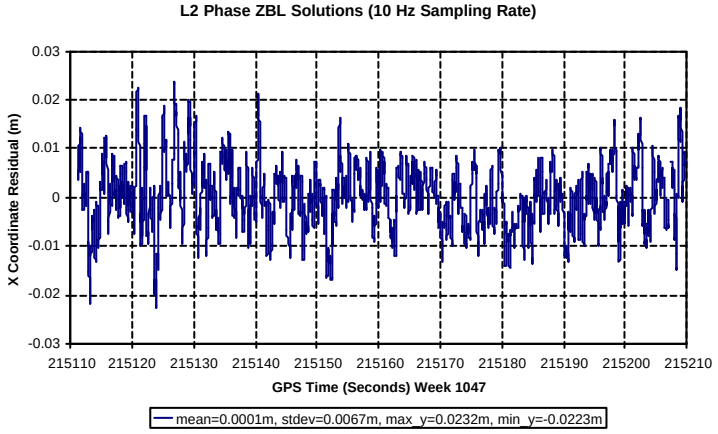

Fig. 3.19. L2 phase solution of X residual (CRS1000)

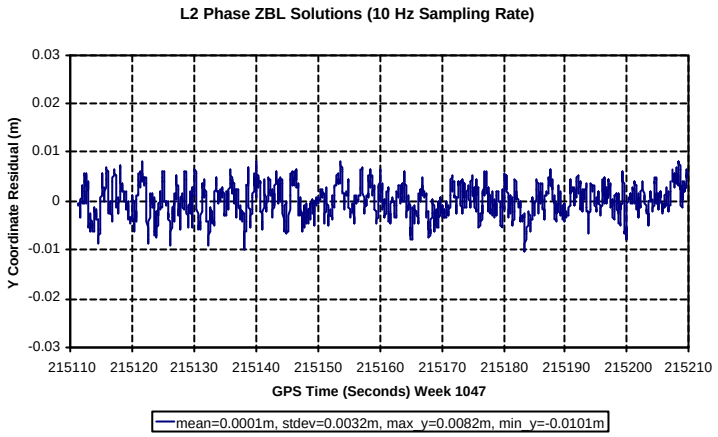

Fig. 3.20. L2 phase solution of Y residual (CRS1000)

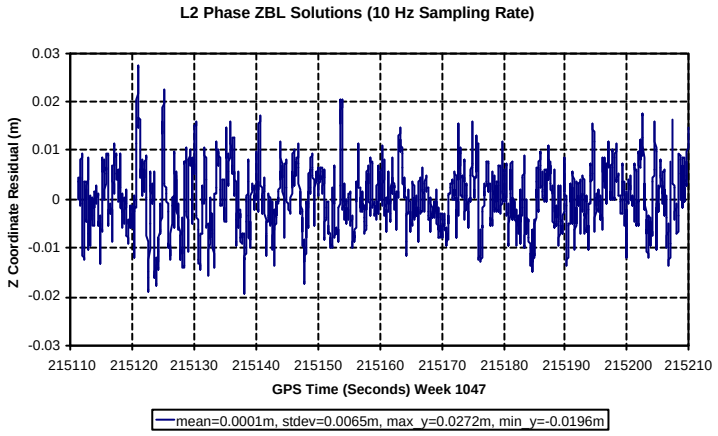

Fig. 3.21. L2 phase solution of Z residual (CRS1000)

3.2.2 ZBL Tests Using Leica SR510 Single Frequency Receivers

The Leica SR510 is a 12 channel, single frequency survey receiver. Together with SKI-Pro L1 software, SR510 provides an easy entry to GPS surveying and a cost-effective solution for many applications. With ambiguities resolved baseline accuracies of 5 to 10mm+2ppm (rms) for static measurements can be achieved in post processing (Leica, 2002). In the SR510 ZBL tests, *stop and go* mode was used to obtain an each epoch solution at a sampling rate of 10 Hz based on a known point initialisation approach.

In the ZBL tests, two SR510 receivers were connected using the splitter to a Leica single frequency antenna AT501 over a known point on the turret of the IESSG

building. Static initialisations with different periods were made at the beginning of data logging and then the receivers were switched to kinematic mode. The data sets were then post-processed with SKI-Pro in kinematic mode. In the processing, the data sets in *stop and go* mode were marked at *init (track)*; this ensures that SKI-Pro relies on the already existing coordinates for this point to fix ambiguities. In the context of bridge monitoring with a moderate deflection, for instance, within 5-10 cm bridge movements, the coordinates of bridge points occupied by SR510 receivers could still be known to the centimetre level. In this case, the static initialisation can be shortened to 20 to 30 seconds (Leica, 2002).

Fig. 3.22 to Fig. 3.25 are the 3D coordinates and baseline residuals. Fig. 3.26, 3.27, and 3.28 are the residual scatter graphs of each coordinate pair (X vs. Y, X vs. Z and Y vs. Z). From the direct observation of the graphs and also from calculation, 99.7% residuals of X, Y and Z coordinates are situated within the intervals (-0.33cm, 0.33cm), (-0.17cm, 0.17cm) and (-0.44cm, 0.44cm)

Autocorrelation analysis has been applied to the X coordinate residual only (Fig. 3.29), but the results for the Y and Z coordinates residuals are the same. The time lag is 0.1 second. This means that each epoch coordinate is independently determined by software.

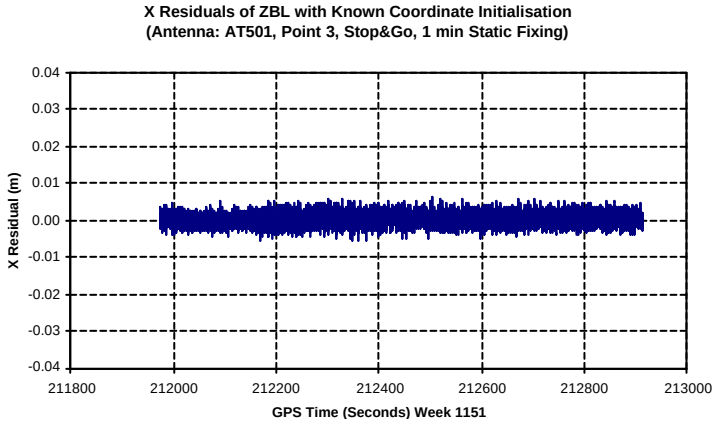

Fig. 3.22. X coordinate residual (SR510)

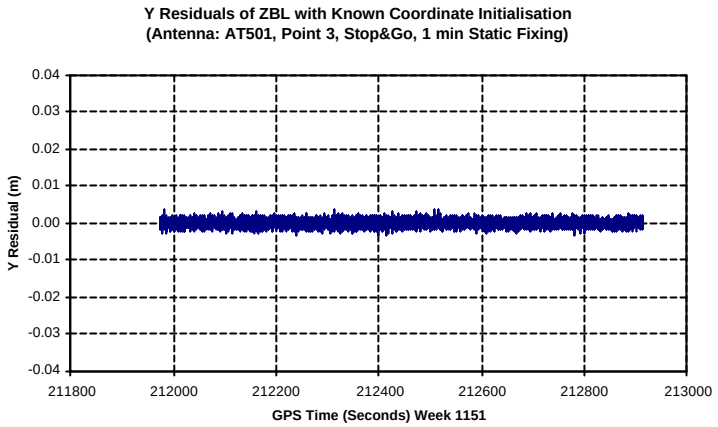

Fig. 3.23. Y coordinate residual (SR510)

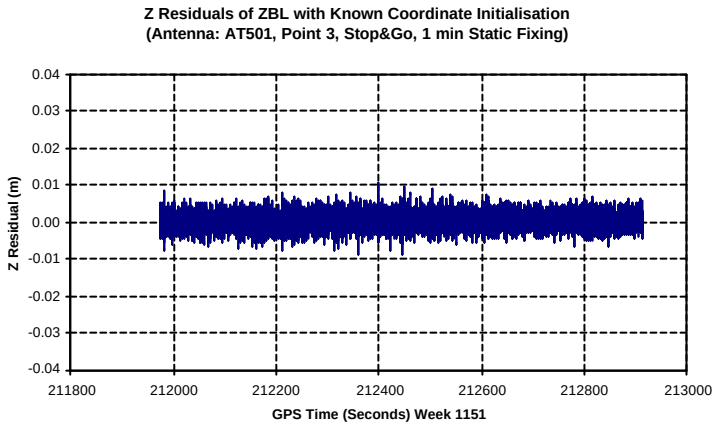

Fig. 3.24. Z coordinate residual (SR510)

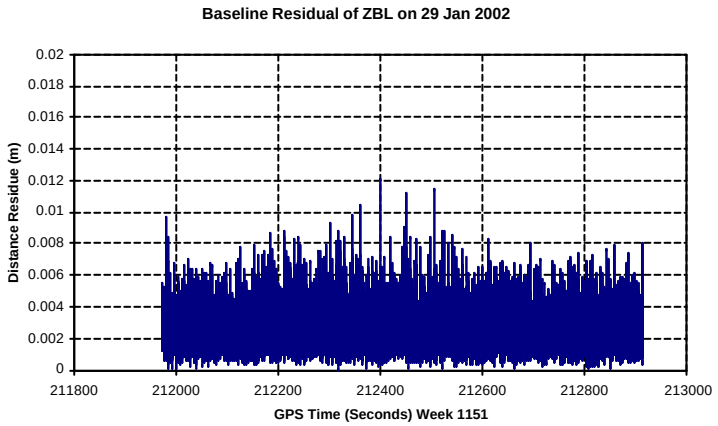

Fig. 3.25. Baseline residual (SR510)

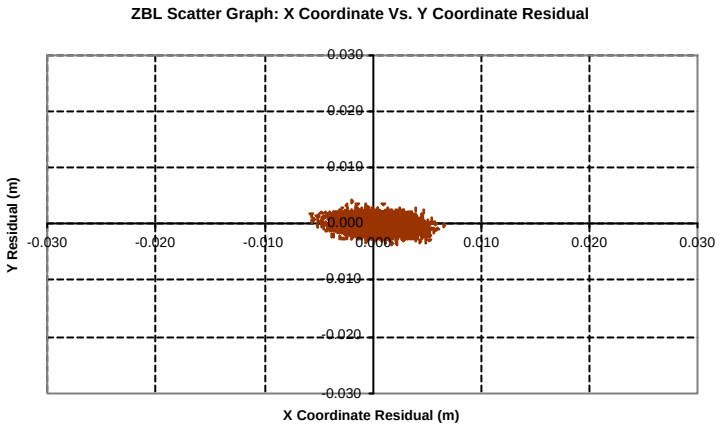

Fig. 3.26. Scatter graph: X vs. Y residual (SR510)

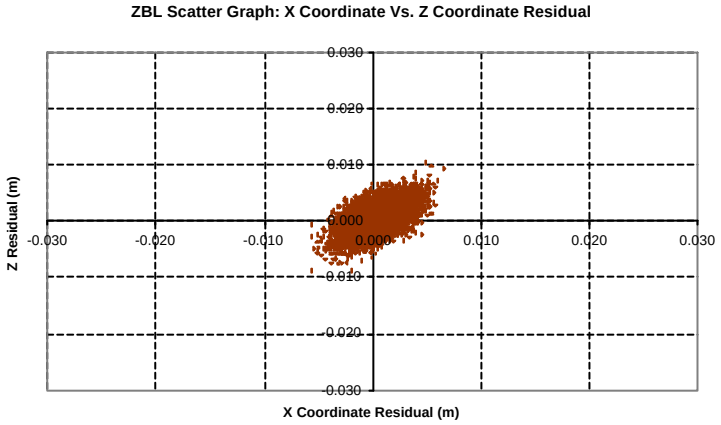

Fig. 3.27. Scatter graph: X vs. Z residual (SR510)

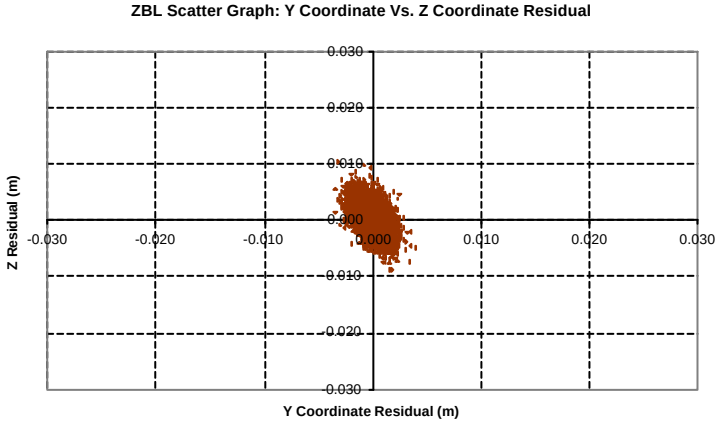

Fig. 3.28. Scatter graph: Y vs. Z residual (SR510)

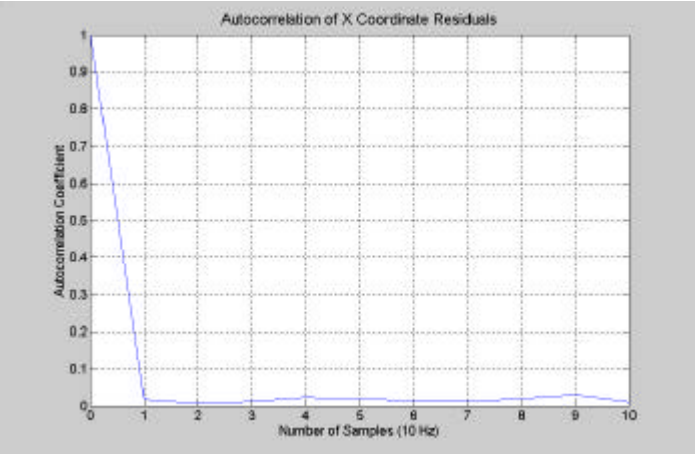

Fig. 3.29. Autocorrelation of X coordinate residual (SR510)

The scatter graphs of each residual pair can be further exploited to calculate the orientations of the main axis of the ellipses. Also, the scatter graphs themselves can be directly used to estimate the achievable 3D precisions. The residual time series can be transformed into the desired coordinate systems to analyse horizontal or vertical precision or the precision in a particular direction by using the error propagation algorithm presented in Section 6.2.

3.2.3 ZBL Tests Using Leica SR530 Dual Frequency Receivers

Leica SR530 dual frequency GPS receiver together with sophisticated chokering antenna AT504 represents state-of-the-art GPS technology. Similar data processing and analysis approaches have been applied to the data sets collected with SR530 receivers as those used in the previous ZBL tests. A 45-minute data set was collected on 7 April 2002. The raw data were directly input into SKI-Pro software and processed in a kinematic OTF mode. The 3D coordinate and baseline residuals are presented in Fig. 3.30 to Fig. 3.33. Three times coordinate SDs for X, Y and Z are 0.4cm, 0.20cm and 0.53cm (99.7% probability), respectively. These values are similar to the positioning solutions from SR510 single frequency receivers with known point initialisation. It demonstrates the possibility to use single frequency receivers to replace expensive dual frequency receivers to achieve high accurate positioning in bridge monitoring, if the ambiguities could be appropriately fixed.

Fig. 3.34, 3.35, and 3.36 are the time series of each epoch SD obtained from data processing. From Fig. 3.34, it can be seen that the precisions of X the coordinates are better than 3mm in most cases. The precisions of the Y coordinates can be higher than 1.5mm, whilst the precisions of the Z coordinates are about 4mm. It is worth pointing out that these are the achievable precisions with these particular instrumentation configuration and satellite sky distribution.

The autocorrelation has been analysed using a Matlab script. The coefficient changes of X coordinate residual over time are represented in Fig. 3.37. Due to the internal filtering algorithm, the calculated coordinates exhibit certain period of autocorrelation themselves. In this example, 1 second or even longer autocorrelation of the positioning solutions can be expected. It is larger than the time lags calculated for the SR510 receiver, which is 0.1 seconds and means with SR510 receiver it is possible to obtain each epoch independent positioning solutions.

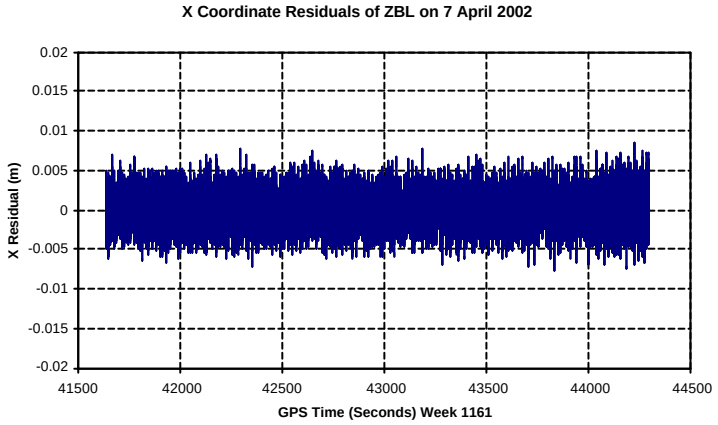

Fig. 3.30. X coordinate residual (SR350)

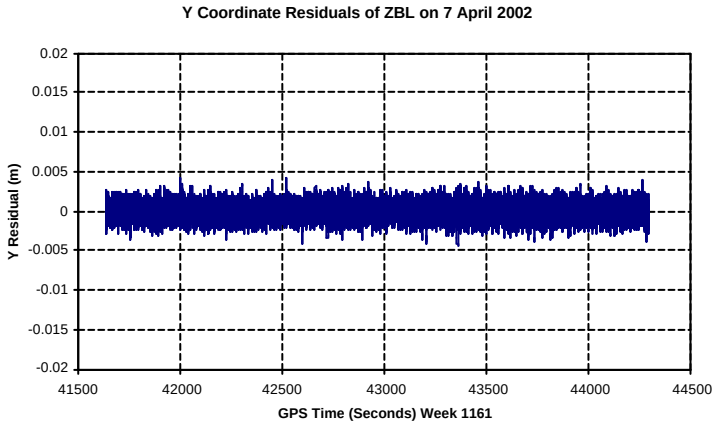

Fig. 3.31. Y coordinate residual (SR530)

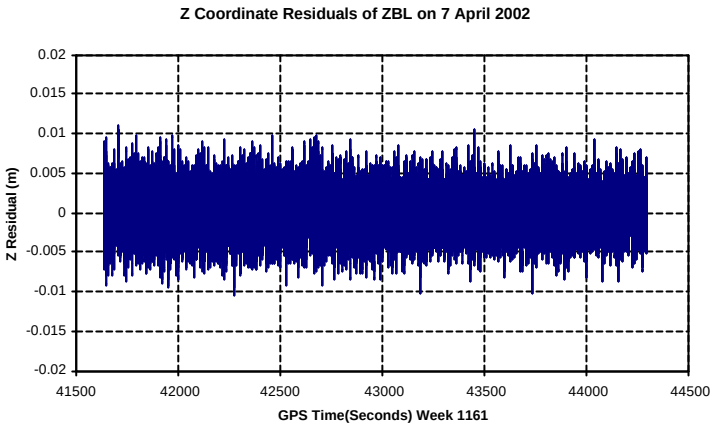

Fig. 3.32. Z coordinate residual (SR530)

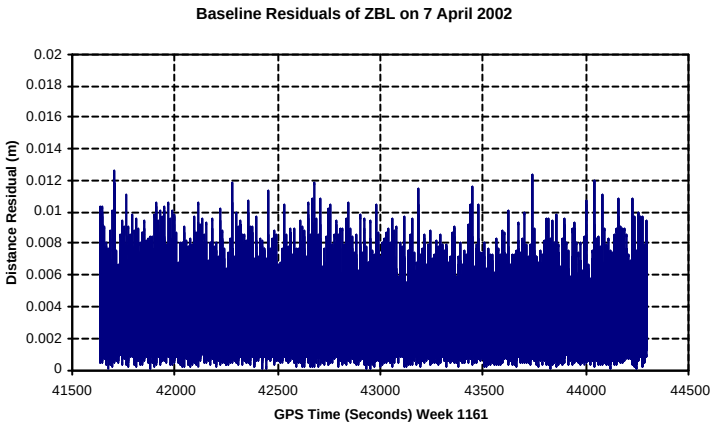

Fig. 3.33. Baseline residual (SR530)

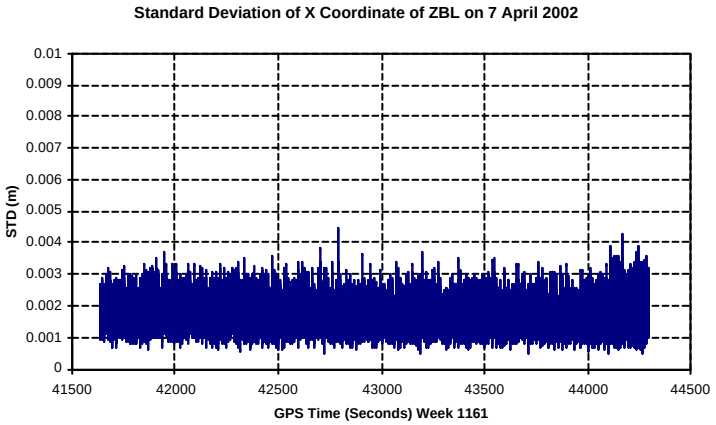

Fig. 3.34. Each epoch SD of X coordinate (SR530)

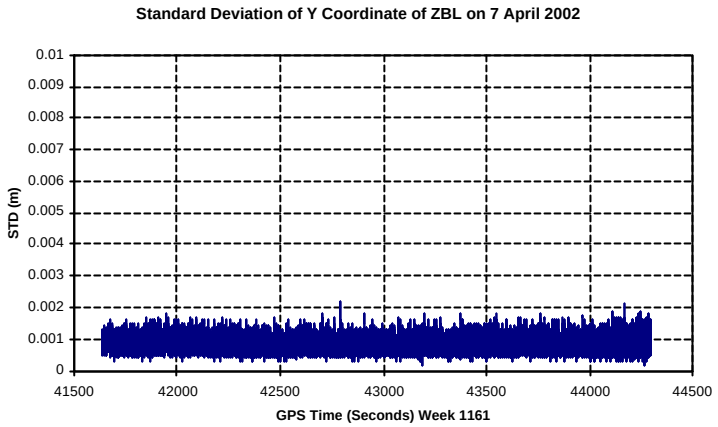

Fig. 3.35. Each epoch SD of Y coordinate (SR530)

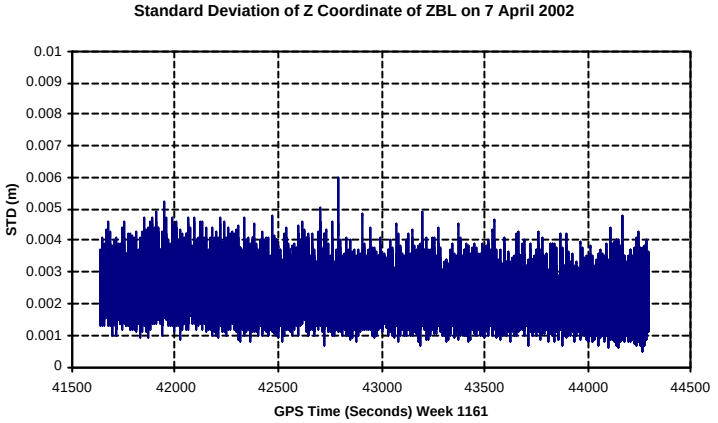

Fig. 3.36. Each epoch SD of Z coordinate (SR530)

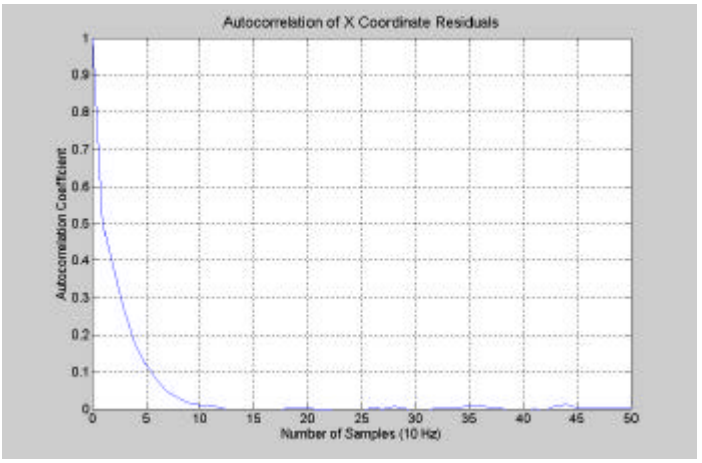

Fig. 3.37. Autocorrelation lags of X residual (SR530)

3.3 SBL Tests Using Leica GPS Receivers

SBL tests were conducted with three types of Leica GPS receivers to investigate their performance at 10 Hz sampling rate. Two antennas were installed over two known points on the turret of the IESSG building.

3.3.1 SBL Tests Using Leica CRS1000 Dual Frequency Receiver

Following the ZBL trials made in November and December 1999, a series of combined ZBL and SBL trials were made in year 2000 using CRS1000 receivers and the IESSG facilities. During these trials, two receivers were connected to the same antenna at a known point to form a ZBL and a third receiver was attached to a separate chokering antenna at another known point (Fig. 3.38). With such a receiver configuration, one ZBL and two SBLs can be formed. In this section the focus will be on the data analysis of SBL trials.

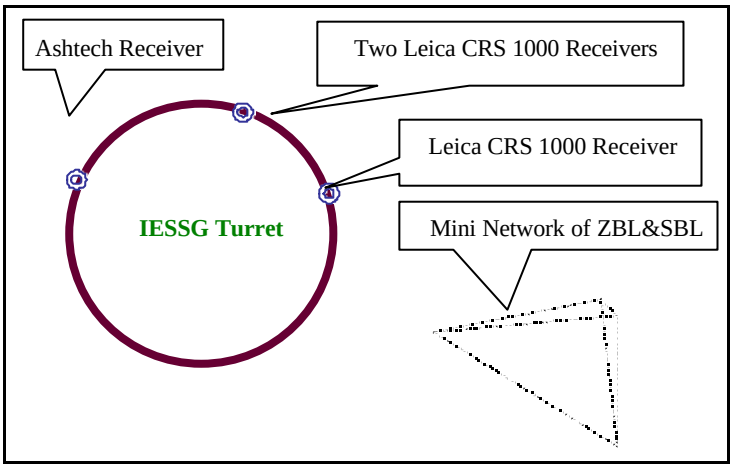

Fig. 3.38. Facility used for ZBL and SBL tests

Partial SBL trials are listed in Appendix A4. The results of the highlighted trials are presented in this thesis. A one-hour SBL trial at sampling rate of 10 Hz on 1 February 2000 is illustrated first, followed by the discussion of the results obtained from a lower sampling rate from long-term SBL trials made from 5 to 7 June 2000. For longer-term SBL trials, precise and broadcast ephemerides are used in the data processing. The results show no differences in positioning solutions due to such a close distance between the two known points of 1.032m apart. The data gathered in

three consecutive days shows significant multipath signatures. SDs of the 3D positioning solutions are also illustrated with coordinate residuals. The baseline residuals calculated are illustrated separately.

Unlike ZBL tests, which can be used to quantify the noise levels of the GPS receivers, the positioning solutions of SBL tests include many similar error sources that are encountered in the actual surveying. Fig. 3.39 to Fig. 3.42 are the X, Y, Z and baseline residual time series from a SBL trial on 1 February 2000. Within one-hour data collection trial, apparent movements caused by multipath make the rover look like a moving point. The 99.7% probability error ranges of X, Y and Z residuals are 1.26cm, 0.76cm and 1.37cm. The maximum baseline residual could reach 1.7cm.

Epoch by epoch SD of 3D coordinate residuals are depicted by Fig. 3.43, 3.44, and 3.45. Sub-centimetre positioning solution can be obtained in this trial, with roughly equivalent precisions in X and Z coordinate and the best precision in Y coordinate. Simulations of the GPS satellite geometry reveals that in the high latitude areas, the horizontal accuracy could degrade to the same level as that of vertical component. This will be further explored in Chapter 6. Fig. 3.46 illustrates the changes of the time lags of the autocorrelation coefficient of X coordinate residual. Recall the autocorrelation time lag is about 1 second for ZBL using CRS1000 dual frequency receivers. The time lag for the SBL test consists of two parts, one caused by receiver noise due to the internal filtering algorithm and another one caused by the slow changing multipath signatures with a cycle period of several minutes, governed by the reflectors in the surveying environment. In this example, the total cycle period identified from autocorrelation time lag is about 480 seconds (8 minutes), mainly caused by multipath signature. It is worth pointing out the autocorrelation coefficients are determined by the instruments used, including antenna type and receiver noise. Different antenna design has different multipath rejection pattern, internal filtering algorithm, and behaves different in the same reflection environment.

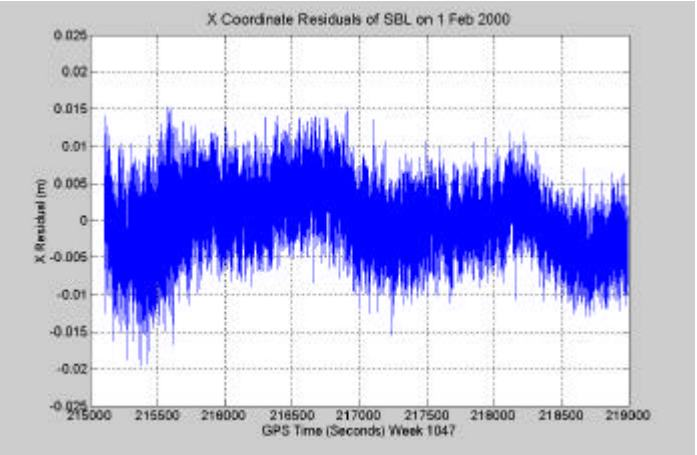

Fig. 3.39. X coordinate residual (CRS1000)

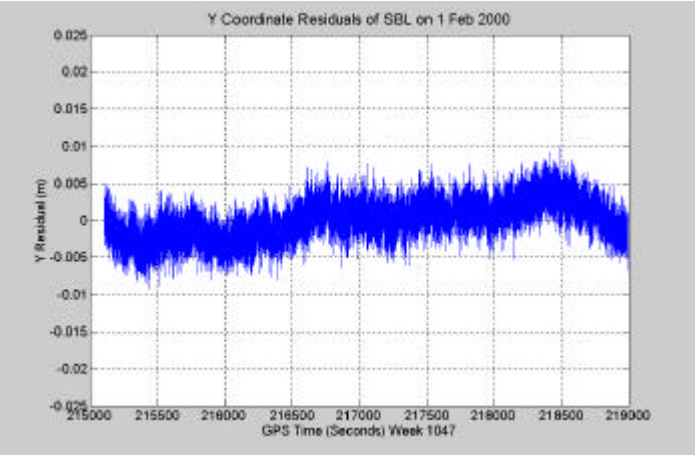

Fig. 3.40. Y coordinate residual (CRS1000)

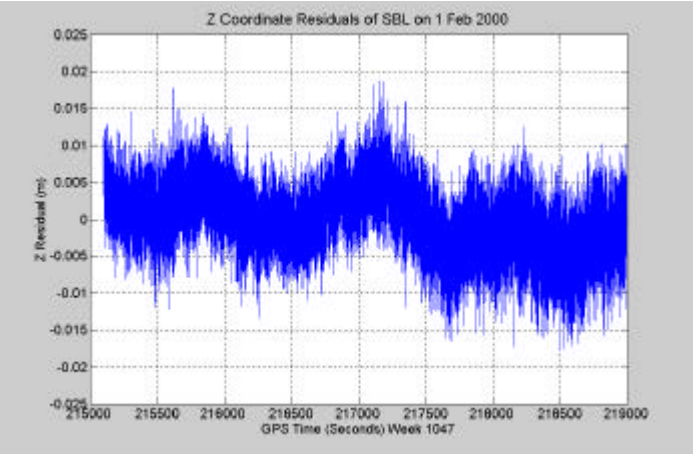

Fig. 3.41. Z coordinate residual (CRS1000)

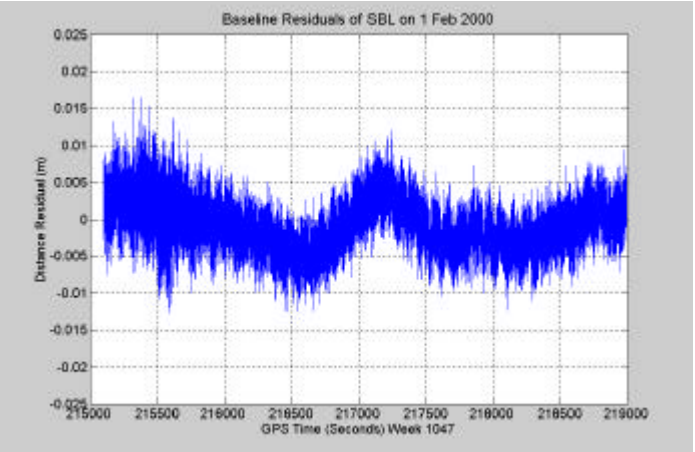

Fig. 3.42. Baseline residual (CRS1000)

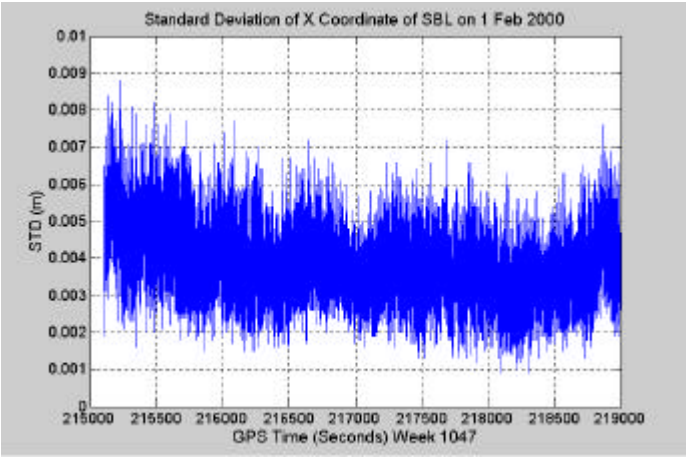

Fig. 3.43. Each epoch SD of X coordinate

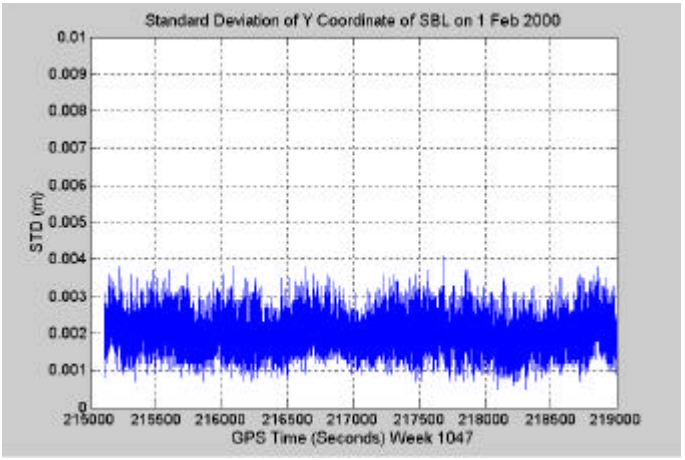

Fig. 3.44. Each epoch SD of Y coordinate

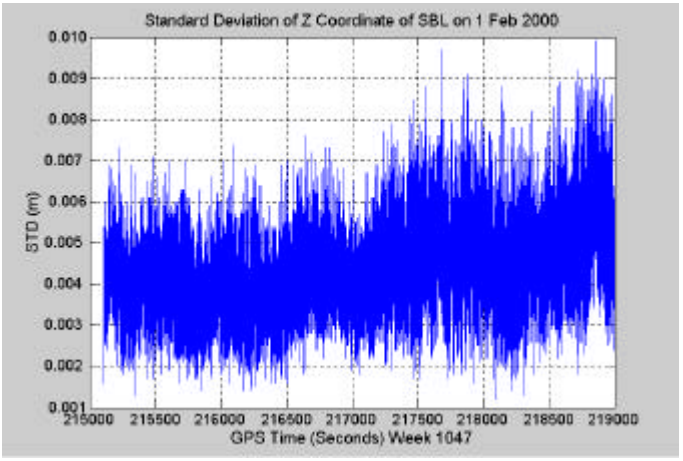

Fig. 3.45. Each epoch SD of Z coordinate

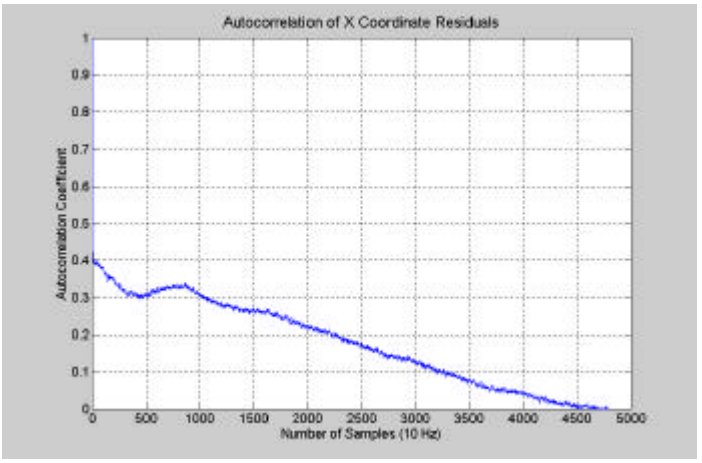

Fig. 3.46. Autocorrelation lags of X residual (CRS1000)

To further study the possible pattern of multipath on the turret of the IESSG building, two 24-hour SBL trials were carried out at a sampling rate of 30 seconds on 5, 6 and 7 June 2000. Fig. 3.47 to Fig. 3.54 are the residual time series of the corresponding coordinates and baselines. Comparing each coordinate and baseline pair, it can be found that the time series patterns are identical. The cross-correlation coefficients of X, Y and Z coordinates for the two data sets are 0.43, 0.46 and 0.47 and demonstrate high level multipath signature in the positioning solutions.

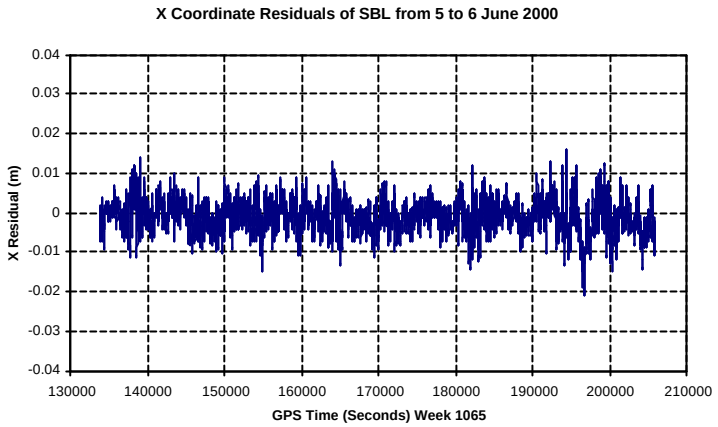

Fig. 3.47. X coordinate residual (CRS1000)

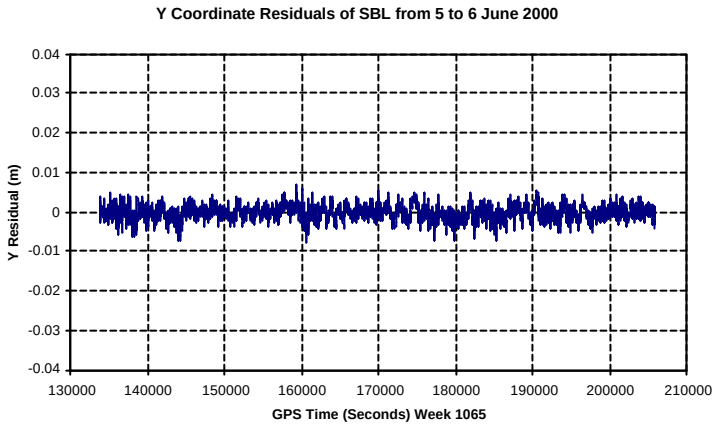

Fig. 3.48. Y coordinate residual (CRS1000)

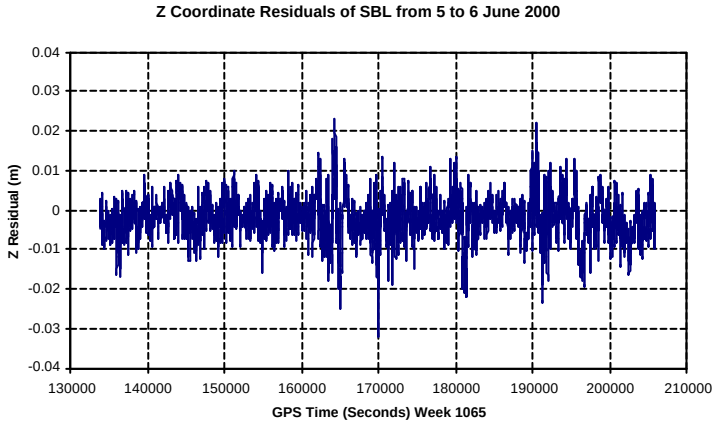

Fig. 3.49. Z coordinate residual (CRS1000)

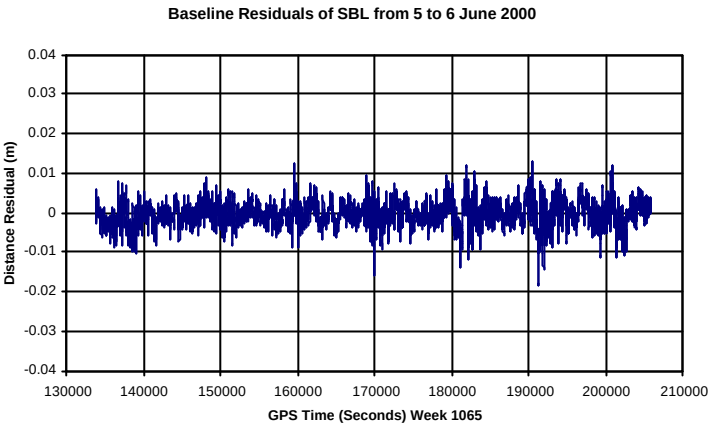

Fig. 3.50. Baseline residual (CRS1000)

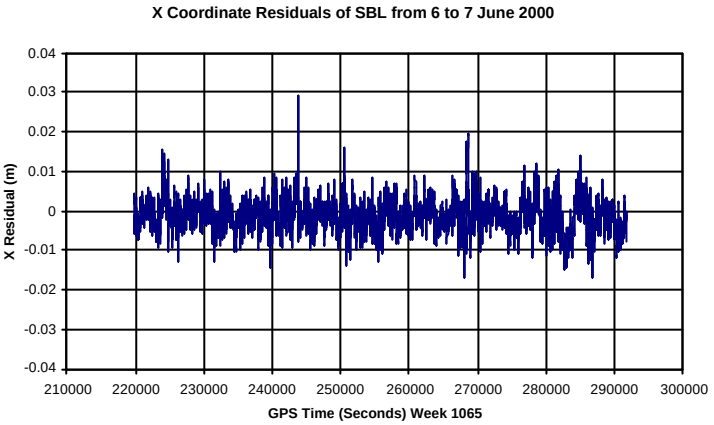

Fig. 3.51. X coordinate residual (CRS1000)

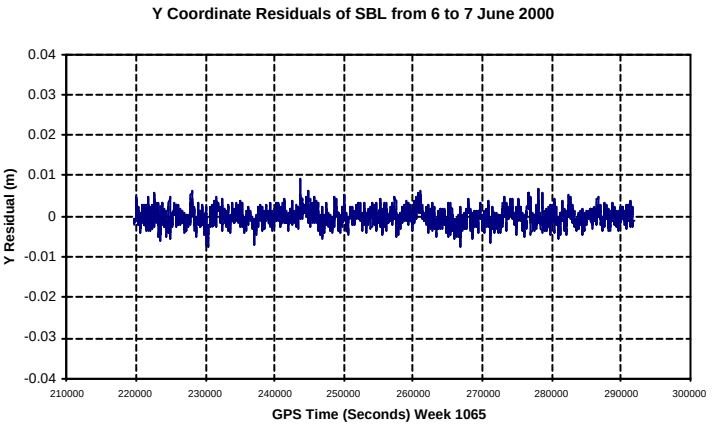

Fig. 3.52. Y coordinate residual (CRS1000)

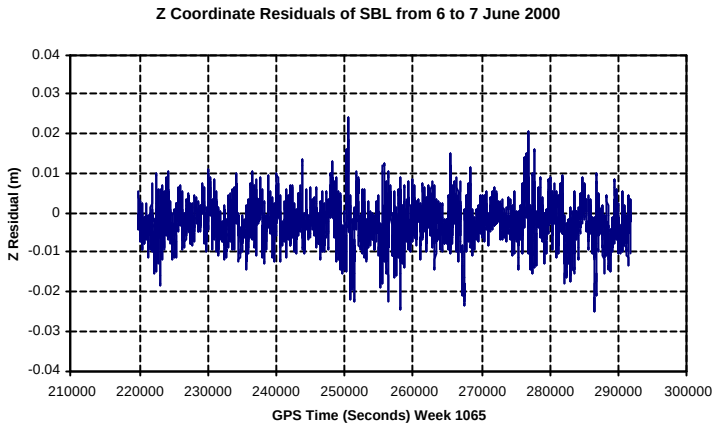

Fig. 3.53. Z coordinate residual (CRS1000)

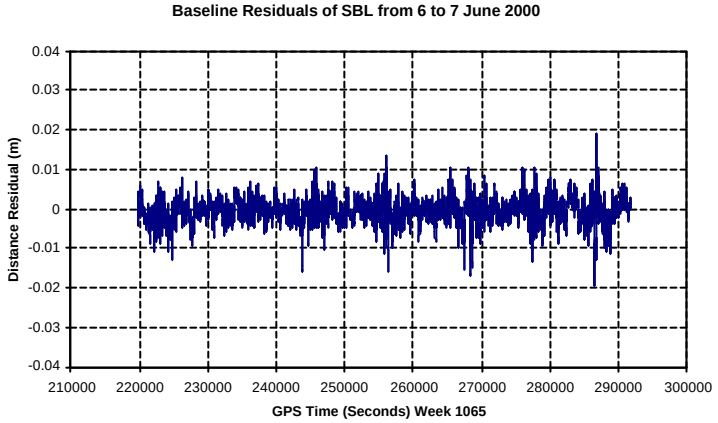

Fig. 3.54. Baseline residual (CRS1000)

Day-to-day multipath of amplitude higher than one centimetre identified on the roof of the IESSG building is apparent even chokering antennas were employed in the tests. Reflections from the nearby surroundings, for instance, the high chimney close to the IESSG building, roof of the IESSG building, meteorological sensor, and the Tower Building, are possibly the major impact factors.

3.3.2 SBL Tests Using Leica SR510 Single Frequency Receivers

Using the same facilities as in the previous sections, SBL tests were conducted with SR510 single frequency receivers. Point P2 and P3 on the turret of the IESSG building were employed. Connected to an AT501 single frequency antenna on point

P3 was a splitter with a SR530 dual frequency receiver and a SR510 single frequency receiver attached. Another SR510 single frequency receiver was connected to an AT501 single frequency antenna at P2. Using this configuration is should be possible to provide corrections for the nearby single frequency receiver to speed up ambiguity resolution, which is the major limitation of single frequency receiver for accurate engineering applications. In this section, the main interest is the achievable accuracy of the SR510 receivers given by a limited time period for the initialisation. The shortest initialisation time conducted was 25 seconds. With such a short period of initialisation, millimetre level positioning accuracy can be achieved using SR510 receivers and AT501 antennas after the multipath have been removed by the approaches proposed in Chapter 7 and 8.

Presented in Fig. 3.55 to Fig. 3.58 are the residuals of X, Y, Z coordinates and the calculated baselines from data collected on 30 January 2002. One receiver on P3 was fixed as the reference station, while another receiver was designated as a rover station. With 25 seconds initialisation, each epoch 3D positioning solution was obtained in a kinematic mode using SKI-Pro. 99.7% probability error ranges for coordinate X, Y and Z are 1.17cm, 0.54cm and 1.8cm, respectively.

From the above error ranges, it can be seen that it is possible to use SR510 single frequency receiver to conduct centimetre level structural deformation applications, and potentially millimetre accuracy is achievable if multipath signature is mitigated. The baseline residuals are less than 2cm with an apparent multipath pattern.

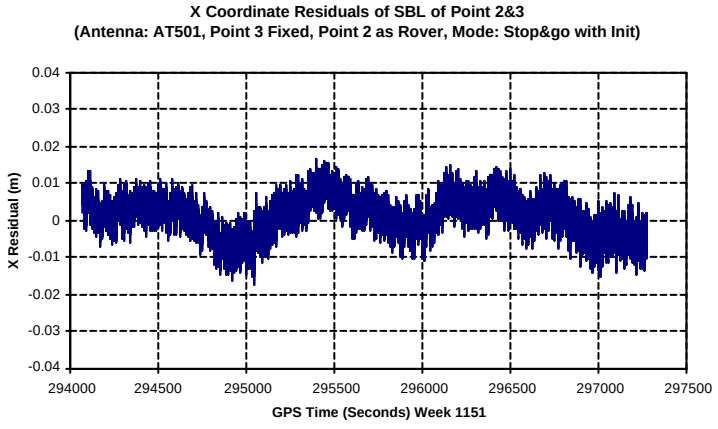

Fig. 3.55. X coordinate residual (SR510)

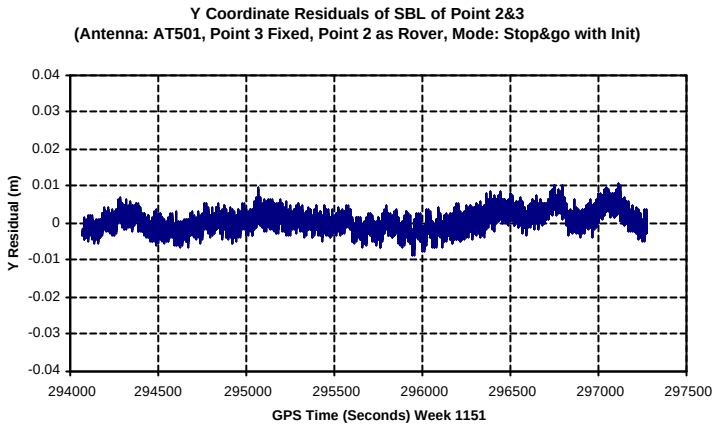

Fig. 3.56. Y coordinate residual (SR510)

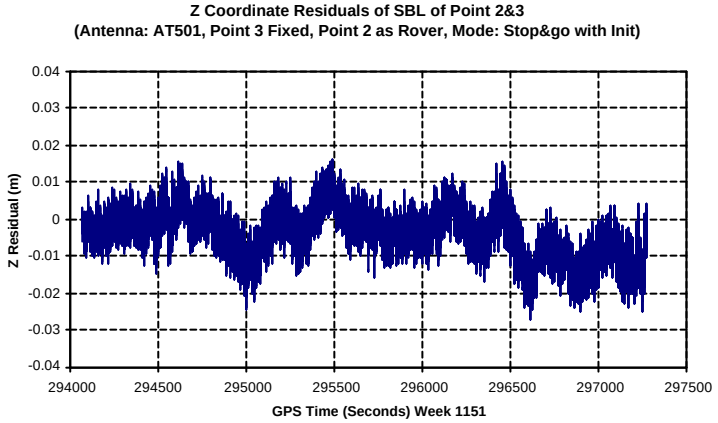

Fig. 3.57. Z coordinate residual (SR510)

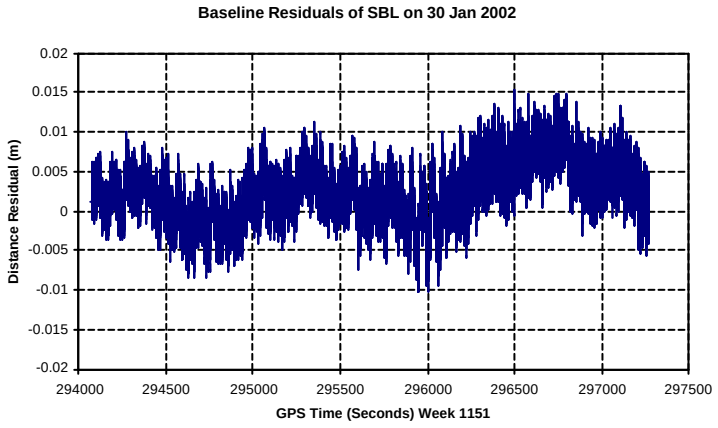

Fig. 3.58. Baseline residual (SR510)

Fig. 3.59 and Fig. 3.60 are time series of the smoothed and residual components of the baseline residuals treated by an MA filter. The filter length of 10 sample has been

applied to the time series of Fig. 3.58. Multipath of long-term period has been removed. It is demonstrated that it is possible to use SR510 single frequency receiver to achieve millimetre positioning accuracy in 3D.

Autocorrelation coefficients of the X coordinate residuals are calculated and illustrated by Fig. 3.61 as an example. Due to the differences in constructions of different antenna types, the pattern of multipath intercepted is different. This introduces a time lag difference in the autocorrelation of the positioning solutions. These time lags could inversely help the identification of multipath cycle periods for mitigation purposes. The time lag for X coordinate residual in this test is 480 seconds (8 minutes). The time lag for SR510 receiver is the same as for CRS1000 receiver. However, autocorrelation decay pattern of SR510 receiver is different from that of CRS1000. It shows different multipath rejection patterns by the different instruments.

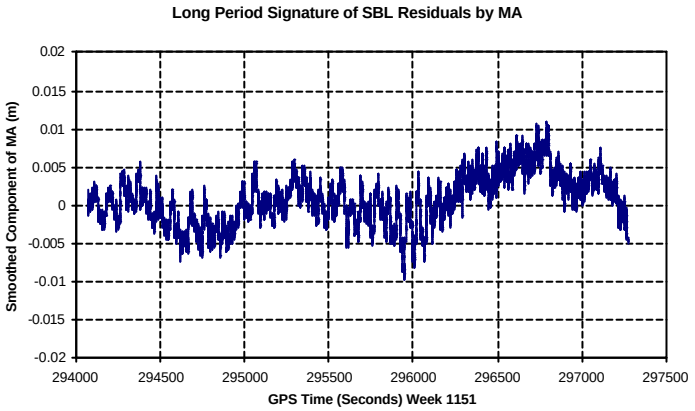

Fig. 3.59. Multipath signature by an MA filter

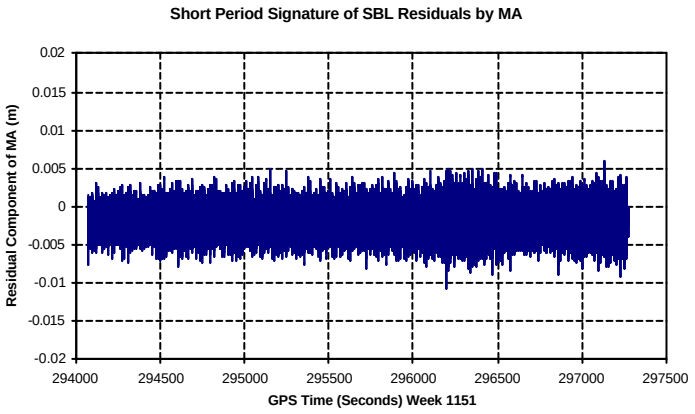

Fig. 3.60. Receiver noise signature by an MA filter

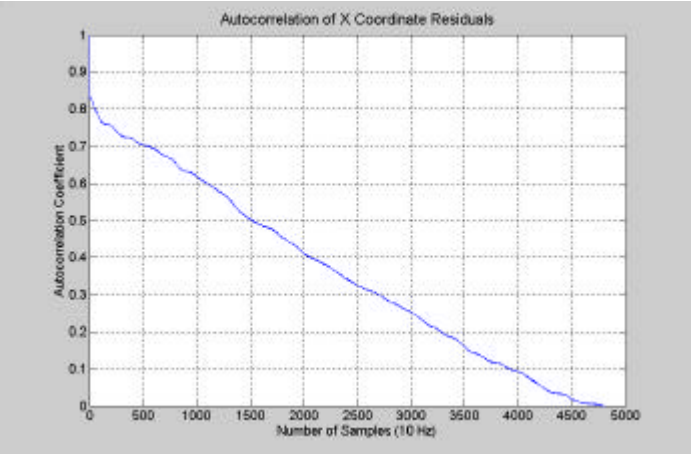

Fig. 3.61. Autocorrelation lags of X residual (SR510)

3.3.3 SBL Tests Using Leica SR530 Dual Frequency Receivers

Using the same known points on the turret of the IESSG building, a SBL test was conducted using two SR530 receivers and AT504 chokering antennas on 7 April 2002. Fig. 3.62 to Fig. 3.65 are the residual time series of 3D coordinates and each epoch baseline. The calculated error ranges of the 3D coordinates are 0.85cm, 0.33cm and 1.06cm, respectively. If the slowly moving pattern in the time series is removed, millimetre level precision in 3D coordinates can be achieved. As discussed previously the time lag of X coordinate residual from the autocorrelation analysis for SR530 receivers is 386.6 seconds (6.43 minutes). It shows a slower and flat pattern due to the better mitigation effect from chokering antennas than SR510 receiver (Fig. 3.66). With a chokering antenna, a sharp decay in the autocorrelation coefficient of SR530 as CRS1000 is noticeable. If 0.2 is defined as week autocorrelation coefficient, the time lags for CRS1000, SR510, and SR530 are 220 seconds, 320 seconds, and 220 seconds, respectively, illustrating different multipath mitigation effects from different receivers again.

SBL tests were conducted with SR530 receivers to verify that there are no biases introduced by different processing modes. The collected data were processed in OTF and *stop and go* modes. Identical position solutions were obtained. This further proves, as integer ambiguities have been resolved, cheap single GPS receivers SR510

could provide similar accuracy kinematic solutions as expensive dual frequency receivers.

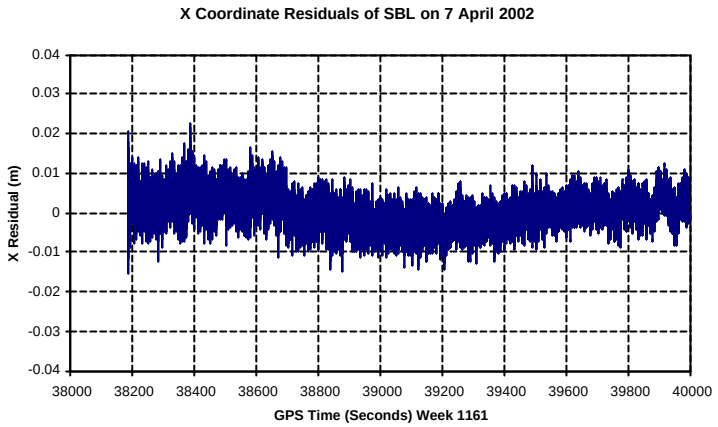

Fig. 3.62. X coordinate residual (SR530)

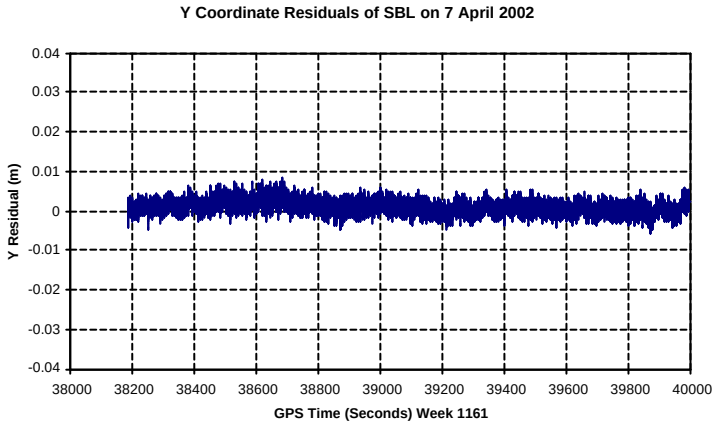

Fig. 3.63. Y coordinate residual (SR530)

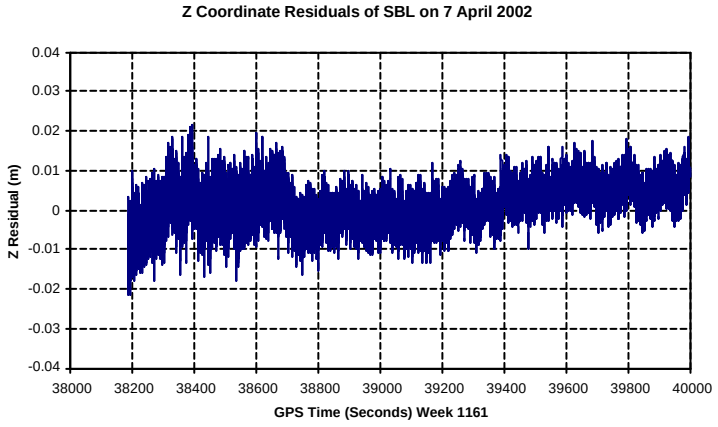

Fig. 3.64. Z coordinate residual (SR530)

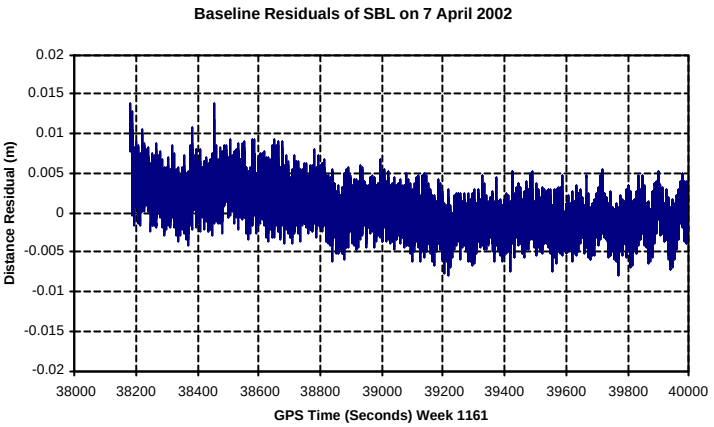

Fig. 3.65. Baseline residual (SR530)

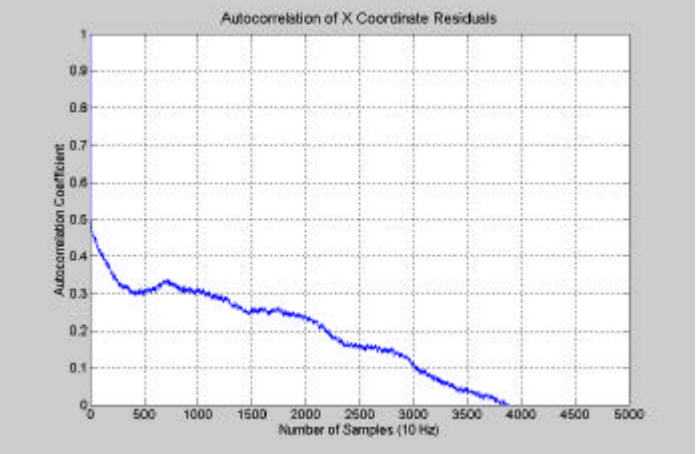

Fig. 3.66. Autocorrelation lags of X residual (SR530)

3.4 Determination of Zero Offsets and Scale Factors of Triaxial Accelerometer

Since GPS is sensitive to multipath and multipath free environments seldom exist in practical applications, it is very difficult to consistently maintain millimetre level accuracy. In kinematic applications, a potential method for mitigating the effects of multipath and increasing the accuracy of the positioning solution is to augment GPS surveying with other sensors, such as the accelerometer. While GPS is capable of sensing long wavelength deformations, the accelerometer, with its higher data rate and short-term stability, is capable of accurately identifying higher frequency movement. Additionally, accelerometers are insensitive to GPS errors such as multipath. In semistatic, or dynamic applications with very small rotations, the GPS

and accelerometer combination can provide the information necessary for reliable long-term millimetre accuracy positioning, without the complexity inherent in full INS systems (Tolman and Craig 1997).

The zero bias or zero offset of a sensor is the signal it gives when there is no input. The errors caused by a misaligned system or one with uncompensated instrument biases, depend on the configuration of the inertial system, be it strapdown or platform, the number and type of gyros and accelerometers, and how the gimbals are arranged. Britting (1971) has provided a unified error analysis for terrestrial inertial systems and used it to compare their performances under different conditions.

An inertial sensor provides an output signal in response to either rotation or acceleration. The signal might be an analogous value such as voltage proportional to the input force. As most systems are now controlled by digital computers, digital output is preferred. Analogue to digital (A-to-D) converters are used to digitise the outputs from the analogue sensors. The scale factor is the ratio between a change in the output signal and the change in the input signal. As most sensors provide an output signal that is directly proportional to the input, the scale factor is a single number, defined as the slope of the best straight line fitted by the method of least-squares to the data obtained by varying the input over a specified range. The scale factor K can be defined as

$$K = \frac{S}{I} \tag{3.5}$$

where S =output signal, I =true input.

Sometimes an instrument will have a different scale factor for positive and negative inputs, this is known as scale factor asymmetry.

Instruments will have at least one IA defined. The IEEE standard defines the IA as the axis along which an input causes a maximum output (Lawrence 1998). It is the direction about which the scale factor is defined. It is often defined as the normal to a mounting plate. To be a stable scale factor, the IA must remain stable over time, temperature, vibration, and shock.

The scale factor may not be exactly linear but may have second- or higher-order terms relating signal to input. To see these, it is usual to run a test in which the acceleration is varied in steps, and the sensor output is measured. The data are fitted to a straight line by the least-squares method, and the residuals are plotted. The residuals are the differences between the actual outputs at a given rate (acceleration) and the value that would be predicted using the calculated scale factor. If the residuals are randomly scattered about the axis, no further modelling is possible, but if they form curves, second- or third-order curve fits can provide a better model for the scale factor. The SD of the residuals, called the standard error, can be used to specify instrument quality.

In the determination of calibration constants of an accelerometer, the earth's gravity is used as the test acceleration. By attaching the accelerometer to a precise rotary table and rotating it about a horizontal axis so that the accelerometer axes are exposed to gravity in each direction, commonly referred to *plus and minus 1 g* excitation tumble. Since the telescope of a theodolite can rotate around its transverse axis with accuracy to arc-second, it can be used as an ideal platform to sense the changes of the analogue outputs. Through the appropriate attachment plate design, a theodolite can replace an expensive calibration platform.

Assuming that an accelerometer gives an analogue output with scale factor K_1 (V/g), the output at any angle θ is

$$V / K_1 = g\cos\theta + K_0 . \tag{3.6}$$

Fitting the output to a best cosine model, the scale factor K_1 and bias K_0 are deduced. Then they are used to calculate the residuals. Or in a more general expression,

$$V = K_0' + K_1 g\cos\theta . \tag{3.7}$$

Using least-squares fitting, the best estimate of the scale factor K_1 and bias K_0 can be made and their accuracy can be also evaluated. If there is non-linearity existing in the output, second order coefficient will be introduced into the formula,

$$V = K_0' + K_1 g\cos\theta + K_2 (g\cos\theta)^2 . \tag{3.8}$$

For linear equation, the relation between the sensed analogue output V and its corresponding acceleration component $g\cos\theta$ can be expressed as

$$V_i = K_0' + K_1 g\cos\theta_i . \tag{3.9}$$

Let

$$x_i = g\cos\theta_i . \tag{3.10}$$

Here, x_i represents the acceleration at the i*th* telescope position.

The general expression of Eq. 3.9 and Eq. 3.10 can be rewritten as

$$\Delta V = AX - V . \tag{3.11}$$

Where

$$\Delta V = [\Delta V_1,\ \Delta V_2,\ \Delta V_3,\ ...,\ \Delta V_n]^T \tag{3.12}$$

$$A = \begin{bmatrix} 1 & 1 & 1 & ... & 1 \\ x_1 & x_2 & x_3 & ... & x_n \end{bmatrix}^T \tag{3.13}$$

$$X = \begin{bmatrix} K_0' \\ K_1 \end{bmatrix} \tag{3.14}$$

$$V = [V_1 \quad V_2 \quad V_3 \quad ... \quad V_n]^T . \tag{3.15}$$

According to least squares, the estimated parameters are

$$X = (A^T A)^{-1} A^T V \tag{3.16}$$

and the variance matrix of the estimated parameters is

$$Q_{XX} = (A^T A)^{-1} = \begin{bmatrix} Q_{K_0'K_0'} & Q_{K_0'K_1} \\ Q_{K_0'K_1} & Q_{K_1K_1} \end{bmatrix} . \tag{3.17}$$

The SD of unit weight of the measurements is

$$\sigma_0 = \sqrt{\frac{\Delta V^T \Delta V}{n-t}} . \tag{3.18}$$

The precision of each estimated parameter

$$m_{K_0'} = \sigma_0 \sqrt{Q_{K_0'K_0'}} \tag{3.19}$$

$$m_{K_1} = \sigma_0 \sqrt{Q_{K_1K_1}} . \tag{3.20}$$

To meet the accuracy requirement set for this research, some initial trials were conducted with a cheap triaxial accelerometer which was on loan from School of Electrical and Electronic Engineering (Meng 2000). The high instrument noise of this accelerometer made it not suitable for this application. Recommended by the colleagues from School of Civil Engineering, a Kistler single axis accelerometer on loan from Kistler Instrument Ltd, UK was tested in the platform trials using the configuration introduced in Section 5.2. Static trials were conducted to investigate instrument noise with this single axis accelerometer. The calculated results suggested its feasibility to be employed to detect deformation according to its measuring range (acceleration in *g*), sensitivity (V/*g*), and frequency range (Hz). In principle, a triaxial accelerometer consists of three single axis accelerometers in a common housing to allow simultaneous shock and vibration measurements in three mutually perpendicular axes. A Kistler K-BEAM triaxial accelerometer 8392A2 was then purchased. This type of accelerometer is designed for low frequency triaxial measurements. It is ideal for laboratory or field operations, modal analysis, robotics, and motion control. Table 3.2 lists some parameters of the main specifications of 8392A2 (Kistler 1999).

Specifications	Units	Values
Accelerations	*g*	±2
Sensitivity	MV/*g*	500
Resonant Frequency	KHz	1.6
Linearity	%FS	±1
Transverse Sensitivity (nom.)	%	1.5
Output at Zero g, ±10%	V	2.5
Phase Shift (10Hz, nom.)	Deg.	2
Resolution (0.5~100Hz)	m*g*/√ms	0.3
Operating Temperature	°C	-40~100
Power Supply	VDC/mA	9~20/30
Weight	g	40

Table 3.2. Specifications of a Kistler triaxial accelerometer, 8392A2

For collecting the analogue data from the accelerometer, a 16-bit resolution PCMCIA analogue to digital (A/D) converter was purchased and used for accelerometer data acquisitions in all the experiments. The heart of this type of board is an analogue to digital converter. Analogue signals are routed to the A/D via an 8:1 differential multiplexer controlled by a register on the board with maximum throughput of 100kHz. Specifications of the PCM-5516-D-16 are listed in Table 3.3. The advantage of the differential converter is that it provides unbiased output compared with single-ended converter (ADAC 1999a, b) and hence supplies more reliable analogue output.

Resolution	Channels	FIFO Buffer Size	Accuracy	Range	Conversion Time	Power Consumption
16 bit	8 Differential	512 Samples	±1.5LSB	±10V	10µS Max	+5V at 70mA, 100mA Max

Table 3.3. Specifications of PCM-5516-D-16 A/D converter

Fig. 3.67 shows the setup of an adapted theodolite and a Kistler triaxial accelerometer used for the zero bias and scale factor determinations of different IAs.

Fig. 3.67a. Calibrating the triaxial accelerometer

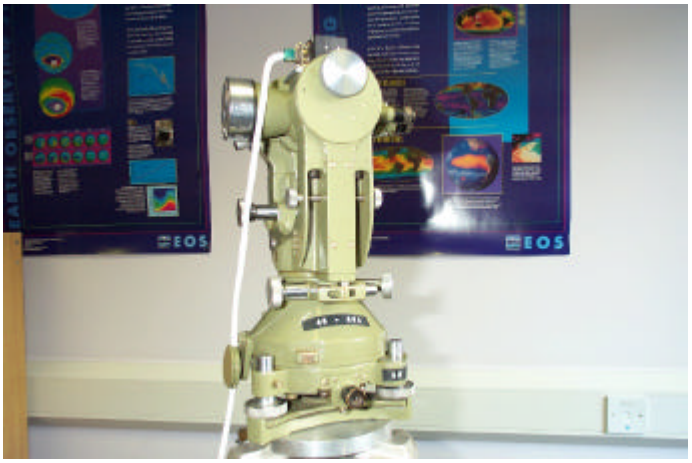

Fig. 3.67b. Calibrating the triaxial accelerometer

The tests have been conducted on a theodolite calibration tripod. This is a very heavy cast iron tripod. All these tests were conducted over weekends at the IESSG research room in order to reduce interference caused by other IESSG personnel. Precise levelling and theodolite calibration are vital for these tests. In each test, the telescope was been rotated in one direction out of three accelerometer axes and readings were

made at 5-degree intervals vertically. Each reading period was set to 1 minute with sampling rate of 200 Hz. At each position on the vertical circle of the theodolite, 12,000 samples were collected on the three input axes simultaneously. These samples are averaged to obtain one representative value for each telescope position (angle). Also the variances were calculated to evaluate the short-term stability of each axis. For each accelerometer configuration, readings on 61 telescope positions with 5° interval for maximum 300° telescope rotation angle have been made. In this case, 61 representative means and variances could be obtained. Through the change of accelerometer axis orientation on the telescope, different outputs are obtained. For instance, when X- and Z-axes coincide on the vertical plane, the axes that can sense acceleration changes are X- and Z-axes. It can be realised through mounting the accelerometer in position 1, which is shown in Fig. 3.67 with X axis of the accelerometer aligned in the same direction as sight axis of telescope. Also the reading on Y-axis can be made when Y and X or Z are in a vertical plane. Due to the misalignment between the mounting plate on the top of the theodolite telescope and telescope axes, the outputs sensed by the accelerometer are different when it is above and below the telescope. To find this misalignment angle, accelerometer readings with 10 minutes interval were further measured with specific angle. For instance with the telescope in the horizontal position, the Z-axis can sense 1 g gravity (maximum reading). When accelerometer axis is not parallel with telescope axis, the reading will not be the maximum value. When finely tuned, the maximum position can be found and the offset angles are then used to correct previous 61 angle values to get theoretical gravity values on each telescope position. When 1 g gravity is used, the sine and cosine values are the actual gravity components on the two axes in the vertical plane. A script with functions to calculate linear and nonlinear coefficients and evaluate the precision of each of the calculated parameters was developed to process the collected data.

Table 3.4 lists the parameters of linear models used for each axis. Listed in the final two columns are the parameters provided by the company (Kistler 2000). It is recommended that re-calibration of the triaxial accelerometer should be conducted every six months and the cost could be two to three hundred pounds. This is the main reason for carrying out these tests with a simple but still accurate device. In the

following tables, X(1) and X(2) stand for the outputs from the two accelerometer configurations, i.e. in XOZ and XOY planes, respectively .

IA	Calculated Parameters from Theodolite Tests				Company Supplied Parameters	
	Scale Factor (V/g)	Zero Bias (V)	m_{a1} (V/g)	m_{a0} (V)	Scale Factor (V/g)	Zero Bias (V)
X(1)	0.5089	2.5117	0.000107	0.000070	0.504	2.52
X(2)	0.5087	2.5116	0.000153	0.000099	0.504	2.52
Y	0.4876	2.5074	0.000260	0.000198	0.491	2.52
Z	0.4997	2.4996	0.000183	0.000139	0.500	2.51

Table 3.4. Linear models

Table 3.5 lists the calculated parameters using a quadratic model and Table 3.6 contains the parameters estimated by a cubic model. Comparing the SDs of scale factors and zero biases calculated by different models, the linear model and related parameters seems to be the best solution for the triaxial.

IA	Calculated Parameters from Theodolite Tests						Company Supplied Parameters	
	Quadratic Factor (V/g/g)	Scale Factor (V/g)	Zero Bias (V)	m_{a2} (V/g/g)	m_{a1} (V/g)	m_{a0} (V)	Scale Factor (V/g)	Zero Bias (V)
X(1)	-0.0008	0.5087	2.5120	0.000199	0.000104	0.000098	0.504	2.52
X(2)	-0.0011	0.5085	2.5120	0.000293	0.000153	0.000144	0.504	2.52
Y	0.0041	0.4876	2.5050	0.000282	0.000122	0.000187	0.491	2.52
Z	0.0029	0.4996	2.4979	0.000205	0.000088	0.000136	0.500	2.51

Table 3.5. Quadratic models

IA	Calculated Parameters from Theodolite Tests							
	Cubic Factor (V/g/g/g)	Quadratic Factor (V/g/g)	Scale Factor (V/g)	Zero Bias (V)	m_{a2} (V/g/g/g)	m_{a2} (V/g/g)	m_{a1} (V/g)	m_{a0} (V)
X(1)	0.0026	-0.0001	0.5072	2.5119	0.000258	0.000143	0.000167	0.000062
X(2)	0.0021	-0.0005	0.5072	2.5119	0.000561	0.000307	0.000363	0.000135
Y	0.0025	0.0041	0.4857	2.5050	0.000414	0.000224	0.000331	0.000148
Z	0.0018	0.0029	0.4983	2.4979	0.000299	0.000162	0.000239	0.000108

Table 3.6. Cubic models

The relationships between voltages and accelerations for each IA are illustrated by Fig. 3.68 to Fig. 3.71. The changes of SDs of the outputs in voltage over each telescope position are described by Fig. 3.72 and Fig. 3.73. With such a device, output precision better than 0.7mv can be achieved to determine the scale factors and zero biases.

The SDs of the calculated accelerometer parameters in Table 3.4, 3.5 and 3.6 can be used to identify calibration models and further employed in an integrated sensor system with GPS when filtering algorithm is applied.

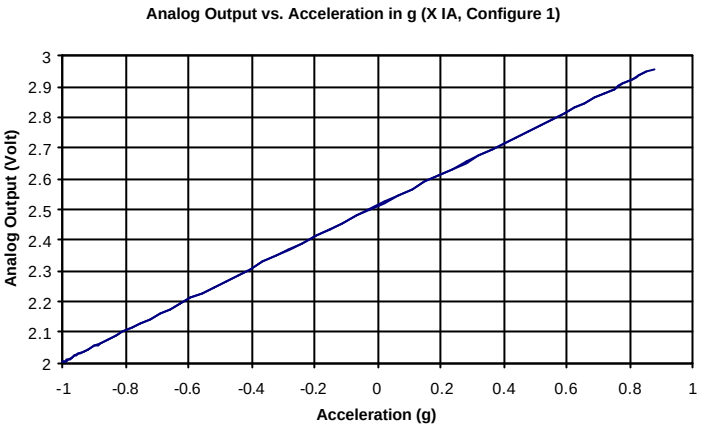

Fig. 3.68. Relation between voltage and acceleration (X1)

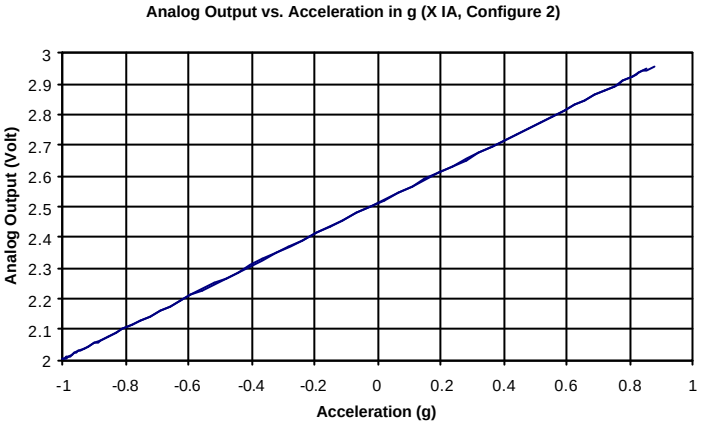

Fig. 3.69. Relation between voltage and acceleration (X2)

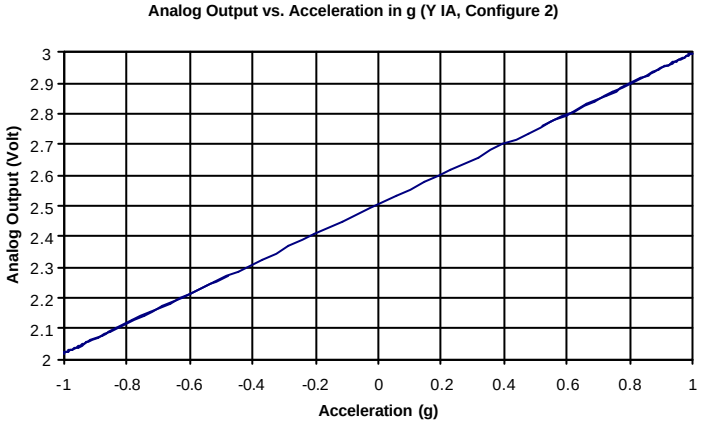

Fig. 3.70. Relation between voltage and acceleration (Y)

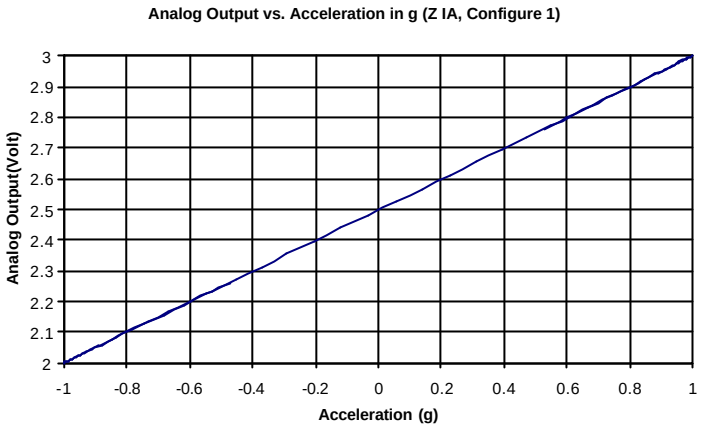

Fig. 3.71. Relation between voltage and acceleration (Z)

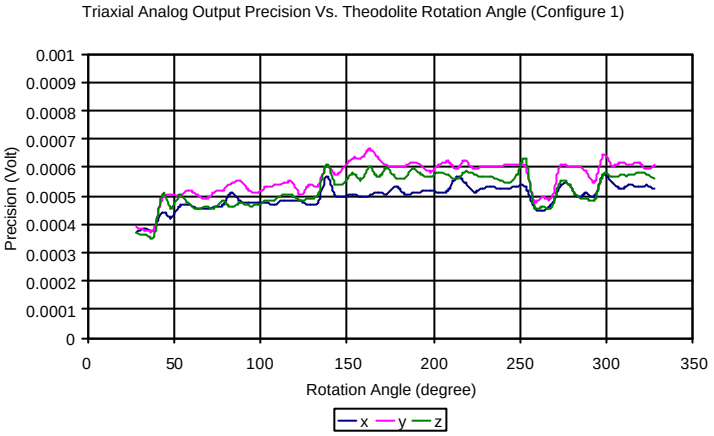

Fig. 3.72. Precision at each telescope position (1)

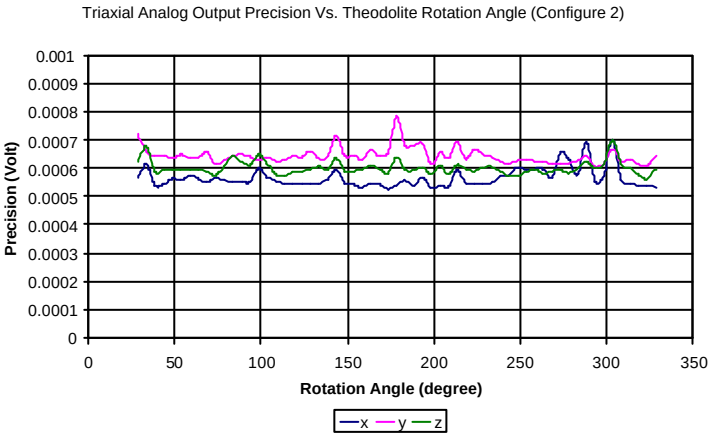

Fig. 3.73. Precision at each telescope position (2)

3.5 Summary

ZBL and SBL tests were conducted with three types of Leica GPS receivers and their associated antennas. The data were processed with Leica SKI-Pro and Ashtech AOSS software to obtain kinematic positioning solutions. Achievable internal accuracy of receivers themselves and multipath signatures at surveying environments were analysed. Statistic approach was employed to evaluate the positioning accuracy. The time lags of the positioning solutions were estimated by autocorrelation, which are important parameters in AF filter length design to mitigate multipath impact. An MA approach is used to filter the multipath signature from the SBL results of SR510 receiver. It demonstrated that with appropriate data processing, it is possible to achieve millimetric positioning accuracy even with single frequency receivers.

A simple but accurate approach using an adapted theodolite for calibrating a triaxial accelerometer was proposed. Models for calculating zero biases and scale factors were derived together with variance estimation of each estimated parameter. Through the comparison of parameter SD, the linear model was chosen as the best model for the estimation of zero biases and scale factors.

Chapter 4

Hybrid Sensor System for BDMS

4.1 Introduction

Local gravity is an important parameter in the determination of displacement from the measured accelerations. In Section 4.2, a simple formula using the latitude and orthometric height at an observation site to estimate local gravity is introduced. Coordinate transformations between WGS84, OSGB, BCS, and body frame of a triaxial accelerometer are discussed in Section 4.3. Approach and device for aligning accelerometer are proposed in this section as well. Instantaneous attitude estimates of the bridge beck movement are used to link the body frame to the geo-frame and they are the prerequisite for the data integration of a GPS receiver and a triaxial accelerometer. Formula derivations are conducted in Section 4.4. Synchronisation of the measurements from a GPS receiver and an accelerometer is important for further data integration. Cross-correlation approach for time synchronisation is illustrated and further improvement to synchronise the time series in a real-time mode is proposed in Section 4.5.

4.2 Determination of Local Gravity

As it is pointed out in Section 2.6, the positioning accuracies calculated from the accelerations depend on the accuracy of the determination of local gravity. A general formula for estimating acceleration a_i on axis i is expressed by Eq. 4.1

$$a_i = g(h) \cdot (\frac{V_i - Z_{i(0)}}{K_i} - C)\,(m/s^2). \qquad (4.1)$$

Where, $g(h)$ is the gravity at orthometric height h(m); V_i, $Z_{i(0)}$, K_i, and C are measured analogue voltage, zero bias, scale factor, and a constant along axis i, respectively.

Eq. 4.2 and 4.3 are the formulae for local gravity calculation using observation site latitude L and height h (m) above sea level (Titterton and Weston 1997).

$$g(0) = 9.780318(1 + 5.3024 \cdot 10^{-3} \sin^2 L - 5.9 \cdot 10^{-6} \sin^2 2L) \ (m/s^2) \quad (4.2)$$

$$g(h) = g(0)/(1 + h/R_0)^2 \ (m/s^2). \quad (4.3)$$

R_0 is the radius of the Earth assuming that the Earth is perfectly spherical in shape.

Using the above formulae the gravity at the IESSG and the London Millennium Bridge are as follows:

$$g(h)_{Nottm} = 9.813132551 \ m/s^2$$

$$g(h)_{London} = 9.812035245 \ m/s^2.$$

Because the resolution of a Kistler triaxial accelerometer is 0.3*mg*, three valid decimals are also chosen for local gravity (Kistler 1999). Together with the zero biases and scale factors listed in Table 3.4, these gravity parameters were used in the acceleration calculations at the Nottingham Wilford footbridge and the London Millennium Bridge.

4.3 Coordinate Systems and Sensor Alignment

The measurements from GPS receivers and triaxial accelerometers are referred to each specific coordinate frame. Data analysis is conducted in a engineering coordinate system. Coordinate transformation are required to convert the data collected by different sensors and related to different reference frames into a same reference frame for analysis and comparison to exploit the advantages of a hybrid system.

4.3.1 Earth-Centred-Earth-Fixed (ECEF) Frame-WGS84

An earth-fixed, terrestrial reference system (Conventional Terrestrial System, CTS) is required for the positions of the observation stations and for the description of results from satellite geodesy. The Z axis of ECEF is identical to the mean position of the earth's rotation axis as defined by the Conventional International Origin (CIO). The

X axis points in the direction of the mean Greenwich meridian. The Y axis completes a right-handed Cartesian coordinate system. Since 1987, GPS has used World Geodetic System (WGS84) as a reference. Associated with WGS84 is a geocentric equipotential ellipsoid of revolution which is defined by four parameters (Hofmann-Wellenhof et al. 1997). The coordinates related to WGS84 are also denoted as ECEF coordinates. A point in the system can be represented by Cartesian coordinates X, Y, and Z, as well as by ellipsoidal coordinates j, l, and h. Unless otherwise stated, WGS84 is used as the reference in the GPS data processing.

4.3.2 Local Geodetic Coordinate System (LGCS) – OSGB36 and National Grid (NG)

The local geodetic coordinate frame is the north, east, and up rectangular coordinate system, which is used by the surveyors in mapping and surveying. It is determined by the fitting of a tangent plane to the geodetic reference ellipse at the point of interest. This point is the origin of the local frame. The N (northings) axis points towards true north. The E (eastings) axis points towards east. The vertical axis H (height) completes the right-handed coordinate system of E, N and H.

The horizontal coordinates of all features shown on Ordnance Survey (OS) maps are determined with respect to OSGB36, which is a traditional geodetic coordinate system of the UK (OSGB 2001). Using seven parameters supplied by OS and applying similarity transformation, the coordinates in ECEF could be transformed into those in OSGB36. The coordinates could then be transformed from one type of coordinates to another type of coordinates for the same point in OSGB36. Map projection is applied to the two-dimensional ellipsoid surface coordinates j, l to obtain plane coordinates E (eastings), N (northings) in OSGB36 NG using a Transverse Mercator map projection. The ellipsoidal height in OSGB36 can be further transformed into the orthometric height if geoidal height is known. In this research, the ellipsoidal height is used to analyse bridge deflections directly. For conceptual consistence, the ellipsoidal height is also transformed together with horizontal coordinates. In this research, Coda 3, a coordinate transformation software package developed at the IESSG is used to transform the coordinates in WGS84 into those in OSGB36 and projected into

OSGB36 NG (IESSG 1997). The data transformations are conducted in a batch mode from a coordinate data file.

4.3.3 Bridge Coordinate System (BCS)

To facilitate the following data processing and interpretation, the origin of BCS used in this research is fixed at the origin of OSGB36 NG and the convention of two-letter code is adopted to reduce the number of the figures as does in OSGB36 NG. The y axis of BCS is parallel to the longitudinal direction of the bridge engineering coordinate system, which is used in the bridge design and construction. The h axis is in the vertical direction. The x axis completes a right-handed coordinate system.

According to Fig. 4.1, the coordinates in OSGB36 NG are transformed into those in BCS by 2D similarity transformation (Eq. 4.4). Eq. 4.5 is the formula for calculating the azimuth of the bridge main axis y, which is estimated by the mean values of plane coordinates of two bridge sites on the same side of a bridge deck determined by GPS receivers, and then fixed as the main axis of BCS for all surveying missions. Since the origin of two systems is the same, the translation parameters are zeros.

$$\begin{bmatrix} x \\ y \\ h \end{bmatrix} = \begin{bmatrix} \cos\alpha & \sin\alpha & 0 \\ -\sin\alpha & \cos\alpha & 0 \\ 0 & 0 & 1 \end{bmatrix} \begin{bmatrix} N \\ E \\ H \end{bmatrix} \tag{4.4}$$

$$\alpha = \arctan\frac{N_{mean2} - N_{mean1}}{E_{mean2} - E_{mean1}} \tag{4.5}$$

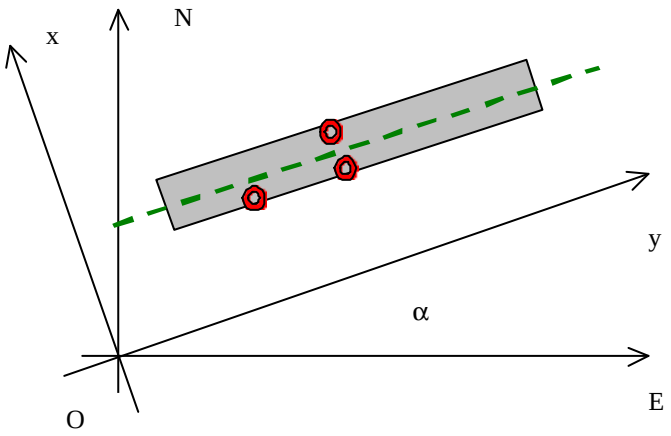

Fig. 4.1. Schematic of coordinate transformation between LGCS and BCS

4.3.4 Body/Accelerometer Frame

In positioning applications, the objective is to determine the movements of the monitored point based on the measurements from the accelerometer attached to a sensor platform on the bridge. The body frame is rigidly attached to the bridge site of interest. The y_{bd} axis of the body frame is aligned to the main axis of BCS. The z_{bd} axis points upward. The x_{bd} axis completes the right-handed coordinate system of the body frame. Unlike WGS84, OSGB36, and BCS, this coordinate system is not unique. It changes its axis directions over time with the movements of the bridge deck.

A triaxial accelerometer attached to the platform will resolve the measurements relative to inertial space along three IAs as mentioned in Section 3.4. These three orthogonal axes form an instrument frame, or accelerometer frame.

In order to avoid misalignment error between accelerometer frame and body frame as well as the representation error caused by the separation of GPS and accelerometer at difference sites, and reduce computation loads, the two kinds of sensors should be seamlessly fixed together to form a uniformed sensor system. At the same time one axis of the triaxial accelerometer frame should be aligned to the body frame, usually the bridge's main axis (longitudinal direction of a BCS). In this case, all the measurements from a GPS receiver and a triaxial accelerometer are collected from exactly the same bridge site.

To meet the above requirements, a specially designed cage is used to mount the GPS antenna and a triaxial accelerometer as well as to align the instrument frame with body frame, as it is illustrated in Fig. 4.2.

Fig. 4.3 and Fig. 4.4 are the plane and section drawings of this cage. It consists of two rotatable plates connected with three bolts. Bolt A in Fig. 4.3 is one of them. The GPS antenna is mounted on the upper plate, which can be orientated to north. The triaxial accelerometer is fixed on the second plate with four screws. Its physical centre B coincides with the plate centre and one axis is located on the straight line marked by A and C. The whole cage can be installed onto any standard tribrach. When the

tribrach is properly levelled, the centre of the GPS antenna, the physical centre of the accelerometer as well as the centre of the tribrach's base are situated in the same vertical axis. Through exact levelling and rotation when the bridge is static, the instrument frame of the triaxial accelerometer can be aligned with the BCS via body frame. No transformation is needed in this case. The displacements by acceleration double integral could be integrated with GPS fixes. The body frame is the second plate housing the accelerometer. When the bridge sways too much to level the tribrach due to the lateral wind or traffic loads, one axis of the accelerometer could still be aligned to the longitudinal direction of a BCS. The instantaneous accelerations sensed by the accelerometer could be transformed into the BCS through the algorithms proposed in Section 4.4 of this chapter. In practice, a G-shaped clamp with centring bolt on top is used to fix the cage onto the bridge's handrail (Fig. 5.14). Fig. 4.5 shows the accelerometer alignment procedure. A theodolite is placed at a side point upon the handrail of the bridge. The simple alignment procedure of body frame/accelerometer frame and bridge axis is realised through targeting the centre bolt of the middle span tribrach as illustrated by Fig. 4.5. The second plate of the cage is finely tuned until markers A and C in Fig. 4.3 are orientated along the bridge's axis.

In the above procedure, the instrument's IA is aligned with the platform axis rigidly by screws and then through alignment of the body frame and one bridge axis, the instrument frame is aligned. The complicated alignment process between platform body frame and accelerometer frame is totally avoided. Therefore, there is no need to apply a misalignment matrix in the accelerometer data processing. In this research there is no distinction made between the body frame and accelerometer frame.

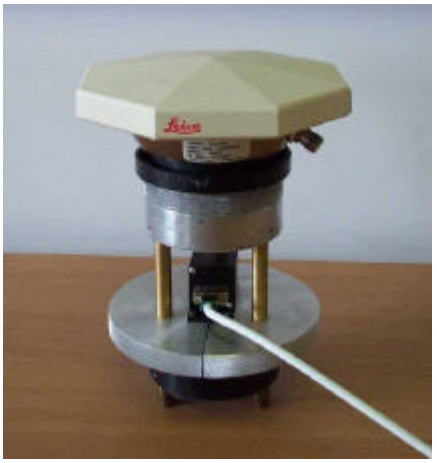

Fig. 4.2. A cage used to house a GPS antenna and a triaxial accelerometer

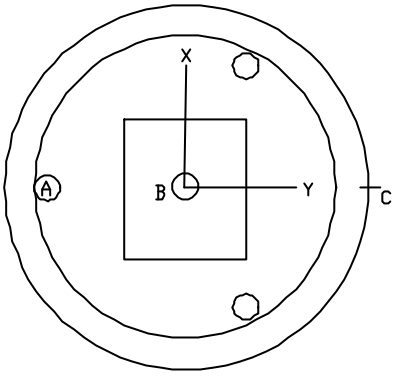

Fig. 4.3. Plan drawing of the cage

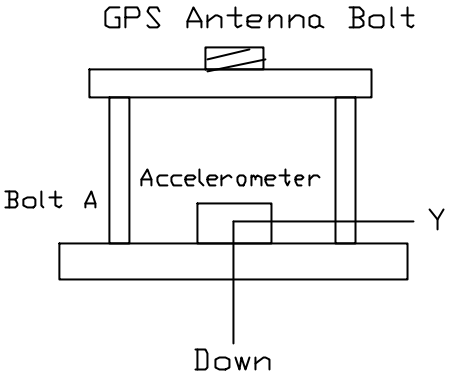

Fig. 4.4. Section drawing of the cage

Fig. 4.5. Theodolite for aligning a triaxial accelerometer (Courtesy of Mr Andrew Nesbitt)

4.4 Attitude Determination and Data Integration

The configuration of GPS receiver and triaxial accelerometer is a gyro-free INS aided GPS structural deflection monitoring system. It is important to obtain the attitude either determined by the measurements of the accelerometer or GPS. The instantaneous pitch, roll, and yaw of the body frame are used to convert the instantaneous 3D accelerations sensed in the body frame into those in three orthogonal directions of a BCS.

When the bridge is in the quasi-static mode (short span bridge with less traffic), yaw y can be set to zero, and pitch q and roll f are very small with even smaller changes over time. The modulus of the acceleration vector measured with the triaxial accelerometer equals $1g$. The coordinate transformation between instrument frame and a BCS can be realised using direct cosine matrixes (Eq. 4.6).

$$X_{bd} = R_{br2bd} X_{br} . \tag{4.6}$$

Where, X_{bd} is the force vector in body frame and X_{br} is the corresponding force vector in BCS. R_{br2bd} is the rotation matrix (direct cosine matrix) between body frame and BCS determined by the following expressions.

$$R_{bd2br} = \begin{bmatrix} a_{11} & a_{12} & a_{13} \\ a_{21} & a_{22} & a_{23} \\ a_{31} & a_{32} & a_{33} \end{bmatrix} \tag{4.7}$$

where the matrix elements can be calculated by the following expressions,

$$a_{11} = \cos(\psi)\cos(\theta)$$

$$a_{12} = \sin(\psi)\cos(\theta)$$

$$a_{13} = -\sin(\theta)$$

$$a_{21} = -\sin(\psi)\cos(\phi) + \cos(\psi)\sin(\theta)\sin(\phi)$$

$$a_{22} = \cos(\psi)\cos(\phi) + \sin(\psi)\sin(\theta)\sin(\phi)$$

$$a_{23} = \cos(\theta)\sin(\phi)$$

$$a_{31} = \sin(\psi)\sin(\phi) + \cos(\psi)\sin(\theta)\cos(\phi)$$

$$a_{32} = -\cos(\psi)\sin(\phi) + \sin(\psi)\sin(\theta)\cos(\phi)$$

$$a_{33} = \cos(\theta)\cos(\phi) .$$

To determine the estimates of pitch and roll, an accelerometer threshold is applied to identify quasi-static moments. The threshold can be estimated through lab tests before conducting real-life data acquisition. When the accelerometer measurements are larger than the threshold, it indicates that there are external accelerations acting on the accelerometer. When the accelerometer is in the quasi-static mode, the following formulae can be used to solve the initial pitch and roll unknowns with the sensed force vector $(\hat{f}_x, \hat{f}_y, \hat{f}_z)^T$ in Eq. 4.8 and Eq. 4.9 (Farrell and Barth 1999).

$$\begin{bmatrix} \hat{f}_x \\ \hat{f}_y \\ \hat{f}_z \end{bmatrix} = -R_{bd2br} \begin{bmatrix} 0 \\ 0 \\ g \end{bmatrix} = \begin{bmatrix} \sin(\theta) g \\ -\cos(\theta)\sin(\phi) g \\ -\cos(\theta)\cos(\phi) g \end{bmatrix} \tag{4.8}$$

$$\begin{bmatrix} \hat{q} \\ \hat{f} \end{bmatrix} = \begin{bmatrix} \arctan 2(-\hat{f}_y,\ \hat{f}_z) \\ \arctan 2(\hat{f}_x,\ \sqrt{\hat{f}_y^{\,2} + \hat{f}_z^{\,2}}) \end{bmatrix}. \tag{4.9}$$

where $\arctan 2(y,\ x)$ is a four quadrant inverse tangent function. $\hat{q}$ and $\hat{f}$ are the estimates of pitch and roll expressed in radian.

The solved pitch and roll estimates together with the measured yaw, which is zero in this application, can be used to relate acceleration vectors to geographical-frame gravity vectors and realise a coordinate transformation. After the determination of initial pitch and roll for a quasi-static moment, the attitude corrections could be estimated from the GPS fixes between two adjacent GPS sites on the bridge deck in a low dynamic mode.

When pitch and roll are very small, the direct cosine matrix could be further simplified by Eq. 4.10

$$R_{bd2br} = \begin{bmatrix} 1 & \psi & -\theta \\ -\psi & 1 & \phi \\ \theta & -\phi & 1 \end{bmatrix}^{-1}. \tag{4.10}$$

For larger bridge movements such as the deflections of long suspension bridges, the pitch, roll, and yaw could be determined by the instantaneous positioning measurements from three GPS sites on the same girder. The positioning accuracy to centimeter level (arc second) at a rate same as that of GPS sampling rate can be achieved. Between GPS sampling intervals, the pitch, roll, and yaw could be assumed to be constants. Or, interpolation could be employed to estimate the pitch, roll, and yaw at the same sampling rate of accelerometer. The transformed accelerations in a BCS are integrated twice and combined with GPS coordinates to output improved positioning solutions in WGS84. This highly accurate physical realization of sensor alignment with the designed cage could avoid the complicated initialization procedure, which requires a quasi-stationary status of the sensor system.

In practice, two adjacent GPS sites along the same bridge handrail, simultaneously gathering data, are used for calculating pitch and yaw (Eq. 4.11, 4.12) and two GPS sites on opposite sides of the bridge deck are used to calculate roll (Eq. 4.13).

$$pitch = \theta = \frac{\Delta H}{\Delta Y} = \frac{H_{site2} - H_{site1}}{Y_{site2} - Y_{site1}} \tag{4.11}$$

$$yaw = \psi = \frac{\Delta X}{\Delta Y} = \frac{X_{site2} - X_{site1}}{Y_{site2} - Y_{site1}} \tag{4.12}$$

$$roll = \phi = \frac{H_{site3} - H_{site1/2}}{\sqrt{(\Delta X^2)_{site1/2,3} + (\Delta Y^2)_{site1/2,3} + (\Delta H^2)_{site1/2,3}}} = \frac{\Delta H}{d}. \tag{4.13}$$

With above approaches, the data sets from three sites of the Wilford footbridge are taken as examples. The data were collected on 20 February 2001. The instrumentation is described in Section 5.3.4. The position solutions of a 200-second period of data from three bridge observation stations comprising two midspan sites and a quarter span site are processed and the results are shown in Fig. 4.6 to Fig. 4.9. Illustrated by Fig. 4.6 is the comparison of instantaneous changes of roll, pitch, and yaw in a decreasing order. Due to the wind load, the lateral movement is the biggest of the 3D deflections. The longitudinal movement is the smallest one because of the two anchorages. The three sites on the handrail are not in a horizontal plane due the design of the bridge and the differences in the tribrach setup heights, which cause mean offsets of –8.84, -47.43 and 5.97 minutes for roll, pitch and yaw, respectively. The instantaneous changes are used as actual roll, pitch and yaw values after subtracting the mean values in the calculation of the direct cosine matrix and acceleration transformation in a BCS.

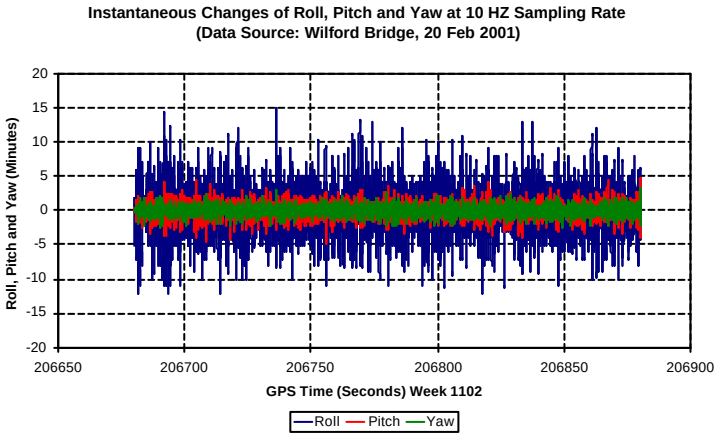

Fig. 4.6. Instantaneous changes of attitude

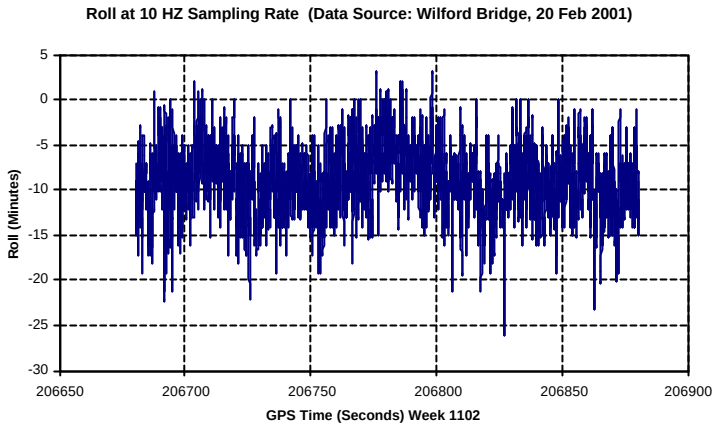

Fig. 4.7. Roll with mean offset of –8.84 minutes

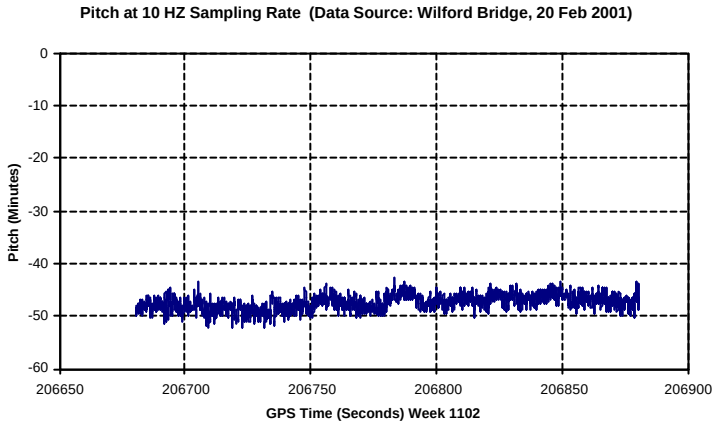

Fig. 4.8. Pitch with mean offset of –47.43 minutes

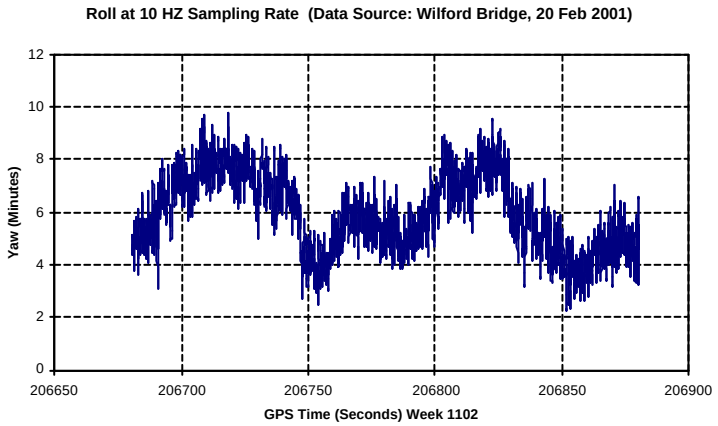

Fig. 4.9. Yaw with mean offset of 5.97 minutes

4.5 Synchronising Time Series from Different Sensors

Synchronisation is important for the data fusion of the time series from a GPS receiver and an accelerometer. In this prototype research, synchronisation between the GPS receiver and the accelerometer is achieved using a cross-correlation algorithm. An on-line synchronisation that uses the GPS time tag will be adopted in future monitoring systems. In fieldwork, the laptop was reset to the GPS time by simply reading the time from a switch-on receiver. The raw measurements were logged by the laptop from the accelerometer and the start and end time tags were recorded into a time file. This time tags was then used to roughly find the corresponding start time from the time series of GPS positioning solutions. Cross-correlation algorithm is applied to find the exact match point of the GPS receiver and the accelerometer data sets. For finding the match point quickly, GPS data with 20-second backward shift from the logged start time tag of accelerometer data can be used. For the data shown in Fig. 4.10, 18.83-second time shift has been noticed between the GPS and the accelerometer. This time shift is then counted in the following data integration. Obviously, this is a time consuming procedure. Some tests have been conducted to using GPS pulse per second (PPS) signal to trig data collection of accelerometer for the synchronisation purpose. Also tests have been made using the on-board counters to trig the kinematic data logging of a GPS receiver. Both approaches showed the possibility to accurately synchronise the two time series from GPS receiver and accelerometer. With this hardware synchronisation, it is also possible to realised on-line match between two kinds of time series.

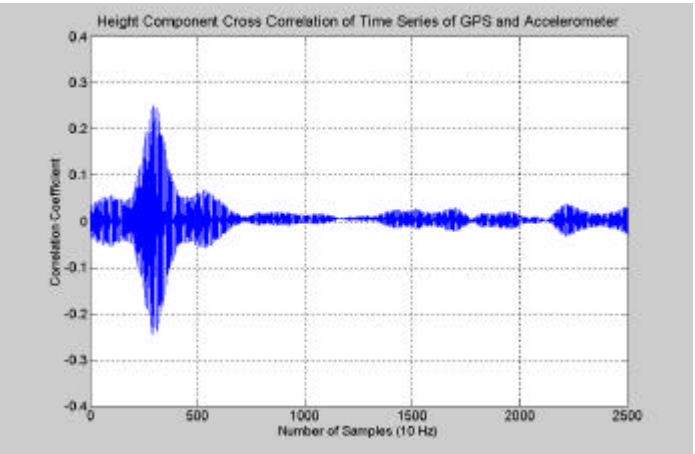

Fig. 4.10. Cross-correlation of GPS and accelerometer data

4.6 Summary

Issues of a hybrid BDMS consisting of a GPS receiver and a triaxial accelerometer are addressed in this chapter. Particularly, the determination of local gravity, definition and transformations of coordinate systems, algorithm and physical realisation of the integration of two sensor system, calculation of instantaneous direct cosine matrix, and synchronisation of different time series are introduced.

Chapter 5

Bridge Trials

5.1 Introduction

A platform was used to simulate realistic bridge dynamics, upon which were attached GPS antennas and a triaxial accelerometer. The configuration and data processing are introduced in Section 5.2. Following the controlled platform tests, the Wilford suspension footbridge over the River Trent in Nottingham was chosen as a test bed for the bridge deflection monitoring trials to investigate the proposed system configuration, implementation, and data processing algorithm due to its convenience. The details of four trials on this bridge are outlined by Section 5.3. Based on the trials on the Wilford suspension footbridge, a three-day trial was carried out on the London Millennium Bridge during the bridge's closure for retrofitting in the late November 2000. This was conducted to demonstrate the viability of state-of-the-art GPS technology for bridge monitoring. This trial is presented in Section 5.4.

5.2 Controlled Platform Tests on the University Campus

For studying the proposed system feasibility and testing algorithm and software, a platform was fabricated at the IESSG before real life bridge trials were conducted. Fig. 5.1 illustrates the platform and the fundamental configuration of the proposed GPS/accelerometer deflection monitoring system. The system consists of one reference station and a platform hung by bungee cords on wooden beams supported by two tripods. The reference station running a Leica 10Hz CRS1000 dual frequency GPS receiver was connected to a Leica AT504 chokering antenna situated on a roof point upon the IESSG Building with known coordinates. Two other AT504 chokering antennas and one Sharpe lightweight antenna were mounted on the platform. A Kistler triaxial accelerometer was installed in the middle of the platform with one axis parallel with one edge of the frame. Three PCs and a dedicated laptop were used to

log the GPS and accelerometer raw data. Of the three receivers, a Leica CRS1000 and a CRS1500 receivers and a Sharpe 10 Hz single frequency code/carrier phase receiver were employed. In the tests, the platform was activated manually in the vertical direction with limited pitch and roll angles to simulate the true structural deflections. A compass was used at beginning to align the accelerometer to the north direction. Multiple section data were collected with PCs/laptop that were driven by the GPS and accelerometer raw data acquisition software.

Fig. 5.1. The setup of a controlled platform test

Two days' data were collected on 16 and 17 August 2000 with the designed platform. The raw data were decoded with the commercial software package supplied by Leica and Kistler after the tests. The RINEX data files were processed with Leica SKI-Pro V1.1 (Leica 1999a) and AOSS (Ashtech 1998). Based on these tests, the initial specifications and the instrumental configuration for the real bridge trials were devised. Power supply to both accelerometer and laptop for longer period data recording were proposed. Algorithms for coordinate transformation and data fusion were developed based on the controlled platform tests.

5.3 Series Trials on the Nottingham Wilford Suspension Footbridge

Four trials have been conducted on the Nottingham Wilford suspension footbridge. In the following sections, the detailed instrumentation, receiver site setup, and the raw data collection and processing will be introduced with visual aids.

5.3.1 The First Bridge Trial

The Wilford suspension footbridge over the River Trent is a 65m long and 3.5m wide wooden deck footbridge (Fig. 5.2). This bridge is also used to conduct drinking water from the Severn Trent Water to the nearby residential area through the pipes built under the bridge deck. It situates about 3.6km away from the main campus of the University of Nottingham. The IESSG received permission to access the bridge from the owner, the Severn Trent Water. Due to its very convenient location and structural type, the Wilford suspension footbridge provides an ideal test bed for the research.

Fig. 5.2. The Wilford suspension footbridge over the River Trent, Nottingham

In the afternoon of 17 October 2000, the first GPS/accelerometer based Wilford suspension footbridge trial was conducted with four Leica SR530 and three CRS1000 dual frequency receivers. A Kistler triaxial accelerometer was employed to record the accelerations together with GPS raw measurements. The trial on the bridge lasted for about two hours and was divided into two sessions with each session period lasting for about one hour.

The aims of the first trial were meant to test the feasibility of Leica CRS1000 dual frequency receivers and triaxial accelerometer for monitoring bridge deflection with a reasonable high data rate. The newly purchased SR530 dual frequency receivers gathered raw data together with CRS1000 receivers for the purpose of general GPS performance evaluation. Fig. 5.3 illustrates the layout of the GPS antennas. CK in the graph refers to Leica AT504 chokering antennas and LW to Leica AT302 lightweight antenna. One CRS1000 receiver was setup as the reference station near the bridge at a

point on the embankment pavement, station Riverside. To obtain the coordinates of the riverside reference station, another chokering antenna connected to a CRS1000 receiver was mounted on a known point at the IESSG Building to log static data simultaneously with the data collection upon the bridge. There were a total of four observation sites on the bridge deck. Two of them located at the two midspan sites, Mid1 running with a CRS1500 receiver and Mid2 with a SR530 receiver located at the opposite side of the bridge width. In the first session, a chokering antenna was installed at Mid1 and a lightweight antenna, Leica AT302, at Mid2. The two antennas were then swapped in the second session. Two chokering antennas connected to two SR530 receivers were situated on two side span sites, Site1 and Site2, on the same side as Mid1. In this trial, a Kistler triaxial accelerometer was stuck with the special glue provided by the manufacturer onto a tribrach, which is located about 0.33m away from Mid1. The accelerometer was then levelled and aligned to the bridge main axis with a theodolite. Two thirty-minute sessions of accelerometer data were recorded simultaneously with GPS data collection using a dedicated laptop running the data logging software. Specially designed G-shaped clamps with bolt on top to hold GPS antennas were attached to the bridge handrails to avoid extra vibration induced by wind loadings.

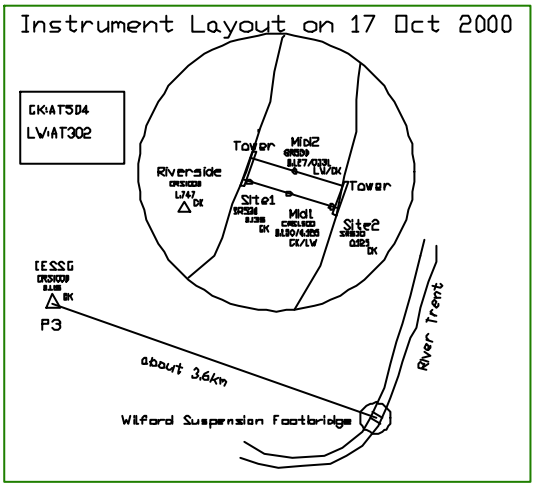

Fig. 5.3. Layout of antennas on the bridge trial, 17 Oct. 2000

The sampling rate of GPS receivers was 10 Hz and 200 Hz for the accelerometer. The data format from Leica CRS1000 GPS receivers is Leica binary 2 (lb2) and uncompressed raw measurements from SR530 receivers. The accelerometer data is stored in a compressed binary data format to save the hard disk space. While the raw

data of SR530 can be directly entered into Leica post processing software, SKI-Pro, the data files in lb2 format needed to be decoded with a firmware l2r2 to obtain RINEX data files. Two-hour data collected at the two reference stations were processed in a static mode in order to obtain the coordinates of the Riverside reference station. Table 5.1 lists the coordinates of the Riverside reference station. Because only the relative movements of the bridge deformations are of interest in this research, WGS84 coordinates at the known point on the IESSG Building were used as initial known parameters to calculate reference station coordinates on the bridge riverside. The calculated coordinates of Riverside are therefore referred to WGS84 as well. The data collected at the observation sites were then processed by SKI-Pro in an OTF mode to get each epoch data referred to either reference stations. The difference in using different reference station for data processing will be discussed in the following chapter.

Ref. name	X (m)	Y (m)	Z (m)
P3 (IESSG)	3851173.924	-80153.645	5066647.323
Riverside	3851909.520	-76664.580	5066111.340

Table 5.1. Coordinates of reference stations, WGS84

Due to the bugs existing in the CRS1000 firmware (Leica, 1999b) at the time the trial was conducted negative observation numbers were created in the header sections of the RINEX data files during decoding 10 Hz raw data, which caused the difficulties in the positioning solutions. The same firmware could work properly when the data were decoded with data rate lower than 5 Hz. The observation numbers on the each satellite in view from the header sections of the decoded 5 Hz RINEX data files had been multiplied by two to get correct the header sections for the 10 Hz RINEX data files. The observation numbers made on each satellite then were manually input into the header sections of the decoded 10 Hz data files.

Missing data was another problem encountered when Leica CRS1000 dual frequency receivers were used for the first bridge trial with 10 Hz data rate. Presented in Fig. 5.4 is the accumulated number of missed data points within 7.5 minutes. There were 30 missed measurements counted during this period of time through comparing the actual time tags from a positioning file with the created correct time tags. The reason

for this is not clear. There were no problems encountered in decoding the collected accelerometer data.

It was recognised that the data collected from GPS and accelerometer on the separate locations could not be generalised to represent the deformation at either location and also the separation could cause problem in aligning the accelerometer. Further improvements both in the software and hardware realisations were needed.

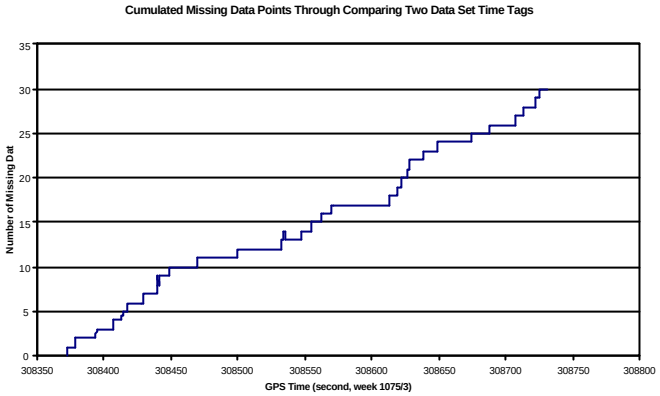

Fig. 5.4. Missing data in a 7.5-minute data set (CRS1000)

5.3.2 The Second Bridge Trial

The second Wilford suspension footbridge trial was conducted in the afternoon of 27 October 2000 with a newly designed cage to house both a GPS antenna and accelerometer together, refer to Section 4.3 for the detailed dimensions of the cage. Three CRS1000 dual frequency receivers were still used as the main instruments and four SR530 dual frequency receivers were employed for the whole monitoring system evaluation. The receiver configuration, satellite elevation cutoff angle and data rate were the same as those applied in the first trial. The whole GPS data collection was lasting for about two hours, which was divided into two sessions. Two data sets of thirty minutes were recorded by the accelerometer at Mid1 with a sampling rate of 200 Hz. Fig. 5.5 is the instrument layout of this trial. The antennas at two midspan sites were swapped between the two sessions while chokering antennas were mounted on the other sites during the whole sessions.

The collected GPS data were further processed with Leica SKI-Pro software and compared with the positioning solutions from AOSS using the decoded RINEX data files in OTF mode. The results revealed noticeable differences between the positioning solutions when different reference stations were employed, with both software packages. Observation site related multipath and relative tropospheric delay were recognised as the main reasons for these. With such uncertainties, a further trial was arranged to study the nature of multipath and relative tropospheric delay at different locations.

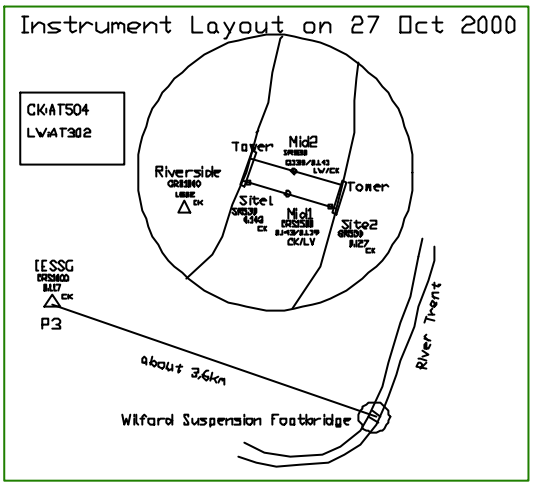

Fig. 5.5. Layout of antennas on the bridge trial, 27 Oct. 2000

5.3.3 The Third Bridge Trial

During two afternoons on 14 and 15 November 2000, the third trial was carried out with four SR530 and three CRS1000 dual frequency receivers. In order to reduce the impacts of multipath and tropospheric delay and investigating the missing data problem in CRS1000 receivers, a dual riverside reference station approach was employed, with one receiver located on the Riverside point established in the previous trial and renamed as Base1. Base2 was setup as a new reference station on the North side of the bridge (Fig. 5.6).

To evaluate the performance of each receiver type and overcome the difficulties encountered in obtaining 10 Hz kinematic positioning solutions from mixed receiver types, a CRS1000 and a SR530 receivers were setup on two known points on the IESSG Building. Table 5.2 lists the coordinates of the reference stations used for this

trial. The coordinates of Base2 were resolved by fixing the IESSG Building site as a reference station and letting Base2 be rover station in a static mode.

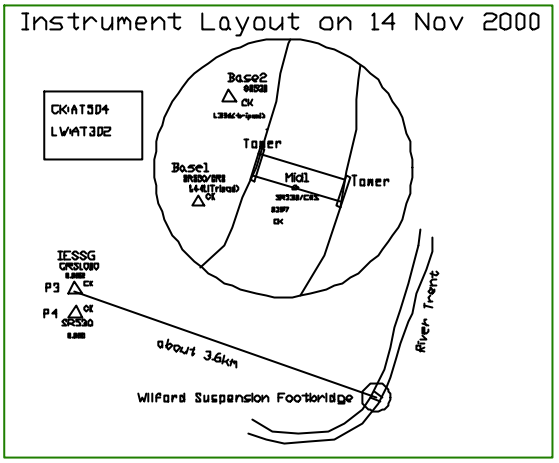

Fig. 5.6. Layout of antennas on the bridge trial, 14 Nov. 2000

Ref. name	X (m)	Y (m)	Z (m)
P3 (IESSG)	3851173.924	-80153.645	5066647.323
P4 (IESSG)	3851173.098	-80153.713	5066647.939
Base1/Riverside	3851909.520	-76664.580	5066111.340
Base2 (North)	3851778.804	-76598.734	5066211.011

Table 5.2. Coordinates of reference stations, WGS84

The data logging was subdivided into two sessions with each lasting for about one hour on 14 November 2000. A SR530 receiver occupied Base2 during the two sessions and another SR530 was installed at Base1 in the first session and then a CRS1000 in the second session. A SR530 receiver was operated at Mid1 in the first session and then replaced by a CRS1000 receiver. The accelerometer was aligned by the theodolite on the side rail of the bridge at the beginning of the trial. Five chokering antennas were connected to the relevant receivers during the two sessions. Four twenty-minute sessions of acceleration data sets were taken from the accelerometer. To ease the data synchronisation, the laptop was set roughly to the GPS time at the beginning of the trial.

A similar instrumentation configuration was employed on 15 November 2000 except for a lightweight antenna was replaced by a chokering antenna as indicated in Fig. 5.7 and an extra receiver was setup at Site1. At Base1, a SR530 receiver was used in the first session and then replaced by a CRS1000 receiver. A CRS1000 receiver was first

mounted at Site1 and then swapped with a SR530 receiver at Base1 in the second session. On the contrary to Site1, a SR530 receiver was first used at Mid1 and then swapped with a CRS1000 receiver in the second session. Again, four twenty-minute sessions of acceleration data were collected from the Kistler triaxial accelerometer. The meteorological data (temperature, air pressure and humidity) were measured together with GPS and accelerometer raw measurements.

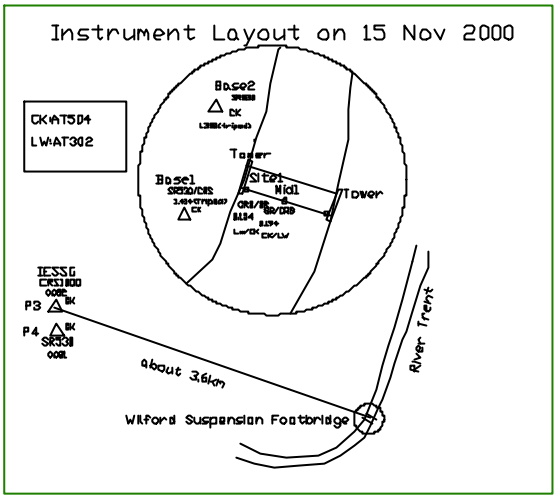

Fig. 5.7. Layout of antennas on the bridge trial, 15 Nov. 2000

The collected data were then processed with SKI-Pro software. The tropospheric delay features caused by the differences in height and climate parameters were further investigated. High multipath signature still existed in the positioning solutions. Special algorithms and receiver layout to cope with high multipath signatures both at the reference stations and observation sites were needed. A Matlab simulator was further developed to examine the effective approach of mitigating multipath using adaptive FIR filtering approach. According to this simulator, the layout of the reference stations was then proposed and applied on the following bridge trial. Due to the failures in the raw data decoding from CRS1000 receivers, especially when data were collected for several hours at 10 Hz, an attempt to use the available CRS1000 receivers to collect bridge deflection monitoring data for reasonable observation periods at 10 Hz rate eventually was given up. SR530 receivers were chosen as the basic instruments in the bridge deflection monitoring system due to their reliability and productivity.

5.3.4 The Fourth Bridge Trial

Three consecutive days' data were collected on 20, 21, and 22 February 2001 from the Wilford suspension footbridge. The main instruments used for this trial consisted of six Leica SR530 dual frequency receivers and one Kistler triaxial accelerometer. One T1 Wild theodolite was used to align the accelerometer to a BCS. Four Leica chokering antennas, one Leica AT 502 antenna and one third-party patch antenna (www.sensorantennas.com) were connected to the GPS receivers. The climate parameters were collected from one barometer, one set of thermometer and hygrometer. Specially designed G-shaped clamps were used to attach four GPS antennas onto the bridge's handrail.

The data rates for each kind of sensors were set to 10Hz and 200Hz respectively. In total six Leica SR530 dual frequency GPS receivers were employed on the first two days' trials and four receivers were used on the final day after returning two receivers on loan to Leica.

A combination of dual riverside reference stations and one on the university campus (IESSG on the first day, Tower Building on the second day) were setup as the reference group for this trial. During this trial the two riverside reference stations were setup on the south side of the bridge. Base1 was located at the same site as the previous trial and Base2 was a new reference station, which is about 6.3m away from Base1 with similar open view (Fig. 5.8). The purpose of this receiver antenna separation is to mitigate multipath at the reference stations according AF algorithm. The height difference between the GPS stations on the Tower Building and the IESSG Building is about 36 metres. The height difference between the stations on the IESSG building and those at riverside is 27 metres. The data sets from both stations were analysed in order to investigate the tropospheric effect due to the height difference and the difference in the local microclimate.

In addition, a permanent station located on the IESSG used for UK tidal gauge monitoring was included into the reference group. There are twofold purposes for this configuration. The first one was to increase the overall stability and productivity of the proposed monitoring system through exploiting the potential usage of the GPS

permanent stations in the close vicinity of the monitored bridge. The second attempt was to investigate the influence of the local microclimate on the positioning precision, such as relative tropospheric delay effect, which can exhibit significant influence on the positioning precision. The tropospheric influence and its mitigation technique will be discussed in the following chapters. Table 5.3 lists the coordinates of reference stations used for this trial.

Fig. 5.8. Reference station setup on the bridge trial, 20, 21 and 22 Feb 2001

Ref. name	X (m)	Y (m)	Z (m)
P1 (IESSG)	3851174.491	-80151.844	5066647.048
P4 (IESSG)	3851173.098	-80153.713	5066647.939
TB (Tower)	3851064.655	-79902.425	5066778.073
Base1/Riverside	3851909.520	-76664.580	5066111.340
Base2 (South)	3851913.157	-76668.829	5066108.525

Table 5.3. Coordinates of reference stations, WGS84

Assuming the multipath effects from the ambient environment were the same in this case, this reference layout could be expected to reduce multipath impact through a properly devised algorithm.

The observation sites on the bridge deck comprised of three GPS receivers for all three days' data collection. Two antennas were mounted on two opposite sites at the midspan and another antenna on the quarter span. The specially fabricated cage (Fig. 4.2) was attached to the same site at the midspan of the bridge during all the trials with a G-shaped clamp. Fig. 5.9 illustrates the instrument deployment.

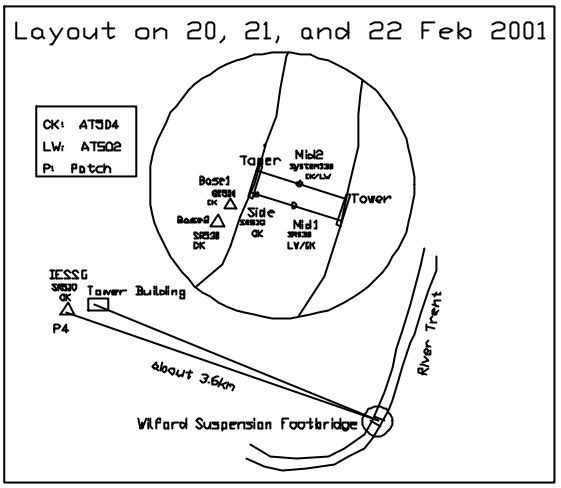

Fig. 5.9. Layout of antennas on the bridge trial, 20, 21 and 22 Feb 2001

The initial alignment procedure was applied using a T1 theodolite. For investigating the multipath rejection effects of different antennas, a special antenna arrangement was adopted in the test (Fig. 5.10). In this figure, capital letters C, L and P refer to Leica AT504 chokering antenna, AT302 lightweight antennas and aforementioned patch antenna. Each was employed on one of the three bridge sites, respectively.

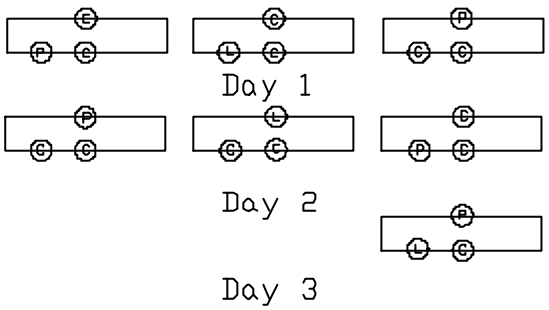

Fig. 5.10. Schematic of the antenna arrangements during three days' bridge trials

In order to establish the relationship between the external loading and response, a organised group of eight pedestrians walked across the bridge during the data collection on the first two days for about half-hour periods on each day (Fig. 5.11).

The data collection was conducted over seven sessions during the three-day trial, with three sessions on the first two days and only one session on the final day. Each session lasted roughly 2 hours. Due to the relative high data rate of the accelerometer,

a 10-minute period was employed. The computer time was reset according to GPS time before the fieldwork for the purpose of data synchronisation.

The physical integration of GPS and accelerometer, time series synchronisation and data fusion, detailed datum transforms between WGS84, OSGB, accelerometer body frame, definition of BCS, data processing algorithms and further analysis of the result for studying relative tropospheric delay and multipath are illustrated in Chapter 4 and the following chapters.

Fig. 5.11. Loading and response test

5. 4 London Millennium Bridge Trial

The London Millennium Bridge is a pedestrian bridge linking the City of London at the St Paul's Cathedral with the new Tate Gallery at Bankside. The bridge's structural diagram is that of a shallow suspension bridge, where the cables are as much as possible below the bridge deck to free the views from the deck. Two groups of four 120mm diameter locked coil cables span from bank to bank over two river piers. The lengths for the three spans are 81m for the north span, 144m for the main span between the piers and 108m for the south span with 4m wide bridge deck. The sag of the cable profile is 2.3m in the midspan, around 6 times shallower than a more conventional suspension bridge structure (Dallard et al. 2001).

It was estimated that between 80,000 and 100,000 people crossed the bridge during its opening day on 10 June 2000. Analysis of the video footage showed a maximum of 2,000 people on the deck at any time, resulting in a maximum density of between 1.3~1.5 people per square meter. When large groups of people were crossing the bridge, greater than expected movement was experienced, mainly excessive lateral vibration. There was amplitude of 50mm movement with a vibration frequency of about 0.77 Hz on the south span (the first south lateral mode), between Bankside and the first river pier. Up to 70mm movements at frequencies of 0.5 Hz and 0.95 Hz (the first and second lateral modes respectively) were experienced on the center span. More rarely, movement occurred on the north span at a vibration frequency of just over 1.0 Hz. From the amplitude of movements on the south and central spans, the maximum lateral acceleration was between 200 and 250 mg. At this level of vibration acceleration, a significant number of pedestrians began to have difficulty in walking and help onto the balustrades for support. No excessive vertical vibration was observed.

The bridge was closed on 12 June 2000 for fully investigating the cause of the movements. The extra £5M was expected to fit anti-wobble dampers and bracing into London's £18M Millennium Bridge (http://www.nceplus.co.uk, New Civil Engineer Plus, 23/11/2000).

From 22 to 24 November 2000, a three-day viability study was carried out on the London Millennium Bridge with the permission of Arup, the engineers of the London Millennium Bridge. Leica dual frequency GPS receivers were evaluated upon the bridge during the bridge's closure for retrofitting. The objective was to validate the use of GPS to measure the deformation and vibration of the structure. This was a viability study, in that the limitations of a proven technique have not been fully investigated.

The other objectives of this trial were to collect data from a new type of suspension bridge with the integrated GPS/accelerometer bridge monitoring system for the preparation of this PhD thesis and to test the system configuration and data logging software package. Further involvement in the bridge deflection and safety monitoring of this notorious suspension bridge was of great research interests at the IESSG. GPS

and accelerometer solutions could supply an alternative approach for understanding the nature of the bridge vibration and deformation with the hope of convincing the structural engineering community that GPS is a feasible and reliable tool for structural deflection monitoring compared with other systems.

Four sets of Leica SR530 dual frequency GPS receiver and associated chokering antennas were used for the trial. This configuration pushed the capabilities of GPS to the forefront of current technology. One Kistler triaxial accelerometer with dedicated laptop for data logging was employed. Meteorological meters, such as thermometer, barometer and hygrometer were used to record climate parameters when the tests were under way.

A total of about 11 hours GPS measurements were taken at a sample rate of 10 Hz and 4 hours raw acceleration data at 200 Hz, giving approximately 1.98 million 3D GPS points and 2.88 million 3D acceleration points.

The data gathering trials were conducted over five sessions during the three days. Each session had the GPS antennas located at three of the 5 observation sites on the bridge deck. The reason to sub-divide whole day's measurement into sessions is due to the capacity limitation of the receiver cards. At the time of the trial conducted, 8Mb cards were used to log the raw data, which can store about 3 hrs 10 Hz data. Fig. 5.12 illustrates the locations of the GPS antennas for the various sessions. Table 5.4 lists the time for the each occupied observation site during each mission. One reference GPS receiver was situated upon a survey point on top of an adjacent building (Fig. 5.13). The survey points upon the bridge were carefully located upon the bridge's handrail using clamps that were especially fabricated for this trial to fit for the ellipse shape of bridge handrail (Fig. 5.14). The various sessions saw the antennas located at 3 of the 5 survey points per session. Point B, however, was occupied during all the sessions. In addition, a Kistler triaxial accelerometer was housed underneath the GPS antenna on point B.

Once gathered, the GPS data were then processed using software packages including Leica SKI-Pro (Leica 2001), IESSG's GAS/KINPOS and self-developed data fusion software. The coordinates of the reference station were resolved used the raw

measurements from a UK tidal gauge station in Sunbury for about 25 km away from bridge site using IESSG's GAS/NOTF (IESSG 1995, 1998). The cycle slips that occurred during the surveying period have been fixed and repaired. Due to the large volume of data files in each three-hour session, the sessions were split into 5 or 6 sub-sessions for processing purposes using Leica SKI-Pro. Subsequently the coordinates in WGS84 were transformed and projected into OSGB coordinate system using the IESSG CODA 3 software (IESSG 1997). The resulting local coordinates were further converted into the bridge coordinate system with the main orientation axis offset 0.58 degrees from the north.

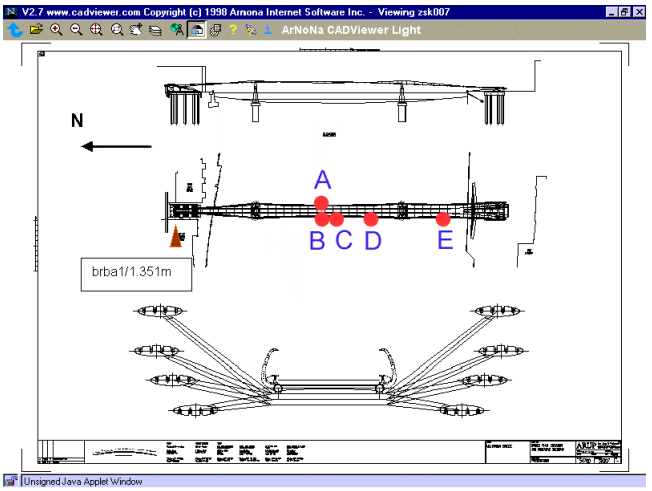

Fig. 5.12. Layout of the observation sites on the London Millennium Bridge

Date	Session No	Start Time	End Time	Antenna Location
22/11/00	1	14.35.42	16.25.52	A
	1	14.36.03	16.24.58	B
	1	14.35.52	16.25.26	C
	1	15.08.12	16.08.14	B (accelerometer)
23/11/00	2	09.51.23	12.13.26	B
	2	09.38.25	12.13.37	C
	2	09.38.58	12.13.22	D
	3	12.37.24	14.50.04	B
	3	12.39.24	14.50.21	C
	3	12.37.57	14.50.13	A
	3	12.42.08	13.42.10	B (accelerometer)
	3	13.46.26	14.46.28	B (accelerometer)
	4	15.14.24	16.47.12	B
	4	15.16.23	16.47.17	C
	4	15.15.24	16.47.28	A
24/11/00	5	08.56.09	12.06.13	B
	5	09.05.15	12.06.36	D
	5	09.15.28	12.07.20	E
	5	09.04.35	10.04.38	B (accelerometer)

Table 5.4. Session times, locations and dates

Fig. 5.13. Reference station setup on the nearby building

Fig. 5.14. One observation site on the bridge

Further data analysis and filtering were conducted using a GPS/accelerometer integration package developed with Visual C++ and a Matlab AF script.

Preliminary results from a selection of measured data were presented in a report to Arup titled “Millennium Bridge Viability Trial” co-authored with Brunel University (Roberts et al. 2000b). The whole raw measurements were processed and analyzed with the procedure proposed by this thesis, but the results are still not available for the public.

During the trial, only sporadic passengers such as researchers from the IESSG and construction workers from Arup crossed the bridge and caused small bridge vibrations. It was very hard to conduct loading and response analysis to identify the

frequency signatures of the bridge vibration from GPS data only because small true 3D movements were buried by various GPS noises.

5.5 Summary

Controlled platform tests were conducted to verify system configuration, practical implementation, associated algorithm and software of a proposed GPS/triaxial accelerometer BDMS initially on the university campus. The system was then employed in the Nottingham Wilford suspension footbridge trials. The details were introduced in this chapter. Through the actual bridge deflection monitoring and data processing, the defects of the proposed system was investigated and an improved system was used to cope with multipath and various other error sources. The issues identified in the actual bridge trials, data processing and deflection analysis form the research objectives of this thesis. In the following chapters, satellite sky distribution, system integration of a GPS receiver and a triaxial accelerometer, multipath mitigation techniques, deflection analysis, and relative tropospheric delay will be further studied.

Chapter 6

GPS Satellite Sky Distribution and Its Impact on Positioning Accuracy for Bridge Monitoring

6.1 Introduction

The current GPS constellation consists of 28 Block II/IIA/IIR satellites deployed in six orbital planes with an inclination of 55° (http://tycho.usno.navy.mil). Of the 28 GPS operational satellites, 4 satellites are Block II type; 18 are Block IIA and 6 are Block IIR satellites. There are 4 satellites in each orbital plane A and C, 5 in each orbital plane B, D, E and F. With such a satellite constellation it is assumed the possibility of twenty four hours, all whether global coverage positioning. However it is not always the case depending on the applications.

For bridge deflection monitoring, uniform accuracy of the raw measurements in each of three directions in a BCS is required for the correct interpretation of the bridge deflection characteristics. To evaluate the accuracy, the propagation of ranging errors under the current GPS sky distribution is analysed in the Section 6.2, through the calculation of various values of DOP. The formulae for calculating DOP values in a BCS are derived based on the DOP calculated in WGS84. The deficiencies of the current sky distribution of GPS satellites for the bridge deflection monitoring applications in the high latitude areas as in the UK are demonstrated through three real bridge monitoring examples in the Section 6.3. The Section 6.4 examines the hybrid positioning solutions for the improvement of positioning accuracy. GLONASS augments GPS by providing more robust observations and an enhanced satellite sky distribution, thereby improving overall performance of satellite based BDMS. This is proved by the positioning solutions from the data processing of the Humber Bridge trial. In this section, the best and worst GPS satellite sky distributions augmented with pseudolites have been simulated by a Matlab simulator. Furthermore, a modified GPS precise ephemeris with different pseudolite locations is employed to simulate the

obtainable accuracy in each of the three axes of a BCS, with an attempt to answer how the pseudolite can improve positioning accuracy through the improvement of DOP values.

6.2 GPS Ranging Error Propagation in a BCS

The one-way GPS measurement equation can be expressed in WGS84 coordinate system as the pseudorange $\boldsymbol{r}_i^j$ between receiver site i and satellite j

$$\boldsymbol{r}_i^j = D_i^j + c \cdot (t_i - t^j) + c \cdot (T_i^j + I_i^j + \boldsymbol{n}_i^j) \tag{6.1}$$

where

D_i^j - true range between receiver site i and satellite j;

c - speed of light in vacuum;

t_i - clock bias of receiver i;

t^j - clock bias of satellite transmitted corrections;

T_i^j - true tropospheric delay;

I_i^j - true ionospheric delay;

$\boldsymbol{n}_i^j$ - combinations of receiver noise, multipath and inter-channel error.

According to Parkinson (1996), Eq. 6.1 can be simplified as Eq. 6.2 for k satellites in the view at receiver site i.

$$\underset{k\times 4}{G} \cdot \underset{4\times 1}{\hat{X}} = \underset{k\times 3k}{A} \cdot \underset{3k\times 1}{\hat{R}} - \underset{k\times 1}{\hat{\boldsymbol{r}}_c} . \tag{6.2}$$

The dots in the above equation represent inner products. G is the design matrix of the measurement equation, with each direction vector from the receiver to each satellite in WGS84 coordinate system as its elements. Vector $\hat{X}$ consists of four unknowns (3D position and a receiver clock bias). A is a matrix which is constructed from the same set of direction vectors to k satellites as in matrix G. $\hat{R}$ is a matrix of the transmitted satellite locations. $\hat{\boldsymbol{r}}_c$ is the corrected pseudorange vector with the modelled tropospheric, ionospheric delay and satellite clock biases for each individual satellite. Based on Eq. 6.1, the fundamental error equation can be derived:

$$\underset{k\times 4}{G}\cdot \underset{4\times 1}{\Delta\hat{X}} = \Delta \underset{k\times 1}{\hat{\boldsymbol{r}}_c}\,. \tag{6.3}$$

$\Delta\hat{X}$ is the error vector of the four unknowns and $\Delta\boldsymbol{r}_c$ comprises all uncorrected residual ranging errors.

The generalised solutions to Eq. 6.2 and Eq. 6.3 can be expressed as

$$\underset{4\times 1}{\hat{X}} = (\underset{4\times k}{G^T}\,\underset{k\times 4}{G})^{-1}\underset{4\times k}{G^T}(\underset{k\times 3k}{A}\cdot \underset{3k\times 1}{\hat{R}} - \underset{k\times 1}{\hat{\boldsymbol{r}}_c}) \tag{6.4}$$

$$\underset{4\times 1}{\Delta\hat{X}} = (\underset{4\times k}{G^T}\,\underset{k\times 4}{G})^{-1}\underset{4\times k}{G^T}\,\underset{k\times 1}{\Delta\hat{\boldsymbol{r}}_c}\,. \tag{6.5}$$

From the error equation, it is obvious that any systematic or random ranging error can propagate into positioning solution through the satellite sky distribution. This is why matrix $(G^TG)^{-1}$ is defined as DOP. Applying error propagation law to Eq. 6.5, the positioning accuracy can be estimated by the multiplication of DOP values and ranging accuracy $\boldsymbol{s}_{r_c}$. Analysis of the structure of matrix $(G^TG)^{-1}$ can reveal the characteristic of error propagation, which can be used to plan the surveying timetable to obtain the optimal positioning solution within the specific surveying scenario. It is worth pointing out that if the elevation cutoff mask is selected too low, the ranging error can be high due to the interference from propagation media, even this might result in very good DOP values with scattered satellite distribution together with the satellites overhead. In most cases a tradeoff between ranging accuracy and satellite locations should be made to obtain the best positioning results. Generally, for bridge deflection monitoring like in the precise geodetic applications, the elevation cutoff angle is usually set to 15° to avoid high chance of multipath and signal blockage by the passing vehicles. In this research, the emphases will focus on the deficiency of the current satellite sky distribution and its potential impact on the positioning accuracy. The combined effects both from ranging errors and satellite geometry will not be further addressed.

The calculated DOP values are usually expressed in the WGS84 coordinate system, which can not be used to analyse the possible positioning accuracy in a local coordinate system. When a local coordinate system with its axes along the local north, east and vertical is used, $(G^TG)^{-1}$ must be transformed into a local cofactor matrix Q_x

(Hofmann-Wellenhof et al. 1997). This transformation can be realised using the zenith distance z_i^j and azimuth α_i^j of the direction vector $\bar{l}_i^j$ between receiver site i and each satellite j.

For satellite j, the direction vector $\bar{l}_i^j$ in WGS84 coordinate system is transformed into a local coordinate system through inner products (Eq. 6.6).

$$\begin{aligned} &\text{North} \quad \bar{l}_i^j \cdot \bar{n} = \sin z_i^j \cos \alpha_i^j \\ &\text{East} \quad \bar{l}_i^j \cdot \bar{e} = \sin z_i^j \sin \alpha_i^j \\ &\text{Up} \quad \bar{l}_i^j \cdot \bar{u} = \cos z_i^j \end{aligned} \tag{6.6}$$

$\bar{n}$, $\bar{e}$ and $\bar{u}$ are three direction vectors in the rotation matrix between WGS84 and the local coordinate system, which can be determined by the latitude and longitude at the receiver site.

For k satellites, the design matrix G can be rewritten as Eq. 6.7 by definition in a local coordinate system in the order of north, east and up.

$$G_{\underset{k\times 4}{loc}} = \begin{bmatrix} \sin z_i^1 \cos \alpha_i^1 & \sin z_i^1 \sin \alpha_i^1 & \cos z_i^1 & 1 \\ \sin z_i^2 \cos \alpha_i^2 & \sin z_i^2 \sin \alpha_i^2 & \cos z_i^2 & 1 \\ \sin z_i^3 \cos \alpha_i^3 & \sin z_i^3 \sin \alpha_i^3 & \cos z_i^3 & 1 \\ \vdots & \vdots & \vdots & \vdots \\ \sin z_i^k \cos \alpha_i^k & \sin z_i^k \sin \alpha_i^k & \cos z_i^k & 1 \end{bmatrix}_{loc} \tag{6.7}$$

Let

$$Q_{\underset{4\times 4}{loc}} = (G_{\underset{4\times k}{loc}}{}^T \, G_{\underset{k\times 4}{loc}})^{-1} = \begin{bmatrix} NDOP^2 & & other & terms \\ & EDOP^2 & & \\ & & VDOP^2 & \\ other & terms & & TDOP^2 \end{bmatrix}_{loc} \tag{6.8}$$

In Eq. 6.8, *NDOP*, *EDOP*, *VDOP* are the DOP values in the north, east and vertical directions in a local coordinate system. *TDOP* is the time DOP. The horizontal DOP (HDOP), positioning DOP (PDOP) and geometric DOP (GDOP) can be estimated

using the above four components of the unknowns. The positioning errors in a local coordinate system can be estimated by Eq. 6.9 with matrix $G_{\underset{k\times 4}{loc}}$ calculated by Eq. 6.7.

$$\Delta\hat{X}_{\underset{4\times 1}{loc}} = (G_{\underset{4\times k}{loc}}{}^{T}\, G_{\underset{k\times 4}{loc}})^{-1} G_{\underset{4\times k}{loc}}{}^{T}\, \Delta\hat{r}_{\underset{k\times 1}{c}} \,. \tag{6.9}$$

To evaluate the impact of current satellite sky distribution on the accuracy in each individual directions of a BCS, the positioning errors in the local coordinate system (north, east and up) need to be transformed into those in BCS using horizontal rotation angle α between two coordinate systems by Eq. 6.10.

$$\Delta\hat{X}_{\underset{4\times 1}{bcs}} = \underset{4\times 4}{R}\,\Delta\hat{X}_{loc} = \underset{4\times 4}{R}(G_{\underset{4\times k}{loc}}{}^{T}\, \underset{\underset{4\times 1}{k\times 4}}{G_{loc}})^{-1} G_{\underset{4\times k}{loc}}{}^{T}\, \Delta\hat{r}_{\underset{k\times 1}{c}} \,. \tag{6.10}$$

Applying the theory of error propagation to Eq. 6.10, the DOP values in a BCS are expressed as follows

$$Q_{\underset{4\times 4}{bcm}} = \underset{4\times 4}{R}(G_{\underset{4\times k}{loc}}{}^{T}\, G_{\underset{k\times 4}{loc}})^{-1}(G_{\underset{4\times k}{loc}}{}^{T}\, G_{\underset{4\times k}{loc}})(G_{\underset{4\times k}{loc}}{}^{T}\, G_{\underset{k\times 4}{loc}})^{-1}\, \underset{4\times 4}{R} = \underset{4\times 4}{R}\, Q_{\underset{4\times 4}{loc}}\, \underset{4\times 4}{R^{T}} = \underset{4\times 4}{R}(G_{\underset{4\times k}{loc}}{}^{T}\, G_{\underset{k\times 4}{loc}})^{-1}\, \underset{4\times 4}{R^{T}} \tag{6.11}$$

where

$$\underset{4\times 4}{R} = \begin{bmatrix} \cos\alpha & \sin\alpha & 0 & 0 \\ -\sin\alpha & \cos\alpha & 0 & 0 \\ 0 & 0 & 1 & 0 \\ 0 & 0 & 0 & 1 \end{bmatrix} \begin{matrix} \text{..... } north \\ \text{..... } east \\ \text{..... } up \\ \text{..... } time \end{matrix} \,. \tag{6.12}$$

The longitudinal, lateral and vertical DOP values can be calculated from the square roots of the diagonal elements of matrix $Q_{\underset{4\times 4}{bcm}}$ on the left side of Eq. 6.11.

6.3 GPS Sky Distribution in Mid and High Latitude Areas and its Impact on Positioning Solutions

It is well known that with the current GPS satellite constellation the accuracy of the vertical component is normally two to three times worse than that of the plan component. However, this is not always the case. Detailed analysis of some of the bridge deflection monitoring results shows that the GPS height accuracy is not as good as the plan accuracy, as expected. However, the North-south component is also

less precise than the East-west component in mid and high latitude areas (latitude>45°) such as in the UK. This is due to the current orbit design and the satellite geometry. The induced errors, due to the satellite geometry, could make it appear as though the structure is moving, or appear to move uncharacteristically. The following section presents the bridge deflection results obtained by an integrated system of GPS and triaxial accelerometer. The GPS data collected are affected by the satellite geometry, which contaminates the resulting movement in the North-South direction. The GPS positioning solutions from data processing for two bridges (one in London and one in Nottingham) are analysed. The instantaneous error ellipses calculated from the covariance matrix in the horizontal plane for both observation sites reveal much higher obtainable accuracy in the East-west direction than that in the North-south direction. The consequences of these characteristics are less precise coordinates along the bridge's main axis when the bridge's main axis is oriented to north. The results at both sites have been further investigated through comparisons with 3D accelerations sensed simultaneously. The IESSG has developed a GNSS simulator, and this has been used to recreate GPS data at the specific observation sites in an attempt to study the influence of satellite sky distribution on the propagation of systematic errors, such as relative tropospheric delay, absolute ionospheric delay, and multipath.

As demonstrated in Section 6.2, the covariance matrix of unknowns (site coordinates, clock parameter etc.) obtained from data processing is a function of GPS satellite sky distribution and propagation medium. In general, the position accuracy can be estimated as the ranging accuracy multiplied by a dilution factor-DOP value (Parkinson 1996). Good DOP values normally mean a well distributed satellite constellation where the use of low elevation angle satellites can give better DOP but introduce other errors. There is necessity to make a compromise between DOP values and elevation cutoff angle to obtain the optimal measurement accuracy. Through studies of the behaviour of the covariance matrix, the impact of satellite sky distribution on the position and on the propagation of many important systematic errors under a specific sky distribution and observation sites can be traced (Geiger 1988).

Because of the inclination of 55° of all GPS orbits, simulated results show that with the current satellite constellation the satellite distribution over the sky at low latitude is almost uniform. At mid-latitude areas, practically no observations are possible in the northern direction (roughly between azimuth 315° and 45°). In the high latitude sites, only observations between elevation angles 0° and 45° can be made in the north direction (Santerre 1991). For the middle and high latitude areas, observations in the north direction will be possible only close to zenith, or to the horizon. This represents a clear lack of the measurable satellites in the aforementioned areas. Fig. 6.1 to Fig. 6.4 show the satellite sky distributions for a period of 24 hours and for the 2 hours when the measurements were collected at the two bridge sites in London and Nottingham, with latitude 51°30′ north and 52°56′ north respectively. To preclude the high level of errors caused by the propagation medium and blockage of the signals by the surroundings, the elevation cutoff angle in both GPS trials is set to 15°. This excludes the possibility of seeing lower satellites in the north direction (between azimuth 45° and 315°) and a big *immeasurable hole* is created. Due to impact, only SV4 temporarily appeared in the north direction with low elevation angle (Fig. 6.2) for the London bridge site and SV23 can be tracked at the Nottingham bridge site (Fig. 6.4). Such a satellite sky distribution results in a poor DOP value and undoubtedly will lead to degradation in positioning accuracy.

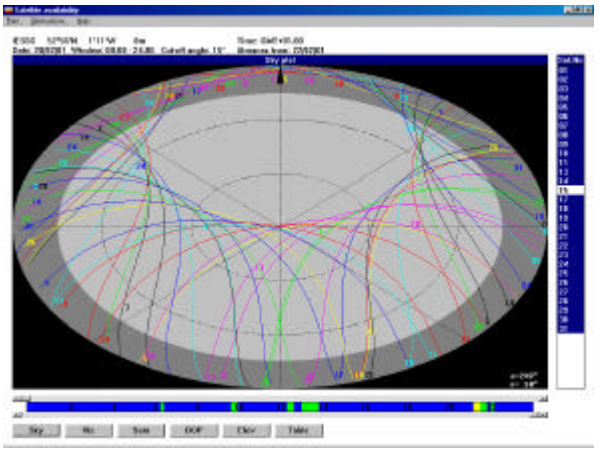

Fig. 6.1. Satellite sky view in London (24 hrs)

Improving the GPS height accuracy to a comparable level with the horizontal counterparts is a current research topic in precise GPS surveying for engineering applications.

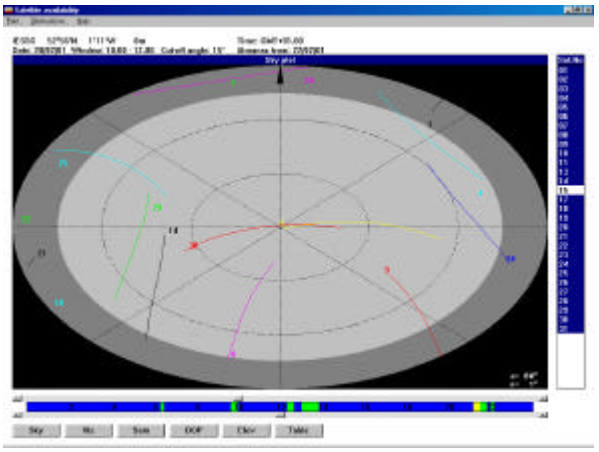

Fig. 6.2. Satellite sky view in London (2 hrs)

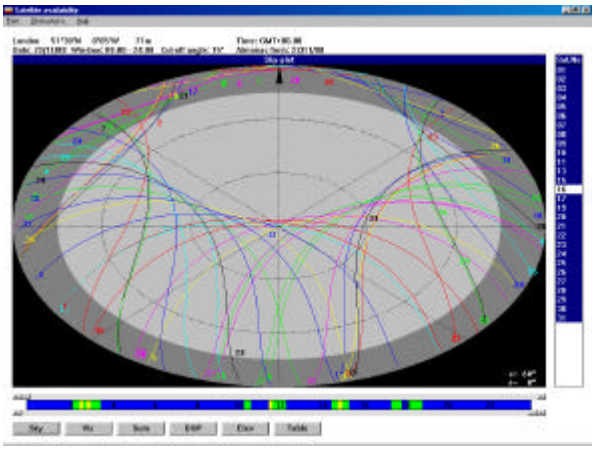

Fig. 6.3. Satellite sky view in Nottingham (24 hrs)

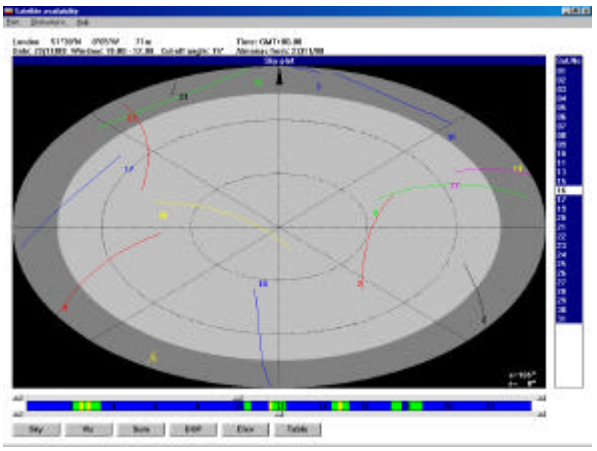

Fig. 6.4. Satellite sky view in Nottingham (2 hrs)

Fig. 6.5 is the instantaneous angle change of the main axis of an error ellipse in the horizontal plane at the middle span on the Wilford suspension footbridge in Nottingham, which is calculated from the covariance matrix of each epoch GPS positioning in WGS84. The fact that the main ellipse axis is offset about 26.7° from

north means that if there is a 1cm horizontal positioning error there will be 8.9 mm error projected into the north direction and about 4.4 mm error into the east direction. Similar phenomena have been found from the covariance matrix analysis of the London Millennium Bridge. In addition, calculations suggest that this will cause similar positioning problems in the data processing along the longitudinal axis of the Humber Bridge because it is orientated to the north-south direction. If GPS is applied to monitor the deflection of these bridges, the satellite sky distribution should be seriously considered in the data processing and the result interpretation. Approaches should be devised to cope with such impacts resulting from the satellite constellation.

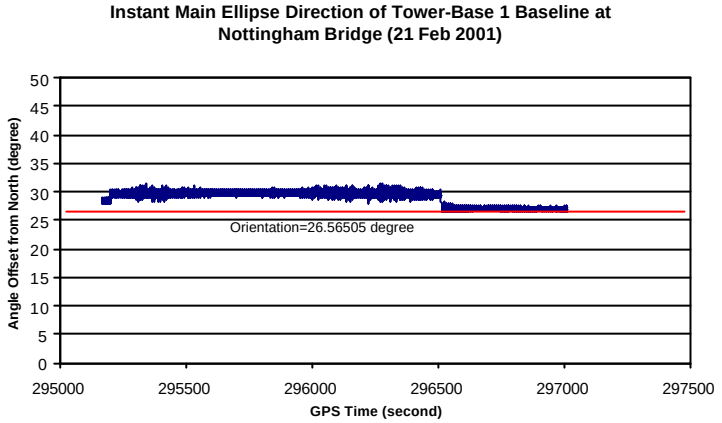

Fig. 6.5. Orientation of the main axis (Nottingham)

The measurements from the two bridges were processed using Leica SKI-Pro software (Leica 2001, 2002). The output coordinates in WGS84 were then transformed and projected to a BCS with the main axis offset from the north by a fixed angle and coinciding with the bridge longitudinal axis in each case. Detailed algorithms and data processing procedures can be found in recent papers (Roberts et al. 2000a; Roberts et al. 2001a; Roberts et al. 2001b).

Fig. 6.6 is the 3D mean bridge movements in a BCS. Fig. 6.7 is the 3D accelerations sensed by a triaxial accelerometer on the London Millennium Bridge, collected simultaneously with GPS data using a specially designed cage, that houses the triaxial accelerometer and GPS antenna together. The bridge's main axis is 0.9° offset from north. Of the 3D relative movements from the GPS measurements the vertical movement is the largest component. There are two reasons for this. The first one is

due to the actual bridge performance, which exhibits itself the largest up and down movement compared with the movements along and across the bridge axis. The second reason for this comes from the impact of the GPS satellite constellation. In the horizontal plane the movement along the bridge axis is notably larger than the lateral movement. This is contrary to the expected dynamics for a bridge of this type. With these results, wrong conclusions about the actual bridge dynamics could be made.

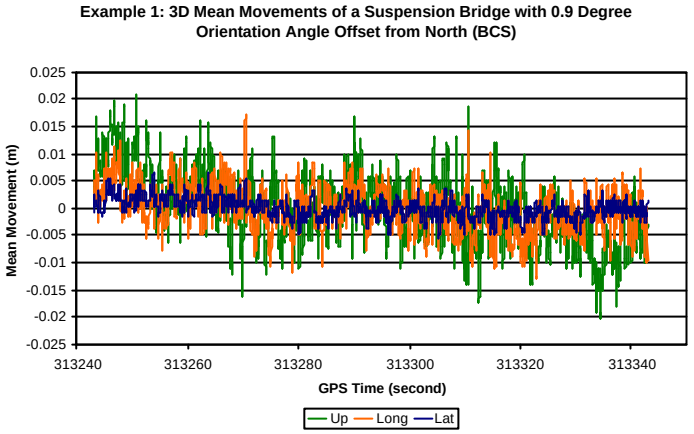

Fig. 6.6. 3D relative movements (London)

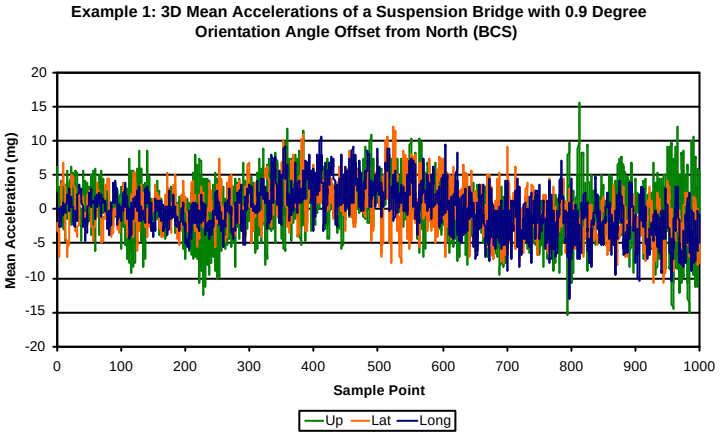

Fig. 6.7. 3D accelerations (London)

The magnitudes of the accelerations measured in each direction agree with the nature of the expected dynamics of the bridge and further prove the problematic results from GPS only solutions (Fig. 6.7).

The GPS positioning solutions and the accelerometer data from the Wilford suspension footbridge in Nottingham with 102° main axis of the bridge offset from

the north were also analysed. Because in this case the main axis of the bridge is nearly parallel to the east-west direction, which is the better accuracy direction of the GPS ellipse in the horizontal plane, reasonable results with the minimum influence from the deficiency of GPS satellite constellation are obtained from GPS measurements (Fig. 6.8). The longitudinal movement of this bridge is the smallest one of the three directions in a BCS. Since the lateral direction of BCS is roughly north, the positioning results could be contaminated by systematic errors propagated through the satellite sky distribution. The interesting thing is the magnitude of lateral movement is at about the same level as that of height. The reason for this might come from the lateral wind loading and inherent poor accuracy in this direction as expected. More research into this issue is needed. Fig. 6.9 shows 3D accelerations sensed by the same triaxial accelerometer used in the Wilford suspension footbridge trial. In this graph the lateral movement is larger than the vertical one due to the influence of very strong wind loading. Again the comparison of the relative movements from GPS measurements in decreasing orders (up>lat>long) and accelerometer (lat>up>long) reveals the impact of the satellite sky distribution on the positioning accuracy and also the real deflection of the bridge under wind loading.

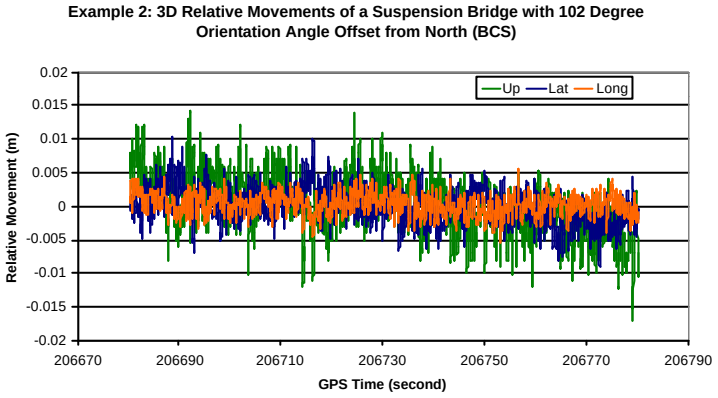

Fig. 6.8. 3D relative movements (Nottingham)

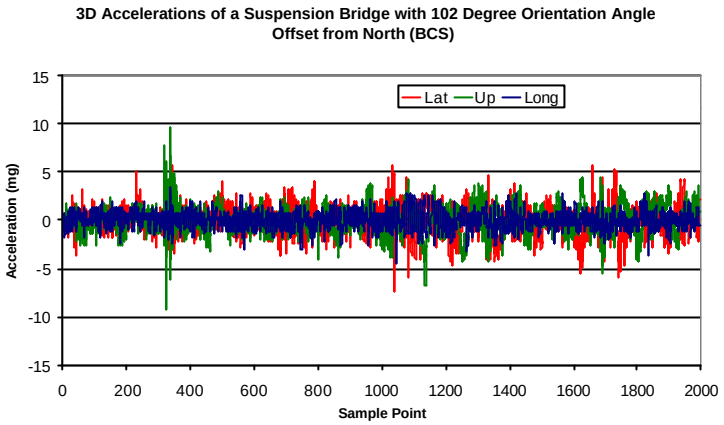

Fig. 6.9. 3D accelerations (Nottingham)

Using the covariance matrix from the GPS data processing, accuracy ratios of each epoch between axes in a local coordinate system have been analysed. The ratios of the SD of the north coordinate over that of the east coordinate, the height SD over that of the north coordinate, and the height standard deviation over that of the east coordinate are calculated. Fig. 6.10, 6.11, and 6.12 are the instant ratio changes of the above SD for the London Millennium Bridge. The fact that the SD ratio of the north coordinate over the east coordinate is larger than factor one illustrates the relative worse accuracy in the north direction due to the satellite sky distribution. With the fact that the SD ratio of the height over the north coordinate is changing, one can conclude that in the high latitude areas the accuracy in the north direction could degrade to the same level as that in the vertical direction. The decreasing accuracy order for the London Millennium Bridge at the observation period are east>north≥height in local coordinate system, or lateral>longitudal≥height in a BCS. Fig. 6.13, 6.14 and 6.15 are the counterparts of Fig. 6.10, 6.11, and 6.12 for the Nottingham footbridge. More stable SD ratios are obtained and also more precise positioning solutions as expected. Since the longitudinal direction of Wilford suspension footbridge is offset 102° from the north direction, the best obtainable measurements in 3D coordinates is roughly on the bridge main axis. The accuracy in a decreasing order for Nottingham Wilford suspension footbridge is east>north>height in a local coordinate system, or longitudinal>lateral>heigh in a BCS. Comparison of the accuracy of the two bridge sites in each direction reveals that the reason for a more stable accuracy in each direction at the Nottingham footbridge site is due to less ranging error effects. In

London, because of the signal obstruction from the surroundings on both sides of River Thames, a more adverse observation scenario caused worse measurements.

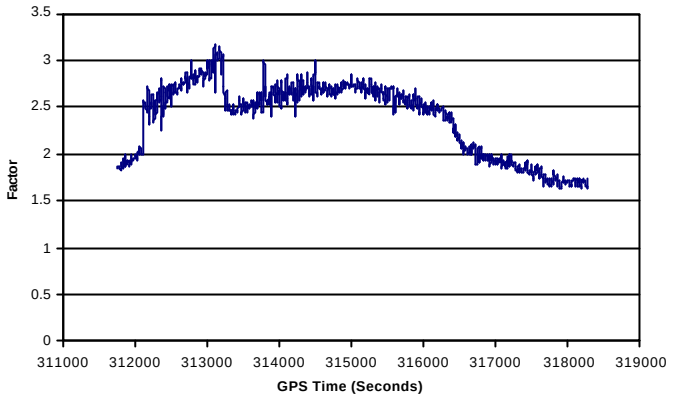

Fig. 6.10. Ratio of north SD over east SD (London)

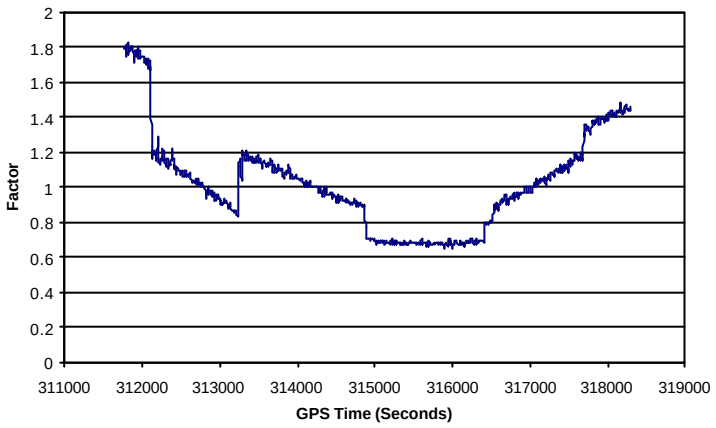

Fig. 6.11. Ratio of height SD over north SD (London)

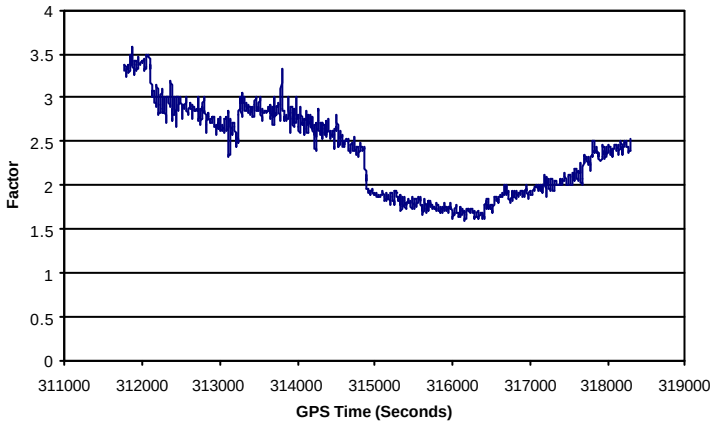

Fig. 6.12. Ratio of height SD over east SD (London)

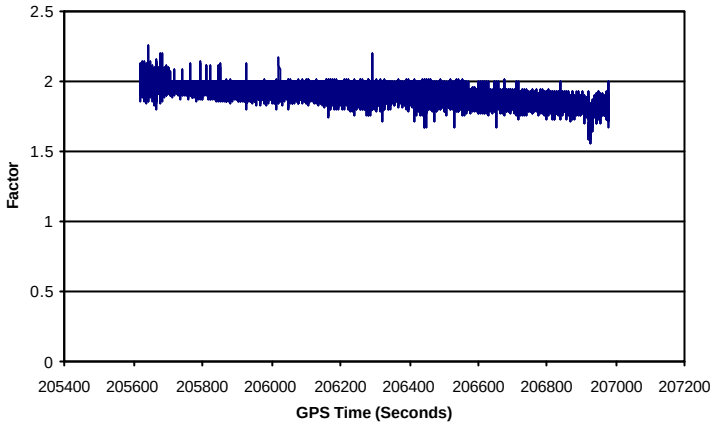

Fig. 6.13. Ratio of north SD over east SD (Nottingham)

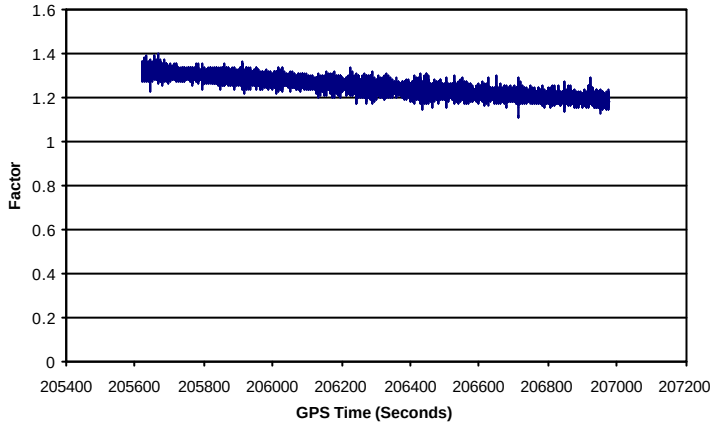

Fig. 6.14. Ratio of height SD over north SD (Nottingham)

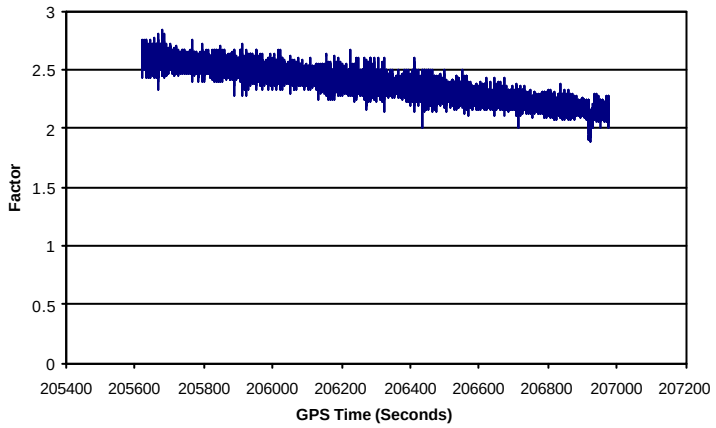

Fig. 6.15. Ratio of height SD over east SD (Nottingham)

6.4 Solutions to Improve Positioning Accuracy under Current GPS Constellation

To improve the accuracy of GPS-based positioning solutions, augmentation techniques need to be adopted to strengthen GPS satellite constellation. Like a GPS and accelerometer integrated bridge deflection monitoring system, other hybrid systems used for bridge deformation monitoring should be feasible and cost-effective. Galileo is still under development with many uncertainties in the future and not likely to be a near future solutions. Even facing many economic and political problems, Russia's GLONASS is still there with seven satellites in the orbits as of March 2002. Pseudolites are another potential option, which could be employed to augment GPS system. The following sections examine the use of GLONASS and pseudolite for the augmentation of GPS sky distribution.

6.4.1 Hybrid GPS/GLONASS Bridge Deflection Monitoring

GLONASS (GLObal Navigation Satellite System) is the Russian equivalent to GPS. GLONASS is still an available option to enhance satellite sky distribution (http://www.rssi.ru/). Its potential was demonstrated by the GPS/GLONASS based deflection monitoring trial on the Humber Bridge, which employed state-of-the-art GPS/GLONASS receivers. The data provided an ideal example for the evaluation of such a hybrid system for augmenting the current GPS system.

The Humber Bridge is located across the Humber Estuary on the east coast of England. Consisting of three sections, in an approximately North-south direction, the bridge spans 2220 m, supported by two towers of 155.5 m in height. The bridge has been designed to withstand movements of up to ±4 m. The Humber Bridge was the longest suspension bridge in the world with a main span of 1410 m when it was officially opened to traffic on 17th July 1981 by H. M. the Queen (http://www.humberbridge.co.uk, 2001).

Fig. 6.16 is the three-span layout of the Humber Bridge.

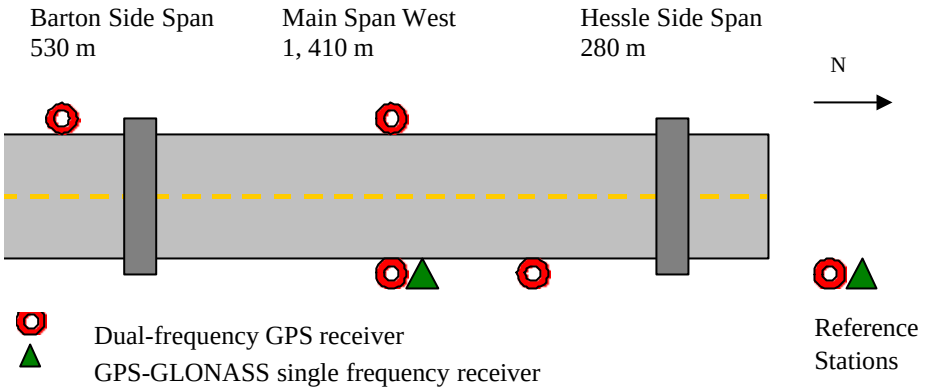

Fig. 6.16. GPS/GLONASS receiver layout (Humber Bridge)

On 16 February 1998, starting at about 1:30 am local time and lasting for about 44 minutes, the Humber Bridge trial was conducted by the IESSG staff. It aimed to assess the viability of satellite positioning technology and finite element modelling for bridge deflection monitoring. The detailed loading tests, receiver layout on the bridge, data processing and result analysis can be found in Roberts, et al. (1999).

Data collected at two reference stations and two midspan observation sites with Ashtech Z12 dual-frequency receivers, which can only record GPS measurements, and GG24 single frequency receivers, which can log both GPS and GLONASS measurements, are taken as the examples to illustrate the impact the current GPS satellite sky distribution on the positioning accuracy. Data are re-processed with Ashtech AOSS post processing software in a kinematic OTF mode. Fig. 6.17 and Fig. 6.18 are GPS satellite sky distribution viewing within 24 hours and the period of time when the trial was conducted. Fig. 6.19 and Fig. 6.20 are GPS/GLONASS satellite sky distribution viewing within 24 hours and the period of time when the trial was conducted. There were five of the twelve operational GLONASS satellites and eight of the twenty-seven GPS satellites in view, giving a total of thirteen measurable satellites (Fig. 6.20).

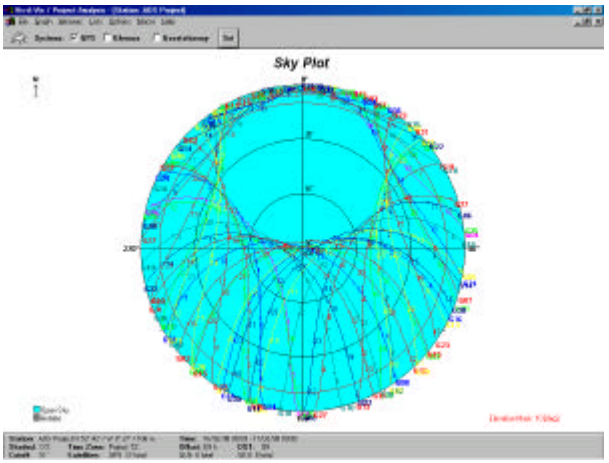

Fig. 6.17. GPS sky distribution (Humber Bridge, 24 hrs)

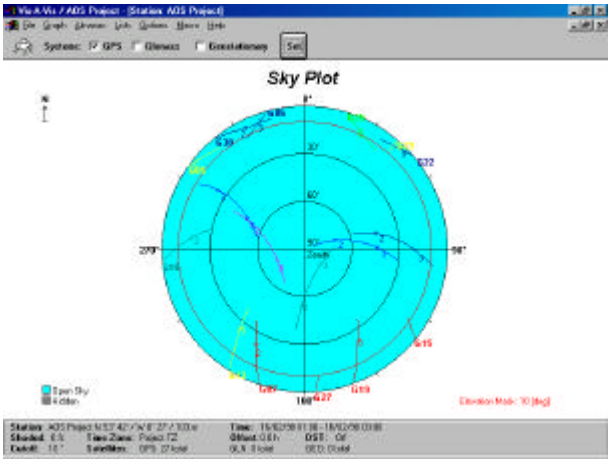

Fig. 6.18. GPS sky distribution (Humber Bridge, 2 hrs)

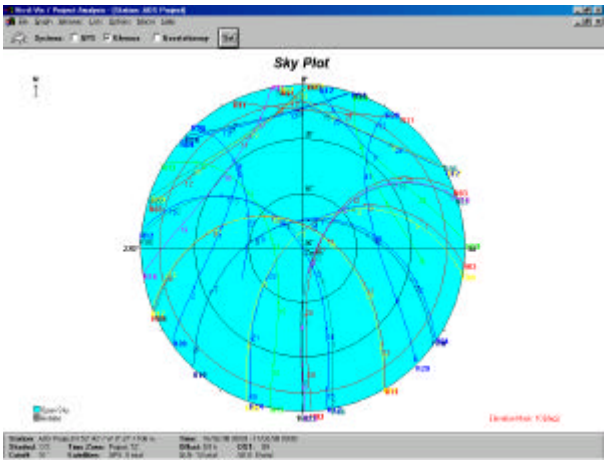

Fig. 6.19. GLONASS sky distribution (Humber Bridge, 24 hrs)

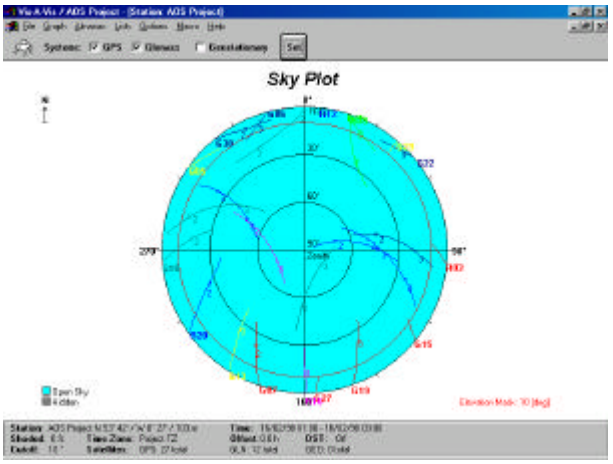

Fig. 6.20. GPS and GLONASS sky distribution (Humber Bridge, 2 hrs)

Since the elevation cutoff angle of both satellite systems was set to 10° in the data collection, it is obvious that the GPS satellites with elevation angles lower than the cutoff angle and azimuth between 315° and 45° have been excluded. The only satellite existing within azimuth 315 to 45° in the north, satellite PRN 25, with azimuth around thirty degrees dropped below cutoff angle when measurement started. The GPS satellites over head of the observation sites could not form a good sky distribution and hence resulted in bad DOP values. In contrast to the GPS sky distribution, GLONASS covers a relatively larger area than GPS due to its constellation design of 64.8° inclination, which is particularly evident in the North direction.

It took 24.6 seconds for Z12 receiver and 268.5 seconds for GG24 to fix the integer ambiguity. Except for a slower integer ambiguity resolution using GG24 single frequency receivers, the positioning solutions of GG24 receivers are the same as or even better than those from Z12 dual frequency receivers.

Usually it takes 10 to 20 minutes for a single frequency GPS receiver to fix integer ambiguity and in a dynamic observation environment, cycle slips will cause the integer ambiguities to be resolved. Once GG24 fixed integer ambiguities, it maintained satellite tracking until the end of data collection, even with up to 1 metre vertical movement under the controlled loadings. This demonstrates the advantages of cheaper single frequency receivers, which could be employed for high accuracy bridge deflection monitoring.

For comparing the relative movements in each direction in BCS, the 5 Hz Z12 data have been resampled to 2 Hz, the data rate used by GG24. Fig. 6.21, 6.22, and 6.23 are the 3D relative movement comparisons in a BCS.

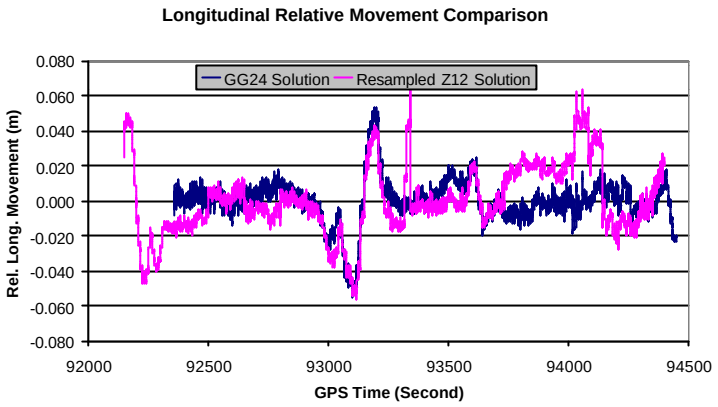

Fig. 6.21. Longitudinal relative movement comparison

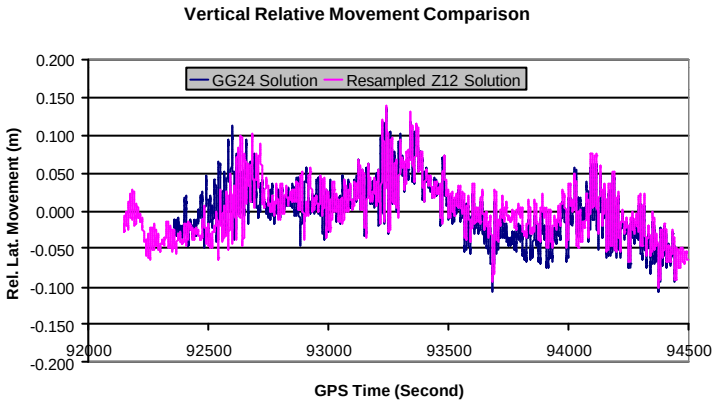

Fig. 6.22. Lateral relative movement comparison

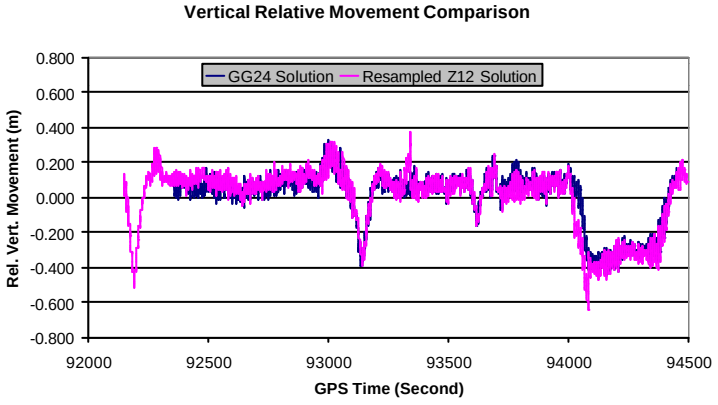

Fig. 6.23. Vertical relative movement comparison

There are obvious abnormal jumps at epoch 93344.7 caused by a cycle slip in longitudinal and height components of the Z12 solutions. The relative movements calculated from the measurements of Z12 dual frequency receiver demonstrate more irregular signatures, especially in longitudinal direction, which are introduced by the deficiency of GPS sky distribution and due to the propagation of ranging errors. With the geometric augmentation from GLONASS, the positioning results show a more reasonable pattern in the longitudinal direction. The abnormality of measured relative movements from GPS only system demonstrates the importance of an augmented satellite system for resulting robust solutions.

The orientation axes of error ellipses in a local coordinate system calculated from standard deviations further demonstrate the deficiency of GPS for bridge deflection monitoring purposes. For the SD from GG24, the orientation angle offsets from north are mostly larger than 45°, and cause the ranging errors to be distributed mainly in the west-east direction (Fig. 6.24). This explains why the positioning solutions from GG24 receivers are much reasonable. From Fig. 6.25, the orientation angles of the main ellipse axis are mostly less than 45° and this will propagate the ranging errors mainly into longitudinal direction in BCS.

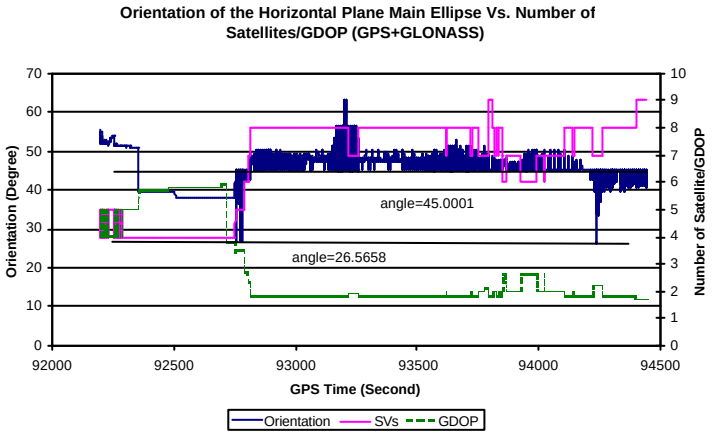

Fig. 6.24. Ellipse orientation vs. SVs (GPS/GLONASS)

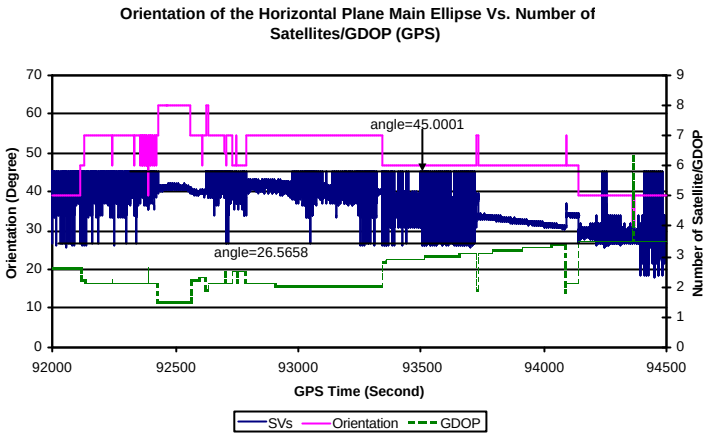

Fig. 6.25. Ellipse orientation vs. SVs (GPS)

6.4.2 Pseudolite Approach – Simulated Results

To simulate the impact of satellite sky distribution (elevation angle and azimuth) on DOP values in the local coordinate system, a Matlab simulator was developed. Optimal and worst satellite sky distributions are analysed according to Parkinson (1996) and the outputs are illustrated in the following figures.

Fig. 6.26 illustrates the changes of DOP values with the changes of satellite positions in an optimal condition. Five satellites symmetrically distributed above and below the horizon at the observation site, with an interval of 72° in azimuth, and another satellite located overhead with 0° azimuth, are employed to simulate best satellite sky distribution. Maintaining the same symmetric spacing in azimuth, the elevation angle is varied, including negative elevation angles to investigate the impact from ground based pseudolites. It can be seen from the graph that HDOP is quite flat over the whole range, which reflects the optimal azimuth configuration even with satellites deployed above the south hemisphere. With the elevation angle higher than -15°, VDOP surpasses HDOP and from 40° the VDOP together with TDOP degrades significantly. Fig. 6.26 also reveals that with the introduction of pseudolites, TDOP and VDOP can be improved with negative elevation angles. With elevation angle lower than 20°, the best GDOP could be obtained.

Similar to the configuration of Fig. 6.26, except for excluding the satellite on the north direction, Fig. 6.27 is the result of DOP changes with elevations. Comparing

these figures, with still very good satellite geometry, there are no many changes in HDOP and TDOP. However VDOP surpassed HDOP at 0° elevation angle instead of -15°.

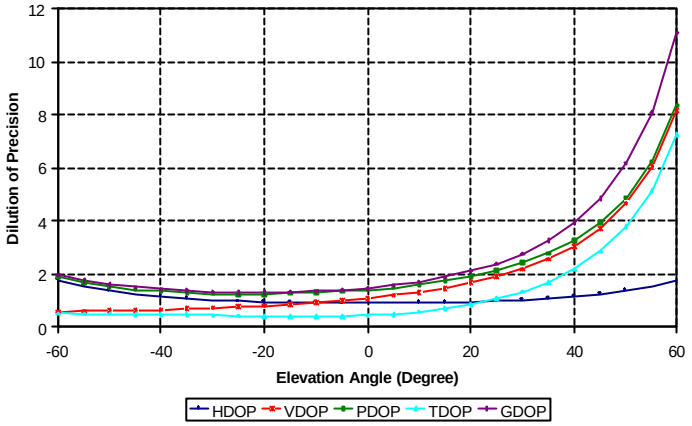

Fig. 6.26. DOP changes for 5 symmetric distributed satellites above and below the horizon at observation site, with an interval of 72° and a satellite overhead.

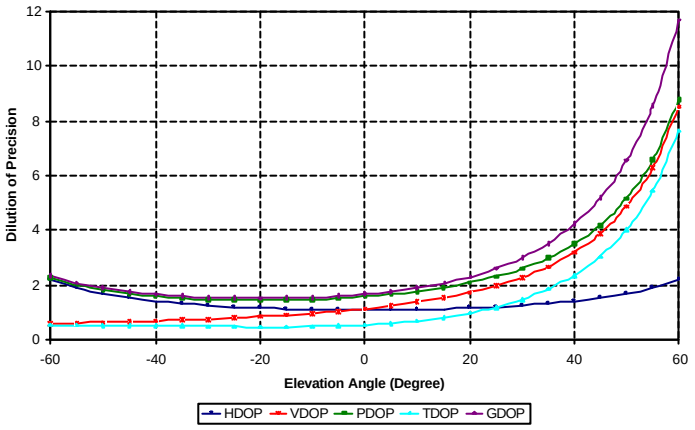

Fig. 6.27. DOP changes for 4 symmetric distributed satellites above and below the horizon at observation site, with an interval of 72° and a satellite overhead.

To simulate the effects of the introduction of a pseudolite, the same satellite sky distributions are employed as in Fig. 6.28. The angle range of the pseudolite is set from –60 to 60° when the elevation angle of GPS is fixed to a specific angle. It can be found that better a HDOP value is obtainable from a lower GPS elevation angle when the elevation angle of pseudolite changes between –60 and 60° (Fig. 6.28). When GPS elevation angle is fixed to 50°, the worst HDOP value appears when the elevation angle of pseudolite equates to 55° because of the bad condition number of the covariance matrix. For other fixed elevation angles, a quite flat HDOP variation over the changes of the elevation angles of pseudolite reveal that the introduction of a pseudolite into the satellite geometry will not significantly improve the HDOP as it

does with VDOP and TDOP. With GPS elevation angle less than 40°, good HDOP can be expected.

In contrast to HDOP, which changes with quite a flat pattern, VDOP can be dramatically improved through an enhanced vertical geometry only when the pseudolite angle is negative (Fig. 6.29). This supplies a guideline for the purposive selection of an effective pseudolite location. To obtain good VDOP value, the elevation angle of a pseudolite higher than 20° should be avoided. Fig. 6.30 illustrates the GDOP changes with the same GPS satellite/pseudolite configuration. Again, for obtaining good GDOP values (less than 6), pseudolites with elevation angles higher than 20° should be avoided.

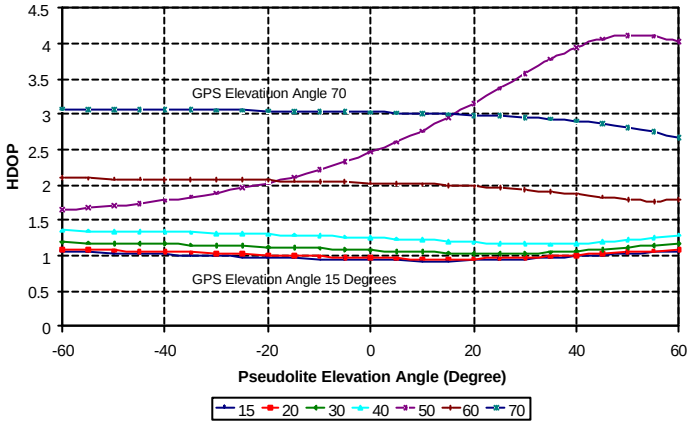

Fig. 6.28. HDOP changes with the changes of the elevation angle of a pseudolite in the north direction and 4 symmetric distributed satellites above the horizon at observation site, with an interval of 72° and a satellite overhead

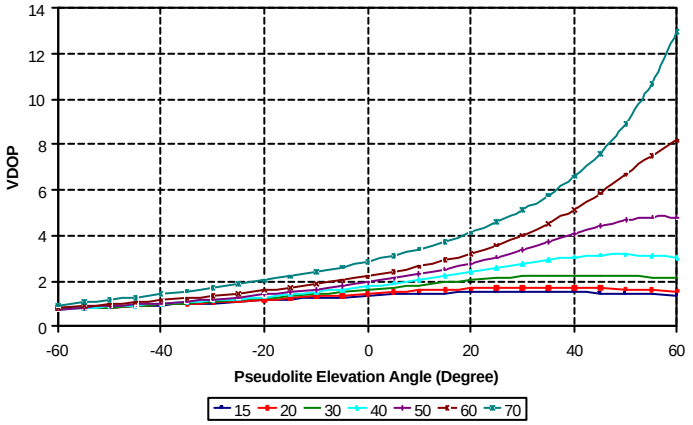

Fig. 6.29. VDOP changes with the changes of the elevation angles of a pseudolite in the north direction and 4 symmetric distributed satellites above the horizon at observation site, with an interval of 72° and a satellite overhead

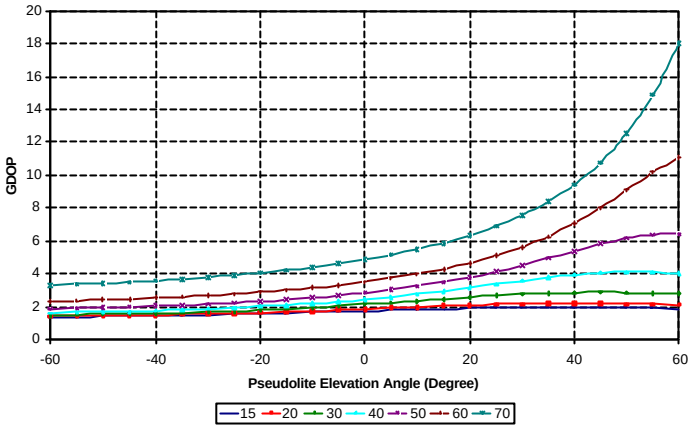

Fig. 6.30. GDOP changes with the elevation angle of a pseudolite in the north direction and 4 symmetric distributed satellites above the horizon at observation site, with an interval of 72° and a satellite overhead.

Based on the above graphs with the GPS satellite sky distributions of specific elevation angles, the best pseudolite sites can be decided in each case. To obtain optimal HDOP and VDOP values, the elevation angle of one pseudolite in the north direction should not be higher than 20°.

The HDOP changes calculated by a GPS sky distribution augmented with three pseudolites located at azimuth angle –22.5°, 0°, 22.5° and varying elevation angle from –60° to 60° are illustrated in Fig. 6.31.

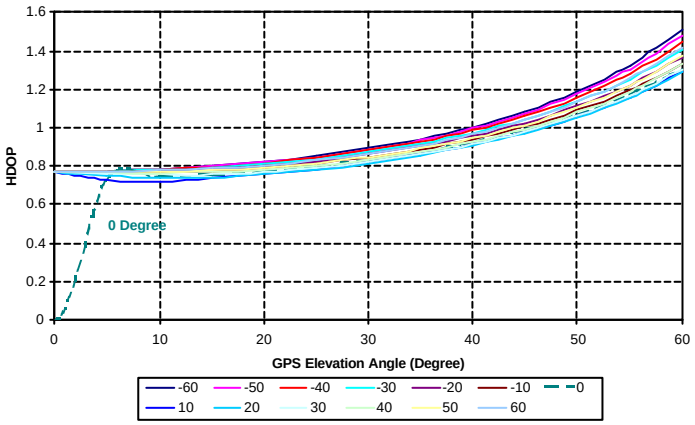

Fig. 6.31. HDOP changes with 7 evenly distributed GPS satellites of 45° azimuth interval between 45°~315° and three pseudolites at azimuths –22.5°, 0°, 22.5° with variable elevation angles –60°~60°

In this case, seven satellites are evenly distributed above horizon without an over head satellite to simulate the potential poor GPS geometry. Seven satellites with azimuth interval of 45° situate from 45° to 315° to simulate the possible sky distribution in the

high latitude areas. Maintaining the elevation angle of pseudolites, GPS elevation angle varies from 0° to 60°. Due to the exclusion of the overhead satellite, poor DOP values will result. However, with the augmentation from these three pseudolites, significant HDOP improvement can be achieved, even to the optimal level as in Fig. 6.26. When the elevation angles of the three pseudolites are set to zero, the singularity of the design matrix in the observation equation will cause the worst HDOP and hence no positioning solution could be made. This is denoted as zero HDOP in Fig. 6.31.

Fig. 6.32 is the VDOP results with the above configuration of GPS satellites and pseudolites. According to this graph, pseudolites with elevation angles from –60° to 60° should not be integrated with a GPS satellite sky distribution lower than 10° to get VDOP values less than 5. With the increase of elevation angles, the VDOP values can reach the same level as HDOP. Similar results in GDOP values are illustrated in Fig. 6.33.

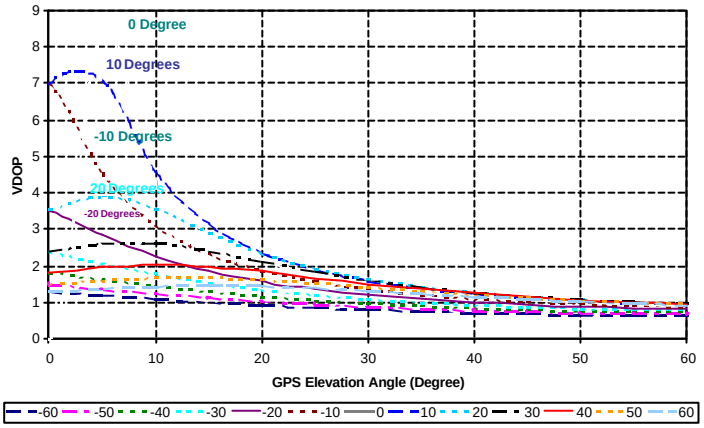

Fig. 6.32. VDOP changes with 7 evenly distributed GPS satellites of 45° azimuth interval between 45°~315° and three pseudolites at azimuths –22.5°, 0°, 22.5° with variable elevation angles –60°~60°

To strengthen satellite sky distribution in the mid and high latitude areas, two scenarios of one pseudolite in the direct north and three pseudolites filled into the empty hole in the north direction with azimuths –22.5°, 0°, 22.5° are simulated. It is found that HDOP could be improved in two cases but the good VDOP values can only be achieved with pseudolite elevation angles less than 20° in the first scenario. Good VDOP values can be obtained by setting three pseudolites with elevation angles higher than 10°. With the simulated GPS satellite sky distributions supplemented with pseudolite(s) in north direction, the above results can only be employed as an general description to the improvement of DOP values.

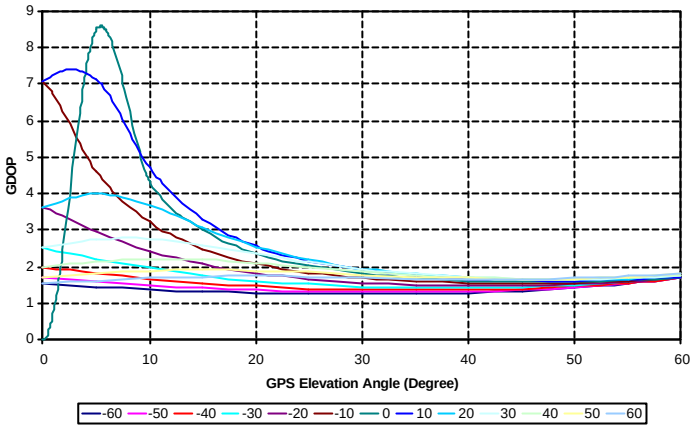

Fig. 6.33. GDOP changes with 7 evenly distributed GPS satellites of 45° azimuth interval between 45°~315° and three pseudolites at azimuths –22.5°, 0°, 22.5° with variable elevation angles –60°~60°

6.4.3 A GPS/Pseudolite Approach Using Modified GPS/Pseudolite Precise Ephemeris

A GNSS simulation tool developed at the IESSG allows synthetic pseudorange, carrier phase and Doppler measurements for any given receiver location to be generated. Using the precise ephemeris for the time at which measurements are to be simulated, the tool calculates the range to each satellite along with the corresponding elevation angle. Errors are then introduced in the ranges to form the simulated measurements. The simulator contains models for the errors associated with the ionosphere, the troposphere, multipath and the satellite and receiver clocks, as well as white noise. Any combination of these models may be selected and the appropriate errors are calculated and included in the simulated measurements. Satellites falling below an elevation mask prescribed by the user are then removed and the remaining measurements are output in the RINEX observation format. The data may then be passed to any standard post-processing tool.

Through modification of the simulation tool it is also possible to demonstrate how the inclusion of additional ranging signals from nearby pseudolites results in an improvement in the position accuracy at this location. The modifications allow the user to specify the (stationary) location of one or more pseudolites along with appropriate identification numbers.

Using the modified simulation tool, data has been generated for the London Millennium Bridge receiver locations using the appropriate GPS satellite constellation and the addition of various numbers of pseudolites.

To obtain precise GPS/pseudolite ephemeris, the locations of the pseudolites have been inserted into original GPS ephemeris. The modified ephemeris is interpolated to the designated data rate (10 Hz in the following examples). For analysing the obtainable accuracy in a local coordinate system, then in BCS, the satellite positions have been projected to the local coordinate system using the observation site as the origin (Fig. 6.34). The azimuths and elevations from the receiver site to each individual satellite then have been calculated by Eq. 6.14 to form a design matrix according to Eq. 6.7. Using the signs of north and east coordinates, the quadrant of the azimuth can be determined. A Matlab script has been developed to calculate azimuth and elevation angles, form G matrix and estimate DOP values. With this script, the DOP values for different configurations analysed in the following paragraphs are estimated and output to a DOP file for further analysis.

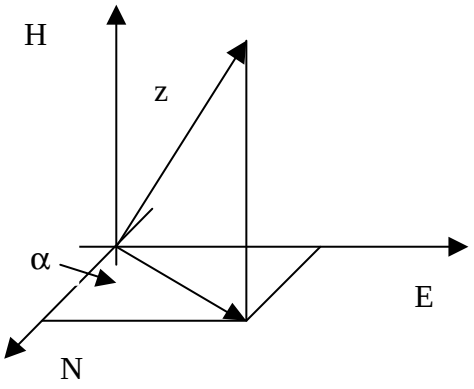

Fig. 6.34. Azimuth and elevation in local coordinate system

$$z = 90 - a\tan(\frac{H}{\sqrt{N^2 + E^2}})$$

if $E \geq 0,\ N > 0,\ \boldsymbol{a} = a\tan(\frac{E}{N})$;

if $E \geq 0,\ N \leq 0,\ \boldsymbol{a} = \boldsymbol{p} - a\tan(\frac{E}{N})$;

if $E \leq 0,\ N \leq 0,\ \boldsymbol{a} = \boldsymbol{p} + a\tan(\frac{E}{N})$;

else if $E \le 0$, $N \ge 0$, $\alpha = 2\pi - a\tan(\frac{E}{N})$. (6.14)

In the following paragraphs, results from seven scenarios are discussed:

1). A single pseudolite located at 100m north of the reference station at a zenith of -57°;

2). GPS only with original ephemeris;

3). A single pseudolite located at 100m north of the reference station at a zenith of 57°;

4). Three pseudolites located at azimuth/zenith angles: -30.46°/75.77°, 0°/57°, 30.46°/75.77°;

5). Three pseudolites located at azimuth/zenith angles: -30.46°/-75.77°, 0°/-57°, 30.46°/-75.77°;

6). Two pseudolites located at azimuth/zenith angles: -30.46°/-75.77°, 30.46°/-75.77°;

7). Two pseudolites located at azimuth/zenith angles: -30.46°/75.77°, 30.46°/75.77°;

In the following paragraphs, pseudolite will be abbreviated as PSV(s) to imitate GPS space vehicle (s). Fig. 6.35 is the comparison of the EDOP under the above scenarios in a local coordinate system with origin at observation site. It can be found that with the inclusion of pseudolite(s) there is no obvious accuracy improvement in the east direction. This is because the current satellite constellation can supply very strong geometry already. Also, there is no general trend in the improvement of the accuracy in each case.

Fig. 6.36 illustrates NDOP changes with different configurations. It can be found that with the configuration 4, the NDOP can be improved to the same level as EDOP and this results in a more uniform error ellipse in the horizontal plane. It shows that it may be possible to raise the longitudinal accuracy to the same level as that of lateral direction in a BCS when the bridge axis is orientated to north. From the graph it can also be concluded that with the pseudolite(s) setup above the horizon of the observation site, the NDOP could be greatly improved. The pseudolite(s) setup below

the horizon of the observation site will not result in significant changes of NDOP values.

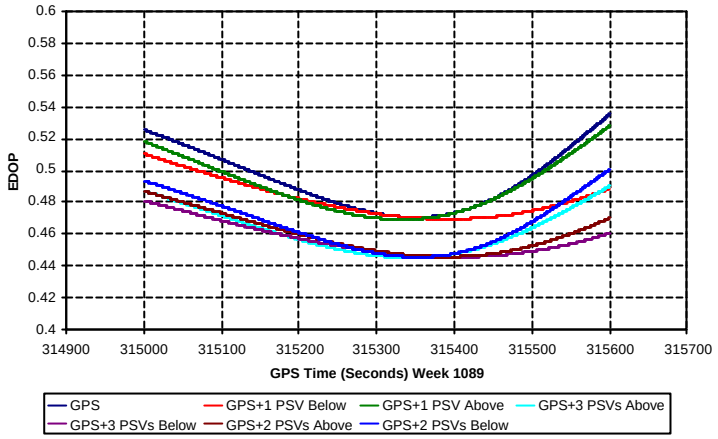

Fig. 6.35. Comparison of East Dilution of Precision (EDOP) in a local coordinate system with modified precise ephemeris on 22 November 2000 at London Millennium Bridge site

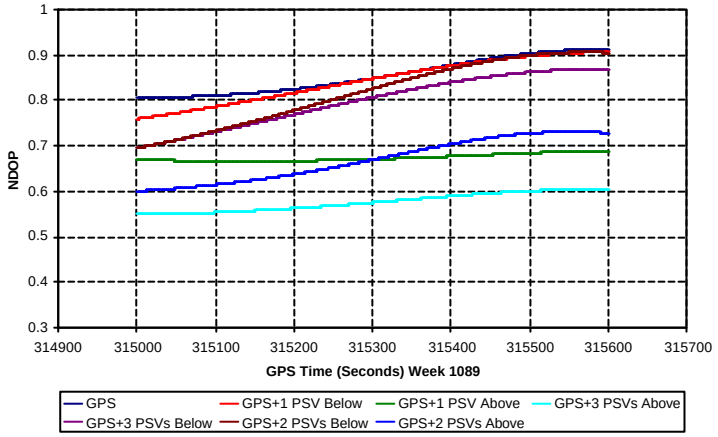

Fig. 6.36. Comparison of North Dilution of Precision (NDOP)

The changes in VDOP under each GPS/pseudolite(s) scenario are depicted by Fig. 6.37. In contrast to NDOP and as a general trend, the vertical accuracy can be greatly improved with either one or three pseudolite(s) below the horizon of the observation site. The pseudolite(s) setup above the horizon of the observation site, which behave like extra GPS satellites, will not induce big improvement for VDOP values.

Again, with pseudolite(s) setup below the horizon, the TDOP can be improved (Fig. 6.38). Similar improvement order as VDOP is obtained for TDOP, i.e., in a increasing order of VDOP values, GPS+3 PSVs (below)<GPS+1 PSV (below)<GPS+2 PSVs (below)<GPS+3 PSVs (above)<GPS+1 PSV (above)< GPS+2 PSVs (above)<GPS only.

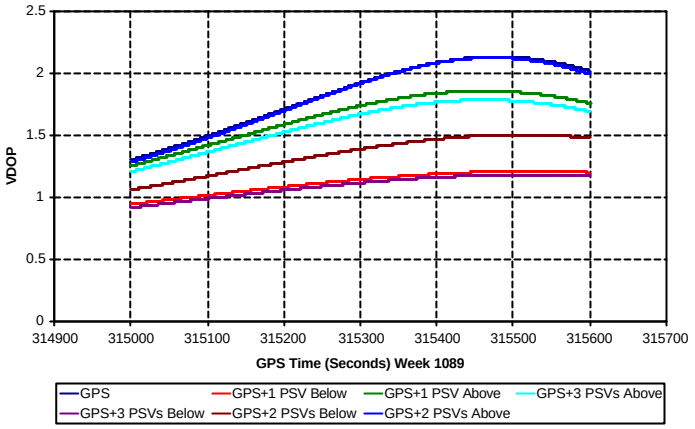

Fig. 6.37. Comparison of Vertical Dilution of Precision (VDOP)

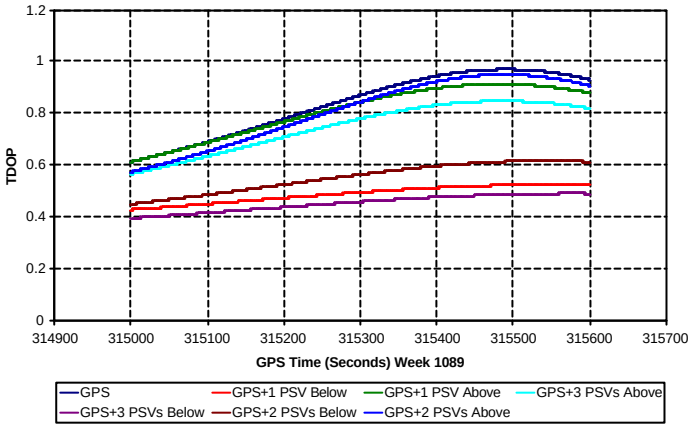

Fig. 6.38. Comparison of Time Dilution of Precision (TDOP)

The HDOP, PDOP and GDOP changes under each GPS/pseudolite sky distribution are illustrated by Fig. 6.39, 6.40, and 6.41. The DOP improvements in seven cases are summarised in Table 6.1 with 1 refers to the best obtainable DOP values and 7 for the potential worst DOP values. The conclusions can be easily made according to this table.

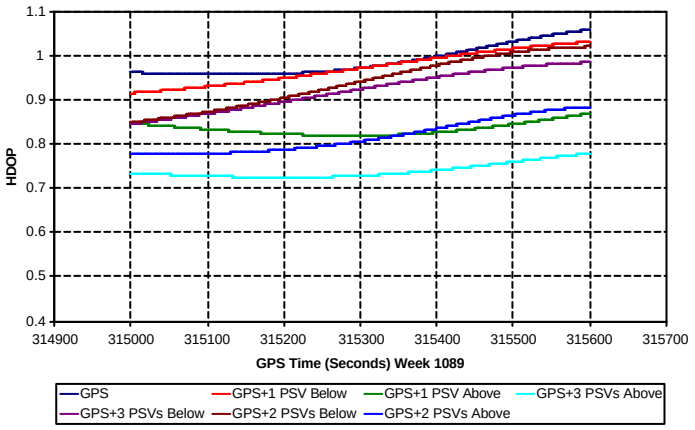

Fig. 6.39. Comparison of Horizontal Dilution of Precision (HDOP)

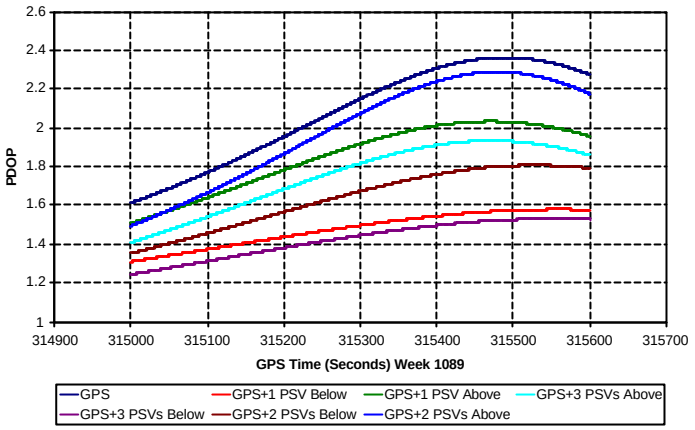

Fig. 6.40. Comparison of Position Dilution of Precision (PDOP)

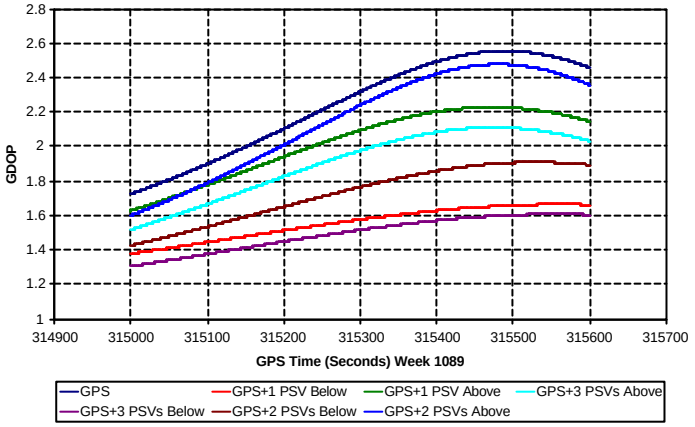

Fig. 6.41. Comparison of Geometric Dilution of Precision (GDOP)

From Table 6.1, certain criteria can be set to purposely improve the DOP values. For instance, if the VDOP is main target of improvement, considering economy and accuracy issues, GPS plus 1 PSV below the horizon of the observation site might be the optimal solution. If improvement of measurements in the north direction is of research importance, the configuration of GPS plus 1 PSV above the horizon of the observation site can be selected. If overall accuracy (GDOP) is required, then the configuration of GPS plus 1 PSV below can selected. Table 6.1 can be used as a general guideline for selecting specific combinations of GPS and PSVs according the purposes and aims of the applications.

	1	2	3	4	5	6	7
EDOP	GPS+3 PSVs below	GPS+2 PSVs above	GPS+3 PSVs above	GPS+2 PSVs below	GPS+1 PSV below	GPS+ 1 PSV above	GPS
NDOP	GPS+3 PSVs above	GPS+2 PSVs above	GPS+ 1 PSV above	GPS+3 PSVs below	GPS+2 PSVs below	GPS+1 PSV below	GPS
VDOP	GPS+3 PSVs below	GPS+1 PSV below	GPS+2 PSVs below	GPS+3 PSVs above	GPS+1 PSV above	GPS+2 PSVs above	GPS
TDOP	GPS+3 PSVs below	GPS+1 PSV below	GPS+2 PSVs below	GPS+3 PSVs above	GPS+1 PSV above	GPS+2 PSVs above	GPS
HDOP	GPS+3 PSVs above	GPS+2 PSVs above	GPS+1 PSV above	GPS+3 PSVs below	GPS+2 PSVs below	GPS+1 PSV below	GPS
PDOP	GPS+3 PSVs below	GPS+1 PSV below	GPS+2 PSVs below	GPS+3 PSVs above	GPS+1 PSV above	GPS+2 PSVs above	GPS
GDOP	GPS+3 PSVs below	GPS+1 PSV below	GPS+2 PSVs below	GPS+3 PSVs above	GPS+1 PSV above	GPS+2 PSVs above	GPS

Table 6.1. DOP values in seven cases investigated in this research (increasing order)

To further investigating the effects of pseudolite location on the improvement of the DOP values, two-pseudolite configurations are simulated with one pseudolite in the north direction and another one on the east or west side. Case 1 presents the scenario 7 in the above paragraphs with two pseudolites situated above the horizon on both sides of the north direction. Case 2 and 3 are used to simulate the circumstance where one pseudolite is on the direct north direction and another on the west with negative and positive elevation angles. Case 4 and 5 present for one pseudolites in the direct north direction and one on the east side with negative and positive elevation angles.

From Fig. 6.42, 6.43, and 6.44, it can be found that there are no differences in DOP values between the pseudolite configurations of different elevation angles, i.e., Case 2 vs. Case 3 and Case 4 vs. Case 5. There are also no obvious differences in DOP values when one pseudolite is setup on the east and west side. No significant accuracy improvements can be achieved with these two-pseudolite configurations.

As an example, the quantified improvements in percentage through the comparison of DOP values of solution 1 (configuration 5, GPS+three PSVs below) in Table 6.1 and those of GPS-alone are illustrated in the following figures. Solution 1 can provide the best GDOP and PDOP values of the seven configurations. It is worth pointing out that the actual locations of pseudolites are limited by the surroundings. Under the scenario of the London Millennium Bridge, two pseudolites can actually be setup on the two

buildings to improve the NDOP values and one pseudolite installed under the bridge can help improve VDOP.

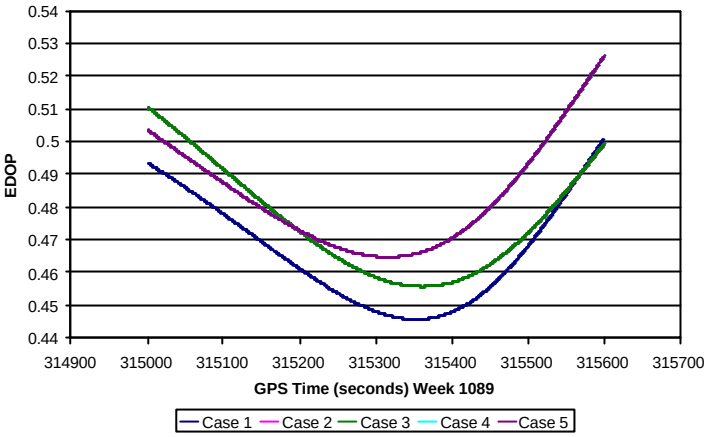

Fig. 6.42. EDOP comparison of two-pseudolite approach

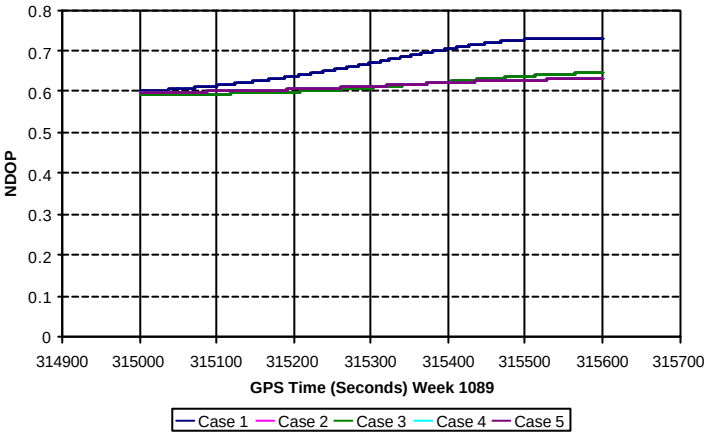

Fig. 6.43. NDOP comparison of two-pseudolite approach

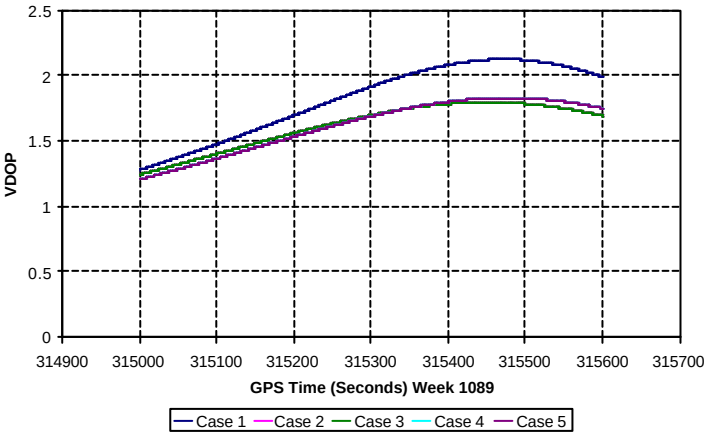

Fig. 6.44. VDOP comparison of two-pseudolite approach

Fig. 6.45 to Fig. 6.50 illustrate the results of these comparisons. With the inclusion of pseudolites into satellite geometry, significant improvement can be achieved on the vertical and time components. Compared with that of GPS only solutions for about 45% improvements can be expected. With only one pseudolite on the north direction there will no significant changes in the accuracy for the east and north components. The improvement for the north component can be realised with the configuration of the three pseudolites on the both sides together with another pseudolite in the north direction. However this configuration will dramatically increase the instrument expense. Fig. 6.51 is the best result for accuracy improvement in the north direction. Over 30% NDOP improvement can be anticipated.

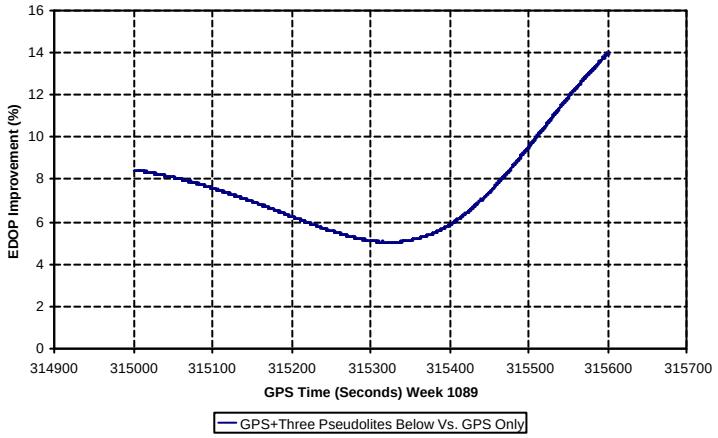

Fig. 6.45. EDOP Improvement in Percentage

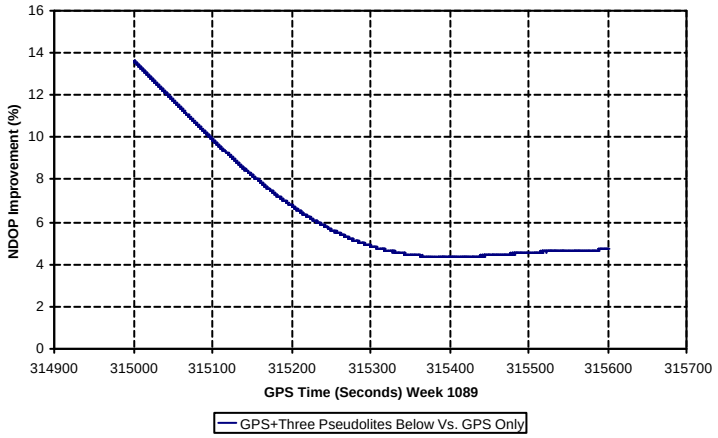

Fig. 6.46. NDOP Improvement in Percentage

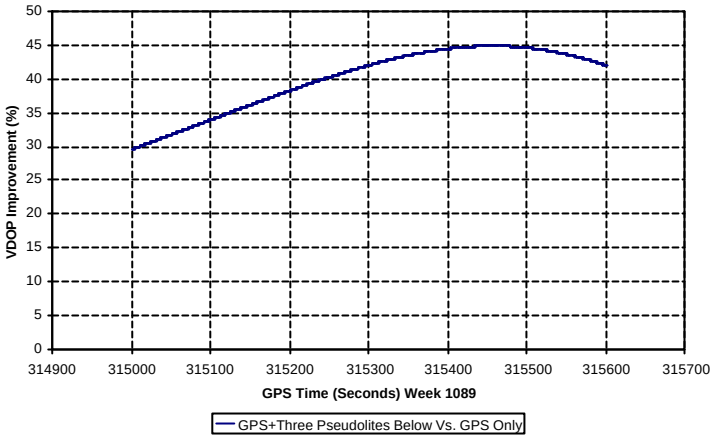

Fig. 6.47. VDOP Improvement Percentage

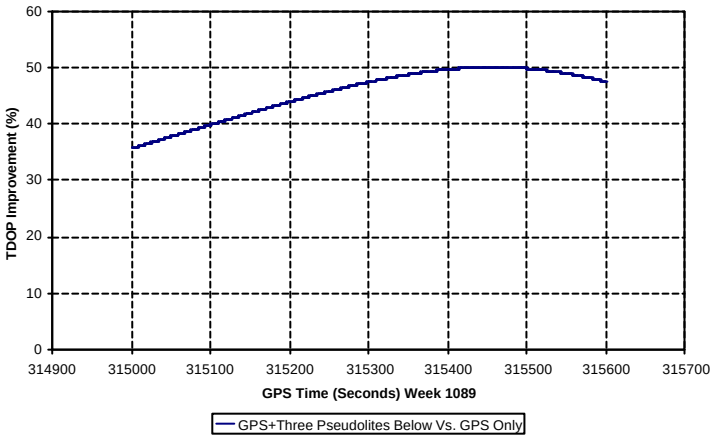

Fig. 6.48. TDOP Improvement Percentage

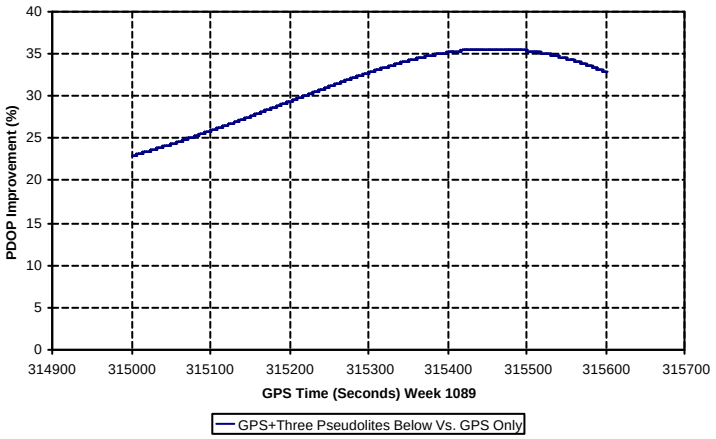

Fig. 6.49. PDOP Improvement Percentage

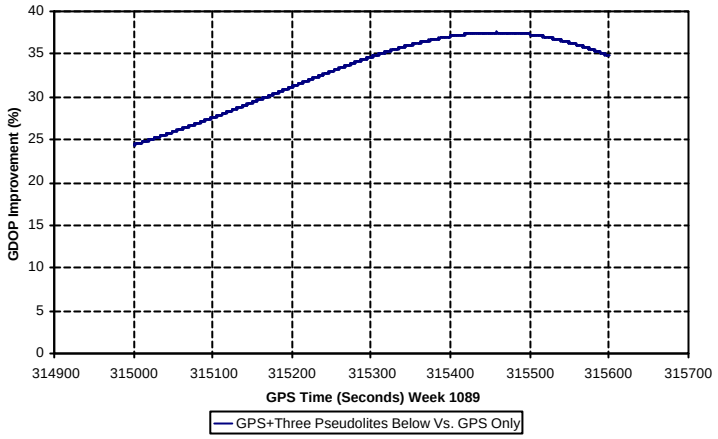

Fig. 6.50. GDOP Improvement Percentage

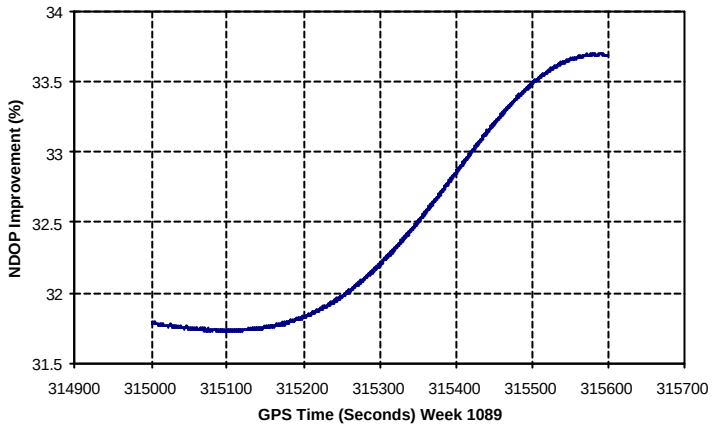

Fig. 6.51. The best obtainable NDOP improvement from a GPS+3 PSVs above

6.5 Summary

An approach for the estimation of DOP values in a BCS has been proposed in this chapter. The error propagation scheme through GPS satellite constellation has been derived to estimate the positioning accuracy from the various ranging errors. With the understanding the defects of the current GPS sky distribution in mid and high latitude areas, three examples of GPS bridge monitoring at different locations in UK have been demonstrated. The results show the significant accuracy degradation in the north direction when a bridge is orientated north. These are the case for London Millennium Bridge and the Humber Bridge, with bridge axis orientation offset from north about 0.9° and 4.17°. Solutions for providing a robust sky distribution for bridge monitoring were proposed using GPS augmented with GLONASS system, GPS/pseudolite system. The effects were simulated with a simulator and an ideal sky distribution,

adverse scenario and modified GPS/pseudolite precise ephemeris. Some guidelines for the selection of optimal pseudolite sites using cost-effectiveness and accuracy as impact factors were illustrated. The achievable improvements in DOP values are calculated using the results from three pseudolite situated below the observation sites with those from GPS receiver sites.

Chapter 7

Adaptive Filtering (AF) and Its Applications in BDMS

7.1 Introduction

As analysed in the previous chapters, the error sources that restrain the accuracy of the GPS positioning solutions under the scenario of a GPS-based BDMS are multipath, receiver random noise, and relative tropospheric delay. The time series of real structural deformations are highly polluted by these noises. Without proper treatments either on the original measurements or on the positioning solutions, it is impossible to conduct any further structural deformation analysis. This emphasises the research importance of GPS error modelling or mitigation techniques.

In this chapter, the fundamentals of AF are introduced in Section 7.2. The difference between AF and moving average (MA) filtering techniques in the data processing is discussed. Whilst MA can be used to mitigate multipath at reference stations, it is very difficult to isolate the components of the time series at monitoring sites which consist of actual bridge movement signature and various error sources. A real-time AF algorithm is proposed in Section 7.3, which can be employed to output cleaned signal on the each epoch basis. Simulation technique is applied to analyse the performance of an AF filter. According to filter theory and the analysis to the GPS signal frequency bands, the autocorrelation time lags of the positioning solutions calculated from zero baseline (ZBL) and short baseline (SBL) tests are recommended to determine the filter length of an optimal filter and this filter can effectively isolate multipath from other signals. Data fusion using discrete Fourier transform (DFT), inverse DFT (IDFT), and AF approach is introduced in Section 7.4. A software flowchart and associated software package developed by Visual C++ programming with functionalities of outlier filtering, data fusion, and data analysis are detailed in this section. Data collected from a controlled platform test, which is illustrated in

Section 5.2, is used as an example of data fusion to verify the feasibility of the proposed approach.

7.2 Fundamentals of Adaptive Filtering

Generally, digital signal processing (DSP) begins with a signal that appears to the computer as a sequence of digital values. From systems-engineering point of view, there are three basic components in any simple DSP, i.e. an input sequence $x(n)$, an operator $D\{\}$, and an output sequence $y(n)$, which form either a close loop or an open system, according to whether there is feedback information. Their general relationship can be expressed as follows (Dodson et al. 2001):

$$y(n) = D\{x(n)\}. \tag{7.1}$$

An equivalent of Eq. 7.1 can be expressed as

$$y(n) = \sum_{q=0}^{Q-1} b_q x(n-q) + \sum_{p=1}^{P-1} a_p y(n-p). \tag{7.2}$$

Where coefficients b_q and a_p are used to define the linear operators $D\{\}$ and $D\{\}$ can be thought of as digital filters with filter lengths P and Q respectively.

There are two generalised classes of digital filters that can be used to process bridge deflection time series depending on the values of coefficients b_q and a_p. The first one is a finite-duration impulse response (FIR) digital filter which has a_p ($p = 1, 2, ..., P-1$) equal to 0. In this case, the previously determined signal outputs will have no impact on the estimates of following outputs. Thus, Eq. 7.2 can be rewritten as

$$y(n) = \sum_{q=0}^{Q-1} b_q x(n-q). \tag{7.3}$$

Since the output is simply a weighted average of the input values, these filters are also called MA filters. Due to their simplicity and stability, these kinds of filters are widely used in signal noise compression and system model identification (Ingle and Proakis 1997).

The second class of digital filters is Infinite Impulse Response (IIR) filters in the form of Eq. 7.4, when all the parameter b_q from $q=1$ to $Q-1$ are set to zeros, in a more general form of Eq. 7.2.

$$y(n) = x(n) - \sum_{p=1}^{P-1} a_p y(n-p)\,. \tag{7.4}$$

From Eq. 7.4, it can be seen that the previously determined outputs will have impact on the estimates of following outputs together with the new input signals.

Compared with a FIR filter, stability, roundoff noise, and sometimes phase nonlinearity could be problematic when using IIR filter. Therefore, much more effort is required in the design and implementation of an IIR filter. Even though IIR filters have their advantage in computational efficiency, the use of modern high-speed processors means that this is no longer as much of a reason for implementing IIR over FIR.

There are two kinds of FIR filters according to the status of filter coefficients b_q, i.e. time-invariant linear FIR filter and adaptive FIR filter.

A time-invariant linear filter with the sum of filter coefficients b_q equal to one is used to convert one time series into another through a linear operation (Chatfield 1984). The applications of MA technique include the analysis of long-term movement or evolution trend of a process. The residuals between the smoothed outputs from an MA filter and the original signal sequence represent the local fluctuations. An MA filter is not an optimal filter since the coefficients are not optimally determined. It cannot adjust its filter coefficients according to the changes of the noise levels of input and output signals. Furthermore, there are difficulties in choosing appropriate filter coefficients or MA window length since the signal frequencies are also the unknown parameters. However, if the signal frequency band is known and maintains a constant status, the MA approach can be effectively employed to separate different signals.

Fig. 7.1 to Fig. 7.6 are the mean positioning solutions using the MA approach at different stations. The data were collected from Wilford footbridge on 20, 21, and 22

February 2001. The details of this trial are described in Section 5.3.4. A ten-second MA filter length is chosen in the data processing. Further explanation of how to choose appropriate filter length can be found in Section 3 of this chapter.

Of these six graphs, Fig. 7.1, 7.2 and 7.3 are used to investigate the multipath level at the reference stations near the bridge using the MA results of the time shifted positioning solutions of two consecutive days. Since the relative tropospheric delay can be assumed to be the same at two stations for this short baseline of 6.3m and due to the first natural frequency of this bridge is higher than 1 Hz with the initial FEM developed by the Cranfield University (Meo et al. 2002), the MA results can represent the impact of multipath at these reference stations. The three graphs show high level multipath signature in the three directions of a BCS using day-to-day positioning solutions. The vertical multipath of centimetre amplitude has the worst effect on the positioning solutions from the reference stations.

The multipath signatures at five sites are further studied using Base1 as the reference station and the other four as rovers. The same MA filter length is used. Through the comparison of each multipath time series, it can be concluded that multipath at each site is mainly introduced by the reference station. While it exhibits a similar pattern as those at other stations, multipath at Mid2 shows a little higher amplitude, which illustrates the tightly observation site relevant characteristic of multipath even though the distance between Mid1 and Mid2 is about 3.5 metres.

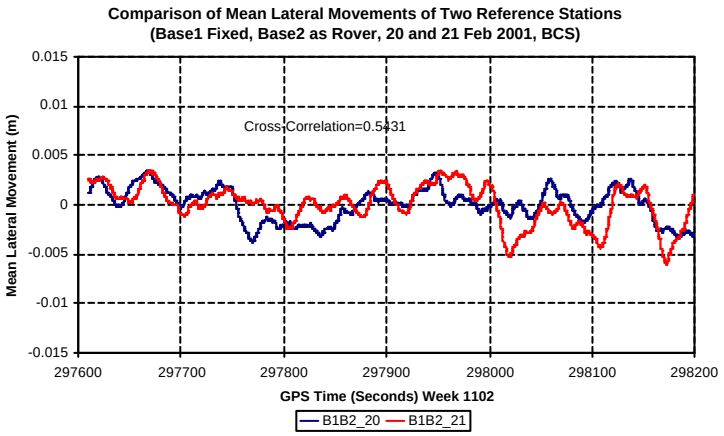

Fig. 7.1. Lateral multipath at reference stations by MA

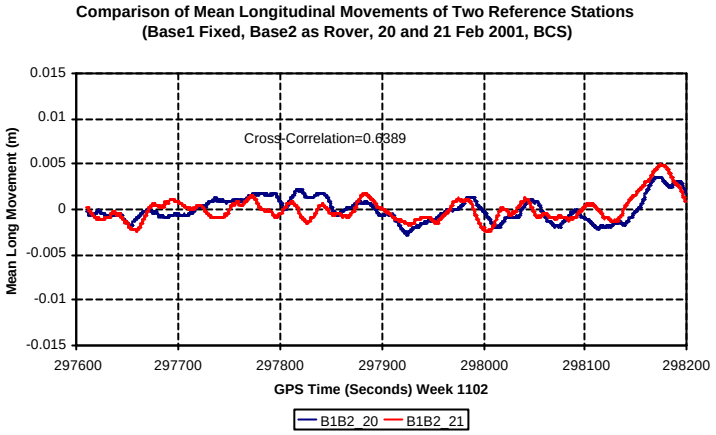

Fig. 7.2. Longitudinal multipath at reference stations by MA

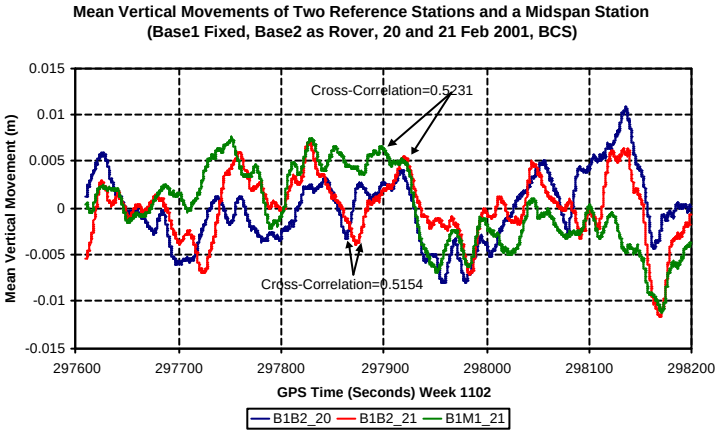

Fig. 7.3. Vertical multipath at reference stations by MA

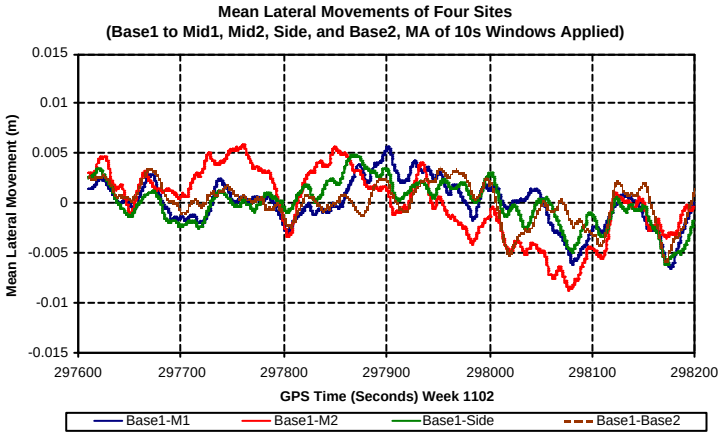

Fig. 7.4. Lateral multipath at four observation sites by MA

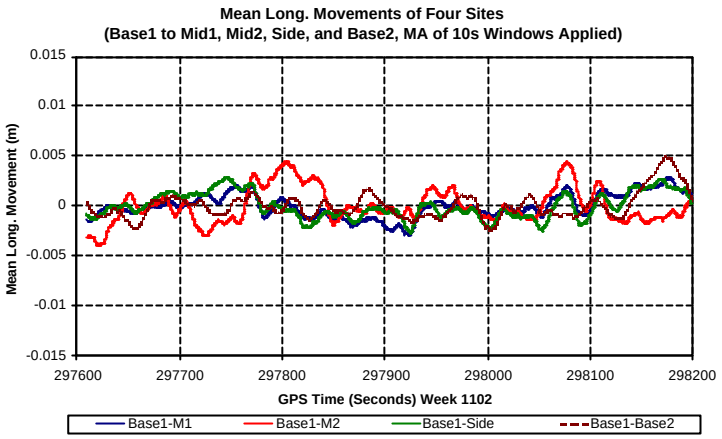

Fig. 7.5. Longitudinal multipath at four observation sites by MA

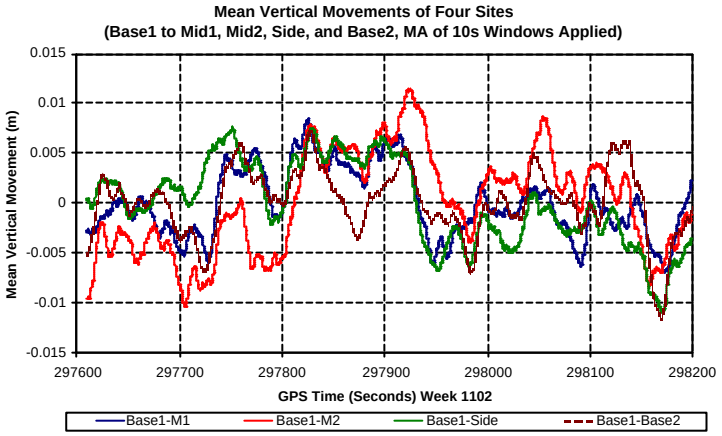

Fig. 7.6. Vertical multipath at four observation sites by MA

MA with constant filter coefficients could be effectively employed to isolate signal with known frequency bands. Even though the multipath at the three bridge sites show the similar patterns, the components of the MA residuals are different for different observation sites. With MA applied to the original positioning solutions, the high frequency components of the time series, which consists of real bridge movements, have been filtered out with receiver noise. It is obvious that a pure MA approach could not satisfy the isolation of noise and real bridge movement. Alternative approached must be investigated.

In contrast, an adaptive FIR filter is an optimal interference canceler. The difference between time-invariant filtering and adaptive filtering of a discrete-time noisy signal is that the signal systems being dealt with in the latter vary with time. Furthermore, AF attempts to adjust to an optimal filter in **real-time** mode, according to the time

varying input and output signals (Roberts et al. 2001b). By using cross-correlation characteristics of two time series to isolate individual components from the common part, and with its base on the solid statistic foundation, the AF approach is a more reliable signal isolation tool. It can be employed flexibly to any kind of time series pairs with potential cross-correlation. It is especially applicable to time series with unknown low and high frequencies contaminated by similar frequency band noises.

According to these benefits of an AF system, adaptive FIR filtering will be adopted in this research due to their implementation simplicity and filter optimisation. As discussed hereafter they are applied to mitigate the random noise of GPS receivers and multipath, both at reference stations and bridge sites to obtain the real bridge movement from the measured coordinate time series. Also, the AF approach is used to suppress the noise of each individual sensor when accelerations are available. The AF approach can also help clean pseudoranges. In Chapter 9, AF approach is proposed to mitigate the effects of relative tropospheric delay.

Determination of optimal linear filters is the kernel of a DSP system. Adaptive filters and adaptive systems attempt to find the optimal set of filter parameters (often by approximating the Wiener optimum filter) based on the time varying input and output signals using the Least Mean Square (LMS) algorithm (Embree 1995). More detailed AF derivation is explained by Haykin (1996).

Fig. 7.7 is a simple schematic of an adaptive system that consists of an FIR filter (processor) and an adaptive algorithm. $\{d(n)\}$ is the application provided input signals or desired sequence. It can be the real measurement time series for a specific process that can be compared to the FIR filter predicted output sequence $\{y(n)\}$. $\{x(n)\}$ is a reference signal sequence.

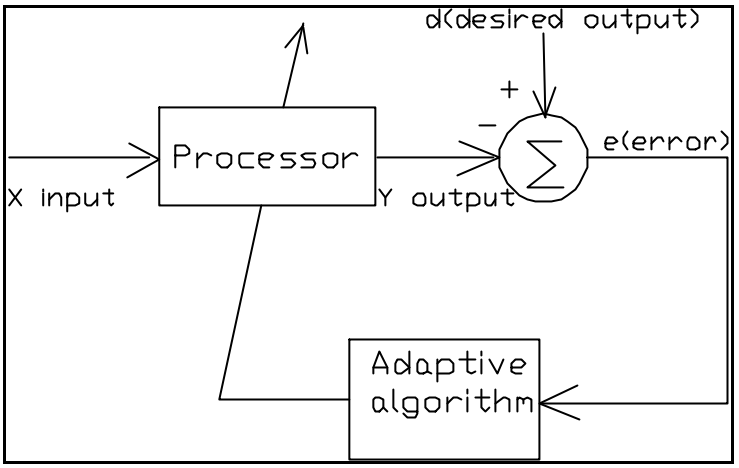

Fig. 7.7. A schematic of closed-loop adaptive FIR filter (Embree 1995)

Suppose there is an FIR filter with adjustable coefficients $\{b(k),\ 0 \le k \le N-1\}$. N denotes the length of the FIR filter. Let $\{x(n)\}$ denotes the input sequence to the filter with sample number $M+1$, and let the corresponding output be $\{y(n)\}$, which can be predicted by Eq. 7.5,

$$y(n) = \sum_{k=0}^{N-1} b(k)x(n-k) \qquad n = 0, ..., M\ . \tag{7.5}$$

Suppose that the desired sequence or real measurement time series for a specific process is $\{d(n)\}$. It can be compared with the FIR filter output $y(n)$. Then the error sequence $\{e(n)\}$ can be formed by taking the difference between $d(n)$ and $y(n)$ at each epoch (Eq. 7.6).

$$e(n) = d(n) - y(n) \qquad n = 0, ..., M\ . \tag{7.6}$$

The optimal coefficients of the FIR filter can then be selected by Eq. 7.7 to minimise the sum of squared error vector $e(n)$.

$$\begin{aligned} \Psi &= \sum_{n=0}^{M} e^2(n) = \sum_{n=0}^{M}\left[d(n) - \sum_{k=0}^{N-1} b(k)x(n-k)\right]^2 \\ &= \sum_{n=0}^{M} d^2(n) - 2\sum_{k=0}^{N-1} b(k)r_{dx}(k) + \sum_{k=0}^{N-1}\sum_{l=0}^{N-1} b(k)b(l)r_{xx}(k-l). \end{aligned} \tag{7.7}$$

Where $\{r_{dx}(k)\}$ is the cross-correlation between the desired input sequence $\{d(n)\}$ and reference sequence $\{x(n)\}$ of the filter, and $\{r_{xx}(k)\}$ is the autocorrelation of the input sequence $\{x(n)\}$.

The sum of squared error Ψ is a quadratic function of the FIR filter coefficients. Consequently, the minimisation of Ψ with respect to the filter coefficients $\{b(k)\}$ results in a set of linear equations (Eq. 7.8 and 7.9). Hence through

$$\frac{\partial \Psi}{\partial b(m)} = 0, \quad 0 \le m \le N-1 \tag{7.8}$$

we have

$$\sum_{k=0}^{N-1} b(k) r_{xx}(k-m) = r_{dx}(m), \quad 0 \le m \le N-1. \tag{7.9}$$

To solve the above linear equations we need to first calculate the autocorrelation sequence and the cross-correlation sequence. Using LMS algorithm we can determine the optimal filter coefficients without explicitly computing the correlation sequences. The algorithm is basically a recursive gradient (steepest-descent) method that finds the minimum of Ψ and thus yields a set of optimum filter coefficients (Ingle and Proakis 1997).

In the actual calculation, it is possible to start with arbitrary initial filter parameters $\{b(k)\}$. Then after each new input sample $x(n)$ enters the adaptive filter, the corresponding output or filter prediction $y(n)$ is calculated and then compared with $d(n)$. The error signal $e(n) = d(n) - y(n)$ is estimated, and used to update the filter coefficients based on the method of steepest descent (Haykin 1996) by Eq. 7.10.

$$\vec{B}_{n+1} = \vec{B}_n + 2\mu e(n)\vec{X}_n . \tag{7.10}$$

Or

$$b_{n+1}(k) = b_n(k) + 2\mu e(n) x_n(n-k). \; 0 \le k \le N-1, \; n = 0, 1, ..., M . \tag{7.11}$$

Where $\vec{B}_n$ is the filter coefficient vector at the n-th step. μ is a parameter that controls the rate of convergence, or convergence parameter of LMS. $\vec{X}_n$ is the input signal vector. This is the recursive algorithm for adjusting the filter coefficients adaptively so as to minimise the sum of the squared error $e(n)$. When LMS is used for selecting optimal coefficients of digital filters, care should be paid on the selection

of the convergence parameter m. If it is too small the coefficient vector will adapt very slowly and may not react to changes in the input signals. Large m will make the algorithm unstable and the system will adapt to noise in the signals and may never converge to the optimal solution with minimum mean squared error (MMSE). In practice, a reasonable value for m is between 0.01 and 0.1 (Embree 1995).

To ensure the stability of an AF algorithm m must be chosen to be in the range according to (Ingle and Proakis 1997) (Eq. 7.12)

$$0 < m < \frac{1}{20NP_x} \tag{7.12}$$

where N is the length of the adaptive FIR filter and P_x is the power of the input signal, which can be estimated by Eq. 7.13,

$$P_x \approx \frac{1}{1+M}\sum_{n=0}^{M} x^2(n) = \frac{r_{xx}(0)}{M+1}. \tag{7.13}$$

$r_{xx}(0)$ is the autocorrelation of the reference signal sequence $\{x(n)\}$ with time lag of zero. In AF application, upper limit of Eq. 7.12 is employed as the convergence parameter m according to the convergence process by using actual bridge deformation data.

7.3 A Real-time Matlab AF Software Package

Using the above algorithm and an M-programming technique (Mathworks 2000), a real-time adaptive filtering script was developed. It can employed as a simulator to investigate the performance of an AF filter, such as the overall efficiency of the designed filter length, convergence parameter, and to finely tune the AF filter. The package consists of two parts. One is the main script M-file, which calls a function M-file. The function M-file is used to realise the LMS algorithm. The outputs are the filter coefficient time series at each epoch to monitor the convergence of the AF procedure, and the correlated and uncorrelated time series of desired and reference signal sequences.

Fig. 7.8 illustrates the realisation procedure of a real-time AF algorithm. With the input of each individual reference signal x_n, a new local reference vector $\overline{X}_n$ with length equal to N is regrouped through pushing the previous input x_{n-1} forward by one position. A new signal prediction $y(n)$ is then made using the previously calculated filter parameter vector $\overline{B}_n$ and reference signal vector $\overline{X}_n$. $y(n)$ is compared with a new desired signal input $d(n)$ to output residual $e(n)$. The LMS algorithm is used to estimate an updated optimal filter parameter vector $\overline{B}_{n+1}$. This procedure is continued until no more signals are input into the AF system.

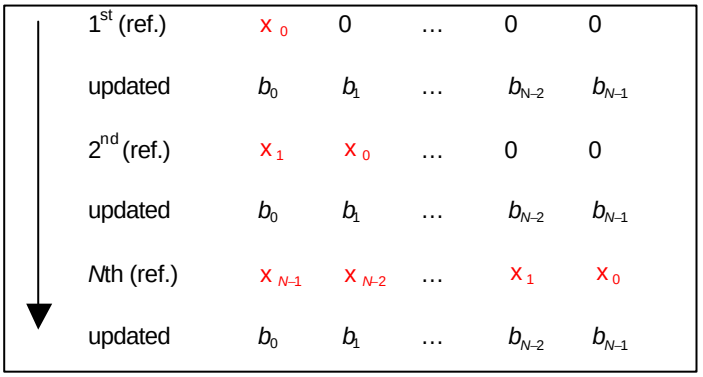

Fig. 7.8. A real-time AF procedure

In specific applications of an adaptive FIR filtering, the desired signal $d(n)$ could be subdivided as signal S and random noise R, and the input sequence $x(n)$ as S' and R'. There is certain degree of correlation between signal parts S and S', and there is no correlation between R and R' or S', or R' and S. To verify the relationship between $d(n)$ and $x(n)$ or S with S' and R with R', simulation calculations are conducted using cosine functions and white noise generators with the developed Matlab package. The summary from the simulation tests is listed in Table 7.1.

Desired Signal $d(n)$ Input Signal $x(n)$	R, R' uncorrelated S, S' correlated (Case 1)	R, R' correlated S, S' uncorrelated (Case 2)
Error Sequence (e)	R	S
Common part (y)	S	R

Table 7.1. Relationship between desired and reference signal sequences

Using these characteristics, certain signal isolation and error suppression techniques can be further designed. For instance, when S and S' are correlated signals, and R and R' are uncorrelated random noise (white noise, Case 1), the signal output will be an estimate of S, the correlated part of $d(n)$ and $x(n)$, and the error sequence will be an estimate of R, the part of $d(n)$, not correlated with any part of $x(n)$. By exchanging the order of $d(n)$ and $x(n)$, the same common part can be obtained from the AF filter. The error sequence is R' which does not correlate to any part of $d(n)$.

These values can be further applied to verify the effectiveness and correctness of an AF filter. The relationship between signal inputs and outputs expressed by their autocorrelation and cross-correlation parameters can be summarised in Eq. 7.14 in Case 1.

$$\begin{aligned} E[S_n S'_{n-j}] &= P_j \quad \forall j,\ n \\ E[S_n R_{n-j}] &= 0 \quad \forall j,\ n \\ E[S_n R'_{n-j}] &= 0 \quad \forall j,\ n \\ E[R_n R'_{n-j}] &= 0 \quad \forall j,\ n \end{aligned} \tag{7.14}$$

where P_j is the cross-correlation function of the correlated signals.

Based on the above discussion, an AF simulator using cosine functions is used to investigate the performance of an AF approach and validate the developed real-time AF algorithm. Simulation 1 uses the following expressions as desired and reference signal generators (Eq. 7.15).

$$\begin{aligned} \mathrm{d} &= 25\cos(\mathrm{n} \cdot \mathrm{pi}/10 + 2 \cdot \mathrm{pi}) + 10\cos(\mathrm{n} \cdot \mathrm{pi}/3) \\ \mathrm{x} &= 25\cos(\mathrm{n} \cdot \mathrm{pi}/10 + 1.0) + 2\cos(\mathrm{n} \cdot \mathrm{pi}/5). \end{aligned} \tag{7.15}$$

In Eq. 7.15, the first parts of d and x are correlated cosine functions, and the second parts are uncorrelated. Fig. 7.9 illustrates the results using signal sequences generated by Eq. 7.15. The first and second rows are the desired d and reference x signals respectively. The third and forth rows are uncorrelated and correlated signal sequences of desired d and reference x signals. To show the efficiency of the AF algorithm, the original uncorrelated part (red) is compared with the isolated uncorrelated sequence (blue), which illustrated in the third row. Except for the difference at the beginning period of AF convergence, similar results demonstrate the

successful signal isolation. The cross-correlation coefficients are 0.50, 0.38, 0.91, 0.02, 0.53, and –0.03 for (d, x), (d, R), (d, S), (x, R), (x, S), and (R, S), respectively.

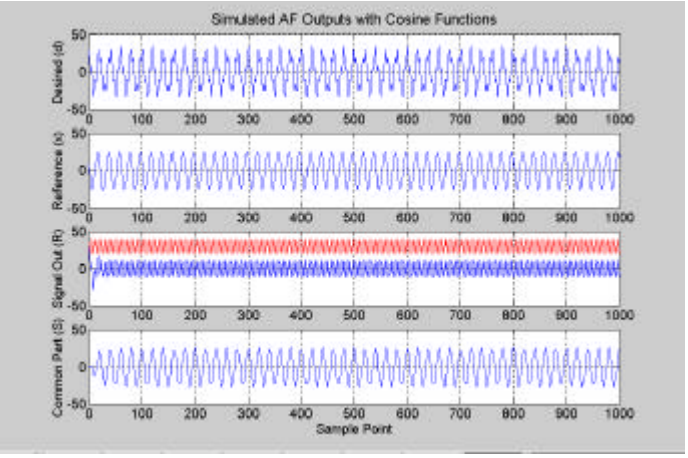

Fig. 7.9. Simulation of AF algorithm (forward)

By exchanging the order of $d(n)$ and $x(n)$ in the simulator (backward), the same correlated part is isolated by the AF filter. The uncorrelated signal sequence is only relevant to the desired signal sequence, which is the second cosine function of the desired signal sequence in Eq. 7.16 and is represented by the red coloured time series of the third row in Fig. 7.10.

$$\begin{aligned} \mathrm{d} &= 25\cos(\mathrm{n}\cdot \mathrm{pi}/10 + 1.0) + 2\cos(\mathrm{n}\cdot \mathrm{pi}/5) \\ \mathrm{x} &= 25\cos(\mathrm{n}\cdot \mathrm{pi}/10 + 2\cdot \mathrm{pi}) + 10\cos(\mathrm{n}\cdot \mathrm{pi}/3). \end{aligned} \tag{7.16}$$

The cross-correlation coefficients are calculated to check the efficiency of the AF filter. Calculated coefficients for the sequence pairs of (d, x), (d, R), (d, S), (x, R), (x, S), and (R, S) are 0.50, 0.17, 0.99, 0.05, 0.50, and 0,03 respectively. Of these cross-correlation coefficients, the theoretical value of (R, S) should be zero, which forms the most important index of the isolation efficiency of the AF procedure.

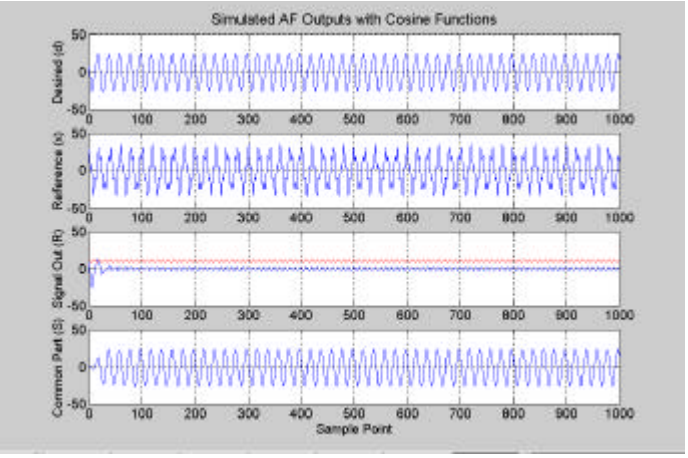

Fig. 7.10. Simulation of AF algorithm (backward)

Fig. 7.11 shows the convergence process of the filter coefficients. In this simulation, the filter length is selected as 10. It can be found that the filter coefficients start to converge when the 10th sample enters into the AF system. It demonstrates good performance of the designed real-time AF.

Through the above analysis and discussion, the ability of an AF system to separate noise from a real signal and a data 'cleaning' process are illustrated, which can be employed to process the positioning solutions from a GPS-based BDMS. For instance, in Case 1, when two adjacent GPS receivers are setup closely on the bridge deck, the GPS receivers can sense the same vibration of bridge deck (the correlated part) but their individual receiver random noises are uncorrelated if the multipath at each site has been mitigated properly. Furthermore, through AF procedure, two adjacently setup reference stations near the monitored structure could help reduce inherent receiver random noise and multipath at the reference sites. Tropospheric effects can be dramatically reduced as well when there are significant height differences or big difference in local microclimate between monitoring stations and reference stations. Also, through the appropriate antenna arrangement, using adaptive filtering, the accuracy of a relatively low cost antenna can be improved, perhaps to the same accuracy as a chokering antenna. This is demonstrated in Section 8.3.2.

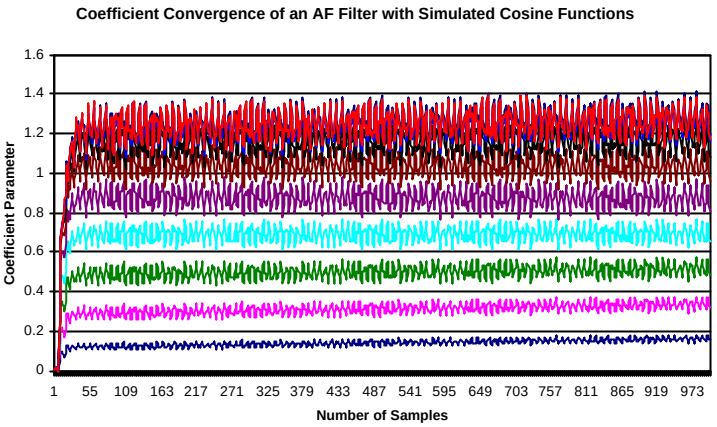

Fig. 7.11. Convergence of an AF process

The determination of the filter length N is another important parameter, which governs the performance of an AF system together with the convergence constant. To choose an appropriate AF filter length really requires considerable experience plus the knowledge of the frequency aspects of the time series analysed. As the name suggests, filters are usually designed to produce an output with emphasis on variation at particular frequencies. So, the determination of an AF filter length is actually application oriented.

Haykin (1996) proposed an approach for the filter length estimation based on the minimum description length (MDL) criteria. It is defined by Eq. 7.17,

$$MDL(N) = -L(\hat{\boldsymbol{q}}_N) + N \ln M / 2 . \qquad (7.17)$$

Where $L(\hat{\boldsymbol{q}}_N)$ is the logarithm of the maximum likelihood estimates of the filter parameters. $L(\hat{\boldsymbol{q}}_N)$ tends to decrease rapidly with the increasing of filter length N while the second term increases linearly with the increasing of N. There is a value of N, which could minimise MDL, representing the optimal filter length (Ge et al. 2000a).

The maximum likelihood method for selecting filter length has its limitation since it requires the knowledge of the distribution function of the random variable in question (Mikhail 1976). It is difficult to determine the distribution function of the samples entered into an AF system since most of the samples dealt with are highly

contaminated by various systematic errors. To estimate the filter parameters of an AF system in this way means solving group functions with dimension N at each epoch when a new sample enters the system. In summary, the proposed approach for estimating an optimal filter length is not feasible for the AF approach used in a BDMS. A practical alternative should be employed.

An adaptive FIR system actually is an MA system with adjustable filter coefficients. It is well known to obtain smoothed values the local fluctuations with high frequency variation should be removed, which refers to the application of a low pass filter. In contrast, if the residuals calculated by the difference of the smoothed time series with the original sequence are of research interest, a high pass filter will be employed.

Fig. 7.12 (Fig. 3.37 in Chapter 3) and Fig. 7.13 (enlarged left part of Fig. 3.66 in Chapter 3) illustrate two autocorrelation results of SR530 ZBL and SBL tests. It can be seen that the frequencies of SR530 receiver noise are higher than 1 Hz. Hence, 10 samples or more could be selected in an AF filter for SR530 receiver to isolate receiver noise and other error source according to their frequency bands. Since the positioning relationship cease after 10 samples (Fig. 7.12), which stands for 1-second period of data in this example, any other autocorrelation should be introduced by other error sources such as multipath, as illustrated by Fig. 7.12. SBL tests of SR530 receivers show the same results of autocorrelation introduced by receiver noise but also a long time autocorrelation of the positioning solutions caused by multipath. So, it is possible to decompose multipath from the receiver noise characterising the high frequency signature by selecting a filter length of 10 samples or more for an AF filter. In the following AF applications, 20 samples are selected as the filter length to assure the separatibilty of receiver noise from other signals with low frequency signatures.

Whilst above filter length could be successfully employed to separate receiver noise from multipath and other time series with low frequency signatures, however, it will be impossible to isolate the real bridge movement of high frequency (>1 Hz) variation from the receiver noise distributed in the same frequency band. When an AF filter with the selected filter length is applied to the positioning solutions in a BDMS, multipath could be separated from the high frequency time series of the mixture of receiver noise and bridge movements. Other approaches should be developed to

further isolate receiver noise from real bridge movements. This is discussed in Chapter 8.

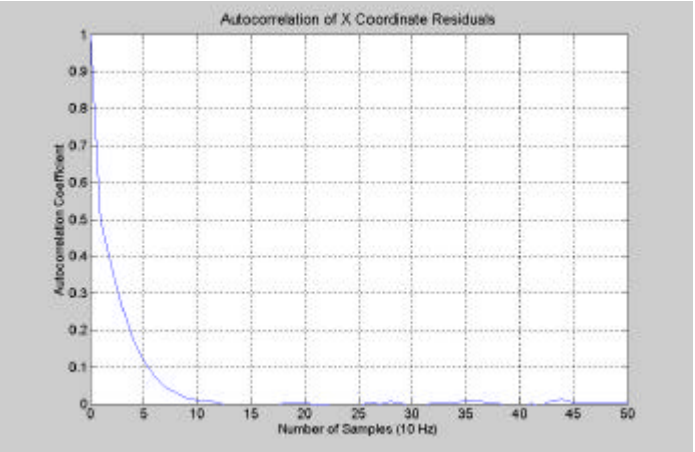

Fig. 7.12. Autocorrelation of a ZBL test (Fig. 3.37 of SR530 receivers)

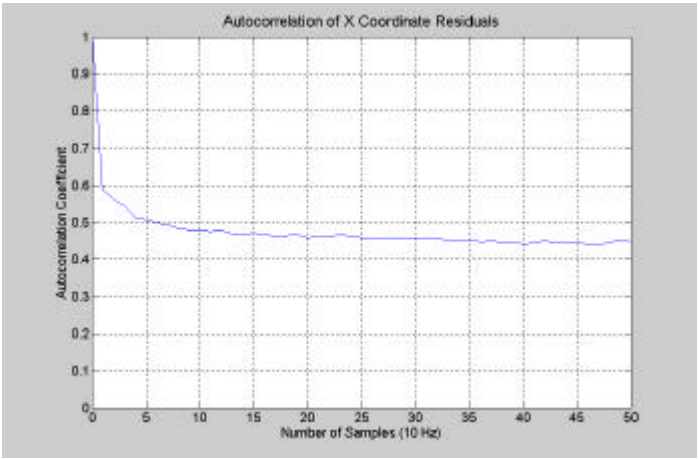

Fig. 7.13. Enlarged left part of Fig. 3.66 (SBL test, SR530 receivers)

7.4 Data Fusion Using Discrete Fourier Transform (DFT), Inverse DFT, and AF Approach

Like other time series the data from GPS receivers and accelerometers could be treated as time sequences from digital signal processing (DSP) point of view. Most DSP operations can be categorized as being either signal analysis or signal filtering (Ingle and Proakis 1997). In signal analysis, the focus is on the frequency-domain operations with the applications in spectral analysis, target detection, and speech recognition. Signal filtering is characterized by the *signal in-signal out* situation,

which uses various filters to remove unwanted background noise, conduct frequency band analysis, and shape the signal spectrum. Signal filtering is usually a time-domain operation.

It is obvious that in GPS and accelerometer signal processing, both frequency-domain and time-domain approaches are required. In this research, frequency-domain spectral approaches are used to identify the distribution of frequencies from the required bridge vibrations and unwanted noises from both sensors. The frequencies detected from the data sets collected at same time by both sensors are compared to confirm the real bridge vibration characteristics and the noise of the each individual sensor could be separated as well from this procedure.

The aim of spectral analysis on the measurements is to clean the data sets. This is realized by digital filters. Three types of filters of low pass, high pass, or band pass characteristics are widely used in the data processing of time-domain sequences.

A software package was developed to conduct spectral analysis, filtering and data fusion of GPS and accelerometer based on DFT and inverse DFT (IDFT) approaches and Eq. 7.18 to Eq. 7.26. Eq. 7.18 and 7.19 are the expressions of Fourier and inverse Fourier transforms (Feng 1978). N is the length of the measurement sequence u. U is the following equations is the Fourier transform of measurement sequence u.

$$U_k = \sum_{j=0}^{N-1} u_j \cos(2\pi jk/N) - i\sum_{j=0}^{N-1} u_j \sin(2\pi jk/N) \tag{7.18}$$

$$u_j = \frac{1}{N}\sum_{k=0}^{N-1} U_k \cos(2\pi jk/N) + i\frac{1}{N}\sum_{k=0}^{N-1} U_k \sin(2\pi jk/N) = \frac{1}{N}(U_j^r + iU_j^c). \tag{7.19}$$

Let

$$u_k^r = \sum_{j=0}^{N-1} u_j \cos(2\pi jk/N) \quad k = 0, ..., N-1 \tag{7.20}$$

$$u_k^c = \sum_{j=0}^{N-1} u_k \sin(2\pi jk/N) \quad k = 0, ..., N-1. \tag{7.21}$$

Then

$$U_k = u_k^r - iu_k^c,\ k = 0, ..., N-1 \tag{7.22}$$

$$u_j = \frac{1}{N}(U_j^r + iU_j^c) = \frac{1}{N}(u_j^{rc} + u_j^{cs}) + i\frac{1}{N}(-u_j^{cc} + u_j^{rs}) \quad j = 0, ..., N-1. \tag{7.23}$$

Where

$$\begin{aligned} u_j^{rc} &= \sum_{k=0}^{N-1} u_k^r \cos(2\pi jk/N) \\ u_j^{cs} &= \sum_{k=0}^{N-1} u_k^c \sin(2\pi jk/N) \\ u_j^{cc} &= \sum_{k=0}^{N-1} u_k^c \cos(2\pi jk/N) \\ u_j^{rs} &= \sum_{k=0}^{N-1} u_k^r \sin(2\pi jk/N) \end{aligned} \quad j = 0, ..., N-1. \tag{7.24}$$

In GPS and accelerometer data, measurements u_j are real values, the above formulae could be further simplified as

$$U_k = u_k^r - iu_k^c,\ k = 0, ..., N-1 \tag{7.25}$$

$$u_j = \frac{1}{N}(u_j^{rc} + u_j^{cs}). \tag{7.26}$$

Through selecting suitable parameters such as sample length, windows, amount of overlap, and data rate, spectral analysis was used for isolating and detecting the dominant structural vibration frequencies from GPS and accelerometer data which are buried by the wide-band noises as illustrated in Fig. 7.14 and Fig. 7.15. As the vibration frequencies can be easily identified from the spectrum of 3D accelerations, it is very difficult to detect these from GPS spectrum since most of the frequency signatures are covered by the same band noise signatures. In the spectrum of GPS positions, very slow frequencies are distributed on the left side of the graphs, which characterise high level multipath. Identification and isolation of multipath is further discussed in Chapter 8 using adaptive filtering approach.

According to this analysis, it is obvious that the spectrum method can be used to clean or suppress higher frequency noise based on the structure type, material etc. Analysis of both the GPS and the accelerometer data can supply mutual checks before further data processing is correctly applied. If the wrong cutoff frequency is applied in the data filtering, the signals of the real bridge movements might be filtered out in the

IDFT process. Due to the nature of long suspension bridge deflections, i.e. lower bridge natural frequencies maybe at the same band as those of multipath and the hostile observation environments, GPS data may be largely contaminated by the various noises. The spectrum approach sometime could not be applicable for extracting the frequencies in these bands. Eliminating the influences from the various noises is a tough task in GPS signal processing. Further research is required in this area and is a topic of research at the IESSG. Without the support from a triaxial accelerometer, it is impossible to select suitable cutoff frequencies in 3D deflection directions. In addition, the accelerometer can supply more redundant measurements, hence the advantage of the hybrid system.

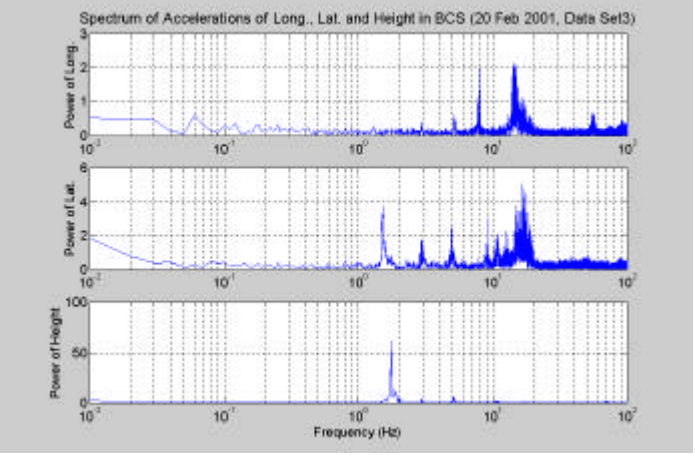

Fig. 7.14. Spectrum of accelerations

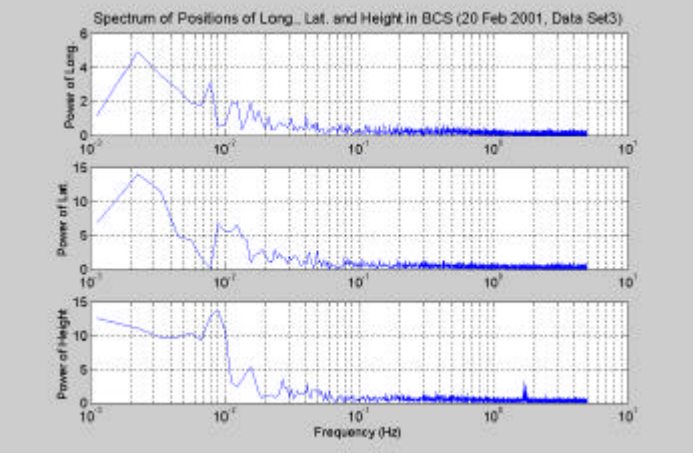

Fig. 7.15. Spectrum of GPS positions

In the data processing, the accelerometer thresholds in three axes obtained from about 1-hour static measurements are applied to further limit noises of accelerometer signals

and calculating the initial attitude of the accelerometer. Fig. 7.16 shows the detailed procedure for the data processing algorithm. A software package has been developed with Microsoft Visual C++ to implement this algorithm. A sample data set of about 1,000 3D GPS position points in OSGB at 10 Hz sampling rate and 20,000 3D accelerometer points at rate of 200 Hz from a controlled platform trial on 16 August 2000 were processed with this package. The detailed description of this trail is described in Section 5.2. Fig. 7.17, 7.18, and 7.19 show the comparisons of both GPS alone and acceleration aided GPS positioning solutions for eastings, northings, and vertical movements in OSGB NG. High agreements can be noticed between the GPS only positioning solutions and those from an integrated system.

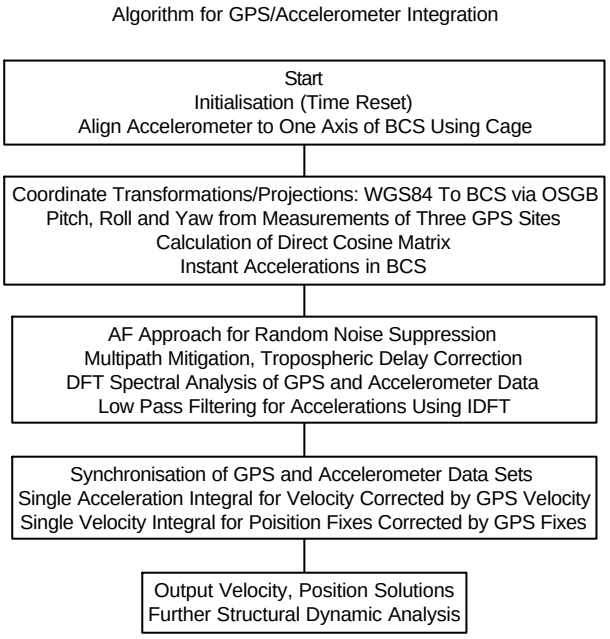

Fig. 7.16. Flowchart of GPS and accelerometer data integration

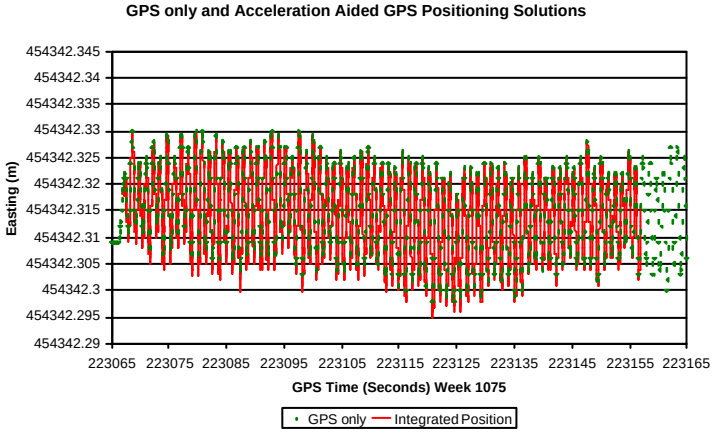

Fig. 7.17. Eastings from GPS only and integrated sensor system

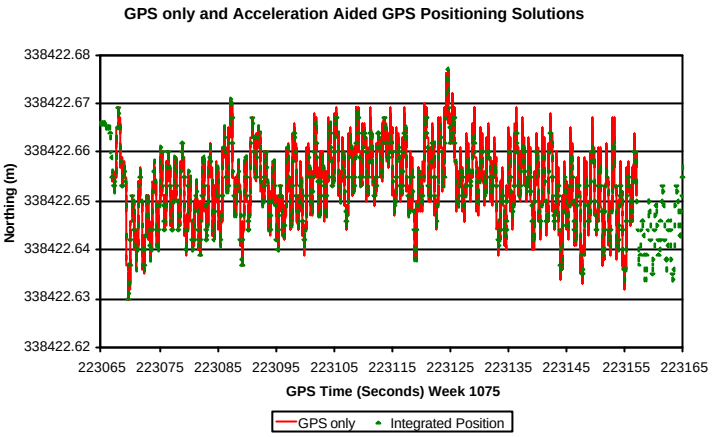

Fig. 7.18. Northings from GPS only and integrated sensor system

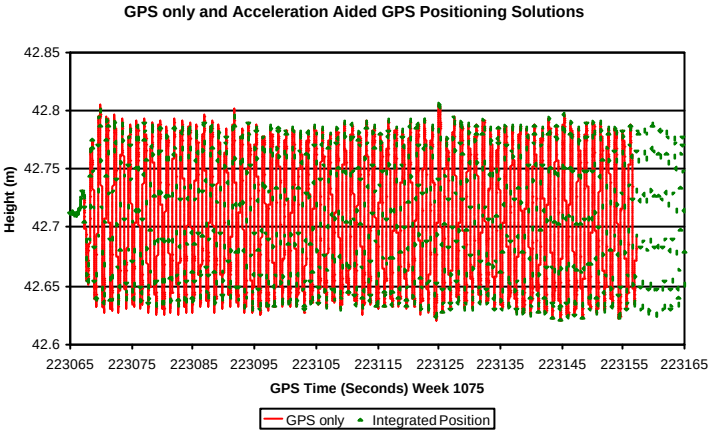

Fig. 7.19. Heights from GPS only and integrated sensor system

7.5 Summary

The fundamentals of adaptive FIR filtering are introduced in this chapter. MA approach for multipath mitigation is compared with AF technique. A real-time AF algorithm is proposed and applied to simulate the performance of the designed AF filters. Based on the filtering theory, the determination of an optimal filter length is suggested according to the statistic characteristics of receiver random noise and multipath. The complex calculation in the determination of optimal filter length is avoided and real-time application of AF becomes possible. The instantaneous adjustment procedure of filter coefficients is illustrated to validate filter convergence. An algorithm based on DFT, IDFT, and AF approach is proposed and a software package is developed for outlier detection and data fusion. Using the measurements collected in a controlled platform test, the efficiency and feasibility of the proposed

approach are analysed. With this algorithm the output data rate can reach the same level of an accelerometer. It should, therefore, be possible to use this system to detect widespread frequencies of bridge vibration.

Chapter 8

Applications of AF and Spectral Analysis to GPS/Triaxial Accelerometer-Based BDMS

8.1. Introduction

The environment surrounding the antennas of GPS receivers significantly affect the signal propagation, and as a consequence, noise is introduced into the measured values of pseudorange and carrier phase observables. Eventually, the GPS positioning solutions are greatly degraded by the inferences of these distorted signals.

In a GPS-based BDMS, multipath is one of the major error sources induced by the surveying environment. Since the reference stations used for deformation monitoring purpose are setup closely to the bridge and short baselines are processed to obtain positioning solutions, ionospheric delay will not be considered as a major error source in this research. In contrast, relative tropospheric delay and receiver noise become the other major error sources. Relative tropospheric delay due to the local microclimate under the bridge monitoring scenario will be discussed in Chapter 9. In this chapter multipath and receiver noise mitigation techniques will be investigated together with the detection of real bridge movements.

Since multipath changes its phase and amplitude all the time with the changes of GPS satellite constellation and fully depends on the ambient environment of a monitoring site, it is very difficult to use mathematical models to quantify multipath signature and reduce its influence (Dodson et al. 2001). In many engineering applications, multipath becomes a very troublesome impact factor (Barnes and Cross 1998).

Research reveals that the amplitude of carrier phase multipath can reach several centimetres in the extreme cases and typically has a period of a few minutes (Langley 1998). It can become the dominant error source and cause measurability problems

when GPS is employed to detect motions with the same period vibration frequencies such as the deflection of long flexible bridge. Due to its practical and academic importance, many researches have been conducted onto the multipath mitigation techniques.

For mitigating multipath at the reference stations, a closely setup multiple antenna array at the reference station was proposed by the Calgary University in Canada (Ray et al. 1999). A Kalman filter based algorithm was developed to use multipath corrupted measurements from these antennas to estimate the multipath and geometric parameters, from which the multipath signatures in the code and carrier phase measurements at each antenna can be estimated. It has the potential to be used in a real-time mode at reference stations to generate corrections for kinematic applications. To realise the above procedure is far from an easy task. It will involve specific receiver hardware design as well receiver firmware development before it can be applied in practical applications. A day-to-day method is adopted to mitigate multipath by using multipath characteristic of repeating its signature within two sidereal days. This approach can improve accuracy of GPS time series by about 50% (Bock 2000). MA is an alternative method used to reduce multipath effects when there are various known frequency band signals from real platform movements as discussed in Chapter 7 and also by Dodson et al. (2001). However, as it has been pointed this approach will not be efficient when the vibration frequencies of the bridge movements situate at the same frequency band of multipath. It is impossible to isolate each other.

New types of antennas can greatly reject multipath (Counselman 1999). These include various expensive chokering antennas available on the market and recently a NovAtel L1/L2 GPSAntenna™ Model 600 is assumed very effective in the multipath rejection (http://www.novatel.com). Using new type of antenna means an increase in instrument expenditure.

Through careful reference and observation site selection aided by software (not always practically applicable), ambient multipath can be detected (Jaksic 2001). In the specific applications such as in bridge deformation monitoring, the selection of an

ideal reference or monitoring station is largely restrained by the application purpose and surroundings.

Multipath modelling, such as signal to noise ratio (SNR) is another multipath mitigation technique proposed by Axelrad et al. (1996). Adaptive techniques are employed to estimate multipath in changing and stable environments. In many cases it is difficult to extract SNR index from raw measurements.

Bruton (1997) and Ge et al. (2000a) studied the feasibility of AF approach to suppress the multipath in the static GPS positioning. Less research has been conducted to investigate the characteristics of multipath and relevant mitigation techniques in the context of bridge monitoring. The recent research focus at the IESSG has been on addressing these issues (Dodson et al. 2001; Roberts et al. 2002a, 2002b). The details are introduced in this chapter.

In structural deflection monitoring, the complexity of the surveying environment and the surrounding infrastructures as well as the limitations in surveying site selection make multipath an unavoidable error source and even a dominant component in the time series of the final coordinates when lower frequency bridge movement is of the research interest. Very strict requirements upon the measurement accuracy, varying deformation ranges from several millimetres up to several meters, and real-time kinematic surveying mode challenge the application of GPS technology to structural deflection monitoring. Research into the effective multipath reduction is of great practical importance.

Simulation reveals the efficiency of an AF approach largely depends on the degree of correlation of the two time series (Meng 2000). The higher the correlation is the better the AF technique is able to strip out the noise from the positioning solutions. In Section 8.2, cross-correlation is first employed to demonstrate the importance of the exact alignment of two time series with the raw GPS measurements of a Wilford suspension footbridge trial. Experiments conducted on the turret of the IESSG building with different Leica GPS antennas are then introduced in an attempt to further explore the day-to-day multipath signature and patterns using kinematic positioning solutions. The cross-correlation algorithm and a Matlab script M-file are

developed and employed to find the time shifts from day-to-day positioning time series. The multipath patterns isolated from normally time shifted coordinate time series (four minutes) are compared with the exactly aligned time series according to the time shift of each individual direction in the relevant coordinate system during two consecutive days.

In Section 8.3, an AF-based hierarchical algorithm is applied to the kinematic positioning solutions for separating real bridge movements from multipath and the receiver random noise both at the reference and observation stations. The data sets collected from the Wilford footbridge trials on 20, 21, and 22 February 2001 are used to demonstrate the feasibility of the proposed approach. Spectral analysis is employed to validate the AF results through the natural frequency comparison with that of the accelerometer data.

Acceleration aided AF approach for error mitigation is represented in Section 8.4 and Section 8.5. A simple algorithm is proposed to estimate the relative displacements from the accelerations sensed by a triaxial accelerometer, which is connected with the GPS antenna. Spectrum analysis approach is applied to the input and output time series to evaluate the efficiency of AF approach in suppressing multipath in a dynamic environment.

8.2 Aligning Day-to-day Kinematic GPS Positioning Solutions

As explained by Roberts et al. (2002a, 2002b), finding the exact match point of two time series is crucial in order to effectively mitigate multipath and isolate deformation through the analysis of the coefficients of cross-correlation.

The time series as the inputs to an AF system can be the processed positions from GPS software, such as coordinates, or raw GPS measurements such as pseudorange and carrier phases as well as the correlated data sets from other sensors collected simultaneously with GPS. Examples are relative displacements from acceleration double integral.

Suppose two time series d_i and x_i, which could be the coordinate time series at one observation site or the raw pseudorange measurements on two consecutive days. d_i and x_i could be vectors of same length or vectors of different length. In the AF approach, only the vectors with same length are considered as the desired and reference input signals.

Data from the first time series, approximately about 2 minute period, is used to compare with the second time series with a longer period for the calculation of each epoch's cross-correlation coefficient. The positioning time series of 2-minute interval which starts at epoch t_{day1} of GPS time on the first day is designated as $d_{i_{day1}}$. The data used from the second day is four-minute positioning time series $x_{i_{day1}}$ for the period [t_{day1}+86040, t_{day1}+86280]. The coefficient of cross-correlation at each epoch j can be calculated by Eq.8.1,

$$\rho_j = \frac{(\sigma_{dx})_j^2}{(\sigma_d)_j (\sigma_x)_j} \tag{8.1}$$

where

$$(\sigma_{dx})_j = \sqrt{\sum_{a=1}^{N} \left((d_a^j - \bar{d}^j)(x_a^j - \bar{x}^j) \right)}$$

$$(\sigma_d)_j = \sqrt{\sum_{a=1}^{N} \left((d_a^j - \bar{d}^j)(d_a^j - \bar{d}^j) \right)} \tag{8.2}$$

$$(\sigma_x)_j = \sqrt{\sum_{a=1}^{N} \left((x_a^j - \bar{x}^j)(x_a^j - \bar{x}^j) \right)}$$

are SDs.

The index of max(ρ_j) is then used as the match point of two time series. For instance, by using this approach and raw pseudorange measurement, day-to-day time shifts can be estimated for each PRN satellite.

To analyse the multipath level and also detect cycle slips on the raw measurements of the each satellite in view, a RINEX data reader was developed by Matlab M-programming and used to separate pseudorange and carrier phase data from RINEX format data files. The outputs are the data files including the raw measurements of the

each individual satellite. The further analysis could be conducted with these raw measurement files.

It is well known with the current GPS satellite constellation, the whole satellite configuration normally advances for about 4 minutes within two continuous days (Hofmann-Wellenhof et al. 1997). However, the time shift for each individual satellite is different. Using cross-correlation algorithm and the raw pseudoranges of each satellite isolated by a RINEX data reader by M-programming from the data sets collected on 22 and 23 November 2000 at one midspan site in the London Millennium Bridge trial, the time shifts for each satellite during two consecutive days are calculated and the results listed in Table 8.1. The time shift of the whole satellite constellation at this site using two days' vertical coordinates was found to be 3'41".

PRN	4	5	6	9	24	25	29	30
Shift	4'06"	3'56"	4'10"	4'08"	4'06"	4'13"	3'50"	4'12"

Table 8.1. Time shift within two days (22 and 23 November 2000)

Analysis reveals that the time shifts are mainly affected by actual satellite orbit perturbation caused by the solar pressure as well as the signal refraction impacts from propagation media. If AF approach is used to isolate the noise components from raw measurements, the time shift of each individual satellite should be considered. However, when the impact of the combination of all satellites is the research emphases with positioning solutions, the total time shift then is used to mitigate errors. Further research on the satellite time shift is required by using GPS satellite ephemeris as it was suggested by Professor Dodson.

AF approach is further explored to analyse the impact of misalignment. Fig. 8.1 and Fig. 8.2 are the AF outputs with the normally aligned (4min) and exactly aligned (3 min 41 sec) two days' relative vertical positions at aforementioned bridge site. The two first rows on both graphs are the relative vertical positions on the second day. The two second rows are the reference signals calculated from the first day's measurements. The third rows are the signals for receiver noise plus small bridge movements relevant to second day only. The final rows are the isolated multipath series. The horizontal axis of the graphs represents the number of points, which are

400-second measurements at a data rate of 10 Hz. Fig. 8.3 is the difference of uncorrelated components of AF results. Fig. 8.4 shows the difference of residual multipath caused by time series misalignment. It reveals that without appropriate alignment of two time series in AF inputs, few-second's misalignment of two time series will introduce centimetre error in the multipath template determination and about two-centimetre error in the isolation of receiver random noise and real deformation. If this multipath template is applied to suppress multipath impact, it will certainly cause positioning distortion.

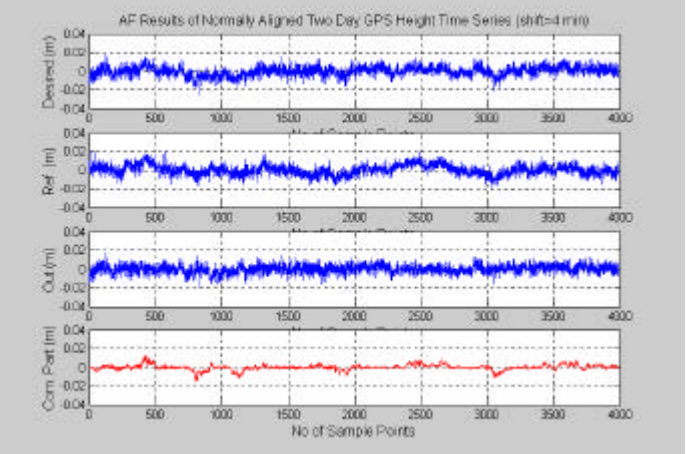

Fig. 8.1. AF results from normally aligned data

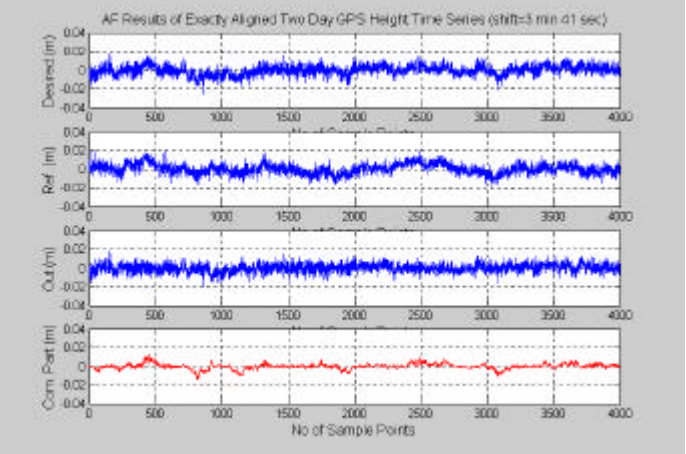

Fig. 8.2. AF results from exactly aligned data

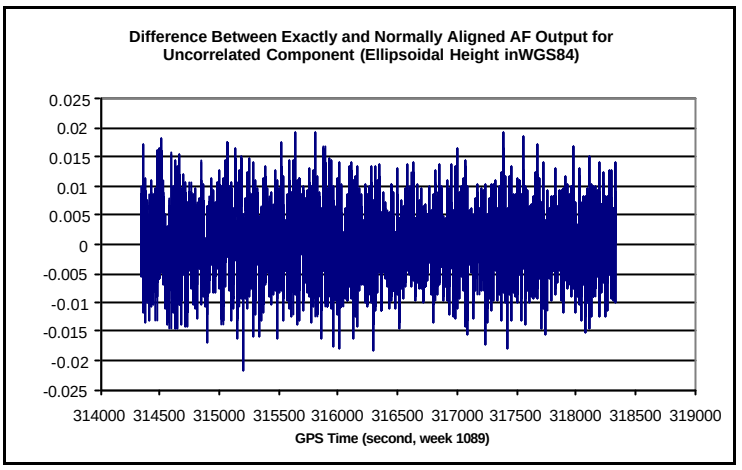

Fig. 8.3. Difference of uncorrelated components

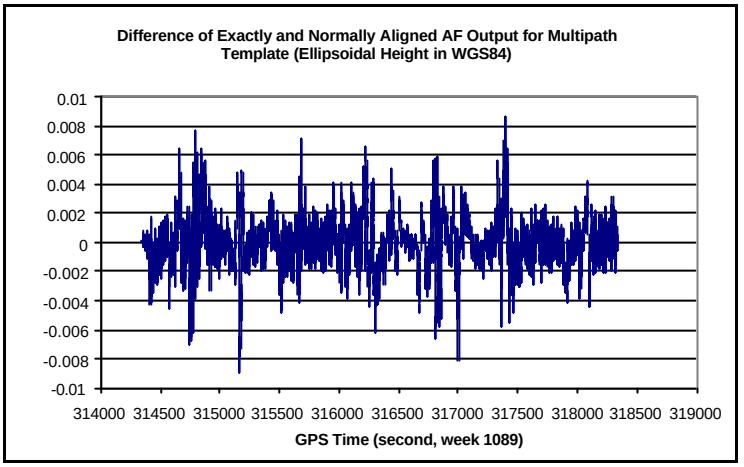

Fig. 8.4. Residual multipath caused by misalignment

To evaluate the performance of newly purchased Leica SR510 single frequency receivers, two-week ZBL and SBL tests were conducted with the IESSG geodetic facilities. Each of the three kinds of Leica GPS antennas, i.e. AT501 single frequency antenna, AT503 lightweight chokering antenna, and AT504 chokering antenna, were used for two consecutive days in the SBL tests with a sampling rate of 10 Hz. The kinematic positioning solutions of these SBL tests were calculated with SKI-Pro by fixing one receiver as reference station and another as a rover. The calculated time shifts for each antenna type are listed in table 8.2 using above cross-correlation algorithm. The differences between the time shifts on X and Y coordinates of same type antenna tests are all within 1 second range, but the differences of time shifts between Z with X or Y could reach several seconds. Also, the results suggest that the time shifts based on the day-to-day kinematic positioning solutions are not necessarily 4 minutes depending on the sampling rate used and the time shifts in 3D coordinates

are different. The calculated maximum cross-correlation coefficients for X, Y and Z using SR510 single frequency receivers and AT501 single frequency antennas are 0.38, 0.35 and 0.74 which are different from those of AT503 lightweight chokering antenna, which are 0.25, 0.65, and 0.51 respectively, due to the different patterns in signal reception and filtering.

Antenna type	X	Y	Z
AT501 (Sample 1)	4’06’’.3	4’06’’.9	4’07’’.8
AT501 (Sample 2)	4’10’’.0	4’09’’.3	4’05’’.0
AT503	4’07’’.6	4’07’’.1	4’01’’.7
AT504	4’09’’.0	4’08’’.7	4’03’’.4

Table 8.2. Time shifts for each antenna type in three directions (WGS84)

Further studies have been conducted with Z coordinates in WGS84 calculated from the measurements collected by SR510 receivers and AT501 antennas to evaluate the impact of misaligned data on the efficiency of the AF approach. The approach and algorithm used here are similar to those illustrated previously. Fig. 8.5 and Fig. 8.6 are the results from two days’ normally (4 minutes) and exactly (4 minutes and 7.8 seconds) aligned data sets from the SR510 single frequency receiver and the AT501 single frequency antenna (red coloured Sample 1 in Table 8.2). The first rows in both graphs are the desired signals of the AF algorithm for about a 2, 000-second period with 10 Hz sampling rate on day one. The second rows are the time shifted reference signals of the following day’s Z coordinate time series. The third rows in both graphs are the uncorrelated signal outputs. Their contents are totally different from the uncorrelated parts of the real bridge data in Fig. 8.3. The components here mainly contain receiver noise and unfiltered multipath residuals caused by the casual interference. The final rows are the correlated components, which represent for the multipath signatures. The residuals are calculated by comparing the corresponding output signals to evaluate the impact of misaligned time series on the efficiency of the AF approach. Fig. 8.7 and Fig. 8.8 are the residuals for the uncorrelated components (receiver noise plus unfiltered casual multipath) and correlated parts (multipath) of both time series. For further investigating the impacts caused by the different antenna types, the same procedure is applied to the kinematic positioning solutions from Leica AT504 and AT503 chokering antennas.

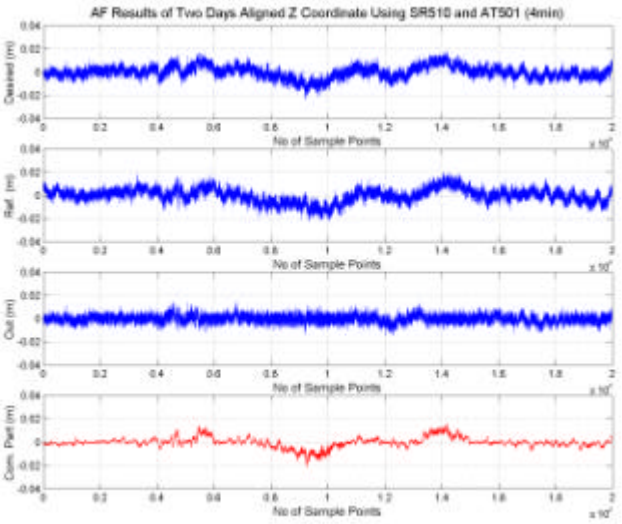

Fig. 8.5. AF results from normally aligned Z coordinates

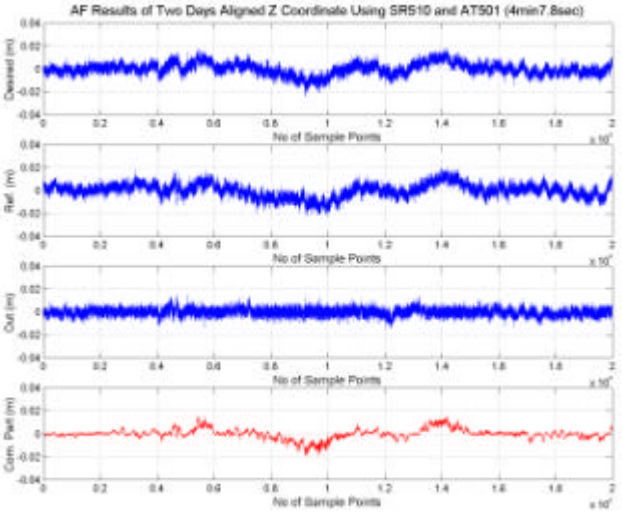

Fig. 8.6. AF results from exactly aligned Z coordinates

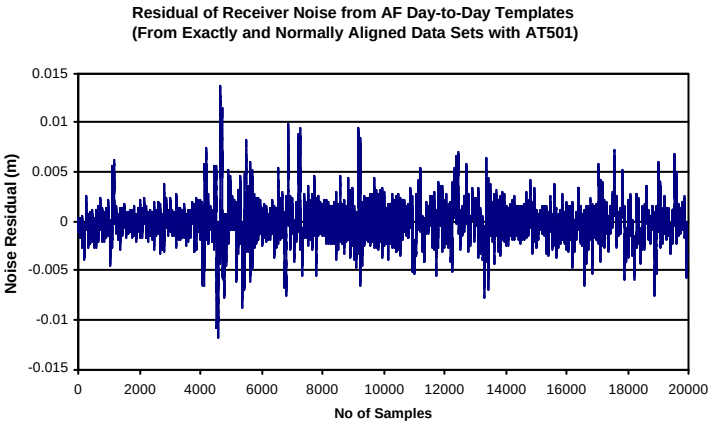

Fig. 8.7. Receiver noise residual due to misalignment (antenna AT501)

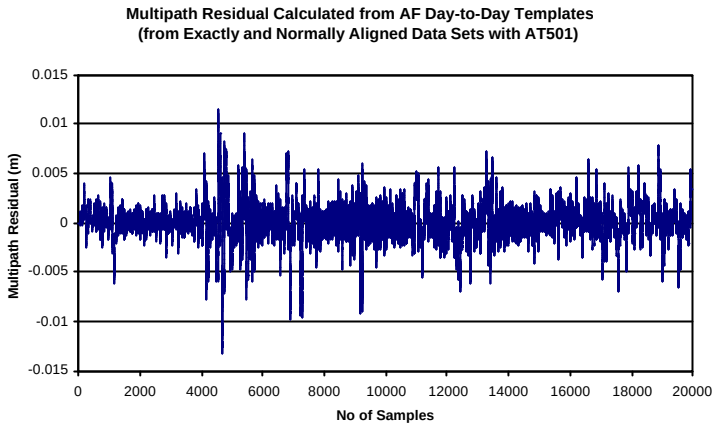

Fig. 8.8. Multipath residual due to time series misalignment (antenna AT501)

Fig. 8.9 and Fig. 8.10 are the residual time series of the receiver noise and multipath signature for AT504 chokering antenna. It is obvious even with a single frequency receiver and the normally aligned time series, if a chokering antenna is employed for data collection, significant improvement in position solutions can still be expected.

Using the cross correlation of day-to-day kinematic positioning solutions, the time shifts are counted in the following real bridge monitoring examples while AF algorithm is used to suppress errors of multipath and receiver noise and to detect the real bridge movements to avoid the introduction of extra errors.

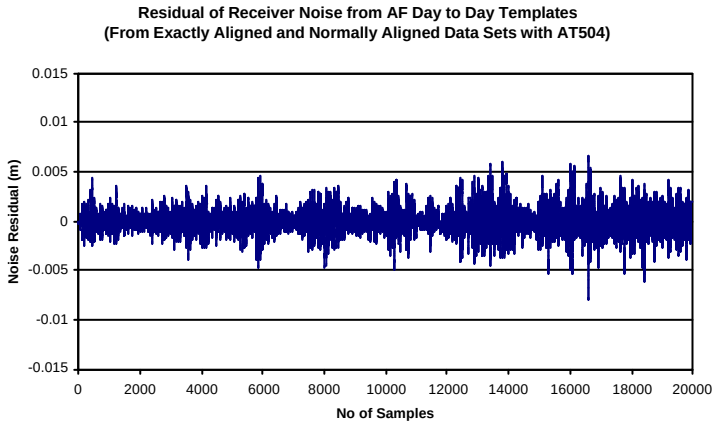

Fig. 8.9. Receiver noise residual due to misalignment (antenna AT504)

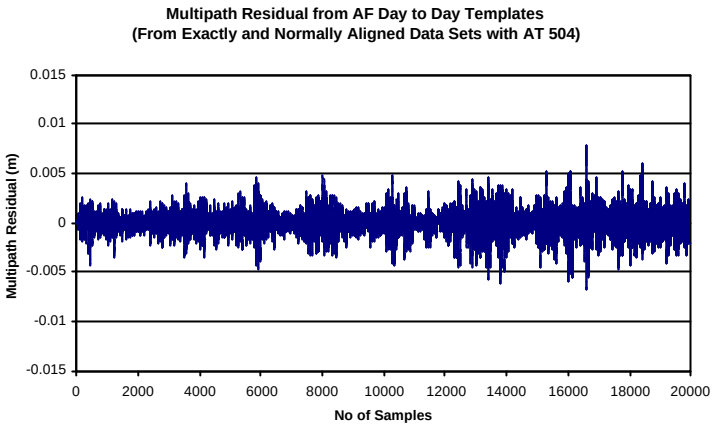

Fig. 8.10. Multipath residual due to misalignment (Antenna AT504)

8.3 AF Approach Applied to GPS Positioning Solutions

Unlike AF applications to CGPS stations suggested by Ge et al. (2000a), which are experiencing small movements, day-to-day characteristic of multipath repeat and other mitigation techniques cannot be directly employed to mitigate multipath and detect real bridge movements. Careful time series ordering is required to successfully isolate time series of different frequency bands. Some research at the IESSG has been presented by Dodson et al. (2001) and Meng et al. (2001). More research is introduced hereafter. A hierarchical real-time AF approach for multipath, receiver noise, and real bridge movement detection is proposed.

8.3.1 Receiver Random Noise and Multipath at the Reference Stations

The spatial distance of the two riverside reference stations at the Wilford footbridge is about 6.3m apart. The multipath signatures are assumed to be similar. MA algorithm has been illustrated to analyse the amplitude of residual multipath of these reference stations in Section 7.2. Centimetre level residual multipath has been evident. As it has been pointed out, MA algorithm cannot be employed to analyse the multipath signature in a BDMS since the frequency band of the multipath is varying especially when there is interference from the passing traffic and also because multipath is mixed with the slow real bridge movements. Most importantly, MA is not an optimal filter.

As an alternative, the capability of AF approach for more general error mitigation at reference stations is further investigated.

Two consecutive days' kinematic positioning solutions are used to estimate the receiver noise level and residual multipath at the reference sites but only the height component in a BCS is chosen from Session One on 20 and 21 February 2001 in the Nottingham Wilford footbridge trial as examples. The kinematic solutions at the reference stations are obtained by fixing one receiver as reference station and let another as rover.

The cross-correlation parameters of 3D kinematic solutions in the BCS at the reference stations during two sidereal days are 0.54, 0.64, and 0.52, in the order of lateral, longitudinal, and vertical directions, respectively, even though chokering antennas were used. Multipath might have been induced by the reflection of the bridge towers, buildings, and foliage near the reference stations.

Fig. 8.11 and Fig. 8.12 illustrate backward and forward AF approaches. The input signals in Fig. 8.11 and Fig. 8.12 are two sidereal days' kinematic solutions at the reference stations, Base1 and Base2. The time series are aligned according to the approach proposed in Section 8.2. The first two plots in Fig. 8.11 and Fig. 8.12 are the desired signal d and reference signal x to an AF filter with a filter length 20, and the third and fourth plots are the uncorrelated receiver random noise R (only related to d) and correlated multipath output S which correlates with both input time series, respectively. It can be seen from Fig. 8.11 and Fig. 8.12 that similar multipath outputs are obtained when the order of the signal inputs is exchanged. This means that the multipath on the reference sites has been successfully extracted. The cross-correlation parameters calculated further verify the effectiveness and correctness of AF output according to Eq.7.14. The input signal cross-correlation parameter (d, x) for Fig. 8.11 is 0.2655, which means that the receiver random noise dominates in the original time series. The cross-correlation parameter between the desired signal with the receiver random noise (d, R) of 0.8422 further verify that receiver noise is the major error source in the reference stations and has been striped out effectively. The cross-correlation parameter between the desired signal with common part output (d, S) is

0.4907 and that of the noise output with the common part (S, R) equates to 0.03, which is crucial index of AF approach and used to check the separability and efficiency of a designed AF filter. The cross-correlation parameter between the reference signal input x and receiver random noise R is 0.001 and it confirms that no common component of the two input time series has been wrongly filtered out into random noise. The counterparts of Fig. 8.12 are 0.2655, 0.8210, 0.5429, 0.03 and 0.001 respectively.

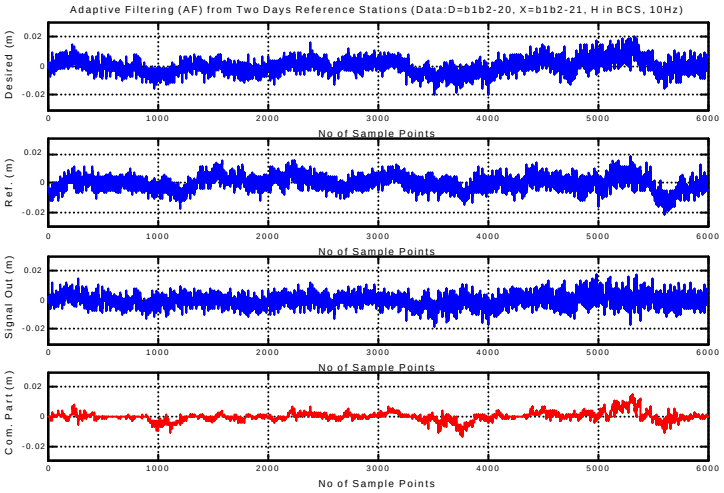

Fig. 8.11. Two sidereal days' AF results of height (backward)

According to the criteria set by Eq.7.14, the correlated part of two time series within the two sidereal days' reference station kinematic solutions has been successfully isolated. The uncorrelated signal sequence is only correlated with the desired signal inputs (third row time series in Fig. 8.11 and Fig. 8.12). This means that there is no systematic error left in the two days' uncorrelated signals. The statistic nature of the output signal is studied through the comparison of the histogram with its theoretical normal distribution (Fig. 8.13). It also reveals the random characteristic of the uncorrelated signal outputs. Further statistical tests of its normality could be conducted according the procedure proposed by Meng et al. (1996).

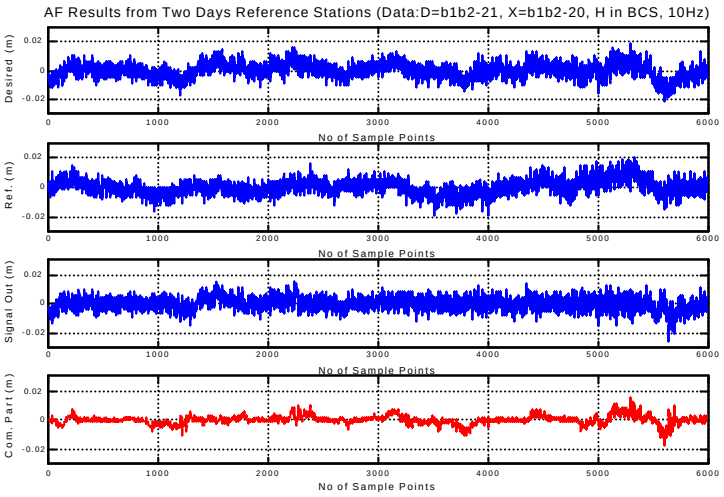

Fig. 8.12. Two sidereal days' AF results of height (forward)

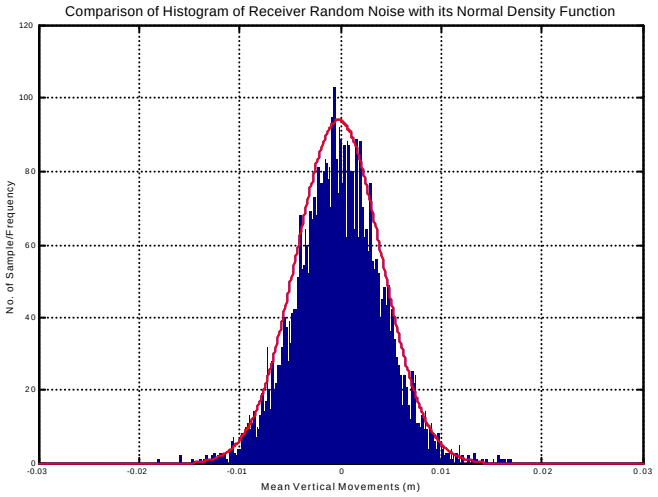

Fig. 8.13. Random noise histogram vs. normal distribution

Furthermore, spectral analysis has been applied to the input and output signals to detect the frequency distribution of different time series. Fig. 8.14 is the lower frequency distribution on the three axes in the BCS of the desired signal *d* from Fig. 8.12, which shows the suspected multipath frequencies at the reference stations. The identified frequencies on the three axes are 0.0039 Hz laterally, 0.0061 Hz longitudinally, and 0.0072 Hz vertically in the BCS, which correspond to 4.27, 2.73, and 2.31 minutes periods respectively. Fig. 8.15 illustrates that through the AF procedure the suspicious vertical multipath is efficiently removed from the desired signal and the third plot is actually presenting the spectrum of the receiver random noise of very weak energy.

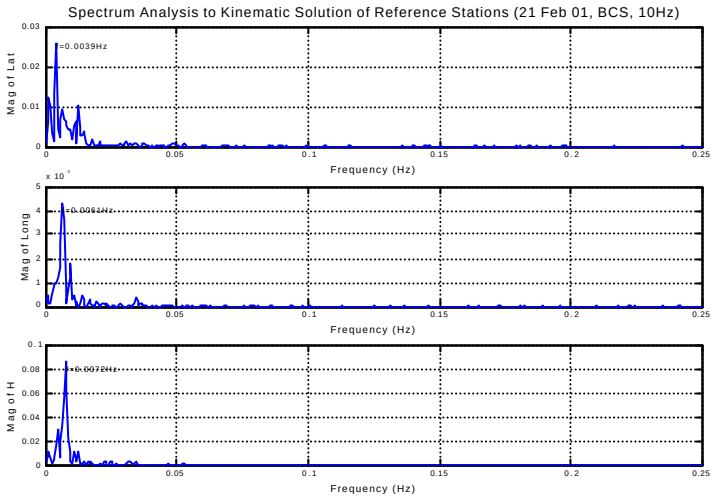

Fig. 8.14. Low frequency band of 3D positioning solutions at reference stations

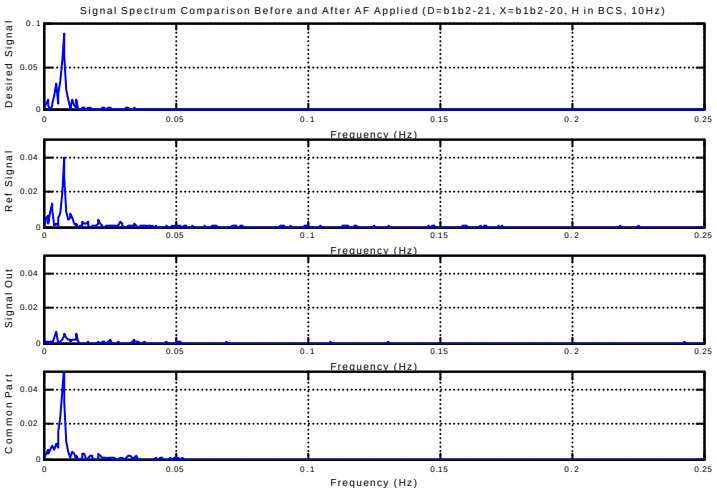

Fig. 8.15. Spectrum analysis for vertical AF results

The above multipath detection approach could be further developed to help select locations of reference stations with relative low-level multipath interference. The detected multipath time series can be integrated with the instantaneous GPS geometry and local topographical surface to conduct detailed and real-time multipath monitor and analysis at specific environment.

8.3.2 Multipath, Receiver Noise, and Real Bridge Movement Detection

From the above analysis, it is apparent that for precise structural monitoring multipath and receiver random noise both at the reference stations and monitoring stations are

the major error sources and they will unavoidably affect the final positioning solution quality at each bridge site. They cannot be fully eliminated even through careful reference station site selection and use of chokering antennas as illustrated in the Section 8.3.1. Without an appropriate error reduction process, it is difficult to extract real bridge movement signal from such noisy coordinate time series and to conduct further analysis of a bridge's long-term and short-term movements, especially when lower frequency bridge movements situate in the same frequency band.

An AF method is developed to remove multipath and receiver random noise influences introduced by the reference stations at each monitoring site. Each day's kinematic solution of reference stations contaminated by multipath and receiver random is used as the reference signal input x in an AF filter. The time series of each bridge sites is employed as the desired signal sequence d. In this case, the correlated parts of two time series are the noise contributors consisting of multipath and receive noise from the reference stations. The uncorrelated parts include the real bridge movement, multipath, and individual receiver random noise at each monitoring site. Fig. 8.16 shows the signal outputs from the AF filter with such a signal arrangement. Fig. 8.17 is the relevant spectrum comparison of the four time series. The lower frequency signature similar to that of the reference station in the desired signal has been successfully removed.

Applying the same approach to another data set for the same bridge site determined by another reference station (Base2), similar reference noise-free uncorrelated AF results (third rows in Fig. 8.16 and Fig. 8.18) are obtained. In these time series the real bridge movements are covered by multipath and receiver noise only relevant to bridge site. Averaging these two AF signal outputs from the two kinematic solutions solved by using two reference stations of each bridge site, relatively cleaned kinematic positioning solutions can be assured. It is worth pointing out, due to the difference in two receivers' random noise levels at two reference stations, the correlated outputs of Fig. 8.16 and Fig. 8.18 are different. Spectrum analysis has been applied to the four signal sequences in Fig. 8.18 and the results are illustrated by Fig. 8.19. Through the comparison of the spectrums of input and output sequences, it can be found that multipath signature is neatly removed (third row of Fig. 8.19).

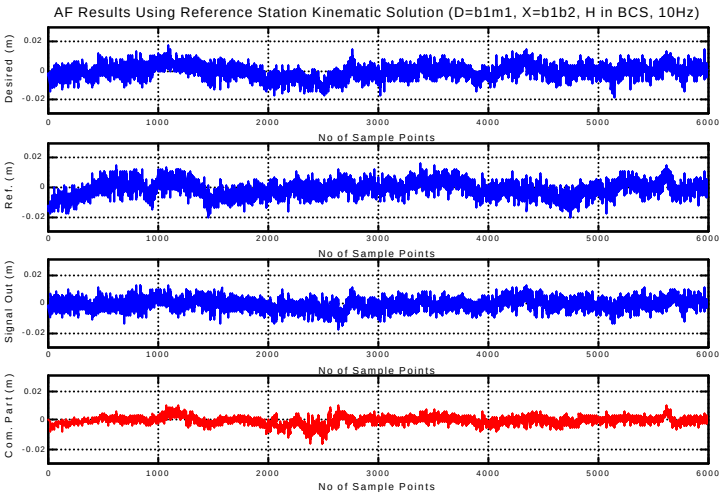

Fig. 8.16. Bridge site vertical AF results using Base1

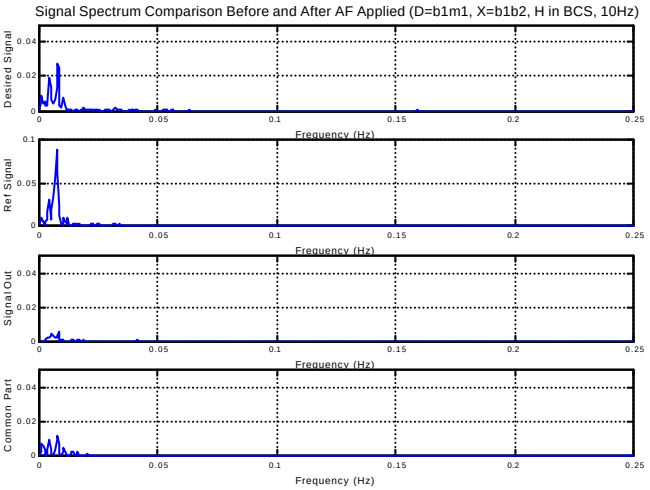

Fig. 8.17. Spectrum analysis of vertical AF time series (ref.: Base1)

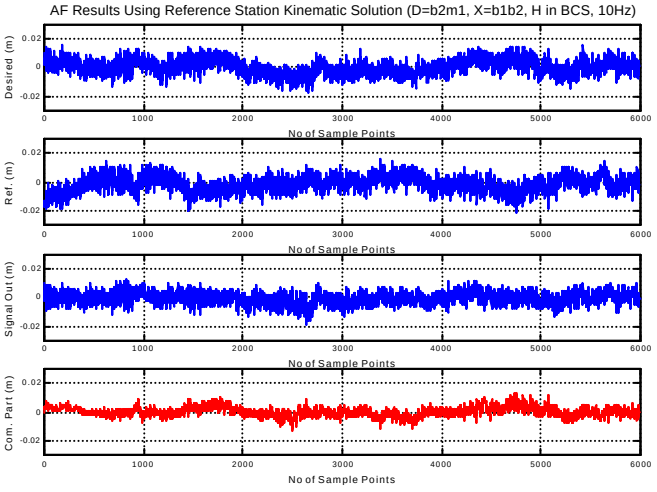

Fig. 8.18. Bridge site vertical AF results using Base2

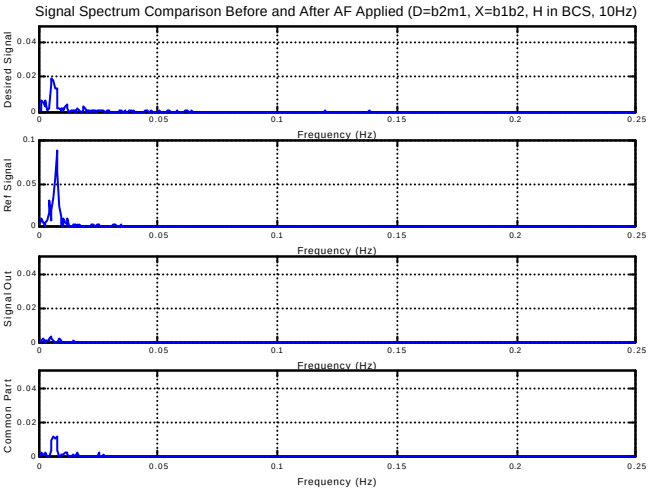

Fig. 8.19. Spectrum analysis of vertical AF time series (ref.: Base2)

After removing multipath and receiver random noise relevant to the reference stations at each bridge site with the above proposed procedures, two consecutive days' AF outputs (uncorrelated parts in Fig. 8.16 or Fig. 8.18) are used as desired and reference signal sequences into another AF filter to remove the multipath influence at bridge site. The first row in Fig. 8.20 is the desired signal sequence, which is the uncorrelated signal output in Fig. 8.16 (21 February 2001 at Mid1). The reference signal sequence is a time series of similarly 'cleaned' AF output on 20 February 2001 at the same bridge site, shifted by the calculated time lag of two consecutive days. The correlated part of these two time series consists of only bridge site's relevant multipath. After AF process, the uncorrelated part includes the real bridge movement coupled by the individual receiver random noise.

Fig. 8.21 is the frequency comparison for the four time series in Fig. 8.20. The identified multipath frequency at bridge site is 0.0082Hz with very weak spectral power output compared with that of the reference stations. This is because there is a more open sky view on the bridge deck.

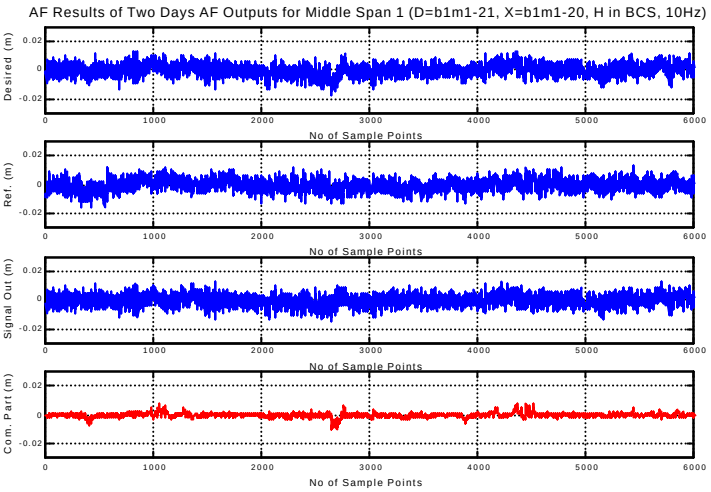

Fig. 8.20. Mitigating bridge site relevant multipath

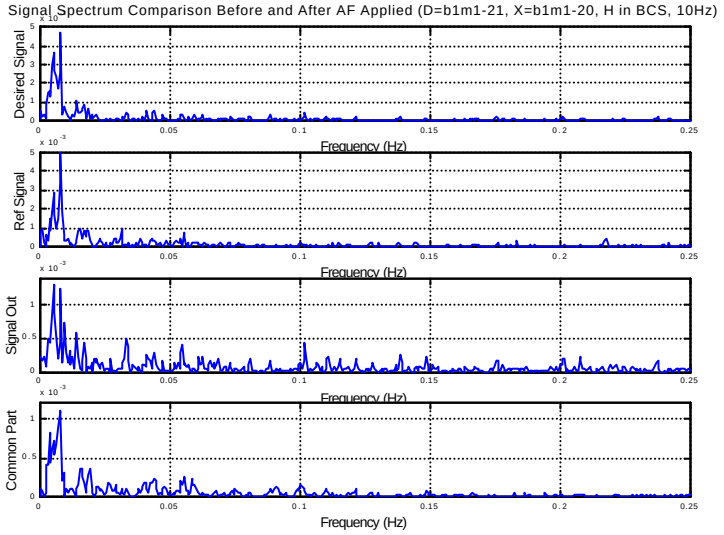

Fig. 8.21. Spectrum of bridge site relevant multipath

Through the above processes, multipath both at the reference stations and bridge sites and the receiver random noise at the reference stations are removed. Further AF filter is designed to separate the real bridge movement from receiver random noise at monitoring station, using two receivers closely setup on the opposite sides at the midspan of the bridge (Mid1 and Mid2). The input signals here again are the multipath free AF outputs (for instance, the uncorrelated part in Fig. 8.20, the third row). Since the two receivers are closely setup, the difference in bridge vibration between the two sites can be ignored. The uncorrelated output of this process is the time series of individual receiver random noise and the correlated part is the common bridge movement (Fig. 8.22). The apparent bridge vibration agitated by the organised

group of pedestrians is revealed after the above recursive AF processes. Through exchanging the orders of input signals, the receiver random noise of another midspan site is obtained (uncorrelated part of AF). Fig. 8.23 is the input and output signal frequency comparison before and after AF has been applied. Relatively cleaner signal output has been obtained after recursive AF process through comparing row 1 and row 4 in Fig. 8.23. The main vibration frequency of Nottingham Wilford suspension footbridge is identified as 1.7487Hz by this approach, which is confirmed by comparing it with that of accelerometer data sets (Fig. 8.24).

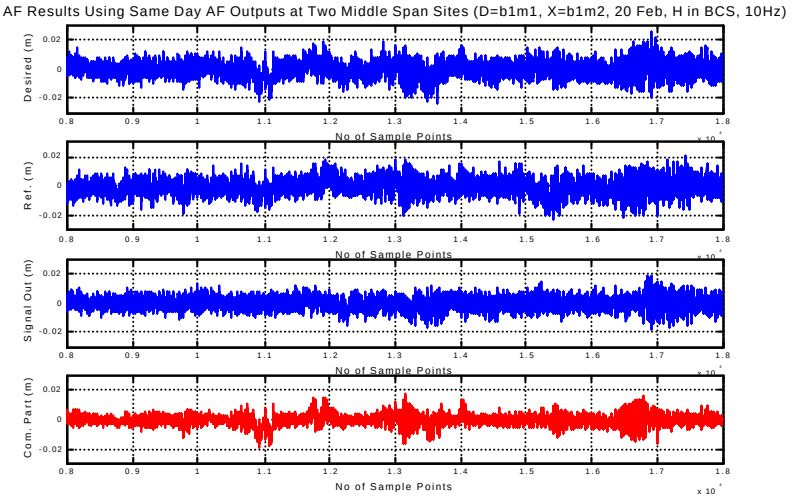

Fig. 8.22. Recursive vertical AF results for bridge Site

Kinematic solutions of two other days' measurements are used as the AF signal inputs at Mid2 (Fig. 8.25). The receivers were connected to a patch antenna during the two days' measurements. The time tags of two time series are shifted to take account of the impact of GPS satellite geometry.

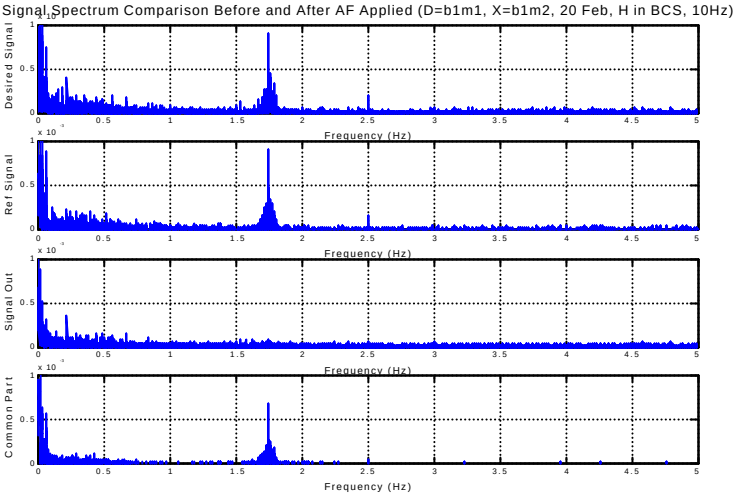

Fig. 8.23. Main vertical bridge vibration frequency

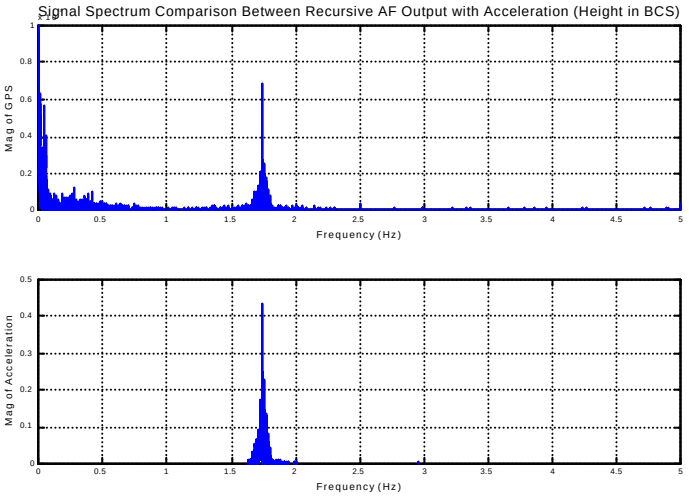

Fig. 8.24. Frequency comparison between AF outputs and acceleration

The third row in Fig. 8.25 consists of real movement of the bridge site, and receiver random noise. The fourth row is the removed multipath time series. The cross-correlation parameters (d, x) of the desired signal with the reference signal is 0.7185 and indicates that the time series using a patch antenna is highly contaminated by multipath. Hence the multipath can be effectively removed according to the analysis in Section 8.2. With the above proposed recursive AF approach, the accuracy of positioning solutions from a cheap GPS antenna can be improved significantly or even reach the standard of a chokering antenna. Fig. 8.26 is the changes of the AF filter coefficients. It is apparent that AF filter coefficients as the name suggests are adjusted to the optimal values instantaneously according to the changes of noise level.

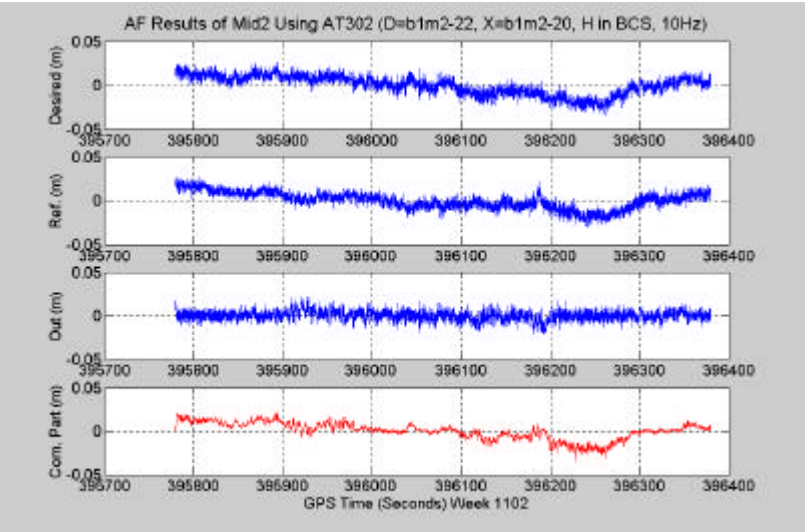

Fig. 8.25. Vertical AF for lightweight antenna Leica AT302

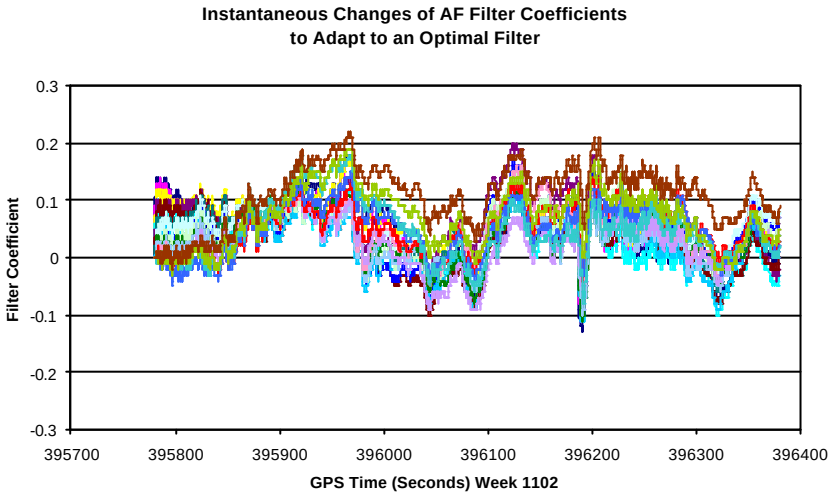

Fig. 8.26. Instantaneous changes of AF filter parameters with filter length 20

8.4 A Simple Algorithm for Calculating Relative Displacements from Accelerations

The raw measurements from a triaxial accelerometer are the discrete outputs in voltage on each axis via an analogue to digital converter. These data can be further converted into accelerations using the zero biases and scale factors corresponding to each axis. The zero biases and scale factors of triaxial accelerometer that are determined by the approach introduced in Section 3.4 are employed to calculate accelerations. These accelerations are multiplied by the gravity constant to obtain acceleration in the metric system (m/s/s). To reduce the computation burden from the

coordinate transformations between different systems, a specially designed cage is used to house a GPS antenna and accelerometer (Roberts et al. 2001a). Even though the two kinds of sensors are physically attached together, the direct comparison of GPS coordinates and accelerations using the AF approach is impossible due to different dimensions. The accelerations need to be converted into relative displacements by double integration. The accelerometer errors such as zero biases and scale factor errors accumulate into distance errors according to the equation of motion (Lawrence 1998)

$$S = vt + 1/2at^2 . \tag{8.1}$$

In Eq.8.1, v is the initial velocity; a is the acceleration measurement; and S is the distance travelled in time period t.

Eq.8.2 is used to calculate velocity from acceleration, an approach to approximate acceleration integral,

$$v(t) = v(t-1) + \frac{\Delta t}{2}(a(t) + a(t-1)) \tag{8.2}$$

where $v(t)$, $v(t-1)$, $a(t)$, $a(t-1)$ are the velocity and acceleration at time t and $t-1$, respectively. Δt is the time interval of data sampling. Eq.8.2 can be applied to velocity to calculate relative displacement.

Since the interest of the research is on the relative displacements, the initial velocity can be set to zero. An MA filter is applied to cope with the drift problems of the velocities and displacements (Eq.8.3). In principle, the MA approach is a low-pass filter. It can be used to isolate longer period movements from the time series of integrated velocity and displacement, which are contaminated by the systematic errors of the accelerometer. The residual between the original time series and the smoothed output from the MA constitutes the local higher frequency variation (high-pass filter), which mainly represents real structural vibration and the impact from high frequency noises. Simulation reveals that the selection of sample number used for averaging is crucial. This requires considerable experience plus knowledge of the frequency aspects of the time series analysed. Spectral analysis is used for the purpose of frequency identification. In the spectral analysis of the bridge data gathered from GPS

and the accelerometer, the frequency band of this research interest is higher than 1 Hz. In order to use the relative displacements calculated from accelerometer data as a reference signal of the AF approach, the accelerations are re-sampled from 200 Hz down to 10 Hz. Simulation results illustrate that noise with frequency slower than 1 Hz is filtered out in the MA procedure via 20 sample averaging, which makes sure that higher frequency signatures of bridge vibration are filtered into the residual time series of MA.

$$MA(a_t) = \frac{1}{|q|+s+1}\sum_{r=-q}^{+s} a_r, -q \le t \le s \qquad (8.3)$$

$MA(a_t)$ is the smoothed output for time series a at time t. a could be acceleration or filtered velocity.

Based on the above fundamental, a Matlab script used for relative displacement calculation was developed, with functionalities of MA sample length selection, velocity and relative displacement calculations, and spectral analysis of output signals.

Fig. 8.27 is the comparison of original vertical acceleration sampled with 200 Hz and the resampled vertical acceleration at sampling rate of 10 Hz. It is obvious that most abnormal acceleration measurements have been filtered out through resampling procedure. The data set illustrated here is chopped from one-hour accelerometer data, which was collected on 20 February 2001 on the Wilford suspension footbridge Detailed experiment was introduced in Section 5.3.4. To investigate the bridge dynamic responses to the pedestrians, 8 people walked repeatedly over the bridge, which caused significant acceleration signatures.

Fig. 8.28 illustrates the MA approach applied to calculate the smoothed velocity and local velocity fluctuation. Apparent bridge movements at a velocity of 0.2(m/s) activated by the pedestrian are appropriately extracted out.

Fig. 8.29 illustrates the results of relative vertical velocity and displacement by using the aforementioned algorithm. The drift due to the double integral has been

successfully overcome. Fig. 8.30 is the result of spectral analysis on the vertical acceleration. Several vibration frequencies have been identified by the accelerometer data. The bridge vibrations with frequencies higher than 5 Hz cannot be detected out by GPS-alone monitoring system. This is another merit of this integrated system. In this case the main vertical vibration frequencies identified up are 1.75 Hz (first natural frequency, the only frequency identified by GPS), 2 Hz, 3 Hz, 5 Hz (which cannot be identified by 10 Hz GPS in considering other error budgets of GPS only system), 9 Hz, 11 Hz, and 70Hz.

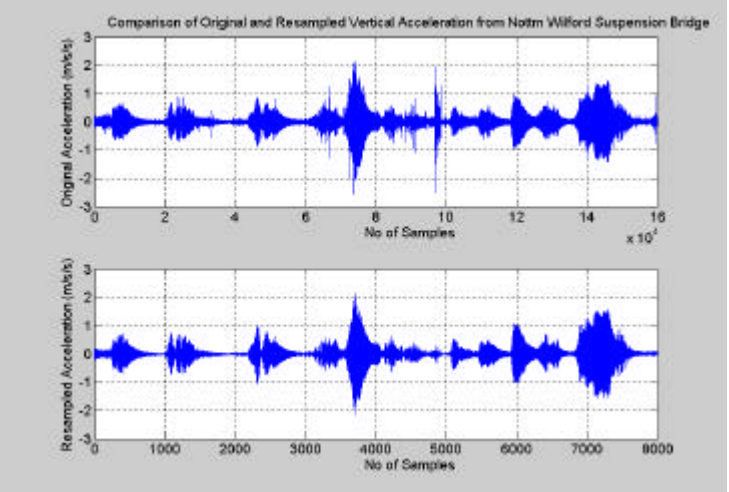

Fig. 8.27. Original acceleration vs. resampled ones

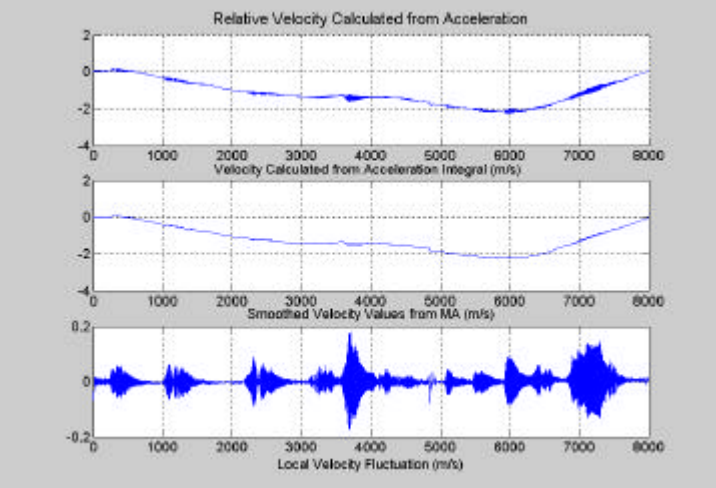

Fig. 8.28. MA approach for velocity calculation

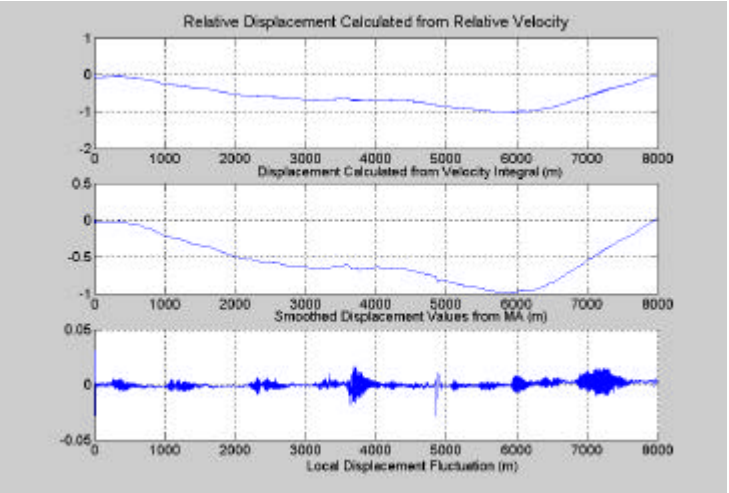

Fig. 8.29. MA approach for displacement calculation

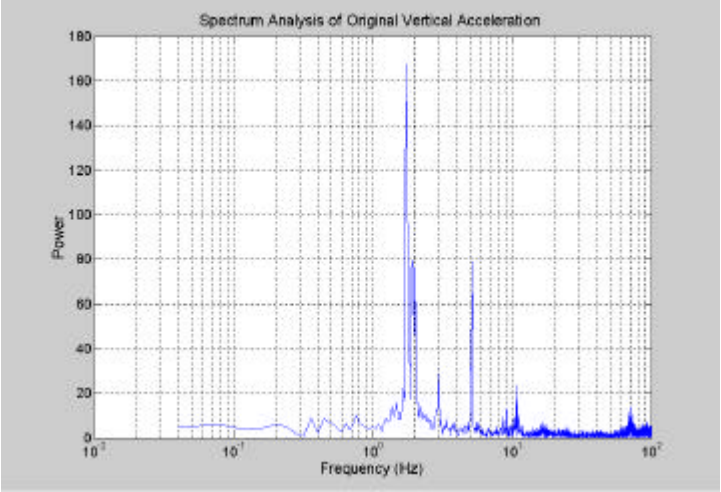

Fig. 8.30. Vibration signatures identified by accelerometer (vertical)

8.5 Acceleration Aided AF Approach for Isolating Relative Bridge Deflections

The relative displacements calculated from accelerations by the proposed algorithm can be further used to mitigate GPS receiver noise and detect the real bridge movements. Due to high degree of multipath signature caused by the surrounding and adjacent structures, accelerometer aided AF approach cannot be directly applied to the kinematic GPS position solutions. Careful treatments are needed. The above procedure is used to gradually reduce the impacts of multipath and receiver noise both at reference stations and monitoring sites, in addition to mitigate the relative tropospheric delay between reference station network. The final results are still

contaminated by certain degree of the residual components aforementioned. This is evident as it is illustrated in Fig. 8.23. It is still difficult to see the clear bridge movements. Since GPS and accelerometer are independent instrument, the only correlated component in both systems is the sensed force or movement. So, it is ideal treatment to use acceleration aided AF approach to isolate relative movement of the bridge. It needs to be clarified that the data fusion approach proposed in Section 7.4 attempts to output the positioning solutions at a rate of accelerometer sampling rate. The AF approach of GPS solutions aided by accelerations tries to output positioning solutions at a data rate same as GPS sampling rate.

Fig. 8.31 is the GPS only AF results using the vertical position solutions of two days' time shifted measurements at the same observation site as the input sequence. Backward AF filter is employed, i.e. the vertical coordinate time series on 20 February 2001 is used as the desired signal sequence and the vertical positions on 21 February is employed as the reference signals. These data sets are exactly synchronised with accelerations using the approach propsoed in Section 4.5. In the reference time series, there were signatures activated by the casual pedestrains passing over the bridge. Fig. 8.32 is the spectrum power distribution of desired signal. The power of multipath is much higher than that of the actual bridge movement and exhibit itself as a very slow movement patterns. It is very difficult to identfy the excited movements without any further treatment or augmentation from indepenent sensors. From Fig. 8.32 the dominant multipath frequencies identified via FFT are 0.0039 Hz and 0.0072 Hz, which are mainly introduced by the multipath interference at reference stations (third row of Fig. 8.14).

Fig. 8.33 is the spectrum of the reference signal. There is no signature of 1.75 Hz vertical movement since there were no excitation tests made at that time on 21 February 2001. However, the same frequency signature of multipath is apparent, which is almost filtered out by the AF procedure. It is evident through the spectrum power comparison between Fig. 32 and Fig. 8.34.

Fig. 8.35 is the AF output using the relative multipath free GPS position solution (the third row in Fig. 8.31, which constitutes the receiver random noise and real bridge movement, as the desired input signal and the calculated relative bridge displacement

from accelerations as the reference signal in the AF algorithm. The outputs are the receiver noise time series (third row) and relative bridge movement (fourth row). Fig. 8.36 illustrates the results of using untreated positioning solution directly to compare with the relative bridge movement sensed by the accelerometer. It shows that it is possible to isolate multipath from the real bridge movement but the detected real bridge movement is distorted at certain periods.

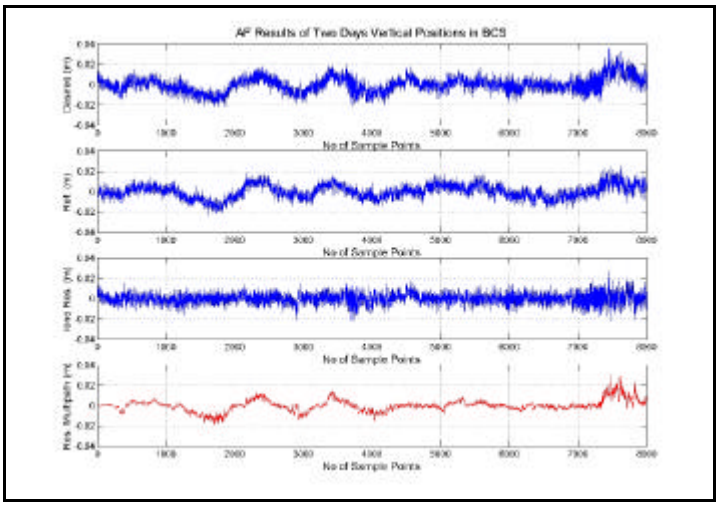

Fig. 8.31.GPS AF results using two day's positioning solution

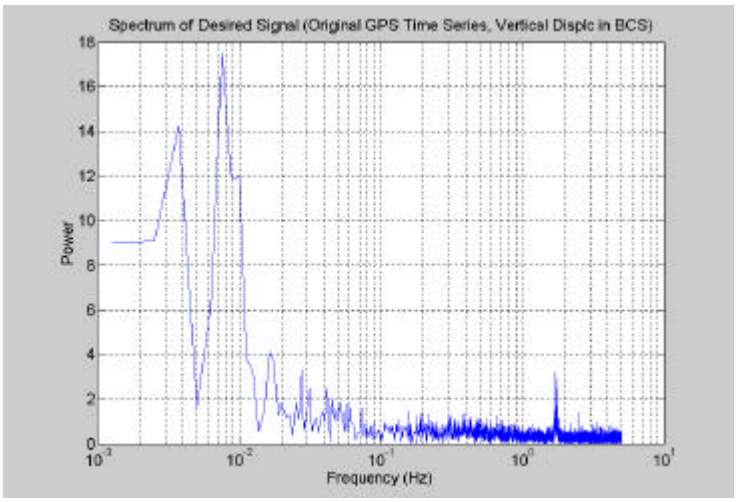

Fig. 8.32. Spectral distribution of desired signal

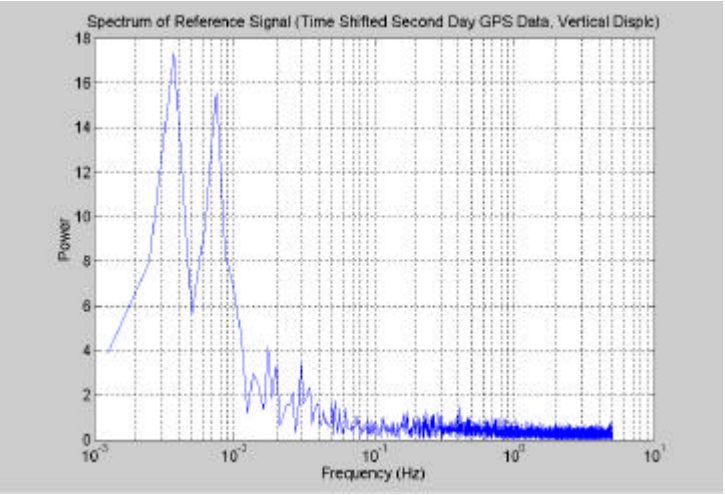

Fig. 8.33. Spectral distribution of reference signal

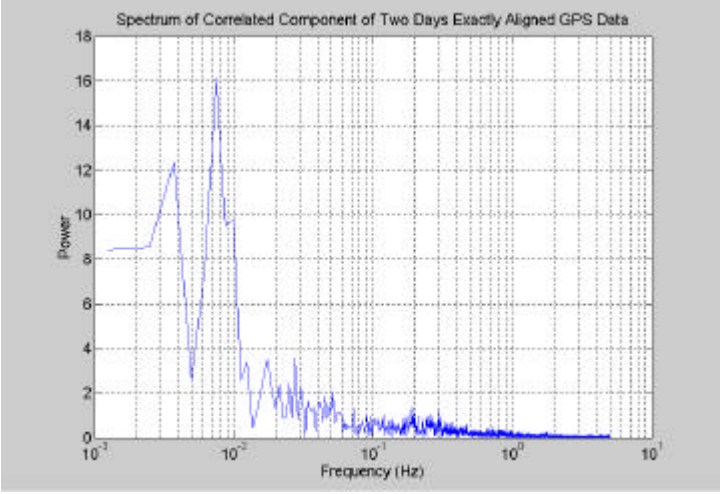

Fig. 8.34. Spectral of isolated multipath signature

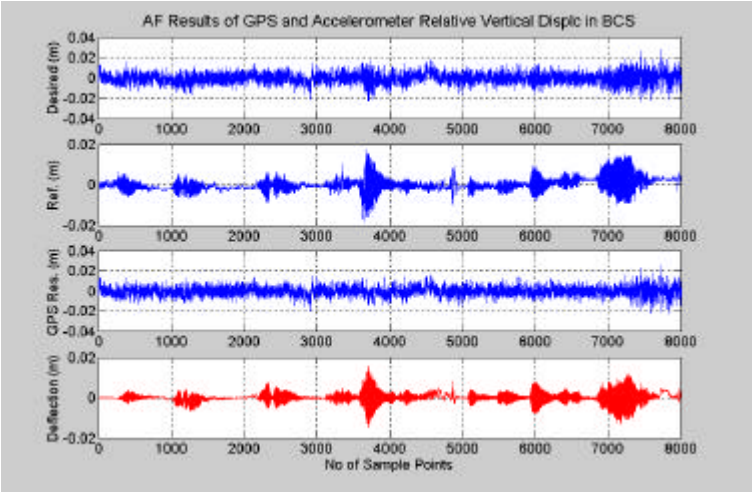

Fig. 8.35. Acceleration aided AF results with AF treated GPS positions

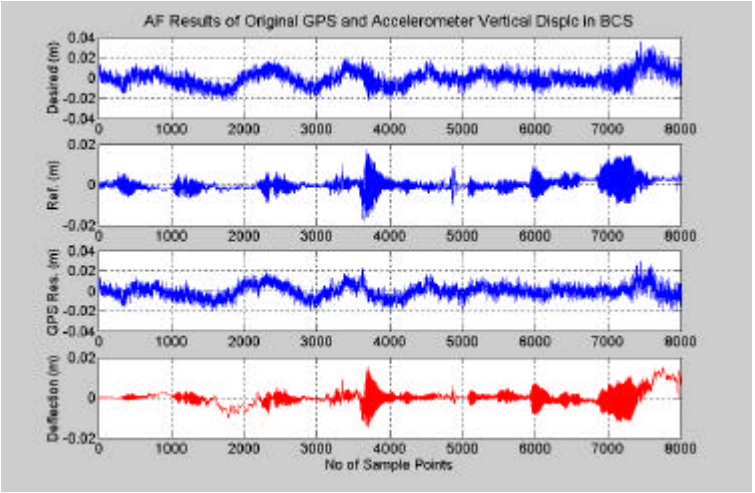

Fig. 8.36. Acceleration aided AF result with untreated GPS positions

Further analyses have been made on the spectrum distributions of the input and output signals of acceleration aided AF approach. Fig. 8.37 shows the spectrum of the desired signal, which is the third row in Fig. 8.31. Significant power reduction of multipath is realised compared with original vertical positions (Fig. 8.32). Fig. 8.38 is the spectrum of the reference signal of relative displacement from resampled acceleration. It is obvious that the resample procedure does not change the spectrum distribution of acceleration, which will not cause any solution distortion.

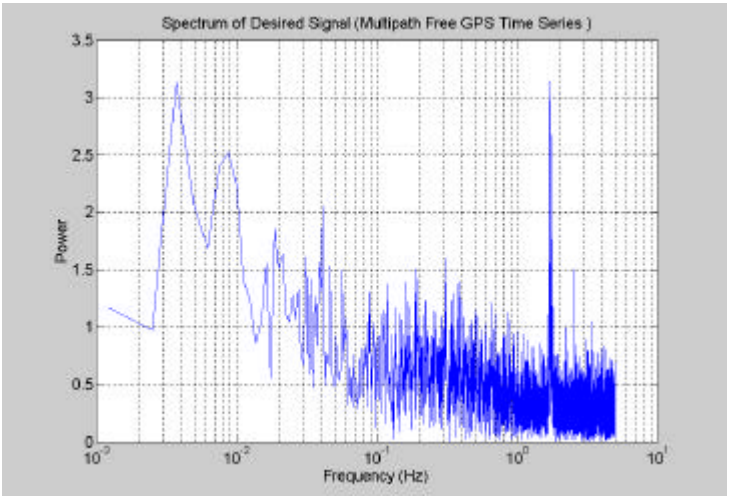

Fig. 8.37. Spectrum of desired signal (treated GPS data)

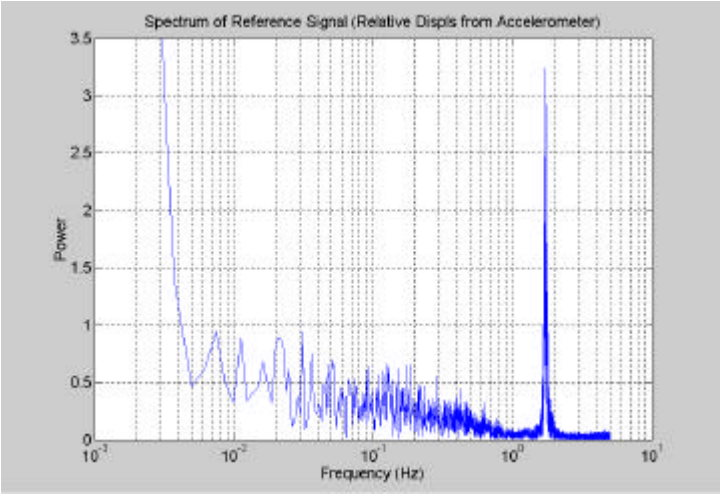

Fig. 8.38. Spectrum of reference signal (relative displacement)

The spectrum of GPS receiver noise via the AF procedure is illustrated by Fig. 8.39. It supplies an opportunity to further analyse the statistical nature of receiver noise. Fig. 8.40 is the final integrated relative displacement from the two sensors. It shows that the instrument related errors have been removed successfully through the above data processing. However, with this system, the detectable frequency is limited to the dominant frequency and other signatures are left undetectable. Further research is needed to answer why the frequencies identified by accelerometer and still within the GPS meaurable range of 5 Hz cannot be detected by GPS solutions.

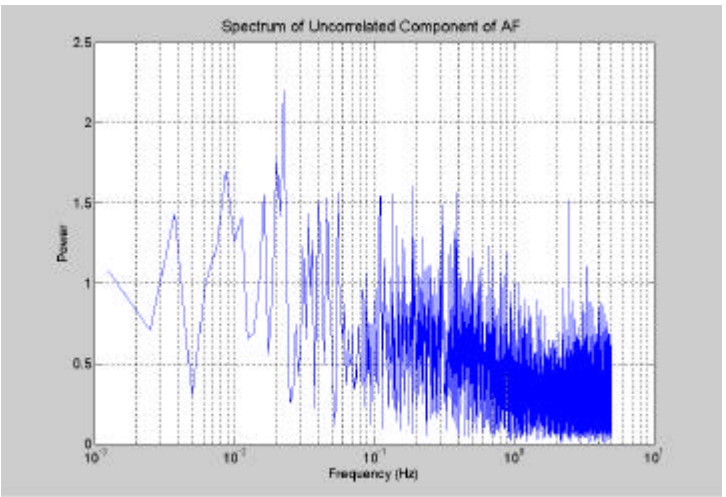

Fig. 8.39. Receiver noise signature

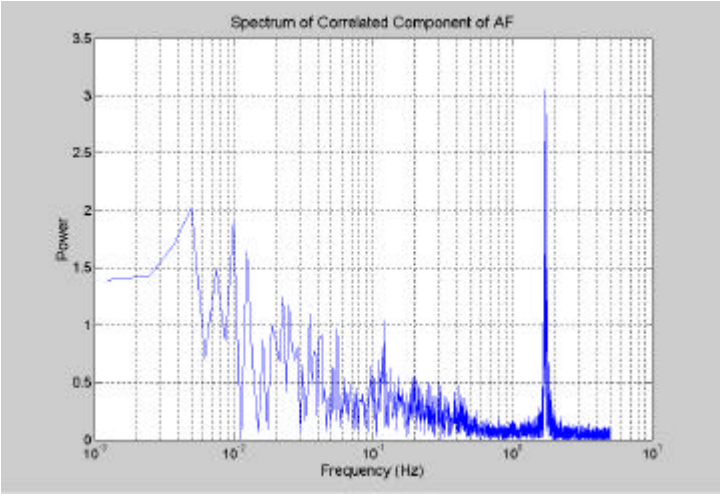

Fig. 8.40. Spectrum of the integrated system

8.6 Summary

Beginning with the comparison of different multipath mitigation techniques, this chapter presents a recursive AF approach used to isolate real bridge movement from receiver noise and multipath both at reference stations and monitoring sites. Spectral analysis is employed to detail the frequency bands of the input and output components. The bridge frequencies detected by GPS are compared with those from a triaxial accelerometer.

To obtain optimal AF output and significantly reduce multipath impact on GPS positioning solutions or raw measurements, exact time match between desired and reference signals is important to achieve maximum cross-correlation coefficients. The time shift of two continuous days' satellite repeatability is estimated on the each satellite basis, which can be used to align the pseudorange measurements. Also the time shift of whole satellite configuration in view is analysed with day-to-day kinematic positioning solutions. The positioning differences between the exactly and normally aligned data sets are used to demonstrate the importance of appropriate time series alignment.

A hierarchy of the proposed recursive AF approach can be summarised as follows,

- Residual multipath analysis at reference stations. The results can be used for the noise level evaluation at the receiver sites and help the selection of reference stations
- Kinematic positioning solutions from two consecutive days' measurements are used to remove reference stations relevant noise and multipath at each monitoring site
- Uncorrelated AF outputs of two days at same monitoring site from previous step are employed to mitigate monitoring site related multipath and receiver noise
- Uncorrelated AF outputs of two close monitoring sites on the same day from previous step are employed to mitigate monitoring site related multipath and receiver noise

A simple MA based algorithm is proposed to cope with the sensor drift according to filtering theory. The acceleration data are double integrated, resulting in relative displacements, which are then used to mitigate the GPS multipath with an AF approach. Results are analysed and the discussions on how to use this technique are made. Spectral analysis is applied to the input and output data resulted by an AF procedure to illustrate the efficiency of the AF approach through the comparison of the change of frequency distribution. The results reveal that significant quality improvements both on the GPS and accelerometer data sets have been achieved.

It is possible to use this method to analyse magnitudes of real structural movements, multipath, receiver random noise, relative tropospheric delay, and other error sources by exploiting their correlation characteristics. Relatively clean bridge deflection data sets can be obtained through such processes.

Chapter 9

Relative Tropospheric Delay and Its Estimation

9.1 Introduction

Atmospheric refractivity affects GPS measurements by introducing ionospheric and tropospheric delays. Since the impacts of ionospheric delay can be effectively removed by using the ionospheric-free linear phase combinations of dual frequencies and the fact that short baselines between reference stations and observation sites are used in GPS-based BDMS, ionospheric delay will not become the main error source. However, if not properly corrected or removed, tropospheric delay will cause position errors.

The effect of the neutral atmosphere is denoted as tropospheric delay. Because roughly 25% of the delay effect is introduced by atmospheric gases above the troposphere, i.e. stratosphere, in the most cases and to be precise, the term tropospheric delay used is somewhat of a misnomer (Spilker 1996). However, the dominant contribution of the troposphere explains the notation (Hofmann-Wellenhof et al. 1997). The troposphere produces attenuation effects that are generally below 0.5 dB and delay effects in the order of 2-25 m. These effects vary with elevation angle because lower elevation angles produce a longer path through the troposphere and also vary with the detailed atmospheric gas density profile over altitude.

Because the propagation of radio waves in the troposphere is frequency independent, a distinction between carrier phase and code range derived from different carriers L1 or L2 is not necessary. The disadvantage is that an elimination of the tropospheric refraction by dual frequency methods is impossible (Hofmann-Wellenhof et al. 1997).

There are two kinds of tropospheric delays, i.e. the delays caused by refraction of a dry and a wet component. Research reveals that about 90% of the tropospheric refraction arise from the dry component and about 10% from the wet component.

While it is easy to estimate the dry tropospheric delay to a high accuracy by using meteorological surface data, it is much more difficult to model the wet portion because of the strong variation of water vapour with respect to time and space. Models and physical approaches such as radio signal occultation have been developed to estimate wet tropospheric delay (Dodson et al. 1996; Hofmann-Wellenhof et al. 1997; Kleusberg 1998). The time-varying zenith delay observed at each GPS receiver in a network can be further transformed into an estimate of the precipitable water overlaying that receiver for meteorology purpose (Bevis et al. 1994).

Compared with other applications, GPS-based bridge deformation monitoring has the following characteristics:

- There is significant height difference between the reference and monitoring sites, which could reach several hundred metres, for instance, the height difference between the bridge towers and deck is 155.5m for the Humber Bridge and 282.8m for the Akashi Kaikyo Bridge
- The meteorological conditions (atmospheric profiles) are different between the bridge towers and deck as well as the reference stations closely located to the bridge, for instance, the differences of the surface pressures, humidity, and temperature are different due to the altitude or local microclimate differences.

For improving the positioning accuracy, local weather stations are setup to collect meteorological parameters. The data from limited locations then are extrapolated to obtain the estimates of the meteorological data at other sites based on their altitudes. These data can be used as inputs for the tropospheric models in the data processing.

In Section 9.2, the kinematic solutions at two reference stations are employed to analyse the interference of relative tropospheric delay, multipath, and receiver noise on the coordinates. Moving average approach is used to detect the contributions from different error sources. Relative tropospheric delay is recognised as the major impact factor responsible for the *movement* of an amplitude of 4 centimetres at a reference station. The impacts of the relative tropospheric delay on the positioning solutions have been further explored using the data sets collected at several different locations of reference stations as well as from the bridge sites. Then comparisons have been

made regarding the relative tropospheric delays estimated from kinematic OTF positioning, a standard model (MAGNET), solutions without tropospheric model applied, and the real-time estimates by AF approach. Similar delay patterns have been obtained and further confirm that relative tropospheric delay has its particular pattern in the context of bridge monitoring. Independent estimate of relative tropospheric delay from a permanent station also suggests this deduction. Since the height differences between stations are within several tens of metres and will not introduce such an amplitude delay according to tropospheric propagation theory, microclimate effect is recognised as the major contributor. This is further proved by a numerical example and the results calculated with the real meteorological data collected along with GPS data and from a weather station at the IESSG, which is introduced in Section 9.3. AF approach is proposed to extract relative tropospheric signature from a reference station group comprising four GPS receivers with each two receivers closely setup at the each end of a baseline in Section 9.4.

9.2 Distinguishing Between Multipath and Relative Tropospheric Delay

Fig. 9.1 is an example of the height time series in a BCS. The data sets illustrated here were collected from the Wilford footbridge trial on 21 February 2001 at two reference stations, with one on the top of Tower Building on the university campus and another one on Base1 on the riverside. The data were processed in kinematic OTF mode by fixing the station on the Tower Building as reference station and Base1 as a rover. The detailed description about this trial is in Section 5.3.4. The apparent height fluctuation of about 4cm amplitude is evident for such a short baseline. The possible impacting factors might be either multipath on reference stations or tropospheric delay caused by the local microclimate. This result emphasises the need to further study and distinguish the nature of error sources before proper error mitigation or modelling approaches could be applied to the data sets.

Fig. 9.2 is the spectral distribution of the height movements of the data set illustrated in Fig. 9.1. The frequencies characterising the signature of multipath or tropospheric

delay vary between 50 seconds to 16.67minutes. However, it is still hard to identify the nature of the error sources.

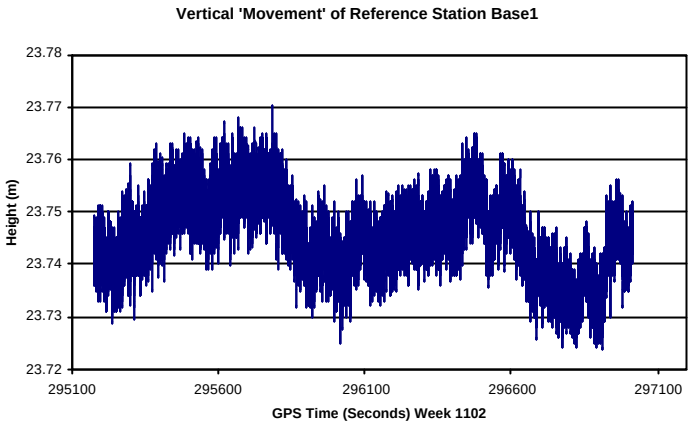

Fig. 9.1.Vertical movements at reference stations (21 Feb 2001)

In order to study the above effects, two reference stations on the top of the Tower Building (Tower) and the IESSG building (IESSG) were employed together with other two reference stations (Base1 and Base2) located next to the bridge. The data sets were collected on 21 February 2001. The coordinates of these four points were accurately determined using long-term static measurements before kinematic OTF data processing was conducted. The height differences between IESSG and Base2, and Tower and Base1 are about 27m and 63m, respectively.

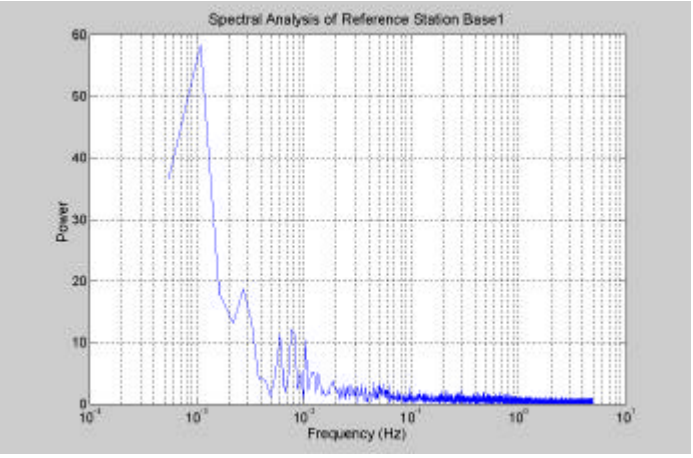

Fig. 9.2. Spectrum of the data set used by Fig. 9.1

The reference station on the IESSG building is one of the UK tide gauge monitoring stations, which conducts continuous measurement using an Ashtech Z12 dual frequency receiver (NOTT) at a sampling rate of 30 seconds. The receivers used on

Tower, Base1 and Base 2 were three Leica SR530 dual frequency receivers gathering raw GPS code and carrier phase data at a data rate of 10 Hz. Each epoch kinematic positioning solutions were obtained between the stations on the campus and riverside independently by setting the two riverside reference stations as rovers and two receivers on the campus as reference stations. For comparison purpose, the data from three Leica receivers were resampled to the same rate as that of the Ashtech receiver.

Fig. 9.3, 9.4, and 9.5 are examples of the coordinate comparisons. In these graphs, mean coordinate fluctuations of about 5cm, 2.5cm, and 7cm for X, Y, and Z axes respectively in WGS84 are apparent. The Cross-correlation coefficients of each pair of time series are 0.83, 0.78, and 0.69. Since these four reference stations were located in relatively open environments with low multipath signature and chokering antennas were used at the four stations, these coefficients should reveal significant evidence of relative tropospheric delay.

Further investigations into the multipath signature were conducted by using day-to-day mean vertical movements of Base1 by fixing NOTT as reference station (Fig. 9.6). The data sets were collected on 20 and 21February 2001 and the time tag of 21 February is shift to 20 February 2001. The cross-correlation coefficient of the two time series is 0.16 and illustrates low multipath signature between the two observation stations. It further proves that the fluctuations of the positioning solutions in the previous graphs are mainly caused by the relative tropospheric delay. Since the height differences between stations are within 70 meters, these results demonstrate that the relative height differences between stations have less effect than that of the local microclimate in this particular case.

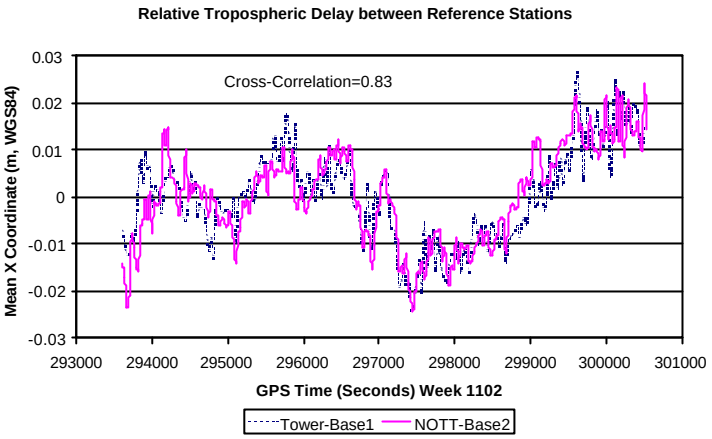

Fig. 9.3. Relative tropospheric delay on X coordinate

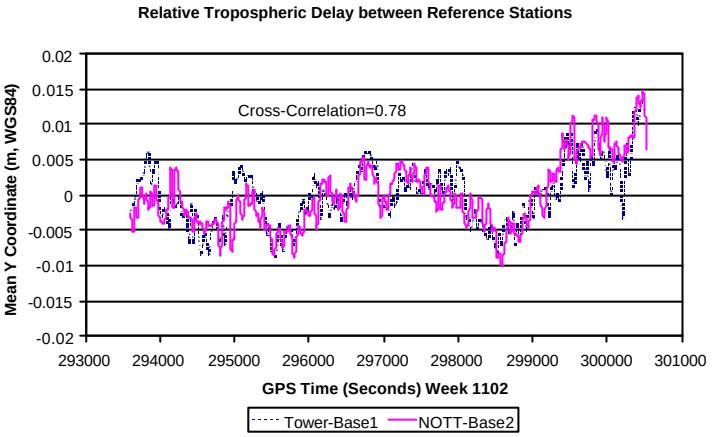

Fig. 9.4. Relative tropospheric delay on Y coordinate

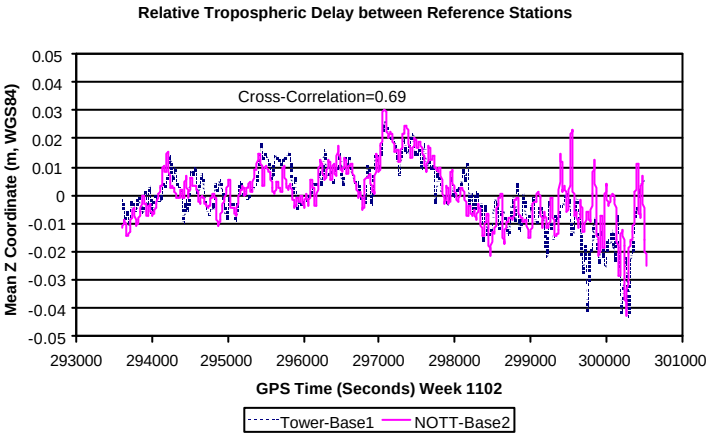

Fig. 9.5. Relative tropospheric delay on Z coordinate

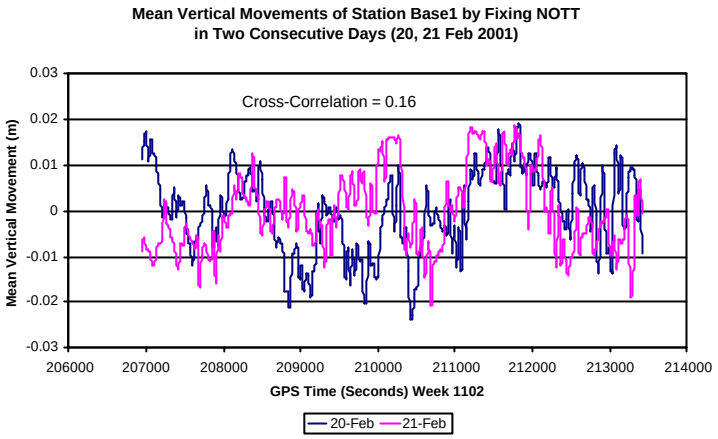

Fig. 9.6. Multipath signature comparison in two days at Ref. Stn.

If this relative tropospheric delay cannot be correctly modelled or removed, the possible results will exhibit an apparent movement as in Fig. 9.1 when there is no actual movement at all. This effect could cause problems when nearby reference stations are used for calculating bridge deflections.

Fig. 9.7 is the mean X coordinate comparison between stations to demonstrate the effect of relative tropospheric delay on the time series at the bridge site. The data sets used here were collected on 20 February 2001. The kinematic positioning solutions of Base1 and Base2 are calculated by fixing NOTT as reference station and the positions of midspan station are estimated by fixing a Leica GPS receiver at P4 on the turret of the IESSG Building as a reference station. Fig. 9.8 illustrates the kinematic positioning solutions of the three rovers, i.e. Base1, Base2, and Mid1 by using the Leica receiver at P4 as reference station on the same day. The similarity in each epoch's position at different rover stations using different reference stations further proves that these fluctuations in coordinates are not introduced by the real bridge movements. This also excludes the potential errors caused by phase centre variation which will occur since the data sets are collected by two types of receivers. It can be concluded that due to the different reflection environments at the riverside stations (Base1) with those on the bridge deck (Mid1), these patterns of slow movements are not caused by multipath. Hence, relative tropospheric delay can be recognised as the major error source in this particular circumstance. Further research is needed to use meteorological data from weather stations in the GPS data collection.

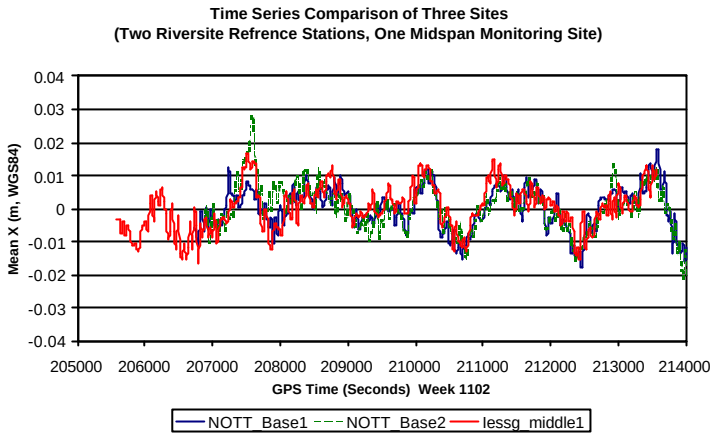

Fig. 9.7. Validating patterns of relative tropospheric delay on X coordinate

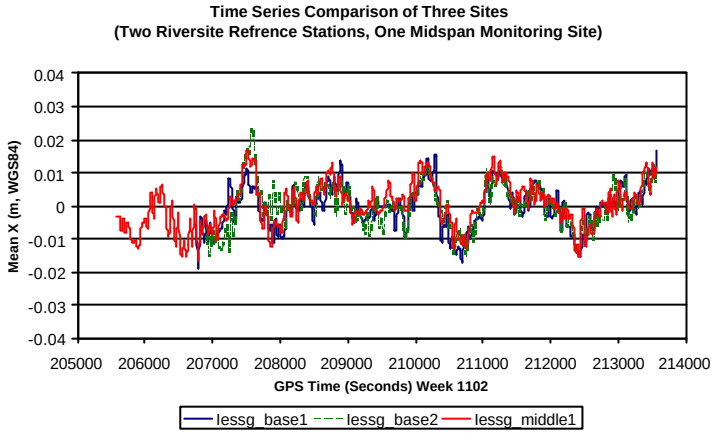

Fig. 9.8. Validating patterns of relative tropospheric delay on X coordinate

Fig. 9.9 is the result comparisons of different tropospheric delay models using the data sets from the Tower Building and Base1 collected on 21 February 2001. Similar patterns in the mean vertical components are obtained from a Hopfield model (SKI-Pro internal model), a standard global model (MAGNET), solution from SKI-Pro without a model applied, and the one from AF approach.

The MAGNET model uses the station latitude, height, and Julian day to estimate meteorological data and hence avoids any error being introduced through poor calibration of instruments or misreading of data (Baker, 1998). KINPOS software developed by the IESSG is used to create relative tropospheric delay with the MAGNET model.

One important conclusion that can be drawn from this comparison is that AF is a reliable approach for the estimation of relative tropospheric delay, which will be

further explored in this chapter. It reveals that when the Hopfield model is applied for data processing, the relative tropospheric delay cannot be eliminated properly in this case due to the differences in the local microclimate at the two ends of the processed baselines. The incorrect meteorological data used by model cannot simulate the actual scenarios and hence cannot effectively remove this relative tropospheric delay.

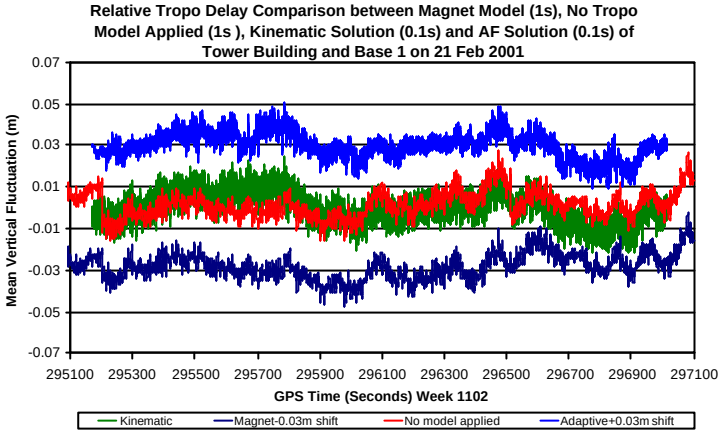

Fig. 9.9. Mean vertical movement comparison with different trop. delay models

While Fig. 9.9 depicts the similar patterns of the mean movements by different models, Fig. 9.10, 9.11, and 9.12 show the absolute coordinate time series in BCS, which reflect the impacts of relative tropospheric delay on the 3D coordinates. Relative tropospheric delay will not introduce significant coordinate differences in the lateral and longitudinal directions in a BCS. However, it causes about 4.8cm drifts between the time series by KINPOS with MAGNET model, and SKI-Pro kinematic model with or without tropospheric delay model applied. Without the correction from the model, the receivers measured a short path between satellite and receiver and hence an elongated height. It seems that the MAGNET model could only make partial corrections to the relative tropospheric delay and more corrections have been made on the height by SKI-Pro software with a built-in model. Further research in this field is required to find an effective way to cope with relative tropospheric delay.

Owing to the limitation of SKI-Pro in processing long period measurements at a 10 Hz sampling rate, only part kinematic solutions are illustrated in Fig. 9.10, 9.11, and 9.12. The data rate of the solutions of KINPOS and SKI-Pro without model applied is 1 Hz. Same raw measurements are used in the data processing.

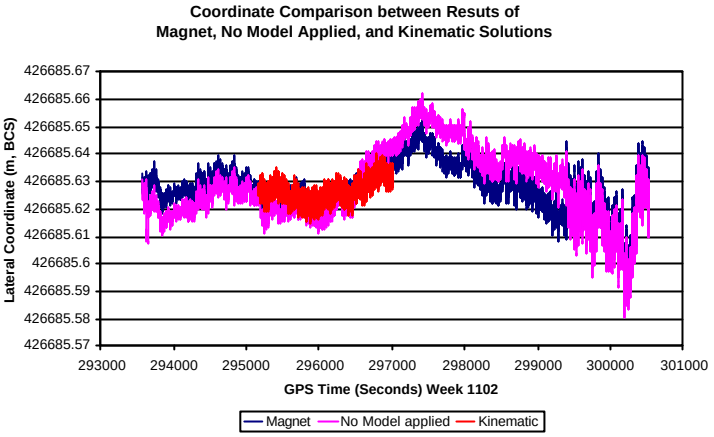

Fig. 9.10. Lateral coordinate with different trop. delay models

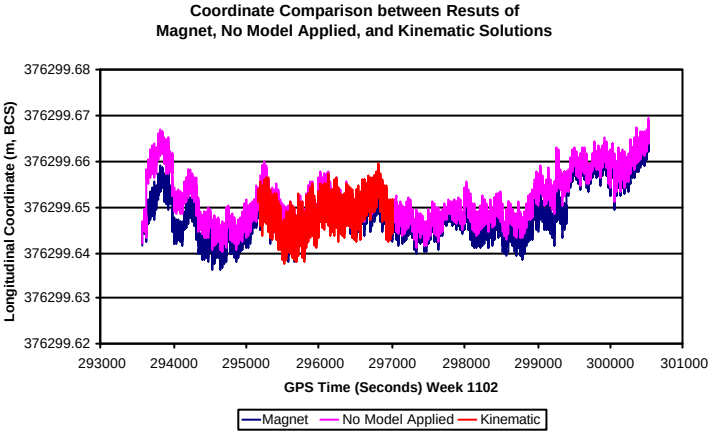

Fig. 9.11. Longitudinal coordinate with different trop. delay models

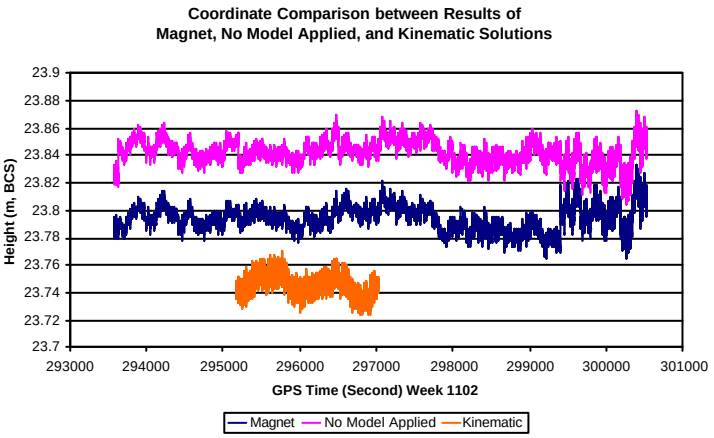

Fig. 9.12. Height time series with different trop. delay models

9.3 Numerical Examples of Local Microclimate Effect to Relative Tropospheric Delay

To verify the effects of relative tropospheric delay and its influence on the structural deflection monitoring, a mathematics derivative has been conducted. Hopfield model and actual meteorological data collected at NOTT and bridge sites are used to create numerical examples of relative tropospheric delay.

Eq. 9.1 and 9.2 are the absolute dry tropospheric delay expression according to Hopfield model at two observation sites A and B (Hofmann-Wellenhof et al. 1997)

$$\Delta_d^{trop}(A) = 10^{-6} N_{d,0}^{trop}(A) \frac{1}{h_d^4} \int_{h=h_A}^{h=h_{d(A)}} (h_d - h)^4 \, dh = 10^{-6} N_{d,0}^{trop}(A) \frac{(h_{d(A)} - h_A)^5}{5h_{d(A)}^4} \tag{9.1}$$

$$\Delta_d^{trop}(B) = 10^{-6} N_{d,0}^{trop}(B) \frac{1}{h_d^4} \int_{h=h_B}^{h=h_{d(B)}} (h_d - h)^4 \, dh = 10^{-6} N_{d,0}^{trop}(B) \frac{(h_{d(B)} - h_B)^5}{5h_{d(B)}^4} \tag{9.2}$$

under the assumption of single polytropic layer with thickness at each site of

$$h_{d(A)} = 40136 + 148.72(T(A) - 273.16) \tag{9.3}$$

$$h_{d(B)} = 40136 + 148.72(T(B) - 273.16) . \tag{9.4}$$

Dry refractivities at site A and B can be estimated by

$$N_{d,0}^{trop}(A) = c_1 \frac{p(A)}{T(A)} \tag{9.5}$$

$$N_{d,0}^{trop}(B) = c_1 \frac{p(B)}{T(B)} \tag{9.6}$$

where $c_1 = 77.64[\frac{K}{mb}]$

and p is the atmospheric pressure in millibars (mb) and T is the temperature in Kelvin (K).

Relative tropospheric delay could then be estimated by Eq. 9.7.

$$\nabla\Delta_d^{trop}(AB) = 10^{-6} N_{d,0}^{trop}(A)\frac{(h_{d(A)} - h_A)^5}{5h_{d(A)}^4} - 10^{-6} N_{d,0}^{trop}(B)\frac{(h_{d(B)} - h_B)^5}{5h_{d(B)}^4}. \tag{9.7}$$

Suppose $T(A)$=12°C, $T(B)$=11°C, $p(A)$=1000mb, $p(B)$=1002mb, h_A=40m, h_B=20m above the earth surface, then $\nabla\Delta_d^{trop}(AB) = 2.272 - 2.282 = -1.0$ cm.

This vertical delay is calculated under an ideal condition by neglecting the curvature of the signal path and assuming the integral of path delay can be solved along the vertical direction. Calculation with Saastamoinen model with same parameters suggests there is about 2.0cm delay caused by the difference in altitudes which is similar to the result estimated by Hopfield model under an actual condition. So, if tropospheric model (e.g. Saastamoinen model) is not applied, a height error of up to 1mm per metre of altitude difference arises. Even if a tropospheric model is applied in the data processing, a height error of about 0.1mm per metre of altitude difference still exists due to any unmodelled biases (Bingley 2002). Hence, other approach is needed to cope with such biases, which is discussed in Section 9.4.

Compared with the actual movements of the structure at amplitude of several centimetres, this relative tropospheric delay is not a relatively small or insignificant value, even with only a few tens of metre height difference between the two stations due to the local microclimate effects. It further proves that the local microclimates are playing a very important role in producing relative tropospheric delay.

Using the meteorological data and above formula, a Matlab script is used to calculate tropospheric delay profile at station NOTT. Also, this script is used to estimate the relative tropospheric delay between NOTT and bridge sites at specific times when meteorological data were collected at bridge sites. Fig. 9.13, Fig. 9.14, Table 9.1, and Table 9.2 illustrate the results of these analyses for two days on 20 and 21 February 2001. The maximum relative tropospheric delay is about 3cm on 20 February and also 3cm on 21 February for the discrete sampling time. It shows the possibility of removing the tropospheric delay from the time series in a near real time mode using the meteorological data collected at a permanent station of sampling rate 30 seconds. The requirement is to setup a weather station at the bridge site.

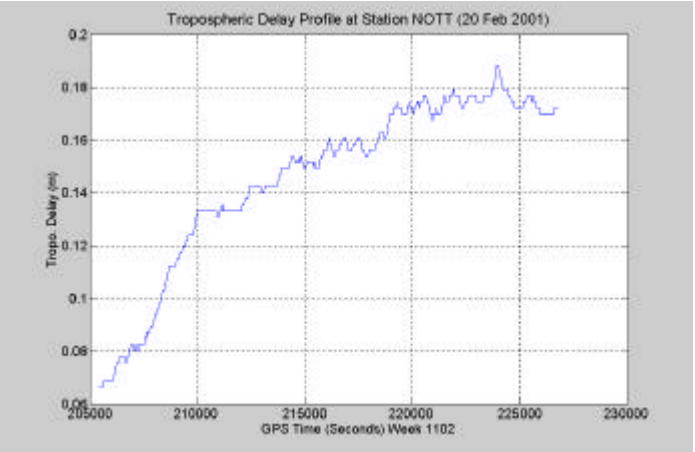

Fig. 9.13. Trop. delay profile at station NOTT (20 Feb 2001)

Obs. No.	Time	Humidity (%) Bridge/NOTT	Temperature (°C) Bridge/NOTT	Pressure (mb) Bridge/NOTT	Relative Trop. Delay (m)
1	10:58	71.9/79.8	6.9/6.0	1032.4/1030.4	-0.030
2	11:49	68.1/74.2	7.5/6.6	1032.2/1029.7	-0.019
3	12:26	64.7/71.1	7.8/6.9	1031.7/1029.2	-0.019
4	13:31	63.8/68.9	8.0/7.4	1031.0/1028.4	-0.017
5	14:24	60.2/67.2	9.5/7.8	1030.5/1027.8	-0.013
6	14:48	63.8/68.5	7.8/7.5	1030.2/1027.7	-0.020
7	15:00	65.1/69.5	7.7/7.4	1030.2/1027.7	-0.020

Table 9.1. Relative tropospheric delay using a Hopfield model (20 Feb 2001)

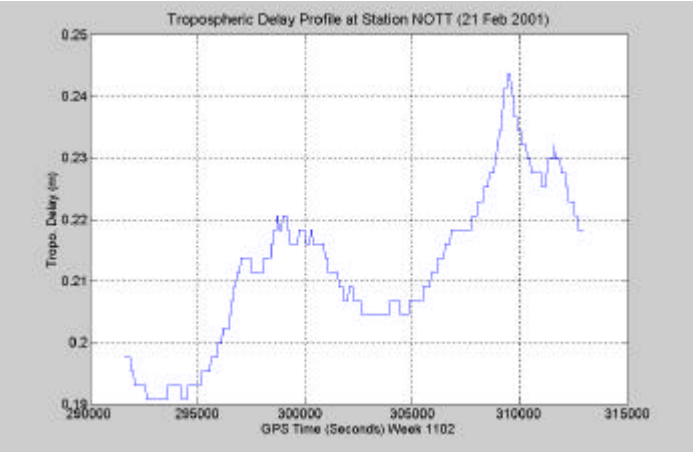

Fig. 9.14. Trop. delay profile at station NOTT (21 Feb 2001)

Obs. No.	Time	Humidity (%) Bridge/NOTT	Temperature (°C) Bridge/NOTT	Pressure (mb) Bridge/NOTT	Relative Tropo. Delay (m)
1	10:10	73.0/84.5	10.6/8.6	1025.7/1023.5	-0.023
2	10:21	71.4/83.9	11.1/8.8	1025.8/1023.6	-0.022
3	10:33	72.6/80.7	10.4/9.3	1025.7/1023.6	-0.027
4	10:54	72.4/81.0	10.7/9.3	1025.3/1023.1	-0.024
5	11:05	74.3/80.5	10.5/9.6	1025.4/1023.2	-0.025
6	11:16	69.9/80.6	12.6/9.4	1025.4/1022.3	-0.023
7	12:34	73.3/82.5	10.0/9.0	1024.8/1022.7	-0.027
8	12:49	76.9/82.1	9.5/9.0	1024.5/1021.4	-0.028
9	13:26	73.5/79.0	10.6/9.5	1024.2/1021.9	-0.022
10	14:02	70.9/76.4	11.2/10.6	1023.8/1021.1	-0.013
11	14:20	69.4/79	12.0/9.9	1023.6/1021.0	-0.013
12	15:25	76.6/82.3	10.3/9.7	1022.9/1020.9	-0.029

Table 9.2. Relative trop. delay using a Hopfield model (21 Feb 2001)

A similar approach as pseudorange/phase double differencing can be employed to analyse and remove the error components through double differencing of the relative tropospheric delay.

Assuming the two closely located reference stations near the bridge site A (as Base1) and B (as Base2), and two other reference stations i (NOTT) and j (Tower) located a few kilometres away, single difference of the error equations may be formed

$$v_A^i = (R^i - R_A)_{receiver} + (M^i - M_A)_{multipath} + \nabla\Delta_{iA}^{trop} \tag{9.8}$$

$$v_B^i = (R^i - R_B)_{receiver} + (M^i - M_B)_{multipath} + \nabla\Delta_{iB}^{trop}. \tag{9.9}$$

Where R denotes receiver noise at both ends of a baseline; M refers to multipath at the observation sites. Since the two GPS receiver pairs at both ends are closely setup, the relative tropospheric delay $\nabla\Delta^{trop}$ could be reasonably assumed be the same.

Single differences at reference stations i and j can be expressed as

$$\Delta v_{AB}^i = (R_B - R_A)_{receiver} + (M_B - M_A)_{multipath} \tag{9.10}$$

$$\Delta v_{AB}^j = (R_B - R_A)_{receiver} + (M_B - M_A)_{multipath}. \tag{9.11}$$

Single difference of Eq. 9.10 and 9.11 is

$$\nabla\Delta v_{AB}^{ij} = 0! \text{ (Theoretically!)} \tag{9.12}$$

Fig. 9.15 is an example of double differencing the error time series to mitigate relative tropospheric delay. The four observation sites used for this example are NOTT, Tower Building, Base1, and Base2 and the data used are the vertical time series calculated from the data sets on 21 February 2001. The vertical component has the worst precision in 3D positioning solutions. It shows that most relative tropospheric delays have been removed via the proposed double differencing. Through this example the potential use of the nearby permanent GPS stations used by other applications with a reasonable sampling rate in the formation of so-called group reference stations to further achieve millimetre or even sub-millimetre accuracy in 3D could be predicted.

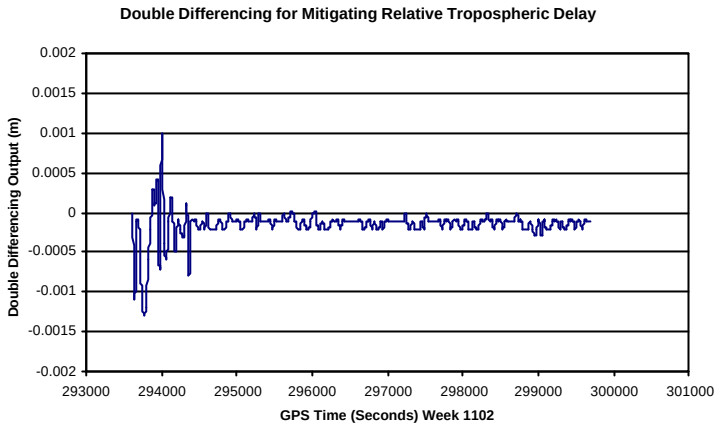

Fig. 9.15. Removal of relative trop. delay by double differencing approach

9.4 Real-time Relative Tropospheric Delay Estimation Using AF Approach

Since the positioning time series are greatly degraded by relative tropospheric delay and they are highly correlated if the proposed group reference stations is used, an AF approach can be employed to properly decompose the correlated parts from these time series in a real-time mode. The benefit is that using this correlation, relatively clear positioning time series can be extracted from the original positioning solutions polluted by tropospheric delay and relative tropospheric delay pattern could be further explored for meteorological applications. Fig. 9.16 is the output of AF approach with kinematic time series at the Mid1 as the desired signal and the another kinematic output at one of the riverside reference station as the reference signal. Both positioning solutions were obtained by fixing a receiver on the Tower Building as the reference station. According to AF theory, the third row in this graph (signal out) is the time series which is only relevant to the desired signal and the fourth row (common part, or correlated part) is the decomposed time series of the relative tropospheric delay between the reference stations on the campus and observation stations on the bridge. Standard deviations of these four time series are 6.7mm, 7.3mm, 3.6mm, and 5.7mm respectively. It reveals that through AF there is about a 46% precision improvement in the coordinate quality due to the proper relative tropospheric modelling.

Similar numerical analysis as discussed in Section 9.3 of this chapter could be applied to estimate the wet part of tropospheric delay. However, the requirement in applying the same algorithm is on the ability to measure the partial pressure of water vapour and this in most cases is not feasible since the cost in data collection is simply too high due to very expensive instruments and manpower fees. Hopfield model is used to estimate the dry part of tropospheric delay with the surface atmospheric pressure and temperature collected by relatively cheap weather stations. The total delay can be estimated via adaptive filtering. The wet part can then be accurately estimated from the differences of total delay and dry part. It is possible to conduct real-time estimation of the wet part delay and furthermore the weather can be predicted at the same rate as that of the current GPS sampling rate. The only requirement is to setup small weather stations at both ends of a baseline with the capability of logging the atmospheric pressure and temperature at required sampling rate.

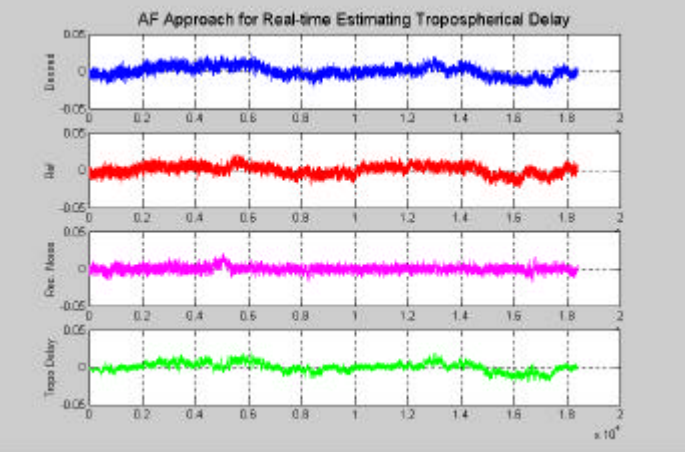

Fig. 9.16. AF-based real-time estimation of relative trop. delay

9.5 Summary

Relative tropospheric delay is recognised as a major error source in GPS-based BDMS. Height differences are usually recognised as a main contributor responsible for such delay. However, for Nottingham Wilford suspension footbridge, the height differences between the two reference stations of 3.6km plane distance are several tens of meters but the kinematic positioning solution of a reference station near bridge characterises an apparent moving pattern of 4 centimetres. Multipath impact has been excluded out from the potential impact factors by using the cross-correlation

coefficients and amplitudes of day-to-day positioning solutions at reference stations. Local microclimate is identified as the major impact factor for the relative tropospheric delay. Numerical examples using the actual meteorological parameters collected at both reference stations also present the similar amplitudes of relative tropospheric delay. Using AF approach, a real-time relative tropospheric delay estimation is illustrated and its potential meteorological applications are predicted.

Chapter 10

Conclusions and Recommendations

10.1 Conclusions

The main research objectives were to

- Develop a prototype of a hybrid BDMS to achieve positioning solutions to an accuracy of a few millimetres on the each epoch basis with the current GPS technology aided by triaxial accelerometers.
- Quantify the measurement qualities of the instruments used in a hybrid BDMS
- Define appropriate coordinate systems and associated transformations to realise the data integration between GPS and accelerometer
- Improve 3D accuracies of kinematic GPS positioning solutions in a BCS
- Mitigate the impact of multipath and isolate real deformations of the monitored bridge using a real-time AF approach
- Reduce the interference of relative tropospheric delay on position solutions

The above topics were addressed in the individual chapters of this thesis. The main achievements are summarised as follows

- A Hybrid BDMS consisting of GPS receiver and triaxial accelerometer is a viable technique for achieving 3D positioning accuracy of a few millimetres in a BCS and with appropriate data filtering more accurate positioning solutions can be anticipated. The proposed system can be used to monitor long-term bridge deformation and short-term deflection
- ZBL tests of three types of Leica GPS receivers, i.e. the CRS1000 and SR530 dual frequency receivers, and the SR510 single frequency receiver with associated antennas, reveal that the internal accuracy is a centimetre for the CRS1000 receivers with the available receiver firmware at the time the tests were made (Leica, 2001), millimetre is available for the SR530

and SR510 receivers. SBL tests demonstrated a good performance of whole receiver system. It illustrated that the baseline residuals of SBL tests with SR510 receiver can be less than 5mm after an MA filter is applied. The time lags estimated from autocorrelation of positioning solutions can be further employed to the design of the filter length of an optimal AF filter.

- Coordinate frames were defined a hybrid BDMS. BCS is recommended as the reference for data integration and analysis owing to its engineering significance. The algorithms of coordinate transformations were proposed and an approach for the attitude determinations of the instantaneous body frame of accelerometer was recommended. A specially designed cage for housing a GPS antenna and a triaxial accelerometer was introduced. Its benefits were analysed in terms of the reduction of computation burden and complexity of sensor system.
- Bridge trials provide the opportunity to validate the reliability and productivity of the whole proposed system. Efficient system configuration, data collection procedure, and data processing were suggested in this thesis. The problems encountered in the fieldwork and data processing helped the improvements of a BDMS and the investigation to address these problems forms the kernel of this thesis.
- The impact of the current GPS satellite sky distribution on the positioning solutions was analysed, especially on the positioning accuracy in the north direction. A ranging error propagation scheme was derived analytically in a BCS. The remedies were proposed to cope with this defect of GPS satellite sky distribution. Data processing to the Humber Bridge trail suggested that the integrated system of GPS and GLONASS could effectively improve the positioning solutions in the north direction, which is the main axis direction of the Humber Bridge and London Millennium Bridge. Based on the analytical derivation, a Matlab simulator was developed to simulate the improvement of positioning solutions through the calculation of DOP values. Guidelines for the selection of the optimal location of pseudolites to achieve the accuracy improvement in specific direction in a BCS were setup according to the results of the simulations.

- A hierarchy consisting of a recursive AF filer and a real-time AF software package based on LMS was applied to the data processing. Spectral analysis and statistic approaches have been employed to validate the results in each filtering procedure. The components of positioning solutions have been successfully isolated by the proposed approach. Acceleration aided AF was studied in the thesis. The algorithm based on filtering theory was used to address the errors of the accelerometer. The relative displacements calculated by the acceleration integral were employed as the reference signals and successfully used to extract the time series of real bridge deflection.
- Relative tropospheric delay is characterised by a positioning error of several centimetres and become a major error source when off-site reference stations are used. The way to distinguish the contribution of multipath and relative tropospheric delay was discussed and the difference in the local microclimate was recognised as the major contributor for the positioning error. Results from different models and numerical calculation using actual meteorological data further verified relative tropospheric delay was the major impact factor. An AF approach to isolate relative tropospheric delay and its potential application in the estimation of wet part of tropospheric delay were proposed.

10.2 Recommendations

The focus of this thesis was on how to effectively improve the positioning accuracy to meet the requirement of monitoring bridge deformations characterising long-term deformations and short-term deflections. Theoretical analyses and field experiments were conducted in this research and some recommendations for a prototype BDMS are made and summarised as follows.

- As demonstrated in Chapter 3, ZBL tests were employed to quantify the internal accuracy of the different types of GPS receivers. It illustrated the importance in updating receiver firmware to assure the stable receiver performance. Autocorrelation coefficients of coordinate time series were used to describe the statistic characteristics of GPS positioning solutions.

The time lags estimated from ZBL and SBL tests are the indicators of the frequency distribution of internal and external error sources. These values can be used to determine the filter length of an AF for isolating the errors located at different frequency bands.

- The most important parameters used in the selection of triaxial accelerometer recognised in this research are the measuring range of the expected peak value of acceleration, sensitivity, and frequency range. The proposed calibration should be conducted within a stable environment and the temperature data should be recorded.
- In Chapter 4, two approaches were proposed to determine instantaneous attitude of a bridge deck. The approach using the measurements from three adjacent GPS receiver sites was recommended to estimate attitude of the local bridge deck since it is very difficult to find an initial condition with quasi-static movement of a bridge.
- In Chapter 5, a simulator was developed to select the locations of pseudolites under the scenario of the monitoring of the London Millennium Bridge. It is recommended that for other bridge monitoring, the location of the observation sites, modified GPS ephemeris, and the local topography can used as the input data to the simulator. The number and the locations of pseudolites should then be determined based on the orientation of the bridge main axis, accuracy requirements, and the deformation magnitudes in 3D.
- In Chapter 7 and 8, recursive AF approach was applied to the coordinate time series to isolate each individual component. It is recommended that the filter length should be determined by the statistic nature of the coordinate time series from specific GPS receivers. The convergence parameter can then be determined by the filter length, number of samples, and the autocorrelation of the reference signal into an AF system.
- If AF is applied to the coordinate time series, the total time shift of day-to-day GPS satellite constellation can be employed to align the input signals. Otherwise, individual time shift should be considered to align raw pseudorange measurements of each satellite in view.

- With the resolution of integer ambiguity, it should be possible to use AF approach to mitigate errors in the carrier phase measurements. It was demonstrated that the relative displacements estimated by the proposed algorithm can act as the reference signal sequence. The resampling procedure might reduce the magnitudes of the accelerations whilst it can filter outliers. The tuning factors determined by the original and resampled accelerations should be applied to the resampled data set to cope with these reductions.
- An AF approach is different from a data fusion algorithm in that it can only result an output time series at the GPS sampling rate. From AF process, other error sources can be extracted whilst a data fusion process can only provide positioning solutions. However, since the data rate of the data fusion can be as fast as the data rate of an accelerometer, the positioning solutions can be used to detect the whole frequency bands of a bridge deformation. As a major objective of AF, multipath mitigation can be realised in practice either on-line by the extracted multipath template stored inside the GPS receivers or by post-processing the coordinate time series.
- In Chapter 9, AF approach was recommended to mitigate the unmodelled relative tropospheric delay caused by the differences in altitude or local microclimate at two ends of a baseline when off-site reference stations were employed to increase the productivity and robustness of a whole monitoring system. In practice, the extracted relative tropospheric delay template from an AF system can be applied to the coordinate time series from the bridge sites to reduce the effect of relative tropospheric delay.

10.3 Future Work

This thesis focused on the viability of a centimetre positioning accuracy in three dimensions with the proposed hybrid BDMS. Whilst it presented some initial findings, the future work is recognised as follows

- The data supporting this research were collected from a small suspension bridge with limited magnitudes of movements. These deformations have

not caused significant problems in integer ambiguity resolution. However, when the system is employed to monitor long span suspension bridges with several metre deformations as the Akashi Kaikyo Bridge and especially when single frequency receivers are used, detection and repair of cycle slips and integer ambiguity resolution caused by the ambient environment should be further studied.

- As AF approach has been successfully used to isolate the components from the time series with high level correlation, its capability to process the time series with large deformation is required to be further studied. In this case, the multipath signature will be buried by actual bridge movements but still contaminates the quality of the measurements. These issues should be addressed in the future work.
- Theoretical simulations reveal that it is possible to improve the accuracy of the positioning solutions along north direction by augmenting a hybrid BDMS with pseudolites. It needs to be further validated in the actual bridge monitoring. Whilst GLONASS demonstrated its potential by providing positioning solutions of uniformed accuracy, the integration of GPS with the future Galileo satellites to improve satellite geometry for bridge deformation purpose need to be explored. This is another area need to be studied.
- Relative tropospheric delay was recognised as a major error source when there was minor difference in the local microclimate at the two ends of a baseline. How to effectively reduce relative tropospheric delay when there are significant height differences between stations coupled by the differences in local microclimate needs to be investigated.
- Further software development in the realisation of a practical hybrid BDMS for continuous bridge deformation is recommended.

References

ADAC, 1999a. PCM-5516-*-16 Manual, Revision 1.2, ADAC Corporation, USA.

ADAC, 1999b. Universal Library Programming Manual, Revision 3.3, ADAC Corporation, USA.

Ashkenazi, V., Dodson, A.H., Moore, T. and Roberts, G., 1997. Monitoring the Movements of Bridges by GPS, ION GPS'97, 10th Int. Tech. Meeting of the Sat. Div. of the U.S. Inst. of Navigation, Kansas City, USA, September 1997, pp. 1165-1172.

Ashtech, 1998. Ashtech Office Suite for Survey (AOSS) User's Manual, Version 1.5, Spectra Precision terraSat GmbH, Germany and Ashtech Inc., USA.

Axelrad, P., Comp, C.J. and MacDoran, P.F., 1996. SNR Based Multipath Error Correction for GPS Differential Phase. IEEE Transactions on Aerospace & Electronic System, 32(2): 650-660.

Baker, H.C., 1998. GPS Water Vapour Estimation for Meteorological Applications. PhD Thesis, The University of Nottingham.

Baker, D.F., 1998. Multipath Modelling for the GPS, MSc Thesis, The University of Nottingham.

Barnes, J.B. and Cross, P.A., 1998. Processing Models for Very High Accuracy GPS Positioning. Journal of Navigation, 51(2): 180-193.

Bevis, M., Businger, S. and Chiswell, S., 1994. GPS Meteorology: Mapping Zenith Wet Delays onto Precipitable Water. Journal of Applied Meteorology, 33(March).

Bingley, R., Dodson, A., Penna, N., Teferle, N. and Baker, T., 2001. Monitoring the Vertical Land Movement Component of Changes in Mean Sea Level Using GPS: Results from Tide Gauges in the UK. J. of Spatial Engineering, 3(1):9-20.

Bingley, R., 2002. Tropospheric Delay. Personal Communication from: richard.bingley@nottingham.ac.uk [Accessed 25 April 2000].

Bock, Y., 2000. Instantaneous Geodetic Positioning at Medium Distances with the Global Positioning System. J. Geophys. Res., 105(B12): 28223-28253.

Britting, K.R., 1971. Inertial Navigation System Analysis. John Wiley and Sons, New York.

Brunner, F.K., Hartinger, H. and Richter, B., 2000. Continuous Monitoring of Landslides Using GPS: a Progress Report. In: S.J. Bauer and F.K. Weber (Editors), Proc. Geophys. Aspects of Mass Movements, Austrian Academy of Sciences, Vienna, pp. 75-88.

Bruton, A., 1997. Reduction of GPS Receiver Noise Using Adaptive Filters, ION GPS'97, 10th Int. Tech. Meeting of the Sat. Div. of the U.S. Inst. of Navigation, Kansas City, USA, September 1997, pp. 645-653.

Cantieni, R., 1983. Dynamic Load Testing of Highway Bridges. Transportation Research Record 950, National Academy of Sciences, Washington D. C.

Chatfield, C., 1984. The Analysis of Time Series: An Introduction. Chapman and Hall, London.

Chen, W., 1992. Integration of GPS and INS for Precise Surveying Applications. PhD Thesis, The University of Newcastle Upon Tyne.

Cooper, J.D., 1998. World's Longest Suspension Bridge Opens in Japan. Public Roads, 62(1): 32.

Cross, P., 2000. Prospects for GPS - New Systems, New Applications, New Techniques. Engineering Surveying Showcase 2000(1): 10-14.

Counselman, C.C., 1999. Multipath-Rejecting GPS Antennas. Proc. of the IEEE, 87(1): 86-90.

Dallard, P., Fitzpatrick, T., Flint, A., Low, A., Smith, R. R., Willford, M., and Roche, M., 2001. London Millennium Bridge: Pedestrian-Induced Lateral Vibration. Journal of Bridge Engineering, 6(6): 412-417.

Das, P.C., 1997. Safety of Bridges. Thomas Telford, London.

Dodson, A.H., Shardlow, P., J, Hubbard, L.C.M., Elgered, G. and Jarlemark, P.O.J., 1996. Wet Tropospheric Effects on Precise Relative GPS Height Determination. Journal of Geodesy, 70: 188-202.

Dodson, A.H., Meng, X. and Roberts, G., 2001. Adaptive Method for Multipath Mitigation and Its Applications for Structural Deflection Monitoring, International Symposium on Kinematic Systems in Geodesy, Geomatics and Navigation, June 5-8, 2001, Banff, Alberta, Canada.

Duff, K., 1997. Deformation Monitoring with GPS, Part 1: System Design and Performance, Symposium on Surveying of Large Bridge and Tunnel Projects (FIG).

Duff, K., 1998. Structural Deformation Monitoring with GPS: Operational Issues, Conference on Structural Materials Technology. Texas Department of Transportation.

Duff, K. and Hyzak, M., 1997. Structural monitoring with GPS. Public Roads, 60(4): 39-44.

Embree, P.M., 1995. C Algorithms for Real-Time DSP. Prentice Hall PTR, New Jersey.

Fairweather, V., 1996. Measuring Bridge Movement. Civil Engineering, ASCE, 66(6): 48.

Farrell, J. and Barth, M., 1999. The Global Positioning System and Inertial Navigation. McGraw-Hill, New York.

Feng, K., 1978. Numerical Methods. National Defence Press, Beijing.

Forward, T., Stewart, M., Penna, N. and Tsakiri, M., 2001. Steep Wall Monitoring Using Switched Antenna Arrays and Permanent GPS Network. Deformation Measurements and Analysis, 10th International Symposium on Deformation Measurements, March 2001, Orange, California, USA, pp. 33-41.

Fryba, L., 1996. Dynamics of Railway Bridges. Thomas Telford, London.

Fujino, Y., Murata, M., Okano, S. and Takeguchi, M., 2000. Monitoring System of the Akashi Kaikyo Bridge and Displacement Measurement Using GPS. In: A.E. Aktan and S.R. Gosselin (Editors), Nondestructive Evaluation of Highways, Utilities, and Pipelines IV, Proceedings of SPIE.

Ge, L., Chen, H.-Y., Han, S. and Rizos, C., 2000a. Adaptive Filtering of Continuous GPS Results. Journal of Geodesy, 74(2000): 572-580.

Ge, L., Han, S. and Rizos, C., 2000b. The Double Interpolation and Double Prediction (DIDP) Approach for InSAR and GPS Integration, The International Archives of Photogrammetry and Remote Sensing (IAPRS), XXIII, Amsterdam, Holland, pp. 205-212.

Geiger, A., 1988. Simulating Disturbances in GPS by Continuous Satellite Distribution. Journal of Surveying Engineering, 114(4): 182-194.

Gordon, S., Lichti, D. and Stewart, M., 2001. Application of High-Resolution, Ground-Based Laser Scanner for Deformation Measurements. Deformation

Measurements and Analysis, 10th International Symposium on Deformation Measurements, 19 - 22 March 2001, Orange, California, USA, pp. 23-32.

Guo, J. and Ge, S., 1997. Research of Displacement and Frequency of Tall Building under Wind Load Using GPS, ION GPS'97, 10th Int. Tech. Meeting of the Sat. Div. of the U.S. Inst. of Navigation, Kansas City, USA, September 1997, pp. 1385-1388.

Harding, J. E., Parke, G. A. R., and Ryall, M. J. (1996). Bridge Management 3: Inspection, Maintenance Assessment and Repair, E & FN Spon, London.

Haykin, S., 1996. Adaptive Filter Theory. Prentice-Hall, Upper Saddle River, NJ.

Hofmann-Wellenhof, B., Lichtenegger, H. and Collins, J., 1997. Global Positioning System: theory and practice. Springer-Verlag, Wien ; New York, xxii, 389 pp.

Hudnut, K.W. and Behr, J.A., 1998. Continuous GPS Monitoring of Structural Deformation at Pacoima Dam, California. Seismological Research Letter, 69(4): 299-308.

Hudnut, K.W., Bock, Y., Galetza, J.E., Webb, F.H. and Young, W.H., 2001. The Southern California Intergrated GPS Network (SCIGN). Deformation Measurements and Analysis, 10th International Symposium on Deformation Measurements, March 2001, Orange, California, USA, pp. 129-148.

Hyzak, M. and Leach, M., 1995. Bridge Monitoring by GPS. Surveying World, 3(3): 8-11.

Hyzak, M., 1997. Practical Application of GPS to Bridge Deformation Monitoring, the 64th FIG Permanent Committee Meeting and Symposium, Washington D. C.

IESSG, 1995. NOTF: Ambiguity Resolution OTF Software User Manual, Version 08.95, The University of Nottingham.

IESSG, 1997. CODA 3, Version 970206, The University of Nottingham.

IESSG, 1998. GPS Analysis Software (GAS) User Manual, Version 2.4, The University of Nottingham

Imakiire, T. and Nakahori, Y., 2001. GPS Earth Observation Network (GEONET) of Japan, New Technology for a New Century, FIG Working Week, Seoul Korea.

Ingle, V.K. and Proakis, J.G., 1997. Digital Signal Processing Using Matlab V.4. PWS Publishing Company, Boston, US.

Jaksic, J., 2001. Running Interference: Multipath Detection for GPS Monitoring Sites. GPS World, 12(2): 32-36.

Kashima, S., Yanaka, Y. and Mori, K., 2001. Monitoring the Akashi Kaikyo Bridge: First Experiences. Structural Engineering International, 11(2): 120-123.

Kistler, 1999. Operating Instructions, Kistler Instrument Corporation, USA.

Kistler, 2000. Accelerometer Calibration Certificate (8392A2), Kistler Instrument Corporation, USA.

Kleusberg, A., 1998. Atmospheric Models from GPS. In: P.J.G. Teunissen and A. Kleusberg (Editors), GPS for geodesy. Springer, Berlin.

Langley, R., 1998. Propagation of the GPS Signals. In: P.J.G. Teunissen and A. Kleusberg (Editors), GPS for Geodesy. Springer, Berlin, pp. 140-143.

Lawrence, A., 1998. Modern Inertial Technology: Navigation, Guidance, and Control. Mechanical Engineering Series. Springer, New York.

Leach, M., 1992. Results from a bridge Motion monitoring Experiment, Proceedings of Sixth International Geodetic Symposium on Satellite Positioning, The Ohio State University, pp. 801-810.

Leica, 1998. MC1000 GPS Receiver Installation, Operation, and Maintenance Manual, Revision D, Torrance, CA, USA.

Leica, 1999a. User Manual/Getting Started with SKI-Pro, Version 1.1, Leica Geosystems AG.

Leica, 1999b. MC-CDU Firmware V6.10, Leica Geosystems AG.

Leica, 2000. MC-CDU Firmware V8.02, Leica Geosystems AG.

Leica, 2001. SKI-Pro GPS Post-processing Software, version 2.1, Leica Geosystems AG.

Leica, 2002. Getting Started with Static and Kinematic Surveys, Leica Geosystems AG.

Lovse, J. L., Teskey, W. F., Lachepelle, G., and Cannon, M. E., 1995. Dynamic Deformation Monitoring of Tall Structure Using GPS Technology, Journal of Surveying Engineering, 121(1): 35-40.

Lowry, A. and MacLeod, R., 1997. PMoS^{TM} - A Real Time Precise DGPS Continuous Deformation Monitoring System, ION GPS'97, 10th Int. Tech. Meeting of the Sat. Div. of the U.S. Inst. of Navigation, Kansas City, USA, September 1997, pp. 923-927.

Mathworks, 2000. Matlab, Release 12, The Mathworks, Inc.

Meng, X., Liu, D. and Zhu, Z., 1996. NL Distribution Tests of Digitisation Errors. Journal of Tongji University, 24(5): 525-529.

Meng, X., 2000. First Year Report of PhD Study, IESSG, The University of Nottingham.

Meng, X., Roberts, G.W. and Dodson, A.H., 2001. Error Analysis and Positioning Precision Improvement in GPS/Accelerometer Structural Monitoring, IAG 2001 Scientific Assembly, 2-7 September 2001, Budapest, Hungary.

Meng, X., Roberts, G.W., Dodson, A.H., Cosser, E. and Noakes, C., 2002. Simulation of the Effects of Introducing Pseudolite Data into Bridge Deflection Monitoring Data. 2nd Symposium on Geodesy for Geotechnical and Structural Engineering, May 2002, Berlin.

Meo, M., Luliano, E. and Morris, A.J., 2002. Health Monitoring of Large Scale Civil Structures, Cranfield University.

Mikhail, E.M., 1976. Observations and Least Squares. IEP-A Dun-Donnelley Publisher, New York.

NCHRP, 1987. Bridge Management Systems. NCHRP Report 300, Transportation Research Board, National Research Council, National Academy Press, Washington, D.C.

NCHRP, 1990. Improvements in Data Acquisition Technology for Maintenance Management. NCHRP Report 334, Transportation Research Board, National Research Council, National Academy Press, Washington, D.C.

NCHRP, 1998. Dynamic Impact Factors for Bridges. NCHRP Synthesis 266, Transportation Research Board, National Research Council, National Academy Press, Washington, D.C.

Norgard, P., 1996. Deformation Survey of the Storebaelt Bridge: GPS Shows Its Merits. Geomatics Info, 10(4): 37-39.

OSGB, 2001. A guide to coordinate systems in Great Britain.

Oshima, T., Rahman, M., Muhamad, S., Mikami, S., Yamazaki, T, Takada, N., Lesko, J. and Kriz R., 2000. Application of Smart Materials and Systems to Long-term Bridge Heath Monitoring. In: A. E. Aktan and S. R. Gosselin (Editor), Proc. of Nondestructive Evaluation of Highways, Utilities, and Pipeline IV, SPIE Vol. 3995, pp. 253-263.

Parkinson, B.W., 1996. GPS Error Analysis. In: B.W. Parkinson, J.J. Spilker, P. Axelrad and P. Enge (Editors), Global Positioning System: Theory and Applications. AIAA, Washington, pp. 469-483.

Ray, J.K., Cannon, M.E. and Fenton, P., 1999. Code Range and Carrier Phase Multipath Mitigation Using SNR, Range and Phase Measurements in a Multi-Antenna System, ION GPS'99, 12th Int. Tech. Meeting of the Sat. Div. of the U.S. Inst. of Navigation, Nashville, September 1999, pp. 712-725.

Rizos, C., Han, S. and Roberts, A. C., 1997. Permanent Automatic Low-cost GPS Deformation Monitoring Systems: Error Mitigation Strategies and System Architecture, ION GPS'97, 10th Int. Tech. Meeting of the Sat. Div. of the U.S. Inst. of Navigation, Kansas City, USA, September 1997, pp. 909-917.

Rizos, C., Han, S., Ge, L., Chen, H.-Y., Hatanaka, Y., and Abe, K., 2000a. Low-cost Densification of Permanent GPS Networks for Natural Hazard Mitigation: First Tests on GSI's GEONET Network. Earth Planets Space, 52: 867-871.

Rizos, C., Han, S., Roberts, C. and Han, X., 2000b. Continuously Operating GPS-Based Volcano Deformation Monitoring in Indonesia: Challenges and Preliminary Results. Springer-Verlag, pp. 361-366.

Roberts, G., 1997. Kinematic GPS. PhD Thesis, The University of Nottingham.

Roberts, G.W., Dodson, A.H. and Ashkenazi, V., 1999. Twist and Deflection: Monitoring Motion of Humber Bridge. GPS World, 10(10): 24-34.

Roberts, G.W., Meng, X. and Dodson, A.H., 2000a. Structural Dynamic and Deflection Monitoring Using Integrated GPS and Tri-axial Accelerometers, ION GPS'2000, 13th Int. Tech. Meeting of the Sat. Div. of the U.S. Inst. of Navigation, Salt Lake City, USA, September 2000, pp. 59-68.

Roberts, G.W., Meng, X. and Brown, C.J., 2000b. The Use of GPS for the Measurement of Bridge Movements: A Viability Study, The University of Nottingham, Brunel University.

Roberts, G.W., Meng, X. and Dodson, A.H., 2001a. The Use of Kinematic GPS and Triaxial Accelerometers to Monitor the Deflections of Large Bridges. Deformation Measurements and Analysis, 10th International Symposium on Deformation Measurements, March 2001, Orange, California, USA, pp. 268-275.

Roberts, G.W., Meng, X. and Dodson, A.H., 2001b. Data Processing and Multipath Mitigation for GPS/Accelerometer Based Hybrid Structural Deflection

Monitoring System, ION GPS'2001, 14th Int. Tech. Meeting of the Sat. Div. of the U.S. Inst. of Navigation, Salt Lake City, USA, September 2001, pp.473-481

Roberts, G.W., Meng, X. and Dodson, A.H., 2002a. Using Adaptive Filtering to Detect Multipath and Cycle Slips in GPS/Accelerometer Bridge Deflection Monitoring Data, FIG XXII International Congress, Washington, D.C. USA, April 19-26 2002.

Roberts, G.W., Meng, X., Dodson, A.H. and Cosser, E., 2002b. Geodetic Signal Diagnosis and its Applications to Structural Deformation. 2nd Symposium on Geodesy for Geotechnical and Structural Engineering, May 2002, Berlin.

Santerre, R., 1991. Impact of GPS Satellite Sky Distribution. Manuscripta Geodaetica, 16(1991): 28-53.

Spilker, J.J., 1996. Tropospheric Effects on GPS. In: B.W. Parkinson and J.J. Spilker (Editors), Global Positioning System: Theory and Applications. AIAA, Washington, pp. 517-546.

Teferle, F.N., Bingley, R.M., Dodson, A.H., Penna, N.T. and Baker, T.F., 2001. Using GPS to Separate Crustal Movements and Sea Level Changes at Tide Gauges in the UK. In: H. Drewes (Editor), Vertical Reference Systems. International Association of Geodesy Symposium, Springer-Verlag.

Thompson, P.D., 1993. Bridge Management 2: PONTIS: the Maturing of Bridge Management Systems in the USA. Thomas Telford, London.

Titterton, D.H. and Weston, J.L., 1997. Strapdown Inertial Navigation Technology. Peter Peregrinus Ltd., London.

Tolman, B.W. and Craig, B.K., 1997. An Integrated GPS/Accelerometer System for Low Dynamics, International Symposium on Kinematic Systems in Geodesy, Geomatics and Navigation, June 1997, Banff, Alberta, Canada.

Wong, K.Y., Man, K.L. and Chan, W.Y., 2001. Monitoring Hong Kong's Bridges: Real-Time Kinematic Spans the Gap. GPS World, 12(7): 10-18.

Xu, Y.L., Sun, D.K., Ko, J.M. and Lin, J.H., 2000. Fully Coupled Buffeting Analysis of Tsing Ma Suspension Bridge. Journal of Wind Engineering and Industrial Aerodynamics, 2000(85): 97-117.

Young, C.A., 1998. Single Frequency OTF Kinematic GPS Bridge Deflection Monitoring. MSc Thesis, The University of Nottingham.

Appendix A

Series No. of Tests	Date for Tests	Data Rate (Sec.)	File Name (XXX.lb2)	Sensor Combinations	Start Time	End Time	Output File Name
1	11 Nov. 1999	0.1	Sen1_01 Sen2_01	1 & 2	16:12	16:26	Test3
2	11 Nov. 1999	0.2	Sen1_02 Sen2_02	1 & 2	16:33	16:49	Test4
3	11 Nov. 1999	0.5	Sen1_05 Sen2_05	1 & 2	16:52	17:09	Test 5
4	11 Nov. 1999	1.0	Sen1_10 Sen2_10	1 & 2	17:10	17:26	Test 6
5	12 Nov. 1999	2.0	Sen1_20 Sen2_20	1 & 2	10:54	11:13	Test 7
6	12 Nov. 1999	3.0	Sen1_30 Sen2_30	1 & 2	11:16	11:33	Test 8
7	12 Nov. 1999	4.0	Sen1_40 Sen2_40	1 & 2	11:35	11:56	Test 9
8	12 Nov. 1999	5.0	Sen1_50 Sen2_50	1 & 2	11:58	12:15	Test 10
9	15 Nov. 1999	1.0	Zo1_1sec Zo2_1sec	1 & 2	11:19	17:21	Test 12
10	15~16 Nov. 1999	10.0	Zo1_10se Zo2_10se	1 & 2	17:23 (15 Nov.)	16:20 (16 Nov.)	Test 13
11	16~18 Nov. 1999	10.0	Z124_10s Z224_10s	1 & 2	17:03 (16 Nov.)	9:54 (18 Nov.)	Test11
12	18 Nov. 1999	0.1	C1_3_01 C3_1_01	1 & 3	10:18	10:49	Test14
13	18 Nov. 1999	0.2	C1_3_02 C3_1_02	1 & 3	11:26	11:48	Test15
14	18 Nov. 1999	0.5	C1_3_05 C3_1_05	1 & 3	11:52	12:06	Test16
15*	18 Nov. 1999	1.0	C1_3_10 C3_1_10	1 & 3	10:53	11:24	Test17 (Test1)
16	18 Nov. 1999	10.0	C1_3_100 C3_1_100	1 & 3	12:20	13:52	Test18
17	18 Nov. 1999	0.1	C2_3_01 C3_2_01	2 & 3	14:20	14:35	Test19
18	18 Nov. 1999	0.2	C2_3_02 C3_2_02	2 & 3	14:38	15:08	Test20
19	18 Nov. 1999	0.5	C2_3_05 C3_2_05	2 & 3	15:10	15:36	Test21
20	18 Nov. 1999	1.0	C2_3_10 C3_2_10	2 & 3	15:37	15:54	Test22
21	18 Nov. 1999	10.0	C2_3_100 C3_2_100	2 & 3	15:55	16:26	Test23
22*	19~22 Nov. 1999	1.0	ZC2_3_10 ZC3_2_10	2 & 3	16:35 (19 Nov.)	11:43 (22 Nov.)	Test24 (Test2)
23	24~26 Nov. 1999	1.0	ZC1_2_10 ZC2_1_10	1 & 2	13:05 (24 Nov)	11:33 (26 Nov.)	Test25
24	26~30 Nov. 1999	30.0	Z1_2_300 Z2_1_300	1 & 2	13:59 (26 Nov.)	12:44 (30 Nov.)	Test26
25	2~3 Dec. 1999	30.0	Z1_3_300 Z3_1_300	1 & 3	10:16 (2 Dec.)	9:26 (3 Dec.)	Test27
26	3~6 Dec. 1999	30.0	Z2_3_300 Z3_2_300	2 & 3	10:15 (3 Dec.)	11:5 (6 Dec.)	Test28

* means two data sets were collected with the same data rate and instrument combination

A1. Details for the data logging and observation duration of ZBL tests (CRS1000)

Sat id :			17	22	6	3
hh:mm:ss	PDOP	GDOP				
21:37:50	17.6	18.0	65/109	76/237	22/ 80	36/264
21:38:00	18.2	18.7	65/109	76/237	22/ 80	36/264
21:38:10	18.9	19.3	65/109	76/236	22/ 80	36/264
21:38:20	19.6	20.1	65/108	76/236	22/ 80	36/264
21:38:30	20.4	20.9	65/108	76/236	22/ 80	36/264
21:38:40	21.2	21.7	65/108	76/235	22/ 80	36/264
21:38:50	22.1	22.6	65/108	76/235	22/ 80	36/264
21:39:00	23.1	23.7	65/108	76/235	22/ 80	37/264
21:39:10	24.2	24.8	65/107	76/234	22/ 80	37/264
21:39:20	25.4	26.0	65/107	76/234	22/ 80	37/264
21:39:30	26.8	27.4	65/107	76/234	22/ 80	37/264
21:39:40	28.3	28.9	65/107	76/233	22/ 80	37/264
21:39:50	29.9	30.6	65/107	76/233	21/ 80	37/264
21:40:00	31.8	32.5	65/106	76/233	21/ 80	37/264
21:40:10	33.9	34.7	65/106	76/232	21/ 80	37/264
21:40:20	36.4	37.1	65/106	76/232	21/ 81	37/264
21:40:30	39.2	40.0	65/106	76/232	21/ 81	37/264
21:40:40	42.5	43.4	65/106	76/231	21/ 81	37/264
21:40:50	46.4	47.3	65/106	76/231	21/ 81	37/264
21:41:00	51.1	52.1	65/105	76/231	21/ 81	37/264
21:41:10	56.8	58.0	65/105	76/230	21/ 81	37/264
21:41:20	64.0	65.3	65/105	76/230	21/ 81	37/264
21:41:30	73.3	74.8	65/105	76/230	21/ 81	38/264
21:41:40	85.8	87.5	65/105	76/229	21/ 81	38/265
21:41:50	--.-	--.-	65/104	76/229	21/ 81	38/265
21:42:00	--.-	--.-	65/104	76/229	21/ 81	38/265
21:42:10	--.-	--.-	65/104	76/228	21/ 81	38/265
21:42:20	--.-	--.-	65/104	76/228	21/ 81	38/265
21:42:30	--.-	--.-	65/104	76/228	20/ 81	38/265
21:42:40	--.-	--.-	65/103	76/227	20/ 81	38/265
21:42:50	--.-	--.-	65/103	76/227	20/ 81	38/265
21:43:00	--.-	--.-	65/103	76/227	20/ 81	38/265
21:43:10	--.-	--.-	65/103	76/226	20/ 81	38/265
21:43:20	--.-	--.-	65/103	76/226	20/ 81	38/265
21:43:30	98.2	--.-	65/102	76/226	20/ 81	38/265

A2. Partial data processing report (CRS1000)

Frequency used/X, Y, Z	**Mean (m)**	**Stdev (m)**	**Max_residual (m)**	**Min_residual (m)**
L1 Phase				
X	0.0001	0.0021	0.0081	-0.0076
Y	-0.0001	0.0011	0.0038	-0.0039
Z	-0.0001	0.0025	0.0075	-0.0079
L2 Phase				
X	0.0001	0.0067	0.0232	-0.0223
Y	0.0001	0.0032	0.0082	-0.0101
Z	0.0001	0.0065	0.0272	-0.0195
L1 Code (C/A)				
X	0.1032	0.1387	0.4961	-0.3105
Y	-0.0907	0.1018	0.1741	-0.5089
Z	0.0053	0.2004	0.5759	-0.6363
L2 Code (P)				
X	0.1710	0.4810	1.3643	-0.9497
Y	-0.0036	0.3250	0.7056	-0.8615
Z	0.1239	0.4531	1.5321	-0.9088

A3. Results for 10 Hz sampling rate (CRS1000, 1000 epoch observations)

Series No. of Tests	Date for Tests	Data Rate (Sec.)	Sensor Combinations	Type of Baselines
1	1 Feb 2000	0.1	1 & 2 1&2/3	ZBL SBL
2	1 Feb 2000	0.2	1 & 2 1&2/3	ZBL SBL
3	1 Feb 2000	0.5	1 & 2 1&2/3	ZBL SBL
4	2 Feb 2000	1.0	1 & 2 1&2/3	ZBL SBL
5	2 Feb 2000	2.0	1 & 2 1&2/3	ZBL SBL
6	3 Feb 2000	3.0	1 & 2 1&2/3	ZBL SBL
7	4 Feb 2000	4.0	1 & 2 1&2/3	ZBL SBL
8	4 Feb 2000	5.0	1 & 2 1&2/3	ZBL SBL
9	5, 6 June 2000	30.0	1 & 2	SBL
10	6 June 2000	1	1&2	SBL
11	6, 7 June 2000	30.0	1&2	SBL

A4. A list of partial SBL trials (CRS1000)